



UNIVERSITÀ  
DEGLI STUDI  
FIRENZE

## DOTTORATO DI RICERCA IN SCIENZE CHIMICHE

CICLO XXXI

COORDINATORE Prof. Piero Baglioni

### **How resonance Raman spectroscopy can give valuable insights into diverse aspects of heme protein structure and function**

Settore Scientifico Disciplinare CHIM/02

**Dottoranda**

Dott. Lisa Milazzo

---

*(firma)*

**Tutore**

Prof. Giulietta Smulevich

---

*(firma)*

**Coordinatore**

Prof. Piero Baglioni

---

*(firma)*

Anni 2015/2018



## INDEX

<b>Abbreviations</b>	<b>7</b>
<b>Abstract</b>	<b>9</b>
<b>Introduction: Raman spectroscopy from the 30's to 2018: old tools, new approaches</b>	<b>15</b>
<b>Chapter 1</b>	
<b>Methods</b>	<b>21</b>
1.1 UV-Vis and second derivative	21
1.2 Resonance Raman at room temperature	21
1.3 Resonance Raman at 80 K	22
1.4 Electron paramagnetic resonance	22
<i>References</i>	23
<b>Chapter 2</b>	
<b>Heme characterisation: spectroscopic techniques</b>	<b>25</b>
2.1 The heme group	25
2.2 Electronic absorption spectroscopy	28
2.3 Resonance Raman spectroscopy	30
2.3.1 High frequency: the core size marker bands	35
2.3.2 High frequency: the $\nu(\text{C}=\text{C})$ stretching modes of the vinyl substituents	37
2.3.3 Low frequency	38
2.3.3.1 The $\delta(\text{C}_\beta\text{C}_\alpha\text{C}_\delta)$ bending modes of the propionate substituents	38
2.3.3.2 The $\nu(\text{Fe}-\text{Im})$ stretching mode	38
2.3.3.3 Exogenous ligands	39
2.3.3.3.1 CO	41
2.3.3.3.2 O <sub>2</sub>	44
2.3.3.3.3 OH <sup>-</sup>	45
<i>References</i>	45

## Chapter 3

### **Cytochrome c as an apoptosis initiator: unravelling the non-native state of the Cytochrome c–Cardiolipin complex**

	<b>49</b>
3.1 Introduction	49
3.2 Materials	57
3.3 Ferric form	60
3.3.1 Cyt c (WT) titration with CL	60
3.3.2 Misligated model compounds	64
3.3.3 His-Fe-His ligation in the Cyt c-CL complex	69
3.3.4 Mutated proteins	69
3.3.4.1 K727273N, K7273N/H26Y, K7273N/H33Y, and H26H33N	69
3.3.4.2 K72A, K72N, K73A, and K73N	76
3.4 Ferrous form	78
3.5 Ferrous-CO adduct	81
3.6 Conclusions	84
<i>References</i>	85

## Chapter 4

### **Resonance Raman structural markers of the coproheme-bound coprohemedecarboxylase from *Lysteria monocytogenes* to follow the catalytic conversion into heme *b***

	<b>91</b>
4.1 Introduction	91
4.2 Materials	97
4.3 The coproheme-WT and -M149A complexes	99
4.3.1 Ferric form: UV-Vis and RR spectra at room temperature	101
4.3.2 Coproheme-WT complex: 5cQS species	105
4.3.3 Coproheme-M149A: 6cLS His-Fe-Gln species	109
4.3.4 Structural information and ferrous form	113
4.3.5 Ferrous-CO adducts	115
4.4 The coproheme complexes of other key residue mutants	121
4.5 The heme <i>b</i> complexes	125
4.6 Assignment of the propionate bending modes	129

4.6.1 Coproheme complexes	130
4.6.2 Heme <i>b</i> complexes	137
4.7 Titration of the coproheme-M149A complex with H <sub>2</sub> O <sub>2</sub>	139
4.8 Conclusions	142
<i>References</i>	143

## **Chapter 5**

### **Resonance Raman to prove the lack of orientation selectivity of the heme insertion murine Neuroglobin**

5.1 Introduction	147
5.2 Materials	151
5.3 Ferric form	152
5.3.1 The WT and the double Gly-loop/F106A mutant	152
5.3.2 Comparison with the single Gly-loop and F106A mutants	160
5.4 Ferrous form	162
5.5 Ferrous-CO adduct	165
5.6 Conclusions	171
<i>References</i>	171

## **Chapter 6**

### **Ligand binding in the truncated hemoglobin of the Antarctic marine bacterium *Pseudoalteromonas haloplanktis* TAC125, Ph-trHbO-2217**

6.1 Introduction	175
6.2 Materials	178
6.3 Structural comparison	179
6.4 Ferric form	182
6.5 Ferrous form	191
6.6 Ferrous-CO adduct	193
6.7 Conclusions	195
<i>References</i>	196

## **Chapter 7**

### **The structural similarity of the heme crevice of the hemoglobins of the Greenland shark *Somniosus microcephalus* with that of human**

<b>hemoglobin</b>	<b>199</b>
7.1 Introduction	199
7.2 Materials	200
7.3 UV-Vis and Resonance Raman characterization	201
7.4 Ferric form	207
<i>References</i>	<i>208</i>

## Abbreviations

5c	Five-coordinated
6c	Six-coordinated
Cyt c	Cytochrome c
CCD	Charge coupled device
CCP	Cytochrome c peroxidase
ChdC	Coproheme decarboxylase
CL	Cardiolipin
CT	Porphyrin-to-iron charge transfer band
EPR	Electron paramagnetic resonance
Gly-loop	YNGR → GGGG Ngb mutant
Hb	Hemoglobin
HEPES	2-[4-(2-hydroxyethyl)piperazin-1-yl]ethanesulfonic acid
HF	High frequency
HH	Horse heart
HRP	Horseradish peroxidase
HS	High spin
IS	Intermediate spin
ImH	Imidazole
LF	Low frequency
Lm	Listeria monocytogenes
LS	Low spin
LT	Low temperature
Mb	Myoglobin
MES	2-(N-morpholino)ethanesulfonic acid
Ngb	Neuroglobin
NMR	Nuclear magnetic resonance
PBS	Phosphate buffer saline
PDB	Protein data bank
Ph	Pseudoalteromonas haloplanktis TAC125
QS	Quantum-mechanically mixed spin
RR	Resonance Raman
RT	Room temperature

S. microcephalus	Somniosus microcephalus
Sa	Staphilococcus aureus
SDS	Sodium dodecyl sulphate
SW	Sperm whale
Tf	Thermobifida fusca
trHb	Truncated hemoglobin
trHbO	Truncated hemoglobin of group II
UV-Vis	Ultraviolet-visible
WT	Wild type

## **Abstract**

Resonance Raman (RR) spectroscopy complemented by UV-Vis absorption spectroscopy is a very powerful technique to investigate the structure-function relationships of heme proteins, a widely distributed and biological relevant class of proteins which can play different biological functions. Since the protein activity is tightly linked to the structure of the heme active site, my study has been devoted to the investigation of several heme proteins involved in important biological processes, to obtain a comprehensive spectroscopic signature, with the aim to highlight the relationship between the heme pocket architecture and the protein function. The studies were carried out on native proteins and selected site-directed mutants, at both room (298 K) and low (80 K) temperature, at various pH, and in presence of various exogenous ligands, spanning the excitation wavelengths from UV to the visible region.

### **Unravelling the non-native state of the Cytochrome c–Cardiolipin complex**

Cytochrome c (Cyt c) is a heme protein with His18 and Met80 as the axial ligands, which undergoes structural variations during the apoptotic process; such changes have been related to modifications occurring in the protein when it forms a complex with cardiolipin, one of the phospholipids constituting the mitochondrial membrane. Although several studies have been performed to identify the misligated species that are formed upon protein-lipid interaction, their nature was still unidentified and it was a matter of debate.

To gain better insights into the Cyt c-CL interaction, I have studied the formation of the CL complex of the ferric horse heart Cyt c, wild type (WT) and selected mutants in which the residues that could replace Met80 as distal ligand (His26, His33, Lys72, Lys73, Lys79) have been mutated.

The titration of Cyt c WT with CL shows that a partial Met80 detachment is observed at very low CL concentration (Cyt c:CL molar ratio of 1:5) with the formation of a misligated form. The

comprehensive spectroscopic results (UV-Vis, RR, and EPR) on the native and selected key mutants, allowed me to unambiguously assigned the misligated form to a 6cLS bis-His species. Since neither His26 nor His33 are located in proximity of the heme iron, the formation of a bis-His species indicates that the extent of the protein rearrangement is long ranging, leading to a more flexible heme structure than in the native protein.

Moreover, I have studied a series of apolar and charged mutants of the Lys residues located at positions 72 and 73 to better define their role in the Cyt c-CL recognition process. The results allowed to conclude that while the 72 position must be occupied by a positively charged residue to assure Cyt c-CL recognition, the 73 position influences the peroxidase activity of the CL-bound protein.

### **Structural markers of the coproheme-coprohemedecarboxylase complex to follow the catalytic conversion into heme *b***

Coprohemedecarboxylase (ChdC) from *Listeria monocytogenes* (*Lm*) is an enzyme that in presence of H<sub>2</sub>O<sub>2</sub> catalyzes the last step of a recently discovered alternative heme biosynthetic pathway, involving the decarboxylation of the propionate group in position 2 and 4 of coproheme into vinyl, thus turning the coproheme in heme *b*.

To obtain a better insight into the structure-function relationships, using UV-Vis and RR spectroscopy at 298 and 80 K, with different excitation wavelengths spanning from 356.4 to 441.6 nm, I have characterized the coproheme- and heme *b*-*Lm*ChdC complexes of WT and selected variants, where residues considered to play an important role in maintaining the active site structure or in the catalytic mechanism have been mutated.

My main findings are: i) the native ferric form of coproheme-ChdC WT is a 5cQS species which is very unusual in biological systems; ii) the residues which are H-bonded with the propionate in position 2 and 4 are crucial to maintain the architecture and stability of the protein: when mutated in the non H-bonding Ala, a 6cLS species with the Gln187 residue as distal ligand is formed. Moreover the data on the CO adducts show that the Met149 residue located near the p2 has an important role

in keeping the Gln187 residue correctly positioned for the closure of the distal cavity; iii) the work on mutants involved in the H-bonds with the propionates groups, allowed to obtain the assignment of the p2, p4, p6, and p7 propionate bending modes; iv) the UV-Vis (298 K) and RR (80 K) titration of coproheme-ChdC with H<sub>2</sub>O<sub>2</sub>, allowed to follow the enzymatic decarboxylation of the coproheme propionate groups in position 2 and 4 which are progressively turned into vinyl groups.

### **The lack of orientation selectivity of the heme insertion murine Neuroglobin**

Neuroglobin (Ngb) is a globin predominantly expressed in neurons and it clearly seems to be involved in neuroprotection. The crystal structure of ferric murine WT Ngb reveals the presence of two 6cLS bis-His species, which differ for the heme insertion, being 180° rotated one to each other with respect to the  $\alpha$ - $\gamma$  meso axis, namely reversed (A, 70% occupancy) and canonical (B, 30% occupancy) conformers.

With my work, for the first time it was possible to identify by RR a reversed heme insertion. In fact, the RR data of WT and selected mutants (with enhanced CO binding capabilities) show a double set of core size marker bands, confirming the presence of two 6cLS species, a canonical, with a distorted heme and bigger core size, and a reversed form, with planar heme and smaller core. The canonical conformer slightly increases in the mutants at the expense of the reversed one. Moreover, only the 4-vinyl group appears to be markedly affected by the heme flipping, changing from the *trans* (canonical) to the *cis* conformation (reversed) as observed from the up-shift of the  $\nu(\text{C}=\text{C})$  stretching frequency.

Despite the native 6cLS coordination, exogenous ligands, such as O<sub>2</sub>, NO and CO, bind the Ngb heme iron by replacement of the distal His residue, being the bis-His endogenous ligation proposed as a unique mechanism for affinity regulation and ligand discrimination. However, its exact mechanism of action still remains to be clarified. To shed light on key features potentially related to Ngb mechanism of action, I studied the CO complexes of mutants with enhanced CO binding capabilities either at the proximal heme side, F106A (the Phe106

hindrance is the main obstacle to the heme sliding deeper in the cavity), or in the CD-loop (which govern the ligand affinity), Gly-loop, and the double Gly-loop/F106A. The RR spectra of the CO-adducts are similar to those previously obtained for other Ngb, suggesting the existence of two Ngb conformations after CO binding: one where the distal His64 strongly interacts with the CO, closing the distal cavity, and one with His64 swung out far from the CO, leaving the distal cavity open.

In the RR spectrum of the CO-bound Gly-loop mutant there is an increased fraction of the open conformation as compared to the WT. This supports the crystallographic data on this mutant that reveal an intermediate state with a swung out His64, but, due to the hindrance of the F106 residue, with the heme still in the unslid position. Accordingly when the F106 residue is removed in the double Gly-loop/F106A mutant, after His swinging out, the heme slides down deeper in the cavity with a partial His64 closing as indicated by the RR data showing that the open/closed conformation ratio is restored to a value similar to the WT.

### **Ligand binding in the bacterial truncated hemoglobin Ph-trHbO-2217**

Truncated Hemoglobins (trHb), globins showing the two-on-two (2/2)  $\alpha$ -helical-sandwich motif, are divided in four groups and the cold-adapted Antarctic marine bacterium *Pseudoalteromonas haloplanktis* TAC125 contains two genes, *PSHAA0030* and *PSHAA2217*, encoding two different trHbs of group II (O): Ph-trHbO-0030 and Ph-trHbO-2217. The aim of my work is to obtain structural information about Ph-trHbO-2217 and compare the results with those previously obtained for Ph-2/2HbO-0030 and for another well characterized trHb of group II, *Thermobifida fusca* (Tf-trHbO) from the thermophilic actinobacterium to highlight the differences in ligand binding and stabilization.

The comparison showed that at neutral pH the internal ligand-coordination is different, giving rise to a 6cHS aquo species in equilibrium with a 6cLS form where the distal residue is an hydroxo ion in Tf-trHbO and a tyrosinate ion (likely due to TyrB10) in Ph-trHbOs.

This latter form, however, is present only in solution, as the 6cHS aquo state is the stable form observed in crystals.

Moreover, despite the high similarity of the distal cavities (the residues in positions G8 (Trp) and B10 (Tyr) are conserved, while the CD1 is a Tyr in Tf-trHbO and a His in the Ph-trHbOs) the ligand binding capability of these three proteins is quite different, being stronger in Tf-trHbO. Moreover the finding that Ph-trHbO-2217 binds ligands more strongly than Ph-trHbO-0030 indicates that the ligand binding mechanism is not determined exclusively by interactions with distal polar residues, but that other changes in the sequence are also involved, being accordingly the sequence identity between the two Antarctic trHbs of only the 24%. This different behavior might be correlated to possible different functional roles in bacterial physiology of the two proteins, taking into account that the axial ligand strength is a fundamental property of a heme protein, capable of influencing the kinetics of ligand binding as well as providing alternative functional roles.

### **The heme crevice of the hemoglobins of the longest-living shark *Somniosus microcephalus***

*Somniosus microcephalus* (a shark living mainly in the Arctic Ocean) is one of the longest-living vertebrate species, with the largest captured animal (502 cm) estimated to be almost 400 years old. The remarkable evolutionary success of such species has raised considerable interest in their respiratory control mechanisms. Therefore my aim is to study the structural properties of the three Hb isoforms (Hb1, Hb2, Hb3) of *S. microcephalus* to gain information on the heme cavity, oxidation and coordination states. The heme cavities of the three isoforms are identical both in the ferric and ferrous forms. In the ferric state the proteins undergo an alkaline transition from a pure 6cHS aquo species at pH 5.0 to His-Fe-OH<sup>-</sup> ligated forms, both 6cHS and 6cLS at pH 10.6; in the ferrous form the proteins are all 5cHS, being the  $\nu(\text{Fe-Im})$  of the  $\alpha$  and  $\beta$  subunits at 207 cm<sup>-1</sup> and 217 cm<sup>-1</sup>, respectively. Moreover the three Hb isoforms equally bind O<sub>2</sub> and CO ligands.

The results suggest that the *S. microcephalus* Hbs are structurally very similar to human HbA rather than to other Hbs from cold-adapted organisms where a hemichrome species (His-Fe-His) is the main form around pH 7.0. Accordingly, functional studies revealed no evidence for differentiation among the three isoforms, similar to other cartilaginous fishes, and also no cold-adaptation patterns to Arctic environment were found in the structure/function relationship of *S. microcephalus* Hbs.

## **Introduction**

### **Raman spectroscopy from the 30's to 2018: old tools, new approaches**

Raman spectroscopy was named after Sir Chandrasekhara Venkata Raman (7 November 1888 – 21 November 1970), an Indian physicist born in India, who won the Nobel Prize for Physics in 1930 for his studies on light scattering.

During the 30's, 40's and 50's [1] spectra were recorded with Hg lamps, prism spectrographs, and photographic plates. With this setup the required integrating time was of days. Moreover, the presence of particles in solution was extremely detrimental, since they would have produced a flash of light that would have ruined the plate. Therefore, the samples had to be extensively purified through multiple distillations, a very long process.

Since that time, the instrumentation has evolved, benefiting from the technological advances. A major turning point was the introduction of lasers which provided a very intense and monochromatic light source for the sample excitation. The first one was built in 1960 [Maiman 1960, Townes 2007] and few years later, in 1966, the first commercial Raman instrument using dispersive gratings and laser as an excitation source, was introduced. Between the 60's and the 70's collection of the spectra took advantage from the use of double and a triple monochromator which reduce stray light by achieving high cut-off values (Coderg, Horiba). In particular, the triple setup greatly improves the spectral resolution. In those years the first tunable lasers [Duarte 1990, Schafer 1990], enabling to select the excitation wavelength, greatly broadened the use of Raman technique [Johnson 1976].

Another important step was the invention of the charge coupled device (CCD) in 1969. Its development progressed at rapid rate and during the 80's was used as detector in Raman spectroscopy, strongly improving

the signal-to-noise ratio (mainly thanks to the multichannel design and to the high quantum efficiency) and providing spectral acquisition at least ten times faster than the conventional instruments [Adar 2007].

Fourier transform (FT) Raman spectroscopy systems have been available since 1987. Commercial systems use a Nd: YAG laser (1064 nm) with a near-infrared interferometer coupled to either a liquid nitrogen cooled germanium (Ge) or indium gallium arsenide (InGaAs) detector. When it was introduced, FT-Raman had three main advantages over the dispersive Raman systems available: i) good for sample that exhibit laser-induced fluorescence; ii) easy operation as with an FT-IR spectrometer; iii) high spectral resolution with good wavelength accuracy. The rationale was that fluorescence was largely eliminated. Thus, high-quality spectra of dyes, for instance, could be obtained that had formerly been impossible. Unfortunately, overtones and combinations of H<sub>2</sub>O vibrations possess significant absorbance in the near IR spectra of aqueous solutions.

Another breakthrough in Raman spectroscopy was the coupling of a microscope to a Raman setup to collect Raman signals from crystals and sample regions as small as few  $\mu\text{m}$  [1]. In fact, through the microscope objective the laser beam could be tightly focused at the sample and simultaneously the Raman light could be efficiently collected. Moreover, these systems allowed to obtain 2D images of the analysed samples. The first Raman microscope (1976) named MOLE<sup>TM</sup> (Horiba) was followed years after (1990) by the confocal Micro Raman that allowed to obtain 3D images of the analysed samples.

Current trends in the development of the instrumentation point towards the miniaturization of the devices, in order to make them easily transportable and suitable for in situ analysis. This process has particularly benefited from the development of optical fibres and the improvement of laser sources and CCD devices and nowadays, there are compact and portable Raman instruments in a wide range of emission wavelengths from the visible to the near infrared [Carron 2010].

Thanks to all these technological advancements, that have made easier-to-use, very sensitive, and compact instruments, Raman

spectroscopy has become a worldwide applied spectroscopic technique both in various academic research fields and in industrial laboratories.

Some examples of applications include [2]:

- acquisition of chemical information from cells without genes manipulation, staining or antibodies marking;
- investigation of the many different carbon structures, and of the new materials used in nanotechnology;
- development of both existing and next generation photovoltaic technologies;
- identification of chemical materials, as well as qualitative and quantitative determination, with no damage;
- investigations of cultural items;
- contaminant identification;
- forensic science applications.

In the academic research fields since the 70's resonance Raman (RR) spectroscopy has been applied to the study of the very widely distributed and biological relevant class of heme proteins, all containing as prosthetic group the heme chromophore which is the responsible of the biological activity. RR is particularly suitable for the study of this kind of complex biological systems because using an exciting wavelength close (in resonance) to the electronic transition of the heme chromophore, only its vibrational modes are selectively enhanced, with a consequent simplification of the vibrational spectrum. Other advantages of RR in studying heme proteins are:

- the possibility to perform the experiments under physiological conditions, in fact, since water has a negligible Raman scattering, protein samples are usually dissolved in the appropriate buffer;
- minimal sample degradation or damage (under appropriate experimental conditions);
- small sample volume (down to 35  $\mu\text{L}$ ) and low protein concentration (between 10 and 200  $\mu\text{M}$ ) are needed;
- the possibility to obtain protein crystal spectra via the micro Raman apparatus and compare them with the crystallographic

data [Smulevich 1993]. In recent times, an important extension of the micro Raman technique is its application to the detection of crystal-induced alteration by X-ray irradiation in situ.

- RR spectra at low temperature have an increased spectral resolution due to the reduction of the bandwidth.

Extensive isotopic labeling studies and normal mode calculations of model porphyrins and, more recently, on heme proteins allowed to extract reliable structural information. Moreover, relationships between the frequency of specific vibrational modes and the heme cavity structure have been established (see Chapter 2).

In the 80's both the polymerase chain reaction (PCR) and site-directed mutagenesis processes were developed by Kary B. Mullis and Michael Smith who won the Nobel Prize in Chemistry in 1993 for their contribution. These methods allow to make multiple copies (amplification) of a specific DNA segment and to make specific and intentional changes to the DNA sequence of a gene, respectively.

These novel findings opened new opportunities for studying the heme proteins structural features which are linked to the functional role: in 1988, for the first time, it was shown that single point mutation of a key residue, resulted in marked alterations in the heme cavity and even in the Fe-ligands interactions, easily detectable by RR. This demonstrated that the combination of site-directed mutagenesis with the RR technique is a powerful approach to highlight proximal and distal dynamic interactions and H-bonds which are important for the protein reactivity [Smulevich 1988].

As described, technological improvements and the large knowledge acquired during years of study have made RR spectroscopy an extremely useful tool to investigate the structure-function relationships of heme proteins.

In my thesis I describe an integrated approach using RR spectroscopy at its full potential, complemented with other spectroscopic techniques, to obtain a comprehensive spectroscopic signature, to investigate heme proteins involved in important biological processes, taking into account the spectral characteristics of each protein. In this respect, an essential

requirement for my work was the findings of specific spectroscopic markers characterizing the protein or the biological mechanism. Moreover, structural information on selected molecular vibrations has been obtained by site-specific isotope or site-directed mutations.

I carefully design the experiments for each individual project, considering the necessity of specific sample preparation and measurement conditions.

A molecular understanding of biochemical reactions and of the structure-function relationships is essential for both fundamental and applied life sciences.

## References

- ❖ [1] [https://www.horiba.com/en\\_en/50yearsraman/](https://www.horiba.com/en_en/50yearsraman/)
- ❖ [2] <https://www.renishaw.com/en/raman-spectroscopy--6150>
- ❖ Adar F., Delhaye M., DaSilva E., J. Chem. Educ. 2007, 84, 50.
- ❖ Carron K., Cox R., Anal. Chem. 2010, 82, 3419.
- ❖ Duarte F.J., Hillman L.W., (1990). Introduction. In Dye laser principles with applications (Duarte F.J., Hillman L.W. Eds.) pp 1-11, Academic Press Inc., San Diego.
- ❖ Johnson B.B., Peticolas W.L., Ann. Rev. Phys. Chem. 1976, 27, 465.
- ❖ Maiman, T.H., Nature 1960, 187, 493.
- ❖ Schafer F.P. (1990) Dye Lasers. In Topics in Applied Physics (Schafer F.P. Ed.) Chapter 1, Springer, Berlin.
- ❖ Smulevich G., Mauro J.M., Fishel L.A., English A.M., Kraut J., Spiro T.G., Biochemistry 1988, 27, 5477.
- ❖ Smulevich G., Mauro J.M., Fishel L.A., English A.M., Kraut J., Spiro T.G., Biochemistry 1988, 27, 5486.
- ❖ Smulevich G., Spiro T.G., Methods in Enzymology 1993, 226, 397.
- ❖ Tompsett M.F., Amelio G.F., Smith G.E., Applied Physics Letters 1970, 17, 111.
- ❖ Townes C.H., Nature 2007, 447, 654.



# Chapter 1

## Methods

### 1.1 UV-Vis absorption

Electronic absorption spectra were recorded using a 5 mm NMR tube (300 nm min<sup>-1</sup> scan rate) or a 1 mm cuvette (600 nm min<sup>-1</sup> scan rate) at 25 °C by means of a Cary 60 spectrophotometer (Agilent Technologies, Glostrup, Denmark) with a resolution of 1.5 nm. Absorption spectra were measured both prior and after RR measurements to ensure that no degradation occurred under the experimental conditions used. The second derivative spectra (D<sup>2</sup>), have been obtained with the Savitzky–Golay method using 15 data points (LabCalc, Galactic Industries, Salem, NH, USA). No changes in the wavelength or in the bandwidth were observed when the number of points was increased or decreased.

### 1.2 Resonance Raman at room temperature

The RR spectra were obtained at 25 °C using a 5-mm NMR tube by excitation with the 356.4, 406.7, 413.1 nm lines of a Kr<sup>+</sup> laser (Innova 300 C, Coherent Inc., Santa Clara, CA, USA), the 441.6 nm line of a He–Cd laser (Kimmon IK4121R-G, Kimmon Koha Co. LTD, Tokyo, Japan), the 514.5 nm line of an Ar<sup>+</sup> laser (Innova 90/5, Coherent Inc., Santa Clara, CA, USA) and the 532.3 nm line of a diode pumped solid state laser (Cobolt Samba 05-01 series, Solna, Sweden). Backscattered light from a slowly rotating NMR tube was collected and focused into a triple spectrometer consisting of two Acton Research SpectraPro 2300i and a SpectraPro 2500i in the final stage with 3600 grooves/mm and 1800 grooves/mm gratings (all Princeton Instruments Trenton NJ, USA), working in the subtractive mode, and equipped with a liquid nitrogen-cooled charge coupled device (CCD) detector. A spectral resolution of 4 cm<sup>-1</sup> and spectral dispersion 1.2 cm<sup>-1</sup>/pixel were calculated theoretically on the basis of the optical properties of the

spectrometer. When necessary to avoid photolysis and minimize sample degradation induced by irradiation, a cylindrical lens, which focuses the laser beam in the sample to a narrow strip rather than the usual point, was used (see figure captions). The RR spectra were calibrated with indene, carbon tetrachloride and acetonitrile as standards to an accuracy of  $1\text{ cm}^{-1}$  for intense isolated bands. All RR measurements were repeated several times under the same conditions to ensure reproducibility. To improve the signal-to-noise ratio, a number of spectra were accumulated and summed only if no spectral differences were noted. All spectra were baseline-corrected.

A spectral simulation program (LabCalc, Galactic Industries, Salem, NH, USA) using a Lorentzian line shape was used to determine the peak-positions, bandwidth, and intensity. The frequencies of the bands were optimized to an accuracy of  $1\text{ cm}^{-1}$  and the bandwidths (full width at half-maximum, in the range of  $9\text{--}14\text{ cm}^{-1}$ ) to an accuracy of  $0.5\text{ cm}^{-1}$ .

### **1.3 Resonance Raman at 80 K**

For the low temperature experiments, a  $50\text{ }\mu\text{L}$  drop of the sample was put in a  $1.5\text{ cm}$  diameter quartz crucible that was positioned in a THMS600 cryostat (Linkam Scientific Instruments, Surrey, UK) and frozen. After freezing the sample, the cryostat was positioned vertically in front of the triple spectrometer and the laser light was directed onto the quartz window. To avoid sample denaturation or photo-reduction, the laser position was changed frequently and, when necessary, a cylindrical lens, which focuses the laser beam in the sample to a narrow strip rather than the usual point, was used. The sample temperature was maintained at  $80\text{ K}$ .

### **1.4 Electron paramagnetic resonance**

Performed by Professor Maria Fittipaldi (University of Florence) for the experiments relative to Chapter 3 and 6, and by Professor Rebecca Pogni's group (University of Siena) for the experiments relative to Chapter 3. EPR spectra were recorded with an Elexsys E500 instrument (Bruker, Rheinstetten, Germany), equipped with a NMR gaussmeter and a microwave frequency counter. An ESR 900 cryostat (Oxford

Instruments, Abingdon, U.K.) was used to obtain low temperatures. Spectra were acquired under nonsaturating conditions using a 1 mT modulation amplitude, and the temperature and microwave power for each sample are reported in the figure captions. The  $g$  values were determined by careful visual inspection of the spectra.

Performed by Professor Christian Obinger's group (BOKU University, Vienna) for the experiments relative to Chapter 4.

EPR was performed on a Bruker EMX continuous wave (cw) spectrometer, operating at X-band (9 GHz) frequencies. The instrument was equipped with a high sensitivity resonator and an Oxford Instruments ESR900 helium cryostat. Spectra were recorded under nonsaturating conditions using 2 mW microwave power, 100 kHz modulation frequency, 1 mT modulation amplitude, and 40 ms conversion time, 40 ms time constant, and 2048 points. Samples (100  $\mu$ L of 100–300  $\mu$ M) were prepared in 50 mM Hepes buffer, pH 7.0, transferred into Wilmad quartz tubes (3 mm inner diameter), and flash frozen in liquid nitrogen. In order to remove O<sub>2</sub>, the tubes were flushed with argon while the sample was kept frozen on dry ice. The measurements were performed at 10 K, after testing temperatures between 4 and 20 K to determine the optimum nonsaturating experimental conditions. The spectra were simulated with the Easyspin toolbox for Matlab [Stoll 2006] using a weighted sum of simulations of the individual high-spin (HS) and low-spin (LS) species. The rhombicity was obtained from  $g_x^{\text{eff}}$  and  $g_y^{\text{eff}}$  and the relative intensities were calculated on the basis of the simulations, following the procedure of Aasa and Vänngard to account for the different integral intensity per unit spin of species that display different effective  $g$  values (as found in LS and HS centres) [Peisach 1971, Aasa 1975].

## References

- ❖ Aasa R., Vänngard T., *J. Magn. Reson.* 1975, 19, 308.
- ❖ Peisach J., Blumberg W.E., Ogawa S., Rachmilewitz E.A., Oltzik R., *J. Biol. Chem.* 1971, 246, 3342.
- ❖ Stoll S., Schweiger A., *J. Magn. Reson.* 2006, 178, 42.



## Chapter 2

### Heme characterization: electronic absorption and Resonance Raman spectroscopies

#### 2.1 The heme group

Heme (also called iron-protoporphyrin IX) is the prosthetic group of a large number of proteins, called therefore hemeproteins.

There are several biologically important kinds of heme which show structural differences one to each other. The heme prosthetic group of the proteins that I studied during my PhD is of the *b* (the most widely distributed type, examples of protein with this kind of heme are: myoglobin, haemoglobin, heme containing peroxidases, neuroglobin, truncated hemeoglobin) and *c* (characteristic of cytochromes, see Chapter 3) kind.

Heme *b* (**Figure 2.1**) and *c* differ for the 2 and 4 substituents of the protoporphyrin IX ring which is an aromatic macrocycle constituted by four pyrrole rings connected by unsaturated carbon atoms. The pyrrole nitrogens are the four equatorial ligands of the iron atom lying in the central cavity. The two axial position can be occupied by one or two axial ligand(s) (5 and 6-coordination, respectively). The tetrapyrrole ring contains different peripheral substituents: in positions 1, 3, 5, 8 there are four methyl groups; in positions 6 and 7 there are two propionate groups; in position 2 and 4 in heme *b* there are two vinyl groups that become saturated being involved in a covalent bond with Cys residues in heme *c*.

Whereas free hemes adopts a planar structure due to extensive delocalization of the electrons in the porphyrin ring, the constraints imposed on the heme group by the protein matrix may result in a deformation away from planarity.

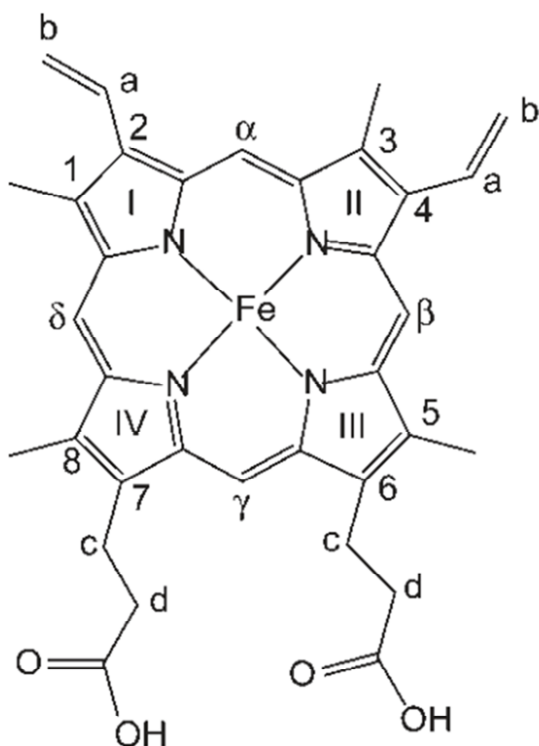


**Figure 2.1.** Structure and labelling of heme *b* (iron-protoporphyrin IX).

In heme proteins the iron can assume two stable oxidation states: the ferric (that has five valence electrons in its 3d orbitals) and the ferrous (that has six valence electrons in its 3d orbitals) forms. In absence of axial ligands the five 3d orbitals are energetically equivalent (degenerate), however, the presence of axial ligands introduce an external perturbation and the 3d orbitals split in two energetically different groups separated by the energy of the ligand-field [Gouterman 1979]: at lower energy there are the  $d_{xy}$ ,  $d_{xz}$ ,  $d_{yz}$  orbitals ( $t_{2g}$  orbitals) whose nodal planes are oriented in the x, y, and z directions; at higher energy there are the  $d_{x^2-y^2}$ ,  $d_{z^2}$  orbitals ( $e_g$  orbitals) whose lobes are oriented in the directions of the ligands.

Therefore, (**Figure 2.2**), when the axial ligands are weak or, as in the 5-coordinate forms, the sixth ligand is missing, the energy difference between the  $e_g$  and  $t_{2g}$  orbitals is smaller than the spin pairing energy, and the electrons occupancy of the orbitals follows the Hund's rule

resulting in a high spin (HS) with the total spin quantum number  $S=5/2$  for ferric heme.

An increase in the  $d_{x^2-y^2}$  orbital energy will favour pairing of the fifth electron in the  $d_{xy}$  orbital, giving rise to an intermediate spin (IS) state,  $S=3/2$  for ferric heme. A particular case is represented by the quantum mechanically mixed spin (QS) state that results from a quantum mechanical admixture of HS and IS states. The electron that in a HS state occupies the  $d_{x^2-y^2}$  orbital is partially delocalized in the  $d_{xy}$ , this latter a characteristic of the IS state. Therefore, the QS state is a single spin state with  $S$ =intermediate value between  $5/2$  and  $3/2$  that varies from a protein to another depending from the HS/IS spin contribution [Maltempo 1974, Maltempo 1976].

Finally, when the axial ligands are strong, the energy difference between the  $e_g$  and  $t_{2g}$  orbitals is larger than the spin pairing energy, and the electrons occupy the  $t_{2g}$  orbitals following the Hund's rule resulting in a low spin (LS) with the total spin quantum number  $S=1/2$  for ferric heme. Since in the LS configuration the higher energy orbitals are unoccupied, the size of the core containing the iron atom is smaller than in the HS configuration and the metal lies in the plane of the tetrapyrrole ring, while the HS iron sits out of plane.

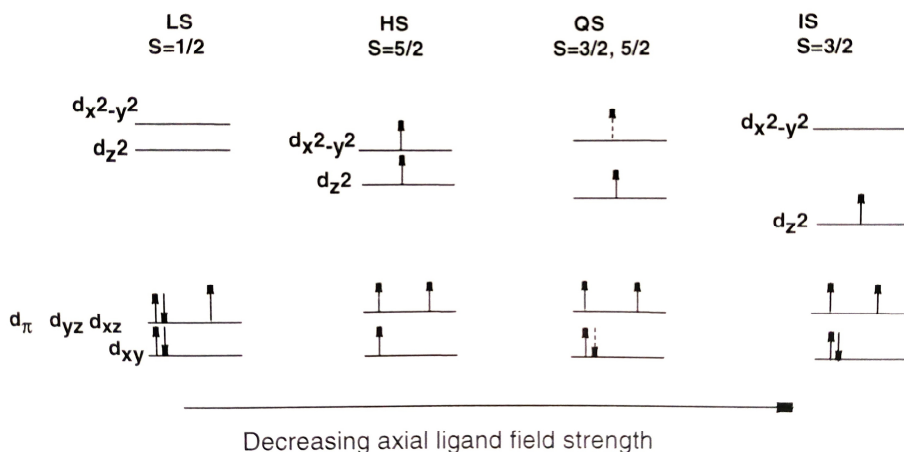


**Figure 2.2.** Electronic configuration of the valence 3d orbitals of the possible spin states of iron(III) in heme proteins.

## 2.2 Electronic absorption spectroscopy

In quantum mechanics the absorption of a photon with a given energy and the consequent transition of one electron from its ground state to an excited state (separated by the same energy of the photon), occurs only if the transition moment between the initial and final states  $M_{fi}$ , a vector given by the integral below is different from zero.

$$M_{fi} = \int \Psi_e^* \mu \Psi_g d\tau \neq 0$$

$\Psi_g$  and  $\Psi_e^*$  are the wavefunctions associated with the ground and excited electronic states, respectively;  $\mu$  is the electric dipole moment operator.

It is possible to evaluate whether the integral is different from zero by symmetry considerations. The transition is allowed when the direct product of irreducible representations (given by the product of the corresponding characters) to which the individual factors belong, is equal or, more generally, contains the total symmetric (TS) representation of the group:

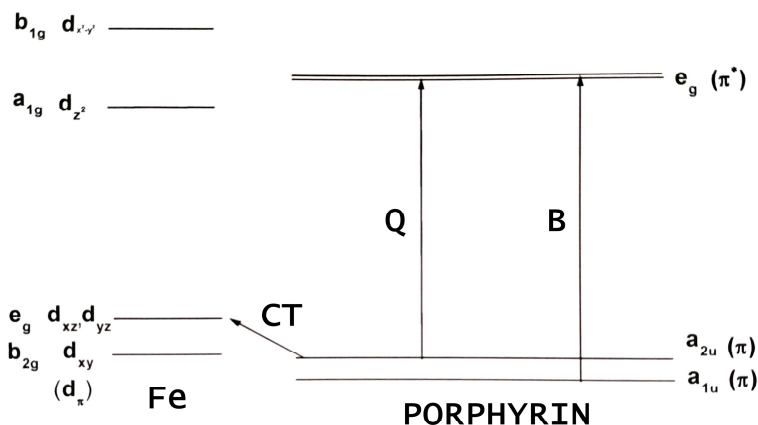
$$\Gamma(\Psi_e^*) \times \Gamma(\mu_i) \times \Gamma(\Psi_g) \subseteq \Gamma_{TS}$$

In heme, which considering the eight side substituents as point masses and neglecting the axial ligands has a  $D_{4h}$  pseudosymmetry, the two lowest unoccupied orbitals (LUMO,  $\pi^*$ ) are degenerate and have  $E_g$  symmetry, while the highest filled  $\pi$  orbitals (HOMO,  $\pi$ ) have  $A_{1u}$  and  $A_{2u}$  symmetry (Gouterman four orbital model [Gouterman 1979] **Figures 2.3 and 2.4**).

The product of the symmetry representation of the ground and excited states wavefunctions of both the HOMO $\rightarrow$ LUMO ( $\pi\rightarrow\pi^*$ ) transitions ( $A_{1u} \times E_g$  and  $A_{2u} \times E_g$ ) is  $E_u$ . Since  $\Gamma(\mu_{x,y})=E_u$ , both the transitions are symmetry allowed and, therefore, two absorption bands of comparable intensity are expected. Indeed, (**Figure 2.4**), the  $\pi\rightarrow\pi^*$  electronic transitions give rise to an intense band at about 400 nm, called Soret or B band, and to less intense bands, called  $\alpha/\beta$  or  $Q_v/Q_0$  at about 500-600 nm. In fact, the HOMO orbitals have nearly the same energy, there is a strong configuration interaction between the two transitions, and as a consequence, the transition dipoles are summed for the higher energy B transition and nearly cancelled for the lower energy  $Q_0$  transition

[Gouterman 1979]. Some intensity (around 10%) is regained by the Q transition via Herzberg-Teller vibronic (electronic and vibrational) mixing of the Q and B transition [Perrin 1969], being therefore the Qv band the envelope of the vibronic transitions [Spiro 1988].

When the conjugation of the porphyrin ring is extended to the vinyl groups (heme *b*) the energy of the Q and B transitions is lowered and consequently the absorption bands red-shifts by about 10 nm.



### PROTOPORPHYRIN IX

**Figure 2.3.** Electronic transitions that occur in a hemeprotein. The orbitals of the heme iron atom and those of the porphyrin with the respective symmetry species are reported on the left and on the right, respectively.

In addition to the Soret and  $\alpha/\beta$  bands in the 600-650 nm region, ferric HS and QS species show weak bands due to charge-transfer (CT) transition from the porphyrin ring  $\pi$  orbital ( $A_{2u}$ ) to the iron orbital  $d_{\pi}$  ( $E_g$ ), called CT1 (**Figure 2.3**). Also LS species show CT bands in the 700-800 nm region. For instance the spectrum of native Cytochrome *c*, a pure 6cLS species with a Met residue as distal ligand, shows a band at 695 nm due to charge-transfer from the sulphur atom of the distal Met residue to the heme iron.

Since the electronic structure of the porphyrin ring is perturbed by the electronic configuration of the heme iron whose orbitals are, in turn, perturbed by the interaction with the axial ligand, the wavelengths of the Soret and  $\alpha/\beta$  and CT bands, change accordingly, and are indicative of

the oxidation, coordination and spin state of the heme iron atom; moreover the wavelengths can provide information on the nature of the axial ligands.

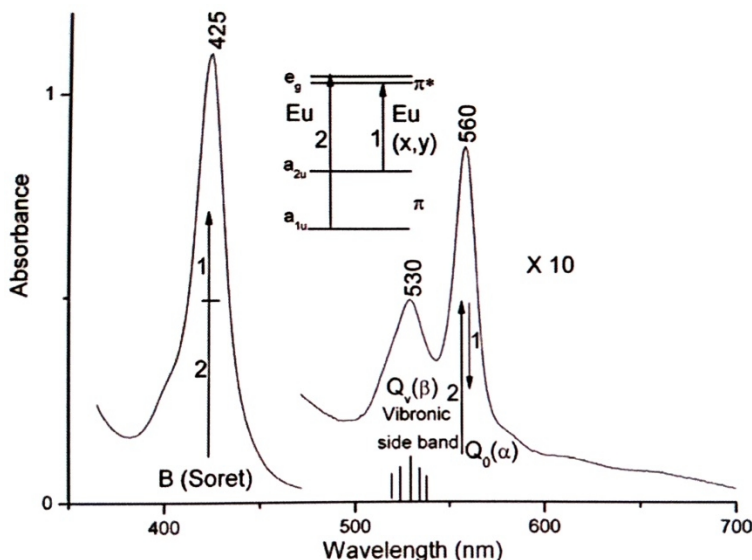


**Figure 2.4.** Absorption spectrum of a ferrous heme protein. The schematic representation of the Gouterman four orbital model for metalloporphyrin is also reported [Gouterman 1979]. The electronic transitions which give rise to the Soret band and the Q<sub>0</sub> (α) band are indicated by the arrows. In the case of the Soret band the two electronic transition 1 and 2 are additive and in the case of the α band the transitions are subtractive. The Q<sub>v</sub> (β) band is an envelope of 0-1 vibronic transitions induced by mixing of the Soret and Q transition. Adapted from (Spiro 1988).

### 2.3 Resonance Raman spectroscopy

Raman spectroscopy is vibrational spectroscopy based on the Raman scattering effect. When light is scattered by matter, the photons of the incident light is scattered either in elastic (more probable event, Rayleigh scattering), with no change in energy, or in an inelastic way (Raman effect). In this latter case, the scattered light has different energy from incident light.

As shown **Figure 2.5**, the molecule is excited to a virtual level that does not correspond to a real vibrational/electronic state. This state is not stable and the photon is immediately re-radiated as scattered light.

In the Rayleigh scattering an electron from the ground level is excited to the virtual state and falls to the original ground level. It does not involve any energy change and, therefore, has the same energy as incident light.

Raman scattering can be classified as two types, Stokes Raman scattering and anti-Stokes Raman scattering. In Stokes Raman scattering an electron is excited from the ground level and comes back to a vibrational level. It involves energy absorption by the molecule thus Stokes Raman scattered light has less energy (longer wavelength) than incident light. Conversely, in anti-Stokes Raman scattering an electron is excited from a vibrational level to the ground level. It involves an energy transfer to the scattered photon, therefore, it has more energy (shorter wavelength) than incident light. Therefore, in both the Stokes and anti-Stokes cases, the frequency of the scattered light will differ from that of the incident source by an amount equal to a vibrational transitions ( $0 \rightarrow 1$  and  $1 \rightarrow 0$ ) of the molecule.

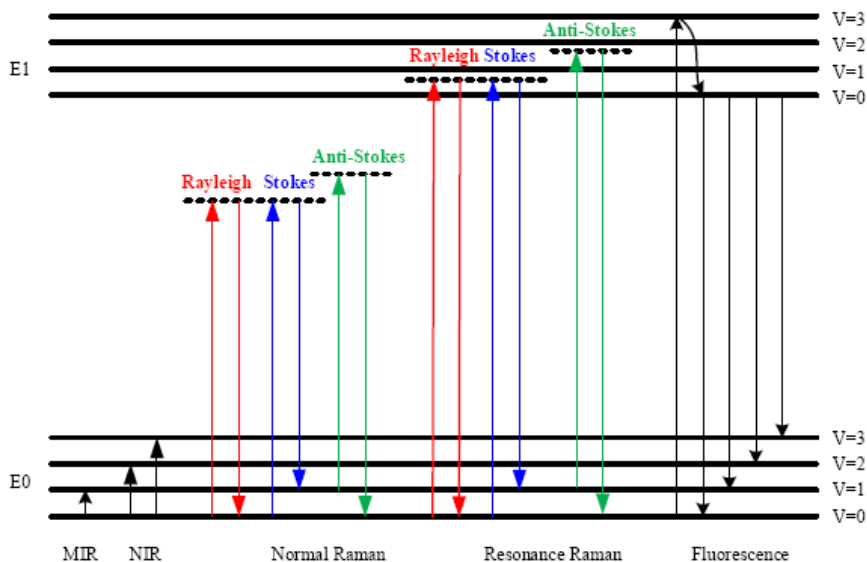


**Figure 2.5.** Energy level diagram related to Raman and resonance Raman scattering (Rayleigh, Stokes and anti-Stokes). Moreover also the IR absorption and fluorescence emission, this latter competing with resonance Raman (RR), are reported.

As for the electronic transition, the transition between two vibrational levels  $v_i$  and  $v_f$  (which are usually the 0 and 1 vibrational levels of the ground electronic state for Stokes scattering that is the one I studied) is allowed only if the vibrational moment transition integral  $M_{fi}$  is different from zero.

$$M_{fi} = \int \Psi_{v_f}^* \alpha_{\rho\sigma} \Psi_{v_i} d\tau_v \neq 0$$

$\Psi_{v_i}$  and  $\Psi_{v_f}^*$  are the wavefunctions associated with the ground (initial) and excited (final) vibrational states, respectively; and  $\alpha_{\rho\sigma}$  ( $\rho = x, y, z$  and  $\sigma = x, y, z$ ) is the second order tensor molecular polarizability.

In order to describe the polarizability tensor, since Raman scattering is a two-photon process, a second-order perturbation theory is required. On this basis Kramer, Heisenberg, and Dirac derived a quantum mechanical description of the molecular polarizability as a summation of a resonant and an anti-resonant terms.

In resonance Raman (RR) the frequency of the incident light is very close to the energy of an allowed electronic transition (**Figure 2.5**) with the consequent intensification of the totally symmetric vibrational modes related to the electronic transition of the chromophore.

RR is a two-photon process too, therefore, introducing the Kramer, Heisenberg and Dirac formula, Albrecht obtained an expression for Raman scattering tensor under a resonance condition (within the Born-Oppenheimer approximation) [Albrecht 1961].

$$\alpha = A + B + C.$$

Since only the a and B terms are important for resonance Raman [Albrecht 1961], the intensity of the Raman scattering, the intensity of the Raman scattering is generally treated by Albrecht's Raman theory, in which the polarizability is expanded into two terms, i.e., the Albrecht's A and B term.

$$A = \frac{2\pi}{h} |M_0|^2 \sum_{v_e} \frac{\langle \Psi_{v_f} | \Psi_{v_e} \rangle \langle \Psi_{v_e} | \Psi_{v_i} \rangle}{v_{v_e v_i} - v_0 + i\Gamma_{v_e}}$$

$M_0$  is the electric transition dipole moment to and from the resonant excited state  $e$  of which  $v_e$  is a particular vibrational level;

$\langle \Psi_{v_f} | \Psi_{v_e} \rangle \langle \Psi_{v_e} | \Psi_{v_i} \rangle$  is the product of Franck-Condon integrals between the intermediate level  $v_e$  and the initial and final levels  $v_i$  and  $v_f$ , respectively;

$\nu_{v_e v_i} - \nu_o$  is the difference between the frequency of the level  $v_e$  ( $\nu_{v_e v_i}$ ) of bandwidth  $\Gamma_{v_e}$ , and the excitation frequency ( $\nu_o$ ).

The A term gives the main resonance scattering mechanism for the allowed electronic transitions that have large values of  $M_0^2$ . For different vibrational modes the relative enhancement depends on the values of the Franck-Condon integrals, which, in turn, depend on the geometric displacements in the excited state along the vibrational coordinates. The Franck-Condon products are different from zero only for totally symmetric modes ( $A_{1g}$ ) that are, therefore, intensified under the A term mechanism.

When the resonant excited state is only weakly allowed, the B term becomes important.

$$B = \frac{2\pi}{h} |M_0| M' \sum_{v_e} \frac{\langle \Psi_{v_f} | \Psi_{v_e} \rangle \langle \Psi_{v_e} | Q | \Psi_{v_i} \rangle + \langle \Psi_{v_f} | Q | \Psi_{v_e} \rangle \langle \Psi_{v_e} | \Psi_{v_i} \rangle}{\nu_{v_e v_i} - \nu_o + i\Gamma_{v_e}}$$

$M'$  can exceed  $M_0$  if there is strong permitted transition (a) nearby, giving intensity by vibronic mixing to the resonant transition:

$$M' = M_{0,a} \frac{\langle a | \delta H / \delta Q | e \rangle}{\nu_a - \nu_e}$$

$\delta H / \delta Q$  is the derivative of the Hamiltonian with respect to the normal mode and  $\nu_a$  and  $M_{0,a}$  are the frequency and transition dipole moment of the mixing state. The active vibrations are those that are effective in mixing the two states and depend on their geometries. The allowed symmetries are given by the cross product of the electronic transition representations.

When the two electronic transitions become degenerate the mixing vibrations are strongly enhanced. This is a limiting case of vibronic scattering, called Jahn-Teller effect and the activated vibrational modes are called Jahn-Teller active modes.

Excitation of the metalloporphyrin in the vicinity of the Soret band produces mainly A term scattering [Strekas 1973, Stallard 1984]. Therefore the total symmetric ( $A_{1g}$ ) modes of the porphyrin ring

dominate the spectra. Moreover, since the excited state is degenerate, also the Jahn-Teller active modes ( $B_{1g}$  and  $B_{2g}$ ) are observed.

Conversely, excitation in resonance with the Q bands produces mainly B term scattering dominated by the vibrations that are effective in mixing the Q and B transitions (Spiro 1972, Shelnut 1966, Shelnut 1977). Since both the transitions are of  $E_u$  symmetry, the allowed symmetries of the mixing vibrations are:

$$E_u \times E_u = A_{1g} + A_{2g} + B_{1g} + B_{2g}.$$

However, due to the high molecular symmetry,  $A_{1g}$  vibrations are ineffective in vibronic mixing (Perrin 1969) and therefore the spectra are dominated by the  $B_{1g}$ ,  $B_{2g}$  and  $A_{2g}$  modes.

The scattered light polarization is given from the intensity ratio of the perpendicular and parallel polarized light as compared to the vector of the incident radiation. The  $A_{1g}$  modes are polarized with a theoretical depolarization ratio,  $\rho_{\perp//} = 1/8$ , the  $B_{1g}$  and  $B_{2g}$  modes are depolarized with a theoretical depolarization ratio,  $\rho_{\perp//} = 3/4$ , and the  $A_{2g}$  modes are anomalously (or inverse) polarized with a theoretical depolarization ratio,  $\rho_{\perp//} > 3/4$ .

The knowledge of the excitation profile and the polarization ratio of a given mode are important for the band assignment.

An idealized metalloporphyrin with  $D_{4h}$  symmetry (where the peripheral substituents are considered as point masses and the axial ligands are neglected), has 37 atoms, which result [Spiro 1985] in 105 ( $3N-6$ ) normal modes of vibrations:

- 71 ( $2N-3$ ) in the porphyrin plane, mainly located in the high frequency region (HF, 1300–1700  $\text{cm}^{-1}$ ) with the following symmetry  $\Gamma_{(\text{in plane})} = 9A_{1g} + 8A_{2g} + 9B_{1g} + 9B_{2g} + 18 E_u$ . The g modes are Raman active, while the  $E_u$  modes are IR active. These latter modes, however, could be weakly activated due to the conjugation of the asymmetrically disposed vinyl substituents which induce a distortion of the  $\pi^*$  excited state along the  $E_u$  vibrational coordinates [Choi 1982a].
- 34 ( $N-3$ ) out of the porphyrin plane, mainly located in the low frequency region (LF, 150–800  $\text{cm}^{-1}$ ) with the following

symmetry  $\Gamma_{(\text{out of plane})} = 3A_{1u} + 6A_{2u} + 5B_{1u} + 4B_{2u} + 18 E_g$ . Only the  $E_g$  modes are Raman active, but could be intensified in RR spectra only by vibronic mixing with in plane  $E_u$  and out of plane  $A_{2u}$  electronic transitions ( $E_u \times A_{2u} = E_g$ ). The other out-of-plane modes may become RR active consequently to a lowering of the molecular symmetry [Choi 1982b, Parthasarathi 1987] (for instance when the metal atom moves out of the porphyrin plane the symmetry is lowered).

The assignment of the RR bands observed both in the high and in the low frequency regions, had been obtained on the basis of the isotopic substitutions ( $^{15}\text{N}$  in the pyrroles, D in the porphyrin ring and propionate and vinyl substituents) [Argade 1984, Hu 1996] performed on metalloporphyrins used as model compounds.

### 2.3.1 High frequency: the core size marker bands

The high frequency region is characterized by the presence of bands due to the stretching vibrations of the porphyrin ring bonds (skeletal modes), called “core-size marker bands” (**Table 2.1**). This name comes from the inverse correlation between the frequency of these bands and the porphyrin core size, defined as the average distance from the four N pyrrole atoms to the centre of the ring [Spiro 1985]. In particular for planar metalloporphyrin an increase of the core size lower the Raman frequencies [Choi 1982b]. A change of only 0.01 Å in the size of the core produces a change of 5-6  $\text{cm}^{-1}$  in the frequency of these bands, being the slope of this correlation roughly proportional to the contribution of the normal modes to the methine bond stretches.

Since the core size depends on the oxidation, coordination and spin state of the heme iron [Spaulding 1975, Choi 1982b], the frequencies of the core size marker bands give important structural information.

In particular the ferric iron atom having in the valence 3d orbitals one electron less as compared the ferrous one [Spiro 1985], has a smaller core and therefore higher frequencies of the core size bands.

Since in the LS configuration the higher energy  $e_g$  orbitals ( $d_{x^2-y^2}$ ,  $d_z^2$ ) are unoccupied, the length of the Fe-N porphyrin bonds is shortened and the size of the core is smaller than in the HS configuration where both

the  $e_g$  orbitals are occupied with a consequent lengthened of the Fe-Nporphyrin bonds [Spiro 1985].

Moreover, 6cHS species, lying the iron atom in the plane of the tetrapyrrole ring, have a bigger core size and lower frequencies of the core size bands as compared to the 5cHS forms where the heme iron is displaced towards the fifth axial ligand and, therefore, a contraction of the macrocycle cavity is induced.

The porphyrin core size of the 5cHS and 6cLS ferrous and 6cHS, 5cHS, and 6cLS ferric species are summarized in **Figure 2.6**.

**Table 2.1.** Core size marker bands of ferrous (5cHS and 6cLS) and ferric (6cHS, 5cHS, and 6cLS) iron-protoporphyrin IX complexes with their RR frequencies ( $\text{cm}^{-1}$ ) [Choi 1982b].

	Fe(II)		Fe(III)		
	5cHS	6cLS	6cHS	5cHS	6cLS
$\nu_4 (A_{1g})$	1357	1359	1370	1373	1373
$\nu_3 (A_{1g})$	1471	1493	1480	1491	1502
$\nu_{11} (B_{1g})$	1547	1539	1545	1553	1562
$\nu_2 (A_{1g})$	1562	1584	1559	1570	1579
$\nu_{19} (A_{2g})$	1550	1583	1560	1571	1586
$\nu_{10} (B_{1g})$	1604	1617	1610	1626	1640

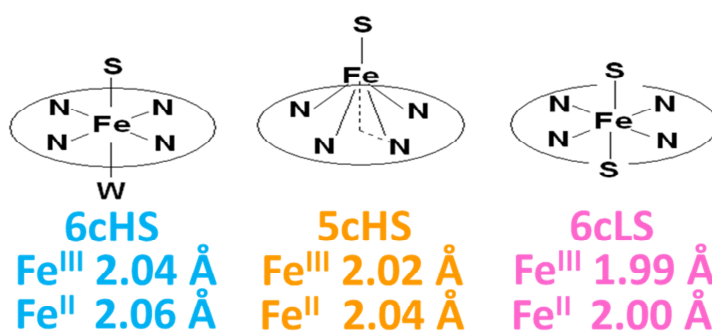


**Figure 2.6.** Porphyrin core size of the 6cHS, 5cHS, and 6cLS ferric and the 5cHS and 6cLS ferrous species (Å). W and S are indicative of a weak and a strong ligand, respectively.

Among the core size bands, the  $\nu_4$  band, which occurs between 1350 and 1375  $\text{cm}^{-1}$ , is the most indicative band of the oxidation state, up-shifting its frequency up to 20  $\text{cm}^{-1}$  from the ferrous to the ferric state. The others core size marker bands are instead more sensitive to the coordination and spin states.

### 2.3.2 High frequency: the $\nu(\text{C}=\text{C})$ stretching modes of the vinyl substituents

In the 1610-1640  $\text{cm}^{-1}$  high RR frequency region, the  $\nu(\text{C}=\text{C})$  stretching modes of the vinyl group substituents in position 2 and 4 occur. The  $\nu(\text{C}=\text{C})$  stretching mode frequency is correlated with the vinyl torsion angles ( $\tau$ ), formed between the  $\text{C}_a=\text{C}_b$  vinyl double bonds and the  $\text{C}_\alpha=\text{C}_\beta$  of the pyrrole (**Figure 2.7, A**), which express the vinyl orientation with respect to the porphyrin plane [Marzocchi 2003]. In particular the  $\nu(\text{C}=\text{C})$  stretching mode frequency downshifts with the increase of conjugation between the vinyl double bonds and the porphyrin aromatic macrocycle, this latter depending on the vinyl orientation in the following order: *trans* (high conjugation; lower frequency) > *twist* > *cis* (low conjugation; higher frequency) (**Figure 2.7, B**).

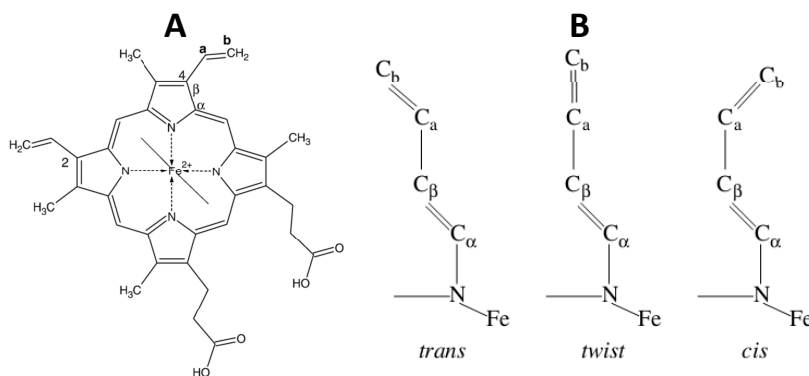


**Figure 2.7. A.** Schematic representation of the heme showing the  $\text{C}_\alpha$ ,  $\text{C}_\beta$ ,  $\text{C}_a$  and  $\text{C}_b$  atoms defining the torsional angle of the vinyl in position 2 and 4. The value of  $0^\circ$  corresponds to the coincidence of the  $\text{C}_\alpha\text{C}_\beta$  and  $\text{C}_a\text{C}_b$  bonds, when viewed along the  $\text{C}_\beta\text{C}_a$  bond. **B.** Schematic representation of different vinyl conformations as found in heme proteins: *trans* ( $\tau = 135^\circ$ ), *twist* ( $\tau = 90^\circ$ ), *cis* ( $\tau = 45^\circ$ ). Taken from [Marzocchi 2003].

The  $\nu(\text{C}=\text{C})$  stretching modes are strongly coupled with the  $\nu_2$  core size band, inducing a down-shift of the latter of up to  $12\text{ cm}^{-1}$ . Consequently when the vinyl group are saturated, as in Cytochrome *c*, the frequency of the  $\nu_2$  band is up-shifted as compared to heme *b* proteins.

### 2.3.3 Low frequency

In the low frequency region are observed:

- the in-plane and out-of-plane skeletal vibration modes,
- the vinyl and propionate substituents bending modes  $\delta(\text{C}_\beta\text{C}_a\text{C}_b)$  and  $\delta(\text{C}_\beta\text{C}_c\text{C}_d)$ , respectively,
- the metal-axial ligand vibrations [Spiro 1988, Kincaid 2000].

If the heme is distorted the spectra are particularly rich of bands since many out-of-plane modes which in the  $D_{4h}$  symmetry are not enhanced become active.

#### 2.3.3.1 The $\delta(\text{C}_\beta\text{C}_c\text{C}_d)$ bending modes of the propionate substituents

A propionate bending mode  $\delta(\text{C}_\beta\text{C}_c\text{C}_d)$  whose frequency is  $\geq 372\text{ cm}^{-1}$  is indicative of a strong hydrogen bond between the propionate group and the aminoacid residue in the heme pocket [Gottfried 1996, Friedman 1996, Cerda-Colòn 1998], like in HHMb ( $376\text{ cm}^{-1}$ ), where a rich H-bond network is formed between Leu89, Ser92, His93, His97 and the heme propionates [Evans 1990, Lloyd 1996]. On the contrary a frequency of the propionate bending mode  $\delta(\text{C}_\beta\text{C}_c\text{C}_d) < 369\text{ cm}^{-1}$  is related to a weak hydrogen bond to the heme propionates [Gottfried 1996, Friedman 1996, Cerda-Colòn 1998], like in *Lucina Pectinata* hemoglobin (HbI), where the propionate low-frequency vibration at  $370\text{ cm}^{-1}$  is consistent with a moderate hydrogen bond between Arg99 and the heme-7-propionate [Cerda-Colòn 1998].

#### 2.3.3.2 The $\nu(\text{Fe-Im})$ stretching mode

Information on the proximal cavity can be obtained by the RR spectra of ferrous 5cHS heme proteins which in the  $200\text{-}250\text{ cm}^{-1}$  region show an intense band due to the iron-imidazole stretching mode  $\nu(\text{Fe-Im})$ , assigned on the basis of isotopic substitution ( $^{56}\text{Fe}$  replaced by  $^{54}\text{Fe}$ ). It is still unclear why in the ferrous 6cLS species this mode is not

observed. Pioneering studies on ferrous 5cHS metalloporphyrin with 2-methylimidazole (2-MeIm) as fifth ligand demonstrated that the  $\nu(\text{Fe-Im})$  frequency is strongly affected by H-bonds interactions between the proximal His N $\delta$  hydrogen atom and nearby accepting residues [Hori 1980, Stein 1980, Teraoka 1981].

In these days, on the basis of the many studies that have been performed on heme proteins, it is generally accepted that the  $\nu(\text{Fe-Im})$  stretching frequency of globins which have a neutral histidine as the proximal ligand, is in the range of 200–230 cm<sup>-1</sup>, being the lowest possible value in the absence of any hydrogen bond. In the presence of strong hydrogen bond interaction with a nearby residue that acts as a H-bond acceptor, the proximal ligand has an imidazolate character, and the  $\nu(\text{Fe-Im})$  stretching frequency is very high, being located in the range of 240–260 cm<sup>-1</sup>, as observed in the heme containing peroxidases [Smulevich 2010].

### 2.3.3.3 Exogenous ligands

Information on the distal cavity can be obtained, upon binding of exogenous ligand (CO, O<sub>2</sub>, OH<sup>-</sup>) which bind the heme iron atom at the distal side. In fact, many Raman studies on heme proteins and model compounds have proved that the Fe-exogenous ligand vibrational frequencies are sensitive to the nature, geometry and orientation of the ligand-interacting distal residues.

The vibrations of the exogenous ligand are identified on the basis of isotopic substitution (<sup>13</sup>CO, <sup>18</sup>O<sub>2</sub>, D<sub>2</sub>O and H<sub>2</sub><sup>18</sup>O); in fact upon isotopic substitution a frequency down-shift is expected, according to the change of the reduced mass  $\mu$ .

$$v = \frac{1}{\pi} \cdot \left(\frac{k}{\mu}\right)^2$$

$v$  is the frequency (cm<sup>-1</sup>) of the vibration;

$k$  is the force constant of the bound that links the atoms involved in the vibration;

$\mu$  is the reduced mass of the atoms involved in the vibration:

$$\mu = \frac{m_1 \cdot m_2}{m_1 + m_2}$$

In general the interaction between diatomic ligands (X-Y, such as CO and O<sub>2</sub>) and a transition metal (Fe) mainly involve two types of bonding:  $\sigma$ - and  $\pi$ -bonding [Kerr 1988].

There are two types of  $\sigma$ -bonding (**Figure 2.8**):

- one involves the interaction of the metal  $d_{z^2}$  orbital with the ligand non-bonding electrons and is especially important with ligands linearly coordinated;
- the other involves the interaction of the metal  $d_{z^2}$  orbital with a ligand  $\pi^*$  orbital and is stronger for those ligands whose  $\pi^*$  orbital have lower energy (O<sub>2</sub><CO).

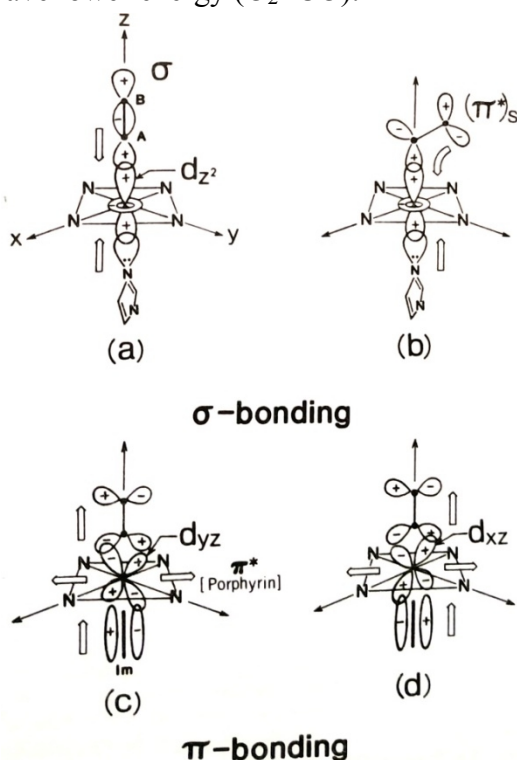


**Figure 2.8.** Schematic representation of the  $\sigma$ - and  $\pi$ -bonds in heme proteins-CO complexes. Taken from [Yu 1986].

There are two types also of  $\pi$ -bonding in which the metal  $d_{\pi}$  ( $d_{xz}$  or  $d_{yz}$ ) orbitals donate electron density to the ligand  $\pi^*$  orbital. The  $\pi$ -back bonding increases the metal-ligand bond order and gives higher stability upon the metal-carbon bond than would be obtained from the  $\sigma$

interaction alone. The increase in electron density of the anti-bonding  $\pi^*$  orbital of the ligand results in i) a strengthening of the metal-ligand bond with a consequent up-shift of the corresponding M-X vibrational frequency ii) a weakening of the X-Y ligand bond with a consequent down-shift of the corresponding X-Y vibrational frequency. Therefore the  $\nu(\text{M-X})$  and the  $\nu(\text{X-Y})$  frequencies are inversely correlated. Moreover the  $\pi$ -bonding component of the metal-ligand bond depends on the degree of competition between the same metal  $d_\pi$  ( $d_{xz}$  or  $d_{yz}$ ) orbitals to form  $\pi$ -bonds with the porphyrin macrocycle and the trans fifth ligand.

The nature of the  $\sigma$ - and  $\pi$ -bonding between the metal and the XY ligand determines the geometry of the M-X-Y linkage. In general the geometry can be predicted on the basis of the sum of the metal d electrons and the ligand electrons that occupy the  $\pi^*$  and  $\sigma^*$  levels. Where the sum  $\leq 6$ , the M-X-Y linkages are essentially linear, while as the sum becomes  $> 6$  a progressively more bent configuration of the M-X-Y linkages is observed.

#### 2.3.3.3.1 CO

CO binds with a very high affinity to the ferrous atom of the heme group linearly, being the sum of the metal d electrons (6) and the ligand electrons that occupy the  $\pi^*$  level (0) equal to 6. When bound to heme, the frequency of the  $\nu(\text{C-O})$  stretching vibration downshifts of about  $200 \text{ cm}^{-1}$  as compared to the free gas: from  $2143 \text{ cm}^{-1}$  (gas) to  $1955 \text{ cm}^{-1}$  (heme-bound). This strong effect is due to the back bonding donation of electrons from the ferrous  $d_\pi$  orbitals to the empty CO  $\pi^*$  orbital which leads to a strengthening of the Fe-C bond and a simultaneous weakening of the C-O bond with a consequent down-shift of the corresponding  $\nu(\text{C-O})$  frequency.

It has been demonstrated that due to the back bonding the  $\nu(\text{Fe-C})$  and the  $\nu(\text{C-O})$  are negatively linearly correlated. In **Figure 2.9** are reported the  $\nu(\text{Fe-C})$  frequencies plotted versus the  $\nu(\text{C-O})$  frequencies of a series of heme proteins and heme containing model compounds with different trans ligand: i) imidazole or pyridine (solid line); ii)

imidazolate or thiolate anions (dashed line); iii) weak His or absent (dotted line) [Ray 1994].

Imidazolate or thiolate anions as compared to imidazole (which is the most common proximal ligand in heme proteins [Kerr 1988]) are: a) more electron-rich thus enhancing the back bonding and b) stronger Fe-trans ligand thus weakening the Fe-C  $\sigma$ -bond by competing for the ferrous  $dz^2$  orbital [Li 1988], this second effect being predominant. Consequently the relative  $\nu(\text{Fe-C})/\nu(\text{C-O})$  correlation line is located below that of heme proteins containing imidazole as trans ligand.

Conversely, a weaker ligand than imidazole or the absence of a proximal ligand induces: a) a back bonding decrease and b) an increase in the Fe-C  $\sigma$ -bond strength, this second effect being predominant. Consequently the relative  $\nu(\text{Fe-C})/\nu(\text{C-O})$  correlation line is located above that of heme proteins containing imidazole as trans ligand.

Finally the position on each correlation lines is influenced by many factors that determine the strength of the back bond donation [Ray 1994].

1. The most important contribution is given from the H-bonding interaction between the CO oxygen atom and the nearby distal residues. These interaction weaken the C-O bond with a consequent strengthen of the Fe-C bond with a back bonding increase. As a consequence the  $\nu(\text{Fe-C})$  frequency increases and the  $\nu(\text{C-O})$  frequency decreases, being the  $\nu(\text{Fe-C})/\nu(\text{C-O})$  point located in the upper part of the correlation line.
2. A similar effect is given also by polar interaction between the CO oxygen atom and the nearby distal residues. In fact since back bonding increases the negative charge on the CO oxygen atom, the presence of a close distal residue positively charged or with a positively oriented dipole can favors the retrodonation [Philips 1999].
3. The steric hindrance gives the lower contribution in back bonding contribution, but it plays an essential role in the affinity of CO binding. In fact large distortion of the Fe-CO unit is precluded by the prohibitive cost in CO binding energy. Since electronic energies associated with distal interactions are not

large, the binding energies decrease more or less in proportion to the steric hindrance energy. Rather than adopt a severely distorted structure, CO does not bind.

In addition to the  $\nu(\text{Fe-C})$  and  $\nu(\text{C-O})$  vibrations another isotopic sensitive band is observed around  $570\text{ cm}^{-1}$ . This band is assigned to the  $\delta(\text{Fe-C-O})$  bending [Kerr 1988]. Actually this mode is an out-of-phase combination of the Fe-C-O bending and the Fe-C tilting [Ghosh 1996] which is responsible of the elevated  $\delta(\text{Fe-C-O})$  frequency that had been a source of controversy over the assignment [Kincaid 2000].

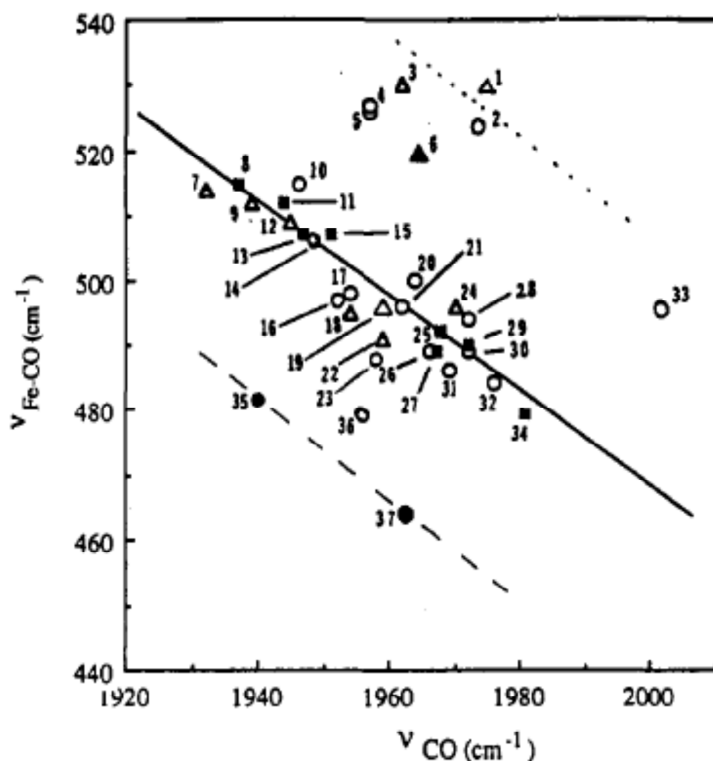


**Figure 2.9.** Plot of observed  $\nu(\text{Fe-C})$  vs  $\nu(\text{CO})$  frequencies in Fe(II)-CO heme adducts of tetraarylporphyrins (open circles), Cp-alkyl porphyrins (open triangles), globins (solid squares), cytochrome P450s (solid circles), and cytochrome oxidase (solid triangle). The numbers correspond to the entries in **Table 2.2**. The solid line indicates the backbonding correlation line for proximal neutral imidazoles [Li 1988]. The dashed line is for anionic thiolates, and the dotted line is for five-coordinate CO adducts with no proximal ligand. Taken from [Ray 1994].

**Table 2.2.** Vibrational frequencies and isotope shifts ( $\text{cm}^{-1}$ ) of the Fe-CO linkage in carbonyl complexes of iron porphyrins and selected heme proteins. Taken from [Ray 1994].

molecule/solvent	$\nu_{\text{FeCO}}$	$\Delta^{13}\text{C}^a$	$\Delta^{18}\text{O}^a$	$\nu_{\text{CO}}$	$\Delta^{13}\text{C}$	$\Delta^{18}\text{O}$	$\delta_{\text{FeCO}}$	$\Delta^{13}\text{C}$	$\Delta^{18}\text{O}$	ref
FeOEP/Bz <sup>r</sup>	531	5	10	1975			n.re. <sup>d</sup>			22b, 83
FeIPP/Bz	524	5	{14} <sup>r</sup>	1973 <sup>r</sup>						22b, 23
FeDeut(THF)/THF	530		{13}	1962		{90}	n.re.			22b
FeTSMP(H <sub>2</sub> O)/pH 7	527 <sup>r</sup>			1957			n.re.			this work
FeTPivP(THF)/THF	526	5	10	1957			n.re.			22a,b
cyt c oxidase	520	4		1964	46		578	14		28a,b
FeSP-13(NMeIm)/MC <sup>h</sup>	514	4		1932	44		579	11		16
elephant Mb, pH 8.2	515	3	6	1937		{91}	579	16	1	42
FeSP-14(NMeIm)/MC <sup>h</sup>	512	4	5	1939	45		578	15	3	16
FePiv <sub>2</sub> C <sub>8</sub> (NMeIm)/Bz <sup>r</sup>	515	5		1948	44		576	21		17
sperm whale Mb, pH 8.4 <sup>r</sup>	512	3	8	1944	48	48	577	14	1	18
FeSP-15(NMeIm)/MC <sup>h</sup>	509	6		1945	44		574	11		16
sperm whale Mb, pH 7.0	507	3		1947			575	16		64, 60b
FePiv <sub>2</sub> C <sub>8</sub> (NMeIm)/Bz <sup>r</sup>	506	5		1948	44		n.re.			17
human Hb A <sup>h</sup>	507	4	9	1951	43	43	578	15	2	18
FePiv <sub>2</sub> C <sub>10</sub> (NMeIm)/Bz <sup>r</sup>	497	3		1952	42		n.re.			17
Fe $\alpha$ -MedPoc(lmH)/MC	498	4	9	1954 <sup>r</sup>	45		567	10	4	38, 8a
heme-5(NMeIm)/MC <sup>h</sup>	495	4	9	1954	44					16
PPDME(lmH)/MC	495			1960 <sup>m</sup>						29
Fe $\alpha$ -PocPiv(NMeIm)/MC	500	4		1964 <sup>m</sup>			568	9		this work, 8a
FeTPivP(1,2-Me <sub>2</sub> Im)/Bz <sup>r</sup>	496	5		1962						22a,b
FeAPC(NMeIm)/Bz <sup>r</sup>	491		{9}	1959			576	{16}		22b, 39
FePiv <sub>2</sub> C <sub>12</sub> (NMeIm)/Tol	488	4		1958	46		n.re.			17
FeOEP(NMeIm)/Bz	496		8	1970						22a, 20a
mutant Mb His(E7)Gly, pH 7 <sup>r</sup>	492			1965						44a
FeTPivP(NMeIm)/Bz	489	4	8	1966-9						22a,b, 8b
sperm whale Mb, pH 2.6	489			1966			n.re.			67, 64, 60b
FeTPP(1,2-Me <sub>2</sub> Im)/Bz	494			1972						22a, 20a
Hb M Boston- $\alpha^M$	490	2	7	1972	48	48				49a
FeTSPP(2MeIm)/pH 7	489			1972			n.re.			this work
FeTSMP(4MeIm)/pH 7	486	4		1969	39		n.re.			this work
FeTPP(py)/Bz	484 <sup>r</sup>	4	9	1976	43	43				42
FeC <sub>2</sub> -Cap(NMeIm)/Bz	497	4		2002 <sup>r</sup>	44		n.re.			this work
mutant pig Mb His(E7)Val, Val(E11)Thr	479			1984						45a,b
cyt P-450 <sub>CAM</sub> from <i>P. putida</i> + camphor	481 <sup>r</sup>	3	8	1940	43		558	14	3	46a,b
FeTPivP(C <sub>8</sub> HF <sub>2</sub> S <sup>-</sup> )/ClBz	479	5		1956 <sup>w</sup>						84a,b
cyt P-450 <sub>CAM</sub> from <i>P. putida</i> (no substrate)	464-9			1963	45		n.re.			46a,b, 52a
Fe $\alpha$ -PocPiv/MC	521						n.re.			this work
Fe $\alpha$ -PocPiv(1,2-Me <sub>2</sub> Im)/MC	502	6					568	8		this work
Fe $\alpha$ -TalPoc(NMeIm)/Bz				1963						8a
mutant Mb His(E7)Tyr, pH 7	494						n.re.			75b
mutant human Hb ( $\beta$ E7)Gly <sup>w</sup>	493			1971						44b
FeTPP(NMeIm)/Bz	486	{11}								22a,b
FeAnth77(NMeIm)/Cf				1966						39
FeAnth66(NMeIm)/Cf				1975						39
FeC <sub>2</sub> -Cap(NMeIm)/Tol				1979						20c
FeOCCO(NMeIm)/Tol				2014						21
PPDME(lm <sup>-</sup> )/MC	490			1942						29
cyt P-450 <sub>SCC</sub> (no substrate)	477 <sup>w</sup>	7		1953	46					46c
cyt P-450 <sub>LM</sub> (no substrate)	474 <sup>x</sup>	5								46e

### 2.3.3.3.2 O<sub>2</sub>

O<sub>2</sub> binds to the ferrous atom of heme proteins in a bent fashion, as demonstrated by the crystallographic structure of oxymyoglobin [Phillips 1980] and oxyhemoglobin [Shaanan 1982], since the sum of the metal d electrons (6) and the ligand electrons that occupy the  $\pi^*$  level (2) is equal to 8. Theoretically, three vibrational modes are expected in the RR spectra, i.e.  $\nu(\text{Fe-O}_2)$ ,  $\delta(\text{Fe-O-O})$  and  $\nu(\text{O-O})$ , but usually only the first one is observed, like in the spectra of oxymyoglobin and oxyhemoglobin, where  $\nu(\text{Fe-O}_2)$  was assigned to the

band around  $570\text{ cm}^{-1}$  by oxygen isotopic shift [Potter 1987, Van Wart 1985, Hirota 1994].

### 2.3.3.3 OH<sup>-</sup>

Hydroxo-bound heme proteins are characterized by an equilibrium of a 6cHS and a 6cLS species [Beetlestone 1964] that shift towards the 6cLS species at low temperature (80 K) [Feis 1994]. Therefore, in the RR spectra at room temperature, two  $\nu(\text{Fe-OH})$  modes are observed, with the LS species at higher frequency [Feis 1994], and can be assigned on the basis of isotopic shift in  $\text{D}_2\text{O}$  and  $\text{H}_2^{18}\text{O}$ .

The  $\nu(\text{Fe-OH})$  frequency is very sensitive to the distal environment, depending especially on the number and strength of H-bonding interactions between the hydroxide and the distal polar residues [Egawa 2005, Smulevich 1991, Lukat-Rodgers 1998, Howes 1997, Feis 1994]. In the absence of any H-bond interaction,  $\nu(\text{Fe-OH})$  are found around  $490\text{ cm}^{-1}$  for 6cHS and  $550\text{ cm}^{-1}$  for 6cLS species. An increase of the H-bond strength between the hydroxo group and nearby proton donor/acceptor residues determines a decrease of the Fe–O electron density, and, as a consequence, a decrease in the frequency of the  $\nu(\text{Fe-OH})$  stretching mode at about  $480\text{ cm}^{-1}$  for 6cLS species strongly H-bonded [Nicoletti 2013]. In presence of a strong H-bond, upon deuteration an upshift can be observed due to the weaker H-bonds formed by deuterium and the consequent increase of the Fe-O bond strength. Also, anomalous isotopic shifts may be caused by the loss of the Fe-OH biatomic oscillator character [Feis 1994].

### References

- ❖ Albrecht A.C., *J. Chem. Phys.* 1961, 34, 1476.
- ❖ Argade P.V., Sassaroli M., Rousseau D.L., Inubushi T., Ikeda-Saito M., Lapidot A., *J. Am. Chem. Soc.* 1984, 106, 6593.
- ❖ Bangcharoenpaupong O., Schomacker K.T., Champion P.M., *J. Am. Chem. Soc.* 1984, 106, 5688.
- ❖ Cerda-Colón J.F., Silfa E., López-Garriga J., *J. Am. Chem. Soc.* 1998, 120, 9312.
- ❖ Choi (a) S., Spiro T.G., Langry K.C., Smith K.M., *J. Am. Chem. Soc.* 1982, 104, 4337.

- ❖ Choi (b) S., Spiro T.G., Langry K.C., Smith K.M., Budd D.L., La Mar G.N., *J. Am. Chem. Soc.* 1982, 104, 4345.
- ❖ Egawa T., Yeh S.R., *J. Inorg. Biochem.* 2005, 99, 72.
- ❖ Evans S.V., Brayer G.D., *J. Mol. Biol.* 1990, 213, 885.
- ❖ Feis A., Marzocchi M.P., Paoli M., Smulevich G., *Biochemistry* 1994, 33, 4577.
- ❖ Friedman J.M., Campbell B.F., Noble R.W., *Biophys. Chem.* 1990, 37, 43.
- ❖ Friedman J.M., Peterson E., In *Proceedings of the XIVth International Conference on Raman Spectroscopy* (Asher S.A., Stein P.B. Eds.), *J. Wiley & Sons Ltd, New York*, 1996, p. 428.
- ❖ Ghosh A., Bocian D.F., *J. Phys. Chem.* 1996, 100, 6363.
- ❖ Gottfried D.S., Peterson E. S., Sheikh A.G., Wang J., Friedman J. M., *J. Phys. Chem.* 1996, 100, 12034.
- ❖ Gouterman M., in *The Porphyrins, Vol. III, Part A* (Dolphin D. Ed.), 1979, Academic Press, New York, pp. 1-156.
- ❖ Gouterman M., *The porphyrins* (Dolphin D. Ed.), 1979, Academic Press.
- ❖ Hirota S., Ogura T., Appelman E.H., Shinzawaitoh K., Yoshikawa S., Howes B.D., Rodriguez-Lopez J.N., Smith A.T., Smulevich G., *Biochemistry* 1997, 36, 1532.
- ❖ Hori H., Kitagawa T., *J. Am. Chem. Soc.* 1980, 102, 3608.
- ❖ Hu S., Smith K.M., Spiro T.G., *J. Am. Chem. Soc.* 1996, 118, 12638.
- ❖ Kerr E.A., Yu N.-T. (1988) Vibrational modes of coordinated CO, CN<sup>-</sup>, O<sub>2</sub> and NO. In *Biological applications of Raman spectroscopy: Resonance Raman spectra of hemes and metal-loproteins* (Spiro T.G., Ed.) Vol.3, pp. 39–95, John Wiley and Sons Inc., New York.
- ❖ Kincaid J.R., in *The Porphyrin Hnadbook* (Kadish K.M., Smith R., Guillard R. Eds.) 2000, Academic Press, San Diego, pp. 227-291.
- ❖ Kitagawa T., *J. Am. Chem. Soc.* 1994, 116, 10564.
- ❖ Li X.-Y., Spiro T.G., *J. Am. Chem. Soc.* 1988, 110, 6024.
- ❖ Lloyd E., Burk D.L., Ferrer J.C., Maurus R., Doran J., Carey P.R., Brayer G.D., Mauk A.G., *Biochemistry* 1996, 35, 11901.
- ❖ Lukat-Rodgers G.S., Rodgers K.R., *J. Biol. Inorg. Chem.* 1998, 3, 274.
- ❖ Maltempo M.M., Moss T.H., *Biochim. Biophys. Acta* 1974, 342, 290.
- ❖ Maltempo M.M.; Moss T.H.; Cusanovich M.A., *Biochim. Biophys. Acta* 1974, 342, 290.
- ❖ Marzocchi M.P., Smulevich G., *J. Raman Spectrosc.* 2003, 725.

- ❖ Nicoletti F.P., Droghetti E., Howes B.D., Bustamante J.P., Bonamore A., Sciamanna N., Estrin D.A., Feis A., Boffi A., Smulevich G., *Biochim. Biophys. Acta Proteins Proteom.* 2013, 1834, 1901.
- ❖ Parthasarathi N., Hansen C., Yamaguchi S., Spiro T.G., *J. Am. Chem. Soc.* 1987, 109, 3865.
- ❖ Perrin M.H., Gouterman M., Perrin T.L., *J. Chem. Phys.* 1969, 50, 4137.
- ❖ Perutz M.F., *Annu. Rev. Biochem.* 1979, 48, 327.
- ❖ Phillips S.E., *J. Mol. Biol.* 1980, 142, 531.
- ❖ Phillips G.N., Teodoro M.L., Li T., Smith B., Olson J.S., *J. Phys. Chem. B* 1999, 103, 8817.
- ❖ Potter W.T., Tucker M.P., Houtchens R.A., Caughey W.S., *Biochemistry* 1987, 26, 4699.
- ❖ Ray G.B., Li X.-Y., Ibers J.A., Sessler J.L., Spiro T.G., *J. Am. Chem. Soc.* 1994, 116, 162.
- ❖ Shaanan B., *Nature* 1982, 296, 683.
- ❖ Shelnutt, J.A., O'Shea D.C., Yu N.T., Cheung L.D., Felton R.H., *J. Chem. Phys.* 1976, 64, 1156.
- ❖ Shelnutt J.A., Cheung L.D., Chang R.C.C., Yu, N.-T., Felton R.H., *J. Chem Phys* 1977, 66, 3387.
- ❖ Smulevich G., Miller M.A., Kraut J., Spiro T.G., *Biochemistry* 1991, 30, 9546.
- ❖ Smulevich G., Feis A., Howes B.D., Ivancich A., (2010) In *Handbook of Porphyrin Science* (Kadish K.M., Smith K.M., Guilard R. Eds.) Vol. 6, pp. 367–453, World Scientific, Singapore.
- ❖ Spaulding L.D., Chang C.C., Yu N.-T., Felton R.H., *J. Am. Chem. Soc.* 1975, 97, 2517.
- ❖ Spiro T.G., Strekas T.C., *Proc. Natl. Acad. Sci.* 1972, 69, 2622.
- ❖ Spiro T.G., *Adv. Protein Chem.* 1985, 37, 111.
- ❖ Spiro T.G., Li X.-Y., *Resonance Raman spectroscopy of metalloporphyrins*, In *Biological Applications of Raman Spectroscopy* (Spiro T.G. Ed.), 1988, vol. 3, pp. 1-37, John Wiley and sons Inc., New York.
- ❖ Stallard B.R., Callis P.R., Champion P.M., Albrecht A.C., *J. Chem Phys.* 1984, 80, 70.
- ❖ Stein P., Spiro T.G., *J. Am. Chem. Soc.* 1980, 102, 7795.
- ❖ Strekas T.C., Packer A.J., Spiro T.G., *J. Raman Spectrosc.* 1973, 1, 197.
- ❖ Teraoka J., Kitagawa T., *J. Biol. Chem.* 1981, 256, 3969.
- ❖ Van Wart H.E., Zimmer J., *J. Biol. Chem.* 1985, 260, 8372.
- ❖ Yu N.-T., *Methods Enzymol.* 1986, 130, 350.



## Chapter 3

### **Cytochrome c as an apoptosis initiator: unravelling the non-native state of the Cytochrome c–Cardiolipin complex**

Federica Sinibaldi, **Lisa Milazzo**, Barry D. Howes, Maria Cristina Piro, Laura Fiorucci, Fabio Polticelli, Paolo Ascenzi, Massimo Coletta, Giulietta Smulevich, Roberto Santucci,  
“The key role played by charge in the interaction of cytochrome c with cardiolipin”,  
*J. Biol. Inorg. Chem.* **2017**, 22, 19.

**Lisa Milazzo**, Lorenzo Tognaccini, Barry D. Howes, Federica Sinibaldi, Maria Cristina Piro, Maria Fittipaldi, Maria Cristina Baratto, Rebecca Pogni, Roberto Santucci, Giulietta Smulevich,  
“Unravelling the non-native state of the Cytochrome c – cardiolipin complex: evidence for the formation of a His ligated species only”,  
*Biochemistry* **2017**, 56, 1887.

**Lisa Milazzo**, Lorenzo Tognaccini, Barry D. Howes, Giulietta Smulevich,  
“Probing the non-native states of Cytochrome c with resonance Raman spectroscopy: a tool for investigating the structure-function relationship”,  
*J. Raman Spectrosc.* (Special Issue-Mini Review) **2018**, 49, 1041.

#### **3.1 Introduction**

Cytochrome c (Cyt c) is a single-chain hemoprotein of 104 amino acids containing three major and two minor  $\alpha$ -helices in the structure, with

the prosthetic group lying within a crevice lined with hydrophobic residues [Bushnell 1990]. The heme is covalently attached to the polypeptide chain by two thioether bridges with residues Cys14 and Cys17 [Louie 1990, Berghuis 1992], while His18 and Met80 are the axial ligands of the six-coordinated low-spin heme iron in the native state (**Figure 3.1**).

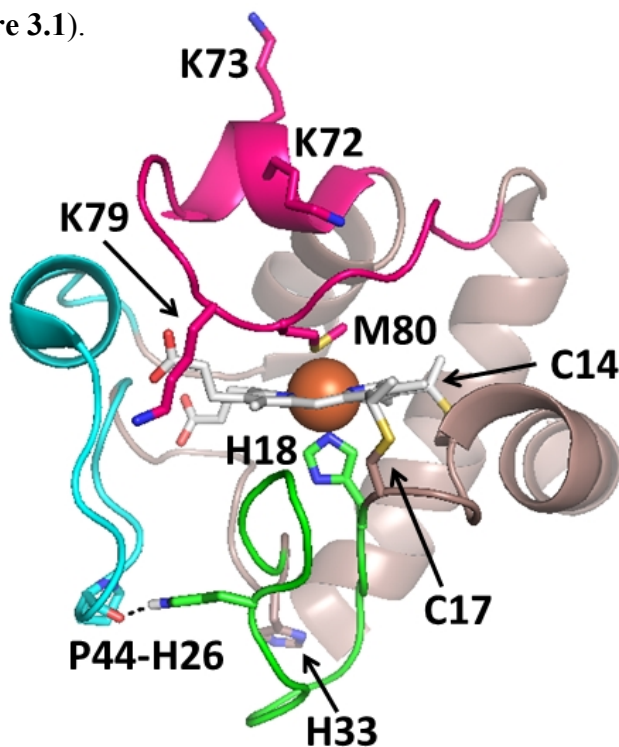


**Figure 3.1.** Ribbon diagram of the Cyt c (1HRC [Bushnell 1990]). This figure highlights the Met80-containing loop (magenta), the 40s  $\Omega$  loop (cyan), and the 20s  $\Omega$  loop (green) and some key residues (see text) shown as sticks: Cys14, Cys17, His18, His26, His33, Pro44, Lys72, Lys73, Lys79, Met80. The His26 $\cdots$ Pro44 H-bond is represented as a dotted line. The figure was made with: The PyMOL Molecular Graphics System, Version 1.7.5.0 Schrödinger, LLC.

Due to the lack of conjugation with the vinyl groups, involved in the formation of thioether linkages, Cyt c shows a blue-shifted maximum of the absorption (409 nm) (**Figure 3.2**) with respect to other 6cLS heme b proteins ( $\sim$ 415 nm [Smulevich 1991]). Another characteristic feature of the UV-Vis spectrum is the band at 695 nm, that is due to a charge

transfer between the Met80 sulphur atom and the heme iron, being thus indicative of the integrity of the Met80-Fe bond and consequently of the native Met distal ligation [Stellwagen 1974]. Moreover, the covalent bonds which anchor the porphyrin ring to the protein impart a predominant nonplanar ruffling distortion to the heme, conserved in the c-type Cyts [Hobbs 1995, Jentzen 1997, Jentzen 1998, Shelnut 1998]. The deformation lowers the overall symmetry of the heme from the ideal  $D_{4h}$  and is responsible for the many differences observed in the RR spectra of Cyt c compared to other heme proteins. A complete and detailed assignment of the RR spectra of ferrous and ferric Cyt c has been obtained via enzymatic reconstitution with isotopically labeled hemes [Hu 1993]. In this study is explained that as a consequence of the heme distortion, the RR spectra of the Cyt c obtained via Soret excitation are particularly rich. The effects can be summarized as follows:

1. the heme core is bigger than that of other planar 6cLS proteins and therefore the frequencies of the core size bands are particularly low, at 1372 ( $\nu_4$ ), 1502 ( $\nu_3$ ), 1584 ( $\nu_2$ ), and 1635 ( $\nu_{10}$ )  $\text{cm}^{-1}$ ;
2. appearance of unusually strong  $B_{1g}$  depolarized bands (as the very strong  $\nu_{15}$  band at 750  $\text{cm}^{-1}$ );
3. appearance of anomalously polarized bands (as the  $A_{2g}$  modes at 1587, 1314  $\text{cm}^{-1}$ );
4. activation of many of the  $E_u$  skeletal modes, otherwise forbidden in the Raman spectra;
5. activation of the out-of-plane modes ( $\gamma_{22}$ ,  $\gamma_{12}$ ,  $\gamma_{21}$ ,  $\gamma_5$ ) which usually are not enhanced in  $D_{4h}$  symmetry but can become Franck-Condon or vibronically active if the porphyrin undergoes an out-of-plane distortion. Consequently, when the Met80 axial ligand is replaced by another ligand and the heme geometry is relaxed, these bands disappear or markedly decrease their intensity (see below).

Therefore the Cyt c RR spectral region below 500  $\text{cm}^{-1}$  (**Figure 3.2**), which is regarded as the fingerprint region for the heme-protein interaction since the modes wavenumber reflect the structure and the

nature of the heme iron ligands, as well as the conformation and orientation of the peripheral substituents [Hildebrandt 1990, Hildebrandt 1996], is particularly rich of bands, whose assignment is reported in **Table 3.1**. The band at  $348\text{ cm}^{-1}$  is due to the  $\nu_8$  totally-symmetric mode ( $A_{1g}$ ) and is a combination of metal-N (pyrrole) stretching and pyrrole substituent bending vibrations, the band at  $361\text{ cm}^{-1}$  is a  $E_u$  mode activated in Cyt c. The weak features at  $374$  and  $382\text{ cm}^{-1}$  are due to the ( $C_\beta C_c C_d$ ) propionyl bending modes, the band at  $398\text{ cm}^{-1}$  is the  $\delta(C_\beta C_a S)$  bending, and the doublet at  $412$  and  $419\text{ cm}^{-1}$  is assigned to the  $\delta(C_\beta C_a C_b)$  bending modes [Hu 1993].

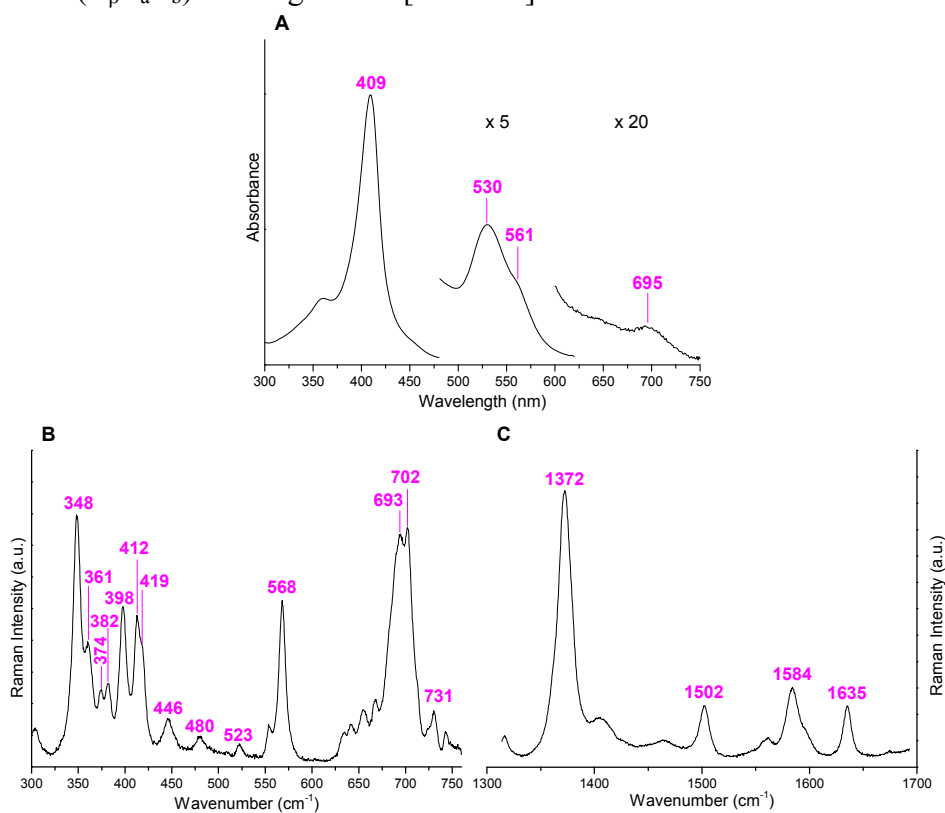


**Figure 3.2.** UV-Vis (A) and RR spectra in the low (B) and high (C) frequency regions of the ferric WT protein. The 470–620 nm and the 600–750 nm regions of the spectra are expanded 5-fold and 20-fold, respectively. The spectra have been shifted along the ordinate axis to allow better visualization and the intensity of the RR spectra is normalized to that of the  $\nu_4$  band. Experimental conditions: excitation wavelength 406.7 nm, laser power at the sample 5 mW, average of 4

spectra with 20 min integration time (B) and average of 5 spectra with 25 min integration time (C).

Besides the native His18-Fe-Met80 conformation, it has been demonstrated that during unfolding, Cyt c can adopt a variety of different non-native (or misligated) states in which the distal ligand Met80 can be replaced by other internal or exogenous ligands depending on the pH, ionic strength (I) or the presence of denaturing agents such as SDS (sodium dodecyl sulfate).

In particular, the following misligated species have been identified:

- a His18-Fe-His form where Met80 is replaced by His26 or His33 [Oellerich 2002, Santoni 2004],
- a His18-Fe-Lys form where Met80 is replaced by Lys72 [Blouin 2001], Lys73, or Lys79 [Döpner 1998, Rosell 1998],
- a His18-Fe-OH<sup>-</sup> form where Met80 is replaced by a hydroxo ion [Ferrer 1993, Döpner 1998, Rosell 1998],
- a His18-Fe-H<sub>2</sub>O form where Met80 is replaced by a water molecule [Dyson 1982, Goto 1990, Jordan 1995, Colón 1996, Indiani 2000, Zhong 2004],
- a H<sub>2</sub>O-Fe-H<sub>2</sub>O form where both Met80 and His18 are replaced by water molecules [Dyson 1982, Goto 1990, Jordan 1995, Colón 1996, Indiani 2000, Zhong 2004],
- two different 5-coordinated forms where either only the Met80 ligand dissociates from the Fe atom, or both the Met80 and His18 bonds are broken and a water molecule is bound to the Fe atom [Dyson 1982, Goto 1990, Jordan 1995, Colón 1996, Indiani 2000, Zhong 2004].

The Schematic representation of **Figure 3.3** summarizes the different misligated states adopted by Cyt c, in different environmental conditions [Theorell 1941, Dyson 1982, Pearce 1989, Goto 1990, Ferrer 1993, Jordan 1995, Colón 1996, Döpner 1998, Rosell 1998, Indiani 2000, Zhong 2004].

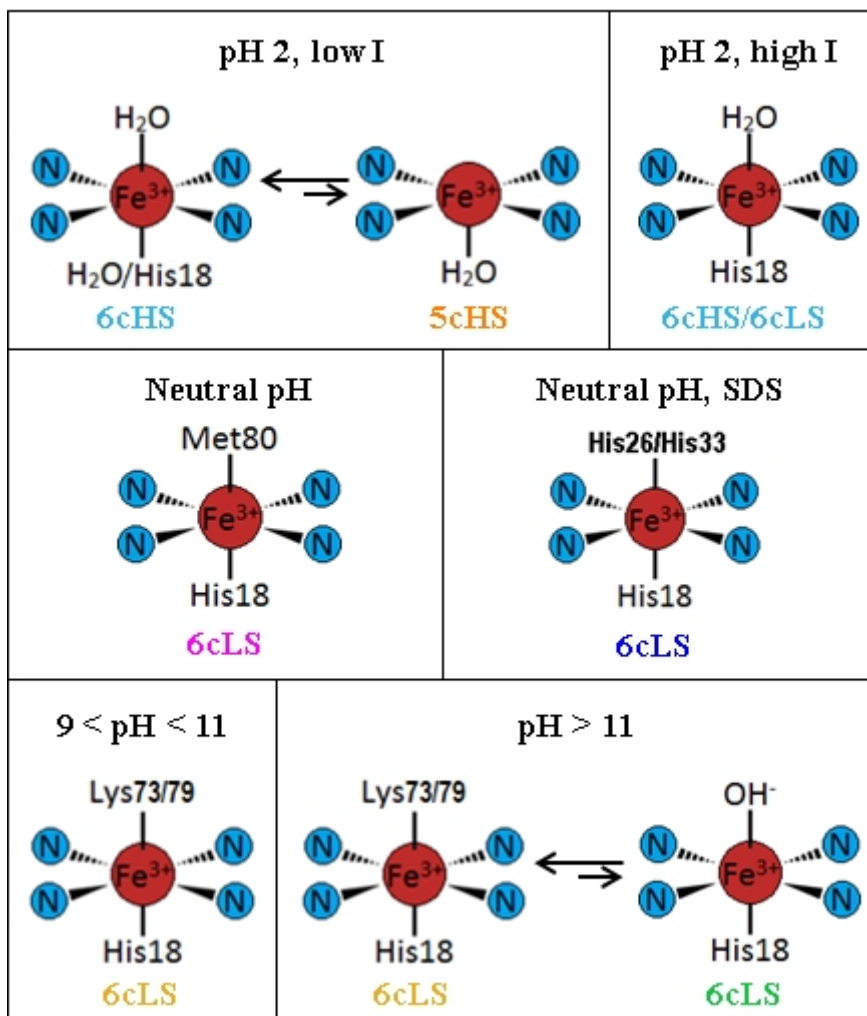


**Figure 3.3.** Schematic representation of the various conformational states of ferric Cyt c formed under different conditions of pH, ionic strength (I) and presence of agents (SDS i.e. sodium dodecyl sulfate).

Spectroscopy has played an important role to disclose the nature of the substituting ligand in the nonnative states [Scott 1996]. Among the various techniques, resonance Raman (RR) spectroscopy has been extensively applied and detailed knowledge of the spectral characteristics that enable the identification of the heme coordination and spin states as well as the nature of the heme ligation is well

established. This knowledge is particularly important because it allows getting deeper inside the physiological roles of Cyt c. In fact, this multifunctional protein plays an important role as an electron carrier in the respiratory chain as well as in programmed cell death, apoptosis [Orrenius 2007, Kagan 2009]. In particular, direct interaction with cardiolipin (CL), a phospholipid of the inner mitochondrial membrane, induces acquisition of peroxidase activity and subsequent release of Cyt c into the cytosol, where it acts as an apoptosis initiator through caspase activation. The appearance of peroxidase activity in Cyt c has been attributed to the partial unfolding of the protein [Kagan 2009, Hanske 2012, Milorey 2016], consequent rupture of the bond between the heme iron and its axial ligand Met80 [Hanske 2012, Kapetanaki 2009, Bradley 2011, Sinibaldi 2011, Capdevila 2015], and formation of alternative non-native conformers. It is notable that such non-native conformers appear also able to induce reversible pore formation enabling translocation of Cyt c more readily across the inner mitochondrial membrane [Bergstrom 2013]. The nature of the misligated species that are formed upon protein-lipid interaction has been the matter of a long standing debate. In particular it has been proposed that the ferric Cyt c-CL complex contains a mixture of 5-coordinate high spin (5cHS) [Kagan 2009], 6-coordinate high-spin (6cHS) [Kagan 2009, Sinibaldi 2011], and misligated 6-coordinate low spin (6cLS) species where the distal ligand has been identified with a Lys, [Bradley 2011, Sinibaldi 2011, Ranieri 2015], a His [Kagan 2009, Capdevila 2015], or an OH<sup>-</sup> ion [Bradley 2011].

Recently, on the basis of experiments carried out at pH 3, it was suggested that the breakage of the His26–Pro44 hydrogen bond is a possible trigger for the CL induced rearrangements [Balakrishnan 2012]. In fact, the His26-Pro44 hydrogen-bond bridges the 20s (residues 18-31) and the 40s Ω-loop (residues 40-57, highly conserved in class I Cytochromes) [Bushnell 1990] maintaining them sterically close (**Figure 3.1**), thus promoting the shielding effect of the 40s loop on the bottom heme edge with a consequent stabilization of the protein tertiary structure. Accordingly, a number of studies have reported that disruption of the His26–Pro44 hydrogen bond has considerable impact

on the native protein conformation [Sinibaldi 2003, Santoni 2004, Caroppi 2004, Balakrishnan 2012, Muenzner 2013, Sinibaldi 2013]. Another still unclear issue concerns the protein site(s) involved in the Cyt c-CL binding: in fact, despite the large body of studies performed over the past decade, a general consensus is still lacking. So far (**Figure 3.4**), three distinct sites on the Cyt c surface have been suggested to be possible regions of interaction with CL: i) the A site, formed by Lys72, Lys73, Lys86 and Lys87 [Kalanxhi 2007]; ii) the C site, located near Asn52 [Rytömaa 1994, Rytömaa 1995, Tuominen 2002, Sinibaldi 2010]; iii) the L site involving Lys22, Lys25, His26, Lys 27, and His33 that operates at low pH [Kawai 2005, Kagan 2009]. Recently, a novel CL binding site, termed the N-site, centered on residues Phe36, Gly37, Thr58, Trp59, and Lys60 has been found by studying the Cyt c-CL interaction in reverse micelle encapsulation [O'Brien 2015].

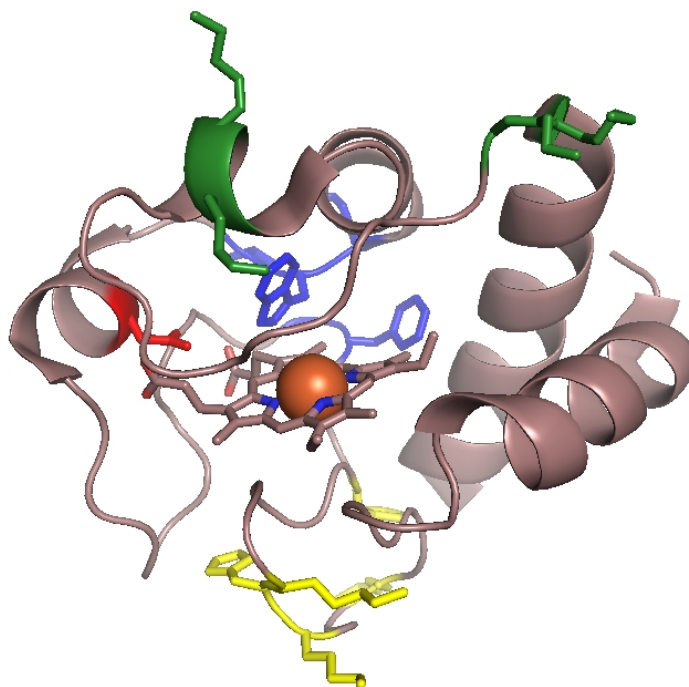


**Figure 3.4.** Ribbon diagram of Cyt c (1HRC [Bushnell 1990]). The sites that have been suggested to be possible regions of interaction with CL are reported in green (A site), red (C site) yellow (L site) and blue (N site). The figure was made with: The PyMOL Molecular Graphics System, Version 1.7.5.0 Schrödinger, LLC.

Among these residues, the invariant Lys72 and the largely invariant Lys73, located in the Met80-containing loop adjacent to the heme pocket region, are expected to play a critical role. A recent work shows that the mutation of the two positively charged Lys residues in the polar, uncharged Asn residues lead to: i) lack of interaction with CL of the K72N mutant; ii) lack of peroxidase activity in the CL-bound K73N mutant [Sinibaldi 2013].

To rationalize the different results so far reported in the literature and to gain better insights into the Cyt c-CL interaction, I have studied the formation of the CL complex of the ferric horse heart Cyt c, wild type (WT) and selected mutants in which the residues that could replace Met80 as distal ligand (His26, His33, Lys72, Lys73, Lys79) have been mutated. Moreover I have compared the Cyt c-CL final spectra with those of Cyt c misligated model compounds.

Finally to better define the role played by the Lys residues located at positions 72 and 73 in the Cyt c-CL recognition process, I studied the Arg (positively charged residue) and Ala (apolar residue) mutants (K72R, K73R, K72A, and K73A) of these residues and I compared the results with those previously obtained for the Asn mutants (K72N and K73N) [Sinibaldi 2013].

It must be noted that horse heart Cyt c, conversely to yeast iso-1-Cyt c, behaves similar to the human Cyt c [Patel 2001] and actively participates in cell apoptosis [Kluck 2000, Sinibaldi 2005, Kagan 2005, Sinibaldi 2011, Bergstrom 2013]).

## **3.2 Materials**

### **Preparation of Cyt c-CL complexes**

Horse heart Cyt c (approximately 95% purity, lyophilized oxidized form) and cardiolipin, as sodium salt from bovine heart (approximately 98% purity, lyophilized powder), were obtained from Sigma-Aldrich (Steinheim, Germany) and used without further purification.

The expression and purification of the recombinant horse heart Cyt c mutant proteins K727379N, K7273N/H26Y, K7273N/H33Y, H2633N, K72R, K72A, K73R, K73A (Lys72Asn/Lys73Asn/Lys79Asn, Lys72Asn/Lys73Asn/His26Tyr, Lys72Asn/Lys73Asn/His33Tyr triple

mutants, His26Asn/His33Asn double mutant, Lys72Arg, Lys72Ala, Lys73Arg, Lys73Ala single mutants) were performed by professor Roberto Santucci's group (University of Tor Vergata, Rome).

Lyophilized ferric Cyt c was dissolved in 20 mM Hepes at pH 7.0 and concentrated solutions of the Cyt c mutants were diluted with the same buffer. To ensure complete oxidation, 1-3  $\mu\text{L}$  of a 3 mM freshly prepared  $\text{K}_4[\text{Fe}(\text{CN})_6]$  solution was added to 40  $\mu\text{L}$  protein solutions.

The Cyt c-CL complexes were prepared following a previously reported procedure [Kapetanaki 2009]. Briefly, CL was dissolved by sonication in ethanol, obtaining a 10 mM solution. The CL ethanol solution was then added to the WT protein and mutants in order to obtain a Cyt c:CL molar ratio (R) of 1:30, corresponding to the final point of the CL titration (see below). To avoid any possible effect on the protein triggered by the ethanol used to dissolve CL, careful controls were made to ensure that no spectral changes were caused by the ethanol added to the protein. The maximum amount of the CL ethanol solution added to Cyt c to form the Cyt c-CL complexes corresponds to 3% ethanol v/v.

**Figure 3.5** demonstrates that the addition of 3% ethanol does not affect the UV-Vis (**A, trace b**) and RR spectra (**B, trace a**) of WT Cyt c (**A, trace a** and **B, trace c**). In fact, the RR spectra of WT Cyt c without ethanol (**B, trace c**) is identical to that obtained after subtraction of the 3% ethanol spectrum (**B, trace b**).

It is noted that the maximum concentration of ethanol that does not cause spectral changes is 10% v/v (**B, traces c-d**). Hence, the level of ethanol added to the protein in this study (3%) is well below that expected to lead to spectral variations. As a consequence of limiting the ethanol concentration to 3%, the Cyt c concentration for a Cyt c-CL molar ratio of 1:30 cannot exceed 25  $\mu\text{M}$ .

Ferrous samples were prepared by addition of 2–3  $\mu\text{L}$  of a freshly prepared sodium dithionite solution (10 mg/mL) to the ferric forms (40 $\mu\text{L}$ ) previously degassed with nitrogen.

The CO adducts were prepared by degassing the ferric protein solution (40 $\mu\text{L}$ ) by flushing firstly with nitrogen, then with  $^{12}\text{CO}$  or  $^{13}\text{CO}$  and reducing the heme by addition of 2–3  $\mu\text{L}$  of a freshly prepared sodium dithionite solution (10 mg/mL).

Cyt c concentrations in the range 10–200  $\mu\text{M}$  were used for WT samples, whereas concentrations in the range 20–25  $\mu\text{M}$  were used for the Cyt c mutants and the Cyt c-CL complexes. The protein concentration was determined using an extinction coefficient ( $\epsilon$ ) of 106  $\text{mM}^{-1} \text{cm}^{-1}$  at 409 nm [Margoliash 1959].

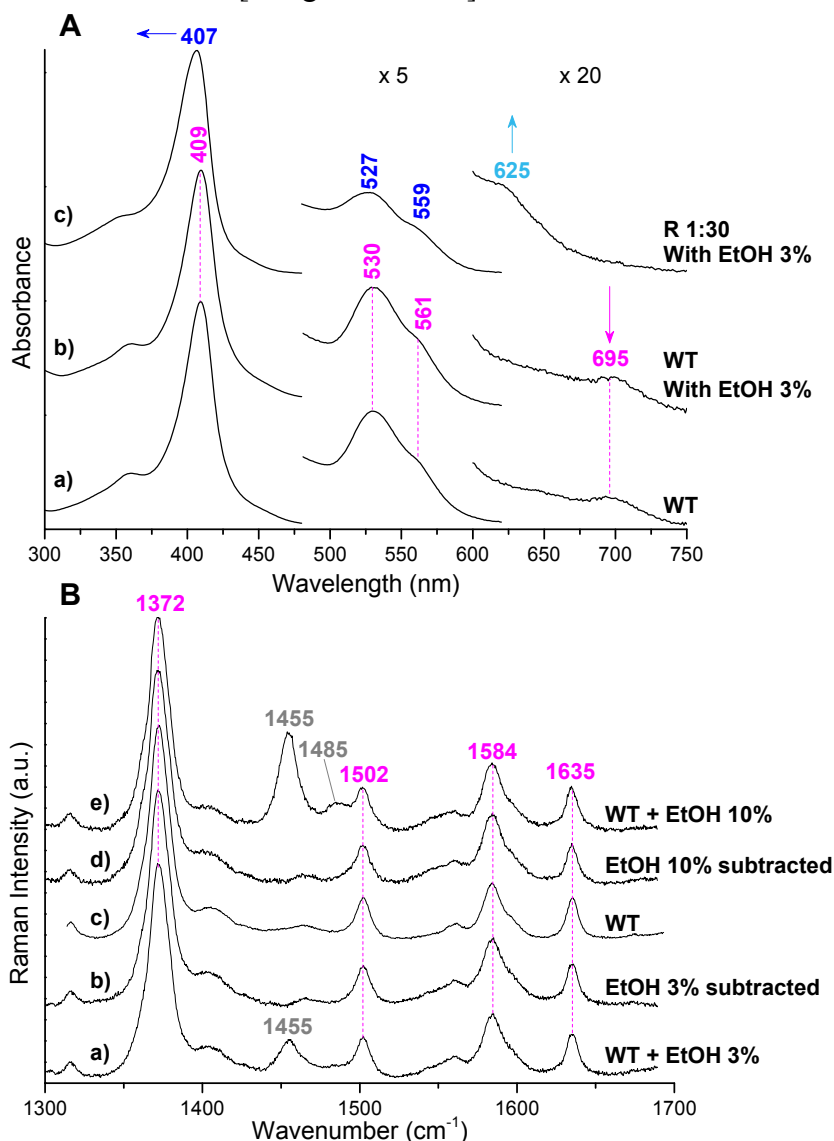


**Figure 3.5. A)** UV-Vis spectra of the ferric WT protein without (a) and with ethanol (b) and of the ferric WT-CL R 1:30 complex (c). The ethanol concentration in spectra (b) and (c) is 3% v/v. The band wavelengths of the His-Fe-Met native species, the His-Fe-His species

and the 6cHS species are shown in magenta, blue and light blue, respectively. The 470–620 nm and the 600–750 nm regions of the spectra are expanded 5-fold and 20-fold, respectively. The spectra have been shifted along the ordinate axis to allow better visualization.

**B)** RR spectra at 298 K in the high frequency region of the ferric WT protein without (c) and with 3% (a) and 10% (e) ethanol v/v. The same spectra after ethanol 3% and 10% v/v subtraction (b and d, respectively) are also shown. The band frequencies of the His-Fe-Met native species and ethanol are shown in magenta and grey, respectively. The spectra have been shifted along the ordinate axis to allow better visualization and the intensity of the spectra is normalized to that of the  $\nu_4$  band. Experimental conditions: excitation wavelength 406.7 nm, laser power at the sample 5 mW, average of 5 spectra with 50 min integration time (a), average of 5 spectra with 25 min integration time (c), and average of 4 spectra with 40 min integration time (e).

### **Preparation of model compounds**

His18-Fe-His (bis-His) model: ferric Cyt c was dissolved in 50 mM phosphate at pH 7.0 to obtain a 50  $\mu\text{M}$  solution. Then 30  $\mu\text{L}$  of a 75 mM SDS solution was added together with 90  $\mu\text{L}$  of a 0.1 M imidazole solution, in order to obtain a sample with a final SDS concentration of at least 10 mM and an imidazole/Cyt c ratio of 2500:1 [Oellerich 2002].

His18-Fe-Lys model: ferric Cyt c was dissolved in 150 mM phosphate at pH 12.1 to achieve a final concentration in the range of 60–100  $\mu\text{M}$ .

His18-Fe-OH<sup>-</sup> model: 85  $\mu\text{L}$  of Cyt c K727379N (horse heart Cyt c Lys72Asn/Lys73Asn/Lys79Asn triple mutant) in 20 mM Hepes at pH 7.0 were diluted with 15  $\mu\text{L}$  of 150 mM phosphate at pH 12.1 to achieve a final concentration in the range of 25  $\mu\text{M}$  at pH 12.0.

His18-Fe-H<sub>2</sub>O model: ferric Cyt c was dissolved in 2 M NaCl at pH 2.0 to obtain a 50  $\mu\text{M}$  solution [Jordan 1995].

To ensure complete oxidation of Cyt 3  $\mu\text{L}$  of a 3 mM freshly prepared  $\text{K}_4[\text{Fe}(\text{CN})_6]$  solution was added to 70  $\mu\text{L}$  protein samples.

## **3.3 Ferric form**

### **3.3.1 Cyt c (WT) titration with CL**

I have followed by electronic absorption, RR and EPR (**Figure 3.6**) the conformational changes induced on WT Cyt c by the addition of CL,

titrating a buffered Cyt c solution with CL. I have used an ethanol solution of CL rather than the more commonly used mixture of liposomes. Many studies in literature have revealed that the complex nature of Cyt c binding to anionic lipids on surface membranes is also dependent on the mixture of lipids that constitute the liposome together with CL [Kawai 2005, Belikova 2006, Trusova 2010, Hanske 2012, Hong 2012, Pandiscia 2015]. However, two recent studies demonstrated that there are negligible effect on the heme structure of the Cyt c-CL complexes prepared either by using CL in an ethanol solution or liposomes constituted by CL/PC (PC=phosphatidylcholine, another phospholipid that constitutes the biological membranes) mixtures. [Kapetanaki 2009, Capdevila 2015].

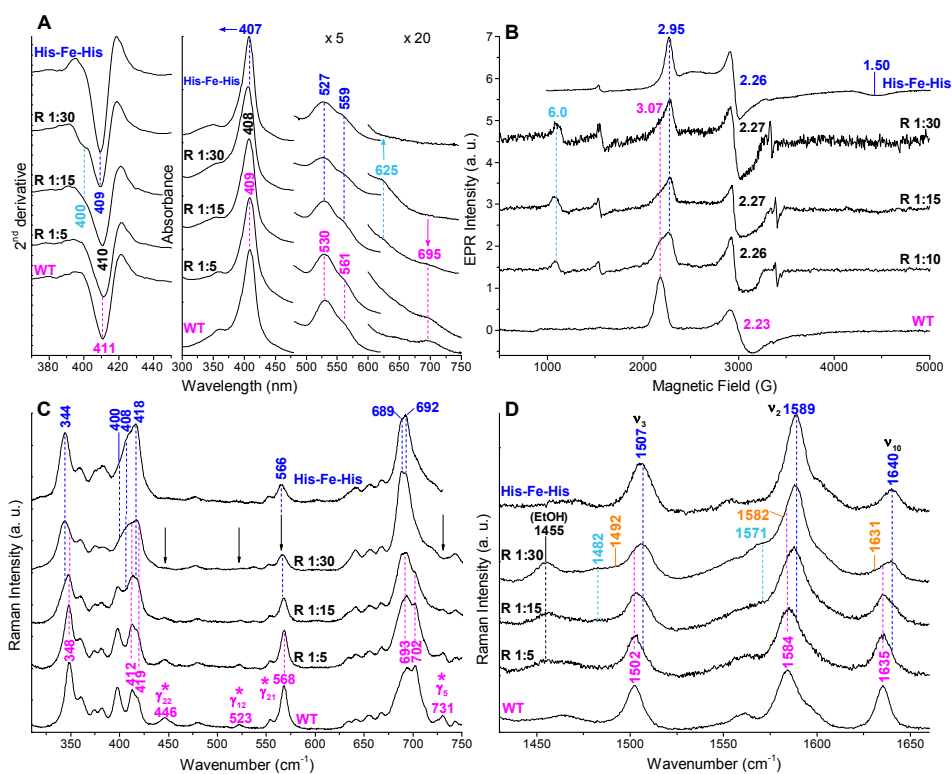


**Figure 3.6.** Titration of WT Cyt c with CL followed by UV-Vis, EPR and RR spectra. UV-Vis and second derivative spectra (panel A), EPR spectra (panel B) and RR spectra in the low (panel C) and high (panel D) frequency regions of the WT protein and the R 1:5 (R 1:10 in panel B), R 1:15, R 1:30 WT-CL complexes. The spectra of the bis-His model

are also shown for comparison. The band positions (wavelengths, frequencies, g-values) due to the His-Fe-Met native species, the His-Fe-His species, the 6cHS and the 5cHS species are shown in magenta, blue, light blue and orange, respectively. The spectra have been shifted along the ordinate axis to allow better visualization. In panel A the 470–620 nm and the 600–750 nm regions of the spectra are expanded 5-fold and 20-fold, respectively. In panels C and D the intensity of the spectra is normalized to that of the  $\nu_4$  band. EPR experimental conditions: **WT protein**: 190  $\mu\text{M}$ , 10 K, microwave power 0.53 mW; **R 1:10** 75  $\mu\text{M}$ , 5 K, microwave power 8.3 mW; **R 1:15** 50  $\mu\text{M}$ , 5 K, microwave power 8.3 mW; **R 1:30**: 25  $\mu\text{M}$ , 5 K, microwave power 8.3 mW; **His-Fe-His**: 255  $\mu\text{M}$ , 5 K, microwave power 8.3 mW. The spectra shown are after subtraction of the cavity signal. RR experimental conditions: excitation wavelength 406.7 nm, laser power at the sample 5 mW; **WT**: average of 4 spectra with 20 min integration time (C) and average of 5 spectra with 25 min integration time (D); **R 1:5**: average of 10 spectra with 50 min integration time (C) and average of 12 spectra with 60 min integration time (D); **R 1:15**: average of 6 spectra with 30 min integration time (C) and average of 4 spectra with 20 min integration time (D); **R 1:30**: average of 12 spectra with 60 min integration time (C) and average of 21 spectra with 105 min integration time (D); **His-Fe-His**: laser power at the sample 10 mW, average of 12 spectra with 60 min integration time (C) and average of 10 spectra with 50 min integration time (D). The asterisks (\*) in panel C indicate the out-of-plane modes.

During the titration I have observed the following spectral changes as compared to the WT (**Figure 3.6**).

1. At a protein-lipid molar ratio (R) of 1:5 the CT band at 695 nm decreases (**A**), indicating an initial rupture of the Fe-Met80 bond. In the high frequency RR spectrum the  $\nu_3$  band at  $1502\text{ cm}^{-1}$  and the  $\nu_2$  at  $1584\text{ cm}^{-1}$  broaden (**D**) and in the low frequency region the out-of-plane  $\gamma_{21}$  band at  $568\text{ cm}^{-1}$ , slightly decreases in intensity (**C**), suggesting the formation of a new 6cLS species with a smaller and more planar core. The WT native species remains nevertheless predominant.
2. At a protein-lipid molar ratio of 1:15 the changes due to the formation of a 6cLS misligated species become more pronounced: there is a further decrease in intensity of the CT

band at 695 nm, a slight blue-shift of the Soret band at 408 nm (A), the appearance of distinct shoulders at 1507 and 1589  $\text{cm}^{-1}$  in the high frequency RR spectrum (D), and a marked intensity decrease of all the out-of-plane modes  $\gamma_{22}$  (446  $\text{cm}^{-1}$ ),  $\gamma_{12}$  (523  $\text{cm}^{-1}$ ),  $\gamma_{21}$  (568  $\text{cm}^{-1}$ ), and  $\gamma_5$  (731  $\text{cm}^{-1}$ ) (C). Moreover, a 6cHS (aquo) species appears as evidence by: i) the new CT band at 625 nm (A) together with the new Soret band centred at 400 nm in the second derivative spectrum (A left); ii) weak bands at 1482 and 1571  $\text{cm}^{-1}$  (D).

3. Upon increasing the molar ratio, the new 6cLS and 6cHS species further increase at the expense of the native form. At the final protein-lipid molar ratio of 1:30 (no further changes were observed for  $R > 1:30$ ), the predominant form is the misligated 6cLS species. Moreover, a detailed curve-fitting analysis of the Cyt c-CL R1:30 RR spectrum (Figure 3.7) revealed the presence of two high spin species (6cHS:  $\nu_3$  1482  $\text{cm}^{-1}$ ,  $\nu_2$  1571  $\text{cm}^{-1}$  and 5cHS:  $\nu_3$  1492  $\text{cm}^{-1}$ ,  $\nu_2$  1582  $\text{cm}^{-1}$ ,  $\nu_{10}$  1631  $\text{cm}^{-1}$ ).

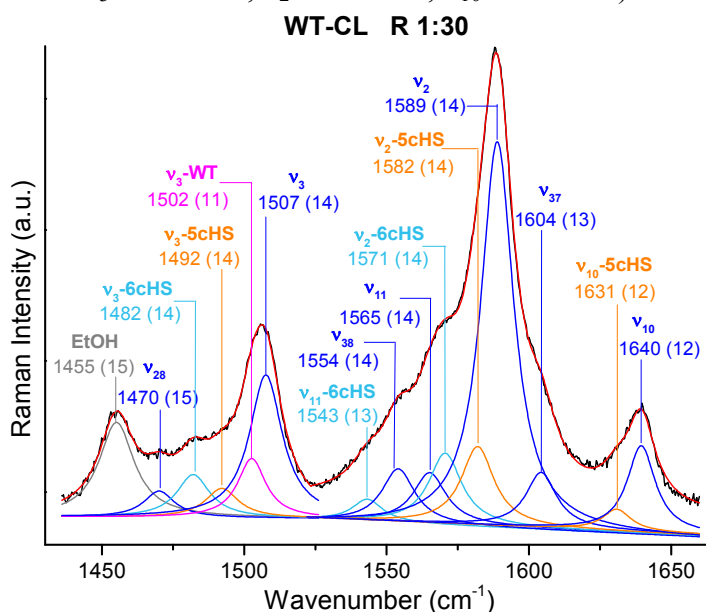


**Figure 3.7.** Curve-fitting analysis of the 1430-1670  $\text{cm}^{-1}$  high frequency region of the R 1:30 WT-CL complex spectrum. The frequencies of the bands due to the 6cLS His-Fe-Met native species, the new misligated 6cLS species, the 6cHS and the 5cHS species are shown in magenta,

blue, light blue and orange, respectively. Experimental conditions: same as in Figure 3.3, D. The bandwidths are reported in brackets.

The EPR spectra obtained by our coworkers from the Universities of Florence (Professor Maria Fittipaldi) and Siena (Professor Rebacca Pogni group) (**Figure 3.6, B**), confirm the presence of a HS form ( $g = 6.0$ ), together with a new 6cLS species ( $g = 2.95, 2.27$ ) and that of WT Cyt c ( $g = 3.07, 2.23$ ) [Brautigan 1977]. The poor quality of the EPR spectra of the CL complexes is due to the obligate use of very dilute samples ( $\sim 25 \mu\text{M}$ ), necessary to maintain the level of ethanol (required to solubilize CL) below that resulting in protein denaturation, and the presence of several spin species. This leads to the consequent difficulties of achieving a good subtraction of the cavity signal at  $g \sim 2$  (ca. 3300 G), which deforms the resultant spectrum in this region.

In detail, the spectroscopic markers of the new 6cLS form are:

- 1) blue-shifted (407 nm) Soret band with respect to the WT (409 nm) and no CT band at 695 nm (**Figure 3.6, A**);
- 2) up-shifted core size marker bands ( $\nu_3$  1507  $\text{cm}^{-1}$ ,  $\nu_2$  1589  $\text{cm}^{-1}$ , and  $\nu_{10}$  1640  $\text{cm}^{-1}$ ), with respect to the WT ( $\nu_3$  1502  $\text{cm}^{-1}$ ,  $\nu_2$  1584  $\text{cm}^{-1}$ ,  $\nu_{10}$  1635  $\text{cm}^{-1}$ ) (**Figure 3.6, D**);
- 3) very weak/absent RR out-of-plane bending modes (**Figure 3.6, C**);
- 4) downshift of the  $\nu_8$  band to 343  $\text{cm}^{-1}$  with respect to the WT (348  $\text{cm}^{-1}$ ) (**Figure 3.6, C**);
- 5) new band at and at 400  $\text{cm}^{-1}$  (**Figure 3.6, C**);
- 6) intensity increase of the  $\delta(\text{C}_\beta\text{C}_\text{A}\text{C}_\text{B})$  band at 418  $\text{cm}^{-1}$  (**Figure 3.6, C**);
- 7) EPR  $g$  values at  $g_1 = 2.95$  and  $g_2$  2.27 (**Figure 3.6, B**).

### 3.3.2 Misligated model compounds

To assign the 6cLS species present in the Cyt c-CL R 1:30 complex, very useful was the comparison of the marker bands of the complex with those observed in the model compounds spectra of Cyt c misligated species.



His) and average of 8 spectra with 40 min integration time (His-Fe-H<sub>2</sub>O).

The most dramatic changes are observed in the fingerprint region, where specific iron-ligand stretching vibrations corresponding to His18-Fe-His and His18-Fe-Lys misligation as well as a specific band pattern for His18-Fe-OH<sup>-</sup> and His18-Fe-H<sub>2</sub>O conformations are observed. Therefore, this spectral region provides a useful marker for the identification of the nonnative conformations [Ferrer 1993, Colón 1996, Zheng 2000, Oellerich 2002, Sinibaldi 2003, Santoni 2004, Caroppi 2004, Fedurco 2004, Sinibaldi 2005, Sinibaldi 2006, Verbaro 2009, Battistuzzi 2012, Ly 2012, Capdevila 2015, Tognaccini 2016, Ciaccio 2017]. In particular in all the misligated forms (**Figure 3.9** and **Table 3.1**) the  $\nu_8$  band down-shift from 348 cm<sup>-1</sup> (WT) to lower frequencies (344-342 cm<sup>-1</sup>). Moreover:

- The His18-Fe-His26/33 species [Othman 1994, Oellerich 2002, Santoni 2004] is characterized by: an intensity increase of the  $\delta(C_\beta C_a C_b)$  band at 418 cm<sup>-1</sup> and the appearance of new bands at 206 and 400 cm<sup>-1</sup>, assigned to the  $\nu_{\text{sym}}(\text{Fe-Im}_2)$  mode [Mitchell 1987, Othman 1994] and  $\nu_{\text{asym}}(\text{Fe-Im}_2)$  modes, respectively. In Cyt c there only two other His residues, beside the proximal His18, namely His26 and His33, and both could act as distal ligand [Colón 1997].
- The His18-Fe-Lys72/73/79 species [Döpner 1998] is characterized by: an intensity increase of the  $\delta(C_\beta C_a C_b)$  band at 412 cm<sup>-1</sup>, the appearance of a new band at 384 cm<sup>-1</sup>, assigned to the  $\nu(\text{Fe-N}_{\text{Lys}})$  stretching vibration and the splitting of the  $\delta(C_\beta C_a S)$  thioether vibration mode in two bands at 394 and 401 cm<sup>-1</sup>. In horse heart Cyt c the Lys that could replace Met80 are located in position 72, 73 and 79 [Döpner 1998, Rosell 1998, Blouin 2001].
- The His18-Fe-OH<sup>-</sup> species [Döpner 1998, Battistuzzi 2012] is characterized by a significant intensity loss of the thioether bending mode  $\delta(C_\beta C_a S)$  at 395 cm<sup>-1</sup>.

- The His18-Fe-H<sub>2</sub>O partially unfolded protein, A state is a mixture of 6cLS (D<sup>2</sup> Soret at 410 nm and core size bands at 1504, 1585 and 1636 cm<sup>-1</sup>) and 6cHS (D<sup>2</sup> Soret at 401 nm, CT band at 625 nm and core size bands at 1481, 1570 and 1611 cm<sup>-1</sup>) species [Jordan 1995]. In the finger print region is characterized by very intense  $\delta(C_{\beta}C_cC_d)$  propionate bending modes at 378 and 385 cm<sup>-1</sup>.

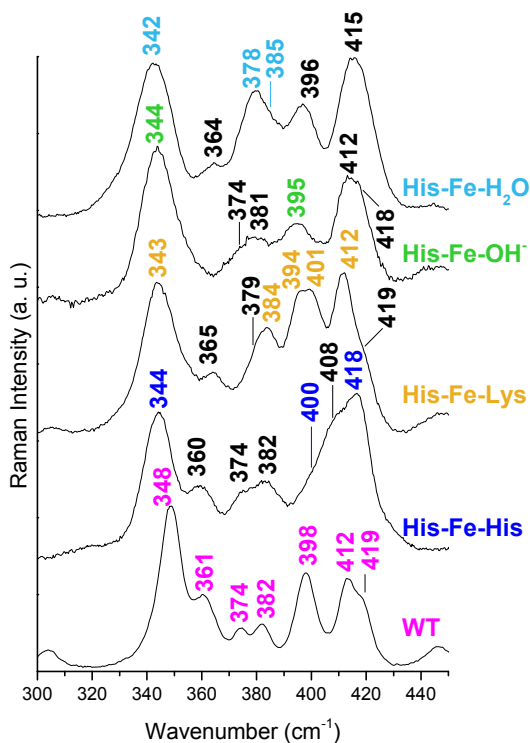


**Figure 3.9.** Comparison of the low frequency RR spectra of horse heart Cyt c for different coordination states: His-Fe-Met (WT), His-Fe-His, His-Fe-Lys, His-Fe-OH<sup>-</sup>, and His-Fe-H<sub>2</sub>O, whose marker bands wavenumbers are shown in magenta, blue, light brown, green and light blue, respectively. The spectra have been shifted along the ordinate axis to allow better visualization. RR experimental conditions:  $\lambda_{exc}$  406.7 nm; laser power at the sample 5-10 mW and average of 4 spectra with 20 min integration time (His-Fe-Met), average of 11 spectra with 55 min integration time (His-Fe-Lys and His-Fe-OH<sup>-</sup>), average of 12 spectra with 60 min integration time (His-Fe-His) and average of 8 spectra with 40 min integration time (His-Fe-H<sub>2</sub>O).

**Table 3.1.** Frequencies ( $\text{cm}^{-1}$ ) of the bands in the fingerprint region of Cyt c in its native and misligated forms. The marker bands of each species are reported in magenta (native His-Fe-Met) blue (His-Fe-His), light brown (His-Fe-Lys), green (His-Fe-OH<sup>-</sup>), and light blue (His-Fe-H<sub>2</sub>O).

Mode	Symm.	WT	His	Lys	OH <sup>-</sup>	H <sub>2</sub> O
$\nu_{\text{sym}}(\text{Fe-Im})$			206			
$\nu_8$	A <sub>1g</sub>	348	344	343	344	342
$\nu_{50}$	E <sub>u</sub>	361	360	365		364
$\delta(\text{C}_\beta\text{C}_c\text{C}_d)$		374	374	379	374	378
		382	382		381	385
$\nu(\text{Fe-N}_{\text{Lys}})$				384		
$\delta(\text{C}_\beta\text{C}_a\text{S})$		398		394	395	396
				401		
$\nu_{\text{asym}}(\text{Fe-Im}_2)$			400			
$\delta(\text{C}_\beta\text{C}_a\text{C}_b)$		412	408	412	412	415
		419	418	419	418	

Also the EPR spectra are very sensitive to the nature of the iron ligand, therefore, in collaboration with Professor Maria Fittipaldi and Professor Rebacca Pogni's group (Universities of Florence and Siena, respectively), we also obtained the EPR spectra of the Cyt c native protein ( $g = 3.07, 2.23, \text{ and } 1.25$ ), His18-Fe-His ( $g = 2.95, 2.26, \text{ and } 1.50$ ), and His18-Fe-Lys ( $g_1$  features near 3.5 and 3.3) (see below, **Figure 3.14**). The  $g$  values of each species are in agreement with those of a previous work [Brautigam 1977]. Unfortunately, all attempts to obtain the EPR spectrum of the K727379N mutant at pH 12 (OH<sup>-</sup> model compound) by applying various conditions of temperature and microwave power failed. The reason for this is unclear; however, the low sample concentration imposed by the impossibility to achieve a sufficiently high yield of protein to prepare a concentrated sample may certainly be a factor. However the His-Fe-OH<sup>-</sup> species markedly differs from the others, giving rise to features at  $g$  values similar to those

observed for the alkaline form of Mb (2.55, 2.17, 1.85) [Brautigan 1977, Gadsby 1987, Kraus 1990].

### 3.3.3 His-Fe-His ligation in the Cyt c-CL complex

The comparison of the marker bands of the 6cLS misligated form present in the Cyt c-CL R 1:30 complex spectrum with those observed in the misligated Cyt c model compounds spectra, highlight that the spectral features of the misligated species that grows in the Cyt c-CL, correspond to the those observed in the 6cLS bis-His model compound. Therefore, in agreement with recent findings [Capdevila 2017], this new species is attributed to a 6cLS bis-His species in which the Met80 residue has been replaced by His26 or His33 (His18-Fe-His26/His33). This clearly results from a global rearrangement of the protein, since neither His26 nor His33 are located in proximity of the heme iron. Accordingly, the new RR band at  $400\text{ cm}^{-1}$  is assigned to the  $\nu_{AS}(\text{Fe-Im}_2)$  mode [Othman 1994, Santoni 2004, Capdevila 2015]. The corresponding  $\nu_S(\text{Fe-Im}_2)$  mode [Mitchell 1987, Othman 1994] is assigned to the band observed at  $206\text{ cm}^{-1}$  (see below, **Figure 3.13, A**).

### 3.3.4 Mutated proteins

#### 3.3.3.1 K727273N, K7273N/H26Y, K7273N/H33Y, and H26H33N

In order to confirm the presence of a bis-His complex and possibly identify which of the two possible His residues bound to the heme Fe in the misligated Cyt c-CL complex, I have studied the CL interaction of CL with Cyt c mutants where the residues that could take the place of Met80 (His26, His33, Lys72, Lys73, and Lys79) have been mutated: K727379N, K7273N/H26Y, K7273N/H33Y, and H2633N. The unligated forms of the triple mutants have been previously studied, showing that the mutations have little effect on the local heme structure [Sinibaldi 2013]. Also for the H2633N double mutant, the UV-Vis and RR spectra demonstrate that the mutation does not alter the protein significantly (**Figure 3.10**).

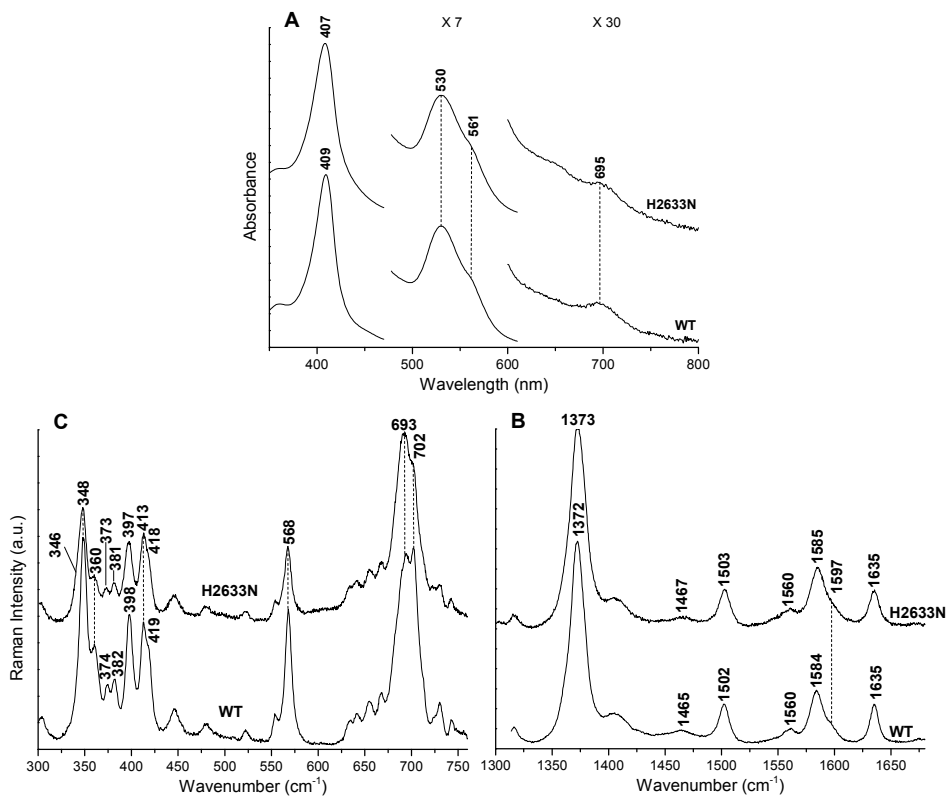


**Figure 3.10.** UV-vis (A) and RR spectra in the high (B) and low (C) frequency regions of the Cyt c H2633N mutant. The spectra of the WT protein are also shown for comparison. The spectra have been shifted along the ordinate axis to allow better visualization. In panel A the 470–620 nm and the 600–800 nm regions of the spectra are expanded 7-fold and 30-fold, respectively. In panels B and C the intensity of the spectra is normalized to that of the  $\nu_4$  band. RR experimental conditions: excitation wavelength 406.7 nm, laser power at the sample 5 mW, average of 19 spectra with 95 min integration time (B) and average of 18 spectra with 90 min integration time (C).

All the triple mutants bind CL giving rise to spectra analogous to that of the WT-CL complex (**Figures 3.11 and 3.12**).

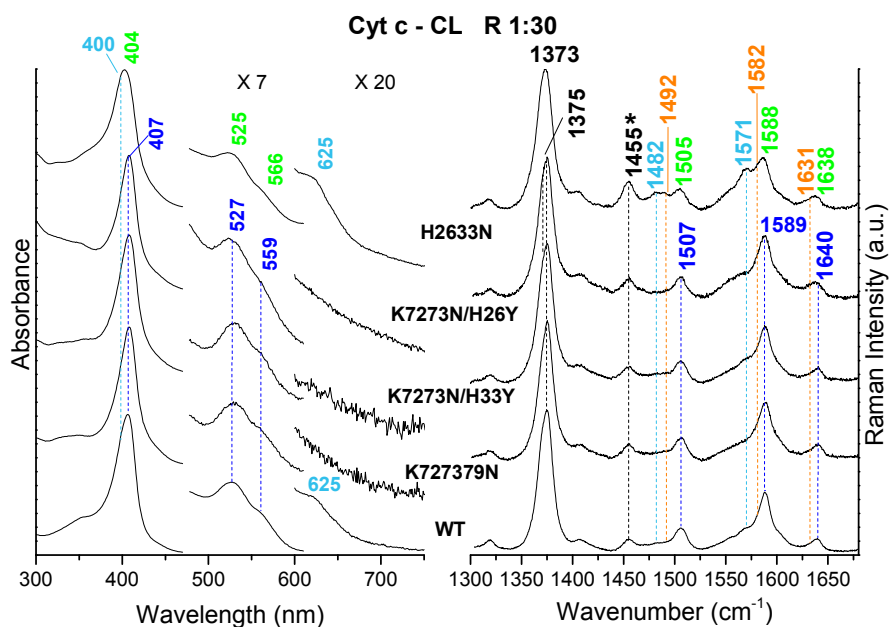


**Figure 3.11.** UV-vis (left) and RR spectra in the high frequency region (right) of the R 1:30 CL complexes of the WT protein and K727379N, K7273N/H33Y, K7273N/H26Y, and H2633N mutants. The wavelengths and frequencies of the bands due to the bis-His species, the OH-Fe-His species, the 6cHS and the 5cHS species are shown in blue, green, light blue and orange, respectively. The spectra have been shifted along the ordinate axis to allow better visualization. The 470–620 nm and the 600–750 nm regions of the UV-Vis spectra are expanded 7-fold and 20-fold, respectively. The intensity of the RR spectra is normalized to that of the  $\nu_4$  band. Experimental conditions: excitation wavelength 406.7 nm, laser power at the sample 5 mW; average of 21 spectra with 105 min integration time (WT), average of 12 spectra with 60 min integration time (K727379N), average of 18 spectra with 90 min integration time (K7273N/H33Y), average of 14 spectra with 70 min integration time (K7273N/H26Y), average of 7 spectra with 35 min integration time (H2633N).

The slight differences that can be observed in the RR low frequency region (**Figure 3.12**) depend on the different amounts of unligated

protein that remains after complexation ( $\nu_8$  at  $348\text{ cm}^{-1}$  and  $(\delta(C_\beta C_a C_b))$  at  $412\text{ cm}^{-1}$ ). Therefore, any involvement of the Lys residues in heme iron coordination in the WT-CL complex can be completely excluded. Moreover, both the K7273N/H26Y, K7273N/H33Y CL-complexes show the presence of a bis-His species, clearly indicating that both His26 and His33 are capable of replacing Met80 in the WT-CL complex, as previously observed for the interaction between Cyt c and CL liposomes [Capdevila 2015].

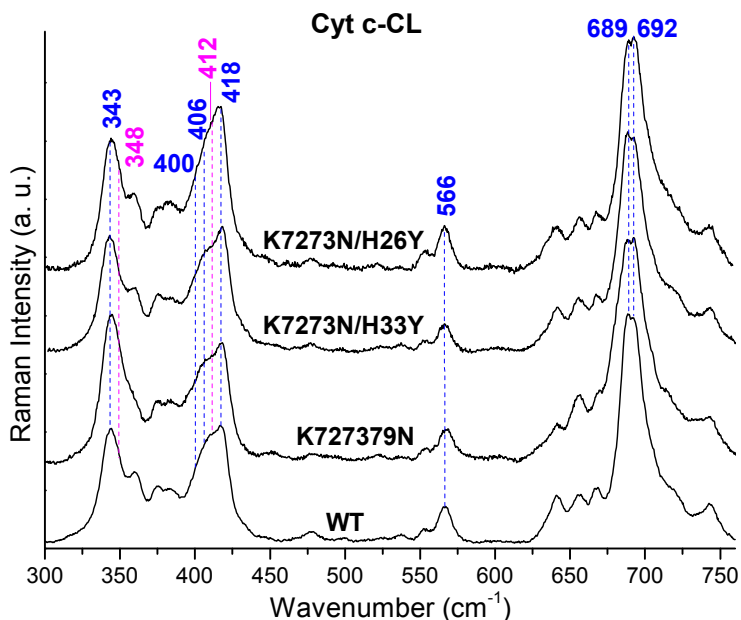


**Figure 3.12.** RR spectra in the low frequency region of the R 1:30 CL complexes of the WT protein and K727379N, K7273N/H33Y, K7273N/H26Y mutants. The frequencies of the bands due to the 6cLS His-Fe-Met native species and of the 6cLS bis-His species are shown in magenta and blue, respectively. The spectra have been shifted along the ordinate axis to allow better visualization and the intensity of the spectra is normalized to that of the  $\nu_4$  band. Experimental conditions: excitation wavelength  $406.7\text{ nm}$ , laser power at the sample  $5\text{ mW}$ ; average of 12 spectra with  $60\text{ min}$  integration time (WT), average of 18 spectra with  $90\text{ min}$  integration time (K727379N), average of 20 spectra with  $100\text{ min}$  integration time (K7273N/H33Y), average of 18 spectra with  $90\text{ min}$  integration time (K7273N/H26Y).

Conversely, the RR spectrum of the H2633N-CL complex (**Figures 3.11 and 3.13**), similarly to what previously reported [Capdevila 2015], is markedly different from that of the WT-CL complex. Interestingly, it has striking similarities with that of the OH<sup>-</sup> model compound. This similarity becomes even more evident in the RR spectra obtained at 80 K. In fact, at low temperature the spectra show an increased resolution, as a consequence of the bands sharpening, and a decreased amount of HS species (particularly abundant in the CL-H2633N complex, see **Figure 3.11**), since, lowering the temperature, heme proteins undergo to a temperature induced transition from high to low spin [Smulevich 1989, Smulevich 1990, Howes 2000, Nielsen 2001].

This contradicts the previous assignment of of the CL-H2633N complex to a Lys-Fe-His coordination [Capdevila 2015]. The EPR spectra confirmed the nature of the sixth ligand in the free and CL complexed H2633N mutant (**Figure 3.14**). The spectrum of the unligated H2633N mutant is identical to that of the WT, confirming that the mutation does not alter the protein significantly. The EPR spectrum of the H2633N-CL complex is very different from that of the His18-Fe-Lys model compound, ruling out a Lys distal ligation. It indicates the presence of a mixture of 6cHS ( $g = 6.0$ ), native 6cLS His18-Fe-Met ( $g_1 = 3.07$ ), and a species with  $g_1 = 2.95$ , which is accidentally identical to the  $g_1$  value of the bis-His species. In the absence of the two His residues (His26 and His33), the most likely interpretation of the  $g_1 = 2.95$  signal is a His-Fe-OH<sup>-</sup> species where the OH<sup>-</sup> ligand is strongly H-bonded, as reported for HRPC and HRPA2 (horseradish peroxidase isoenzymes C and A2) at alkaline pH [Blumberg 1968, Howes 2000]. As mentioned before, we were unable to obtain the EPR spectrum of the His18-Fe-OH<sup>-</sup> model compound for comparison.

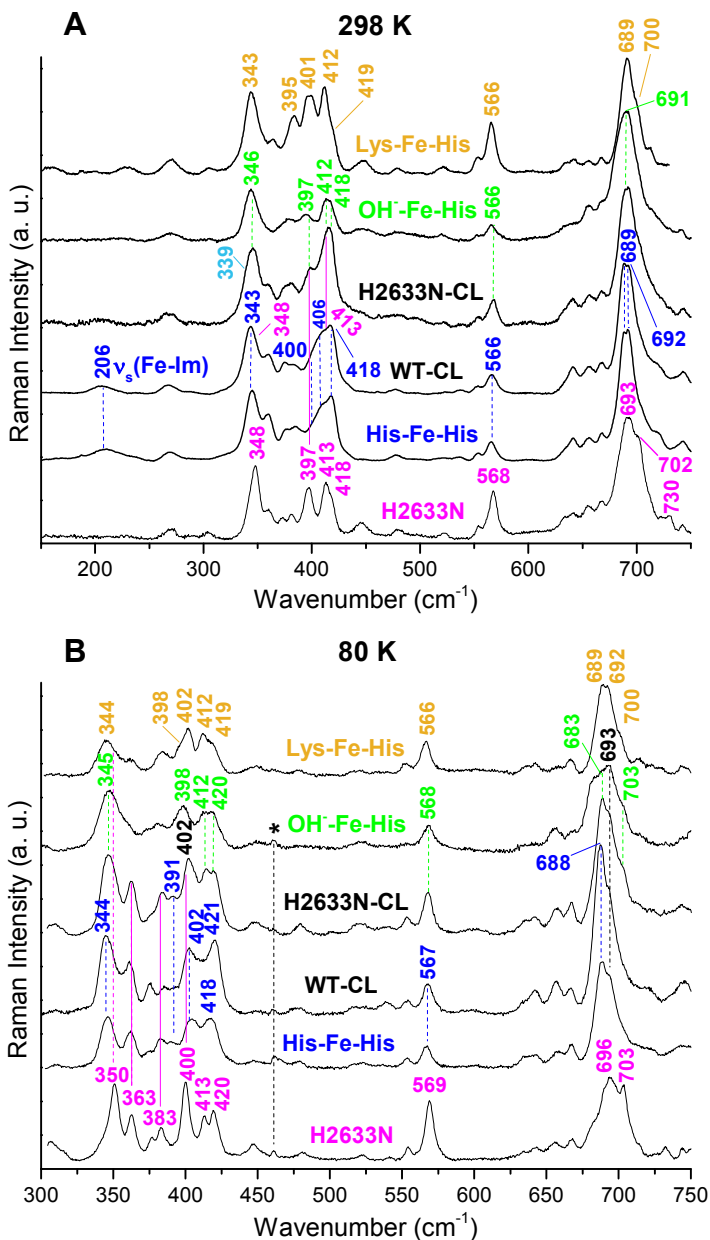


**Figure 3.13.** RR spectra at 298 K (panel A) and at 80 K (panel B) in the low frequency region of the H2633N mutant and the CL-complexes of the WT protein and the H2633N mutant. The spectra of the bis-His, OH<sup>-</sup>-Fe-His, and Lys-Fe-His models are also shown for comparison. The frequencies of the bands assigned to the Met-Fe-His native species, the His-Fe-His species, the OH<sup>-</sup>-Fe-His species and the Lys-Fe-His species

are shown in magenta, blue, green and light brown, respectively. The spectra have been shifted along the ordinate axis to allow better visualization and the intensity of the spectra is normalized to that of the  $\nu_4$  band. The spectra at 298 K were obtained using a spherical lens while those at 80 K were obtained using a cylindrical lens. Experimental conditions: excitation wavelength 406.7 nm, laser power at the sample 5-10 mW; **H2633N**: average of 18 spectra with 90 min integration time (A) and average of 30 spectra with 60 min integration time (B); **His-Fe-His**: average of 12 spectra with 60 min integration time (A) and average of 29 spectra with 145 min integration time (B); **WT-CL** (R 1:30): average of 12 spectra with 60 min integration time (A) and average of 11 spectra with 55 min integration time (B); **H2633N-CL** (R 1:30): average of 24 spectra with 120 min integration time (A) and average of 40 spectra with 80 min integration time (B); **OH-Fe-His**: average of 11 spectra with 55 min integration time (A) and average of 27 spectra with 54 min integration time (B); **Lys-Fe-His**: average of 11 spectra with 55 min integration time (A) and average of 20 spectra with 10 min integration time (B).

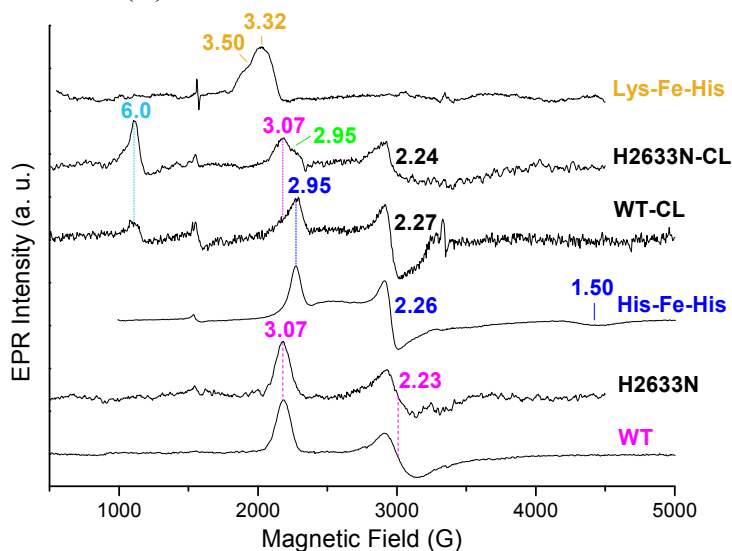


**Figure 3.14.** EPR spectra of the WT protein, the H2633N mutant and their CL-complexes in 20 mM Hepes pH 7.0. The spectra of the bis-His and Lys-Fe-His models are also shown for comparison. The g-values of the bands assigned to the Met-Fe-His native species, the His-Fe-His species, the Lys-Fe-His and the 6cHS species are shown in magenta, blue, light brown, and light blue, respectively. The spectra shown are after subtraction of the cavity signal and have been shifted along the

ordinate axis to allow better visualization. Experimental conditions: WT protein: 190  $\mu\text{M}$  10 K, microwave power 0.53 mW; H2633N mutant: 50  $\mu\text{M}$ , 15 K, microwave power 4.2 mW; His-Fe-His: 255  $\mu\text{M}$ , 5 K, microwave power 8.3 mW; WT-CL (R 1:30): 25  $\mu\text{M}$  5 K, microwave power 8.3 mW; H2633N-CL (R 1:30): 25  $\mu\text{M}$ , 15 K, microwave power 4.2 mW; Lys-Fe-His: 150  $\mu\text{M}$  15 K, microwave power 4.2 mW. In order to minimize accumulation times, some spectra were recorded for a reduced sweep width.

### 3.3.3.2 K72A, K72N, K73A, and K73N

To further investigate the role of the charge of the Lys residues located at positions 72 and 73 on the Cyt c-CL interaction, I have studied the Arg (positively charged residue) and Ala (apolar residue) mutants of these residues: K72R, K73R, K72A, and K73A.

Interestingly, the substitution of Lys72 or 73 affects the protein in the same manner, but the spectroscopic properties depend on the substituting residue.

The spectroscopic study shows that (**Figure 3.15**):

- the Arg mutation does not affect the protein, being the UV-Vis and RR spectra of the K72R, K73R mutants, both in the high and low frequency regions, identical or very similar to those of the WT;
- conversely, the Ala mutants display spectral variations similar to those of the Asn mutants (previously characterized [Sinibaldi 2013]), although less marked. In particular, a slight decrease of the CT band at 695 nm, the upshift of the  $\nu_2$  core size marker band, the slight decrease in intensity of the bands at 568 and 701  $\text{cm}^{-1}$ , the downshift of  $\nu_8$  at 349  $\text{cm}^{-1}$ , an increase in the intensity of the 413  $\text{cm}^{-1}$  band, suggest the presence of a small amount of a subpopulation with an alternative low spin His18-Fe-Lys ligation [Döpner 1998], which grows in the Asn mutants, being the spectroscopic markers more evident.

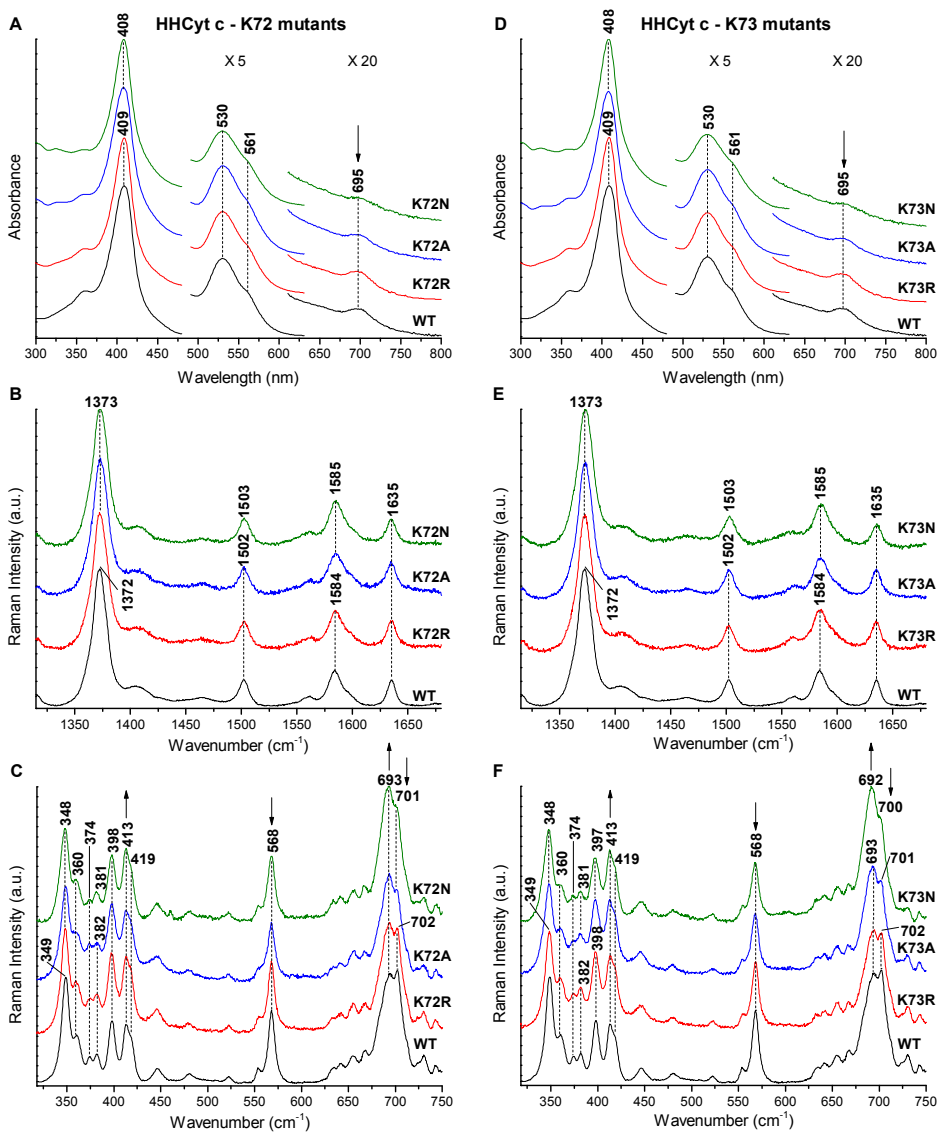


**Figure 3.15.** UV-Vis (A, D) and RR spectra spectra in the high (B, E) and low (C, F) frequency regions of K72R and K73R (red), K72A and K73A (blue), K72N and K73N (green) mutants compared with WT Cyt c (black). The spectra have been shifted along the ordinate axis to allow better visualization. In panel A and D the 470–650 nm and 650–800 nm regions are expanded 5-fold and 20-fold respectively. RR experimental conditions: excitation wavelength 406.7 nm; laser power at the sample 5 mW, average of 5 spectra with 25 min integration time (WT, B and E) and average of 4 spectra with 20 min integration time (WT, C and F);

average of 6 spectra with 30 min integration time (K72R, B) and average of 8 spectra with 40 min integration time (K72R, C); average of 6 spectra with 30 min integration time (K72A, B) and average of 8 spectra with 40 min integration time (K72A, C); average of 5 spectra with 25 min integration time (K72N B, C), average of 6 spectra with 30 min integration time (K73R E and F); average of 6 spectra with 30 min integration time (K73A, E) and average of 8 spectra with 40 min integration time (K73A, F); average of 4 spectra with 20 min integration time (K73N, E) and average of 3 spectra with 15 min integration time (K73N, F). The intensities are normalized to that of the  $\nu_4$  band.

Since the spectroscopic characterization indicates that only the Arg mutants show a native structure with the Met80 residue coordinating the heme iron atom, the CL binding and peroxidase activity of only the K72R and K73R mutants have been studied by circular dichroism and stopped flow kinetic experiments (experiments carried out by Professor Santucci's group, Tor Vergata University, Rome) The results show that:

- the K72R mutant interacts with CL, unlikely to the K72N mutant which couldn't bind CL [Sinibaldi 2013]. Thus we concluded that position 72 must be occupied by a positively charged residue to assure Cyt c-CL recognition;
- the peroxidase activity of the CL-bound K73R mutant is strongly increased as compared to the native CL-complex. This result is very different to that previously obtained on the K73N mutant that does not show peroxidase activity [Sinibaldi 2013]. Hence, we concluded that the position 73 influences the peroxidase activity of the CL-bound protein.

In conclusion, the Lys72 and Lys73 residues play a crucial role in the Cyt c-CL binding.

### **3.4 Ferrous form**

The absorption spectrum (**Figure 3.16, A**) of the ferrous form of the WT-CL complex is characteristic of a 5cHS form (428 and 560 nm) in equilibrium with the 6cLS WT protein, as clearly indicated by the second derivative spectra in the Soret region (416 nm). Therefore, upon reduction, a certain amount of CL detaches from Cyt c.

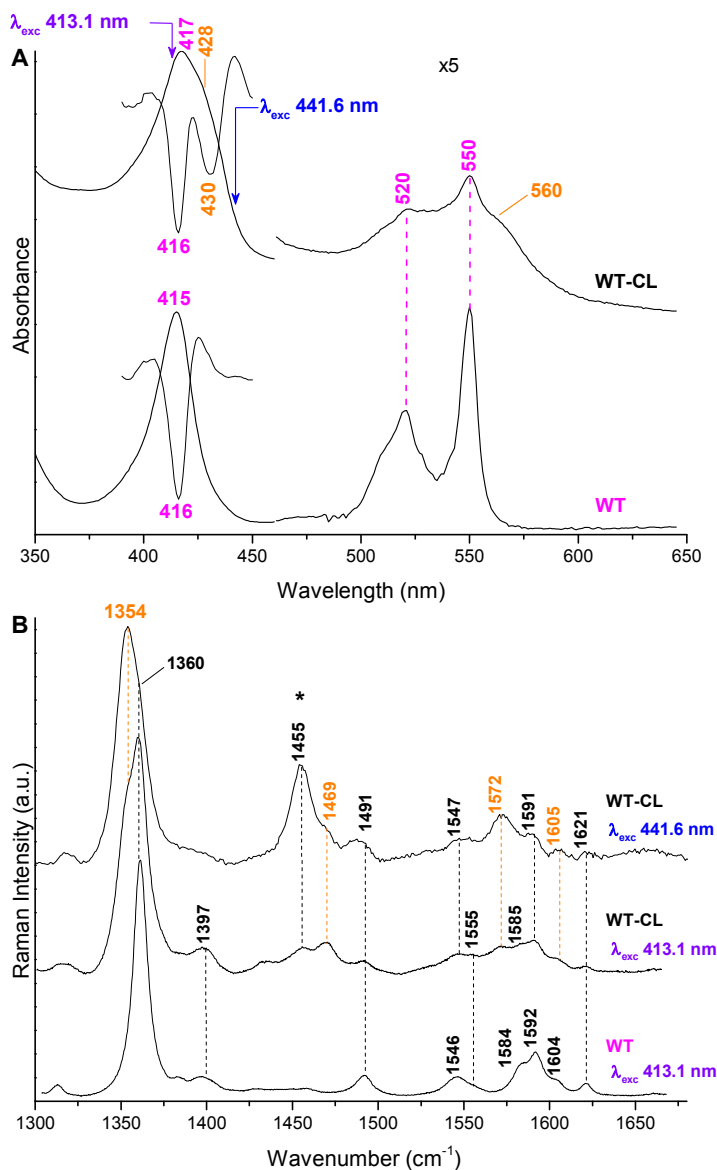


**Figure 3.16.** UV-vis and RR spectra in the high frequency region of the ferrous WT protein ( $\lambda_{\text{exc}}$  413.1 nm) and the WT-CL R 1:30 complex ( $\lambda_{\text{exc}}$  413.1 nm and  $\lambda_{\text{exc}}$  441.6 nm). The wavelengths and frequencies of the bands assigned to the His-Fe-Met native species and the 5cHS species are shown in magenta and orange, respectively, and the two excitation laser lines at 413.1 nm and 441.6 nm are shown in violet and blue, respectively. The spectra have been shifted along the ordinate axis to allow better visualization. The 470–650 nm region of the UV-Vis spectra is expanded 5-fold. RR experimental conditions: WT: excitation

wavelength 413.1 nm, laser power at the sample 5 mW, average of 4 spectra with 20 min integration time; WT-CL: laser power at the sample 6 mW, average of 15 spectra with 75 min integration time ( $\lambda_{\text{exc}}$  413.1 nm) and laser power at the sample 26 mW, average of 3 spectra with 15 min integration time with a 1800 grooves/mm grating ( $\lambda_{\text{exc}}$  441.6 nm).

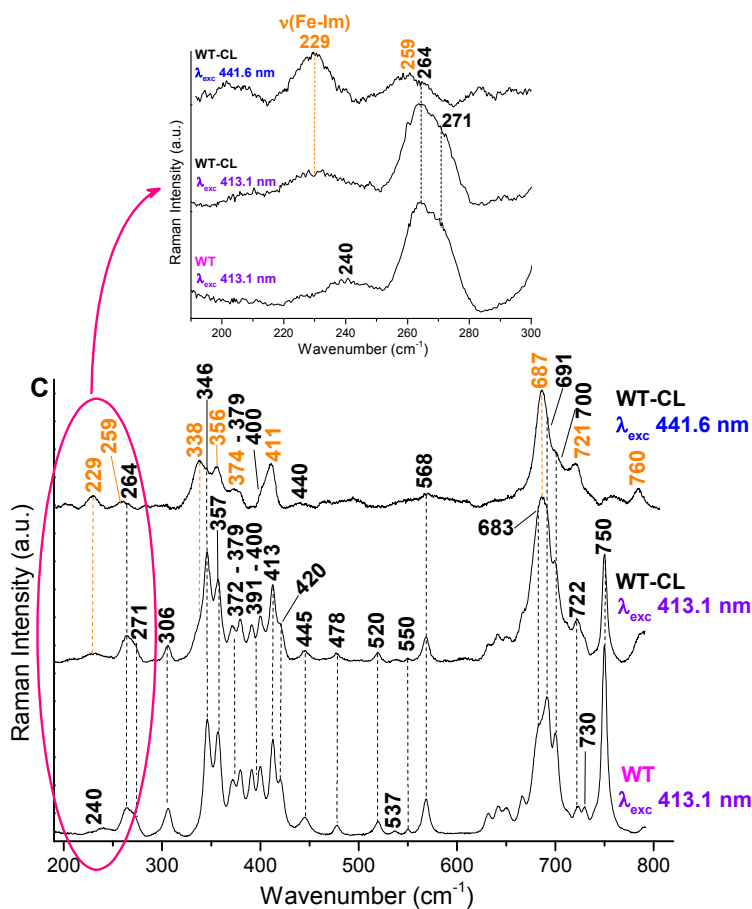


**Figure 3.17.** RR spectra in the low frequency region of the ferrous WT protein ( $\lambda_{\text{exc}}$  413.1 nm) and the WT-CL R 1:30 complex ( $\lambda_{\text{exc}}$  413.1 nm and  $\lambda_{\text{exc}}$  441.6 nm). The frequencies of the bands assigned to the 5cHS species are shown in orange. The spectra have been shifted along the ordinate axis to allow better visualization and the intensity of the spectra is normalized to that of the  $\nu_4$  band. Experimental conditions: WT: excitation wavelength 413.1 nm, laser power at the sample 5 mW, average of 4 spectra with 20 min integration time; WT-CL: laser power at the sample 6 mW, average of 15 spectra with 75 min integration time ( $\lambda_{\text{exc}}$  413.1 nm) and laser power at the sample 26 mW, average of 15

spectra with 75 min integration time ( $\lambda_{\text{exc}}$  441.6 nm). **The inset** shows the 190-300  $\text{cm}^{-1}$  region expanded and the  $\nu(\text{Fe-Im})$  mode.

The corresponding RR spectra in the high (**Figure 3.16, B**) and low frequency regions (**Figure 3.17**) confirm the presence of these two forms, being the vibrational modes of the 5cHS and 6cLS species selectively enhanced with the 441.6 nm (Soret band of the 5cHS species at 428 nm) and 413.1 nm (Soret band of the 6cLS species at 417 nm) excitation lines, respectively.

The reduced form of the Cyt c-CL complex does not have any functional relevance, but its RR spectra can give information on the status of the proximal Fe-His bond, which is a characteristic mode of the 5cHS heme protein with an imidazole as fifth ligand and is therefore strongly enhanced for 441.6 nm excitation. As explained in Chapter 2, the  $\nu(\text{Fe-His}_{18})$  stretching mode frequency, is very sensitive to the presence of H-bonds interactions between the proximal His  $\text{N}_\delta$  hydrogen atom and nearby accepting residues [Stein 1980, Teraoka 1980, Kitagawa 1988]. The frequency of the  $\nu(\text{Fe-His}_{18})$  band in the WT-CL complex is at 229  $\text{cm}^{-1}$ , which is a fairly high frequency, suggesting that the bond between the heme iron and the  $\text{N}_\epsilon$  of the proximal His18 is strong. Hence it is likely that the His18  $\text{N}_\delta$  hydrogen is involved in the formation of a strong hydrogen bond with an accepting group. In analogy with a previous work [Santoni 2004] and on the basis of the X-ray structure of Cyt c [Bushnell 1990], a good candidate as a hydrogen bond acceptor group is the oxygen of the carbonyl group of Pro30 at 2.7 Å from His18.

### 3.5 Ferrous-CO adduct

The 5cHS ferrous species of the WT-CL complex binds CO, giving rise to a 6cLS complex with bands at 415, 532 and 562 nm in equilibrium with the ferrous WT protein (550 nm) (**Figure 3.18**).

As the ferrous form, also the ferrous-CO adduct of the Cyt c-CL complex does not have any functional relevance, but its RR spectra can give information on the architecture of the distal heme pocket, being the Fe-CO back-bonding modulated by polar interactions and, in particular,

by the formation of H-bonds between the bound CO and the distal protein residues (see Chapter 2).

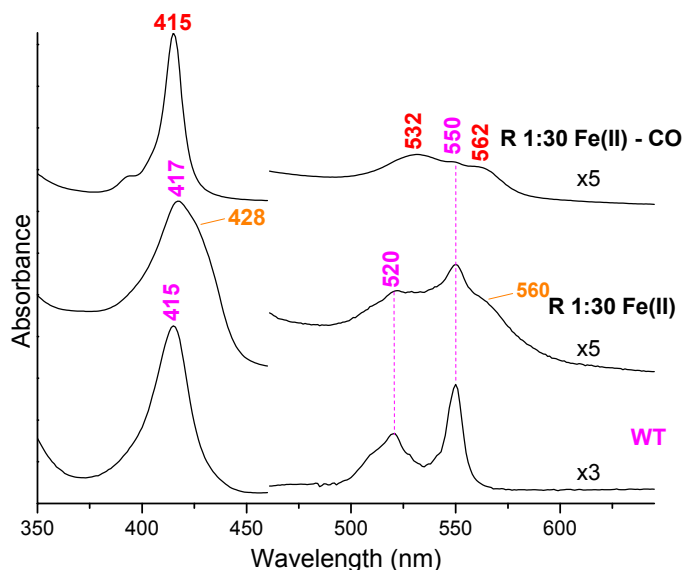


**Figure 3.18.** UV-vis spectra of the ferrous WT protein, the WT-CL R 1:30 complex and the WT-CL R 1:30 CO adduct. The wavelengths of the bands assigned to the His-Fe-Met native species, to the 5cHS species and to the CO complex are shown in magenta, orange and red, respectively. The 470–650 nm region of the spectra is expanded 3- or 5-fold. The spectra have been shifted along the ordinate axis to allow better visualization.

In **Figure 3.19** is reported the plot of the inverse linear correlation of the  $\nu(\text{FeC})$  and  $\nu(\text{CO})$  stretching modes (see Chapter 2) of the CO adducts of several Mbs characterized by different distal interactions with the CO [Phillips 1999]:

- in Elephant (E) Mb the CO strongly interacts with the polar distal Gln residue;
- in sperm whale (SW) Mb the CO interacts with the less polar His distal residue;
- the His64Val mutant of SW Mb where the apolar Val residue replaced the polar His, does not interact with CO.

The  $\nu(\text{Fe-C})$  and  $\nu(\text{CO})$  of the CO adduct of the WT-CL complex are at  $491\text{ cm}^{-1}$  and  $1966\text{ cm}^{-1}$ , respectively (**Figure 3.19**). Thus the

$\nu(\text{FeC})/\nu(\text{CO})$  position along the correlation line is very close to that of the His64Val SW Mb mutant, meaning that the CO molecule is bounded in an upright conformation with no polar distal interactions, i.e. the distal cavity of the WT-CL complex is open.

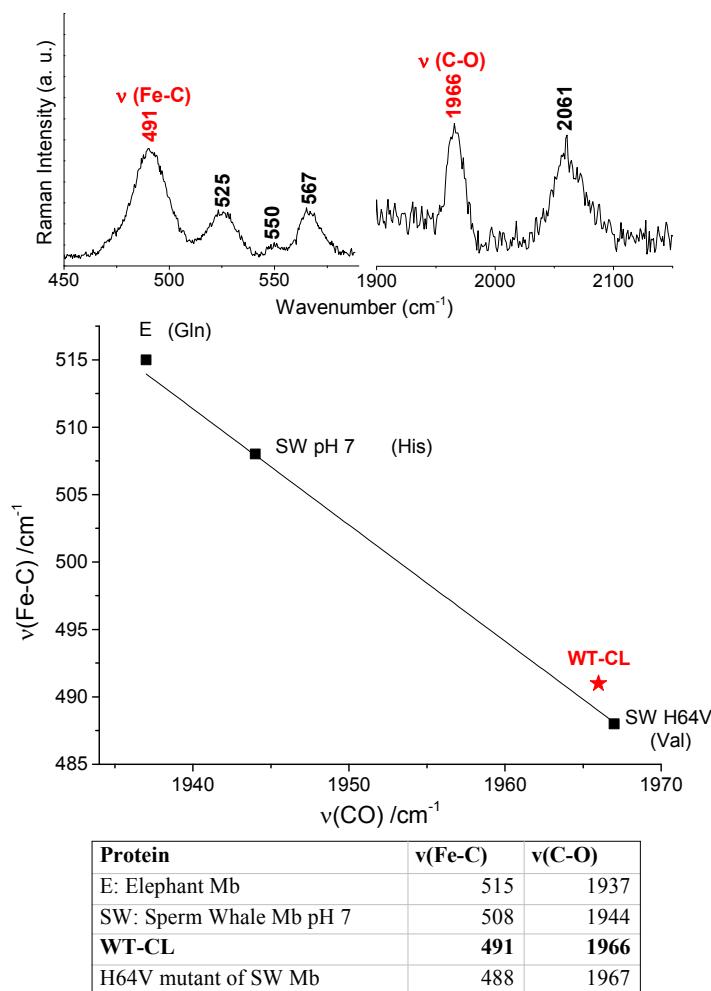


**Figure 3.19.** WT-CL (R 1:30) complex CO adduct. (Top) RR spectra of the ferrous WT-CL CO adduct in the low and high frequency regions. The  $\nu(\text{Fe-C})$  and  $\nu(\text{C-O})$  frequencies are shown in red. (Bottom) back-bonding correlation plot for the  $\nu(\text{Fe-C})$  and  $\nu(\text{C-O})$  stretching frequencies of various Mbs: E, SW pH 7.0, SW H64V mutant where His64 has been substituted with a Val. The interpolation point of the  $\nu(\text{Fe-C})$  and  $\nu(\text{C-O})$  frequencies of the WT-CL R 1:30 CO adduct is

shown as a red star. The frequencies of the various CO adducts are reported in the table.

### 3.6 Conclusions

I have followed the structural changes induced in Cyt c by progressive additions of CL using electronic absorption, RR, and EPR spectroscopies. The titration of Cyt c with CL shows that a partial Met80 detachment is observed at very low CL concentration (Cyt c:CL molar ratio of 1:5) and the spectroscopic data clearly indicate that the native ligand is replaced at this phase by a His. I have unambiguously assigned the misligated form to a 6cLS bis-His species via the comparison with 1) model compounds of the misligated forms of Cyt c 2) the CL complexes of selected mutants, in which residues able to replace Met80 (i.e. His26, His33, Lys72, Lys73, Lys79) have been mutated.

As the CL concentration increases, the proportion of the bis-His species increases at the expense of the native Met80-Fe-His18 form which, however, remains in a small amount up to the end of the titration.

Since neither His26 nor His33 are located in proximity of the heme iron, the formation of a bis-His species indicates that the extent of the protein rearrangement is long ranging, leading to a more flexible heme structure than in the WT protein. Moreover, the formation of a 6cHS (H<sub>2</sub>O-Fe-His18, aquo) species, observed at molar ratios greater than 1:5, and a 5cHS (Fe-His18) species at the end of the titration, probably indicates some degree of lability of the misligated distal His and reflects a further increase of protein flexibility. This finding is supported also by the RR spectrum of the CO-adduct, characterized by  $\nu(\text{FeC})$  and  $\nu(\text{CO})$  stretching mode frequencies typical of an open form with the CO molecule bounded in an upright conformation with no polar distal interactions. On the contrary, the fairly high frequency of the  $\nu(\text{Fe-His18})$  stretching mode ( $229\text{ cm}^{-1}$ ) observed in the 5cHS ferrous form suggests the presence of a hydrogen bond between the N<sub>δ</sub>(His18) hydrogen and an accepting group, consistent with a closed proximal cavity.

Moreover also the Lys72 and Lys73 residues play a crucial role in the Cyt c-CL binding:

- the 72 position must be occupied by a positively charged residue to assure Cyt c-CL recognition: the K72R mutant allows the CL binding, while the K72N mutant does not;
- the 73 position influences the peroxidase activity of the CL-bound protein: no peroxidase activity has been observed in the K73N-CL complex, but in the K73R-CL complex is higher than in the native WT-CL complex.

## References

- ❖ Asher S.A., Schuster T.M., *Biochemistry* 1979, 18, 5377.
- ❖ Balakrishnan G., Hu Y., Spiro, T.G., *J. Am. Chem. Soc.* 2012, 134, 19061.
- ❖ Belikova N.A., Vladimirov Y.A., Osipov A.N., Kapralov A.A., Tyurin V.A., Potapovich M.V., Basova L.V., Peterson J., Kurnikov I.V., Kagan V.E., *Biochemistry* 2006, 45, 4998.
- ❖ Berghuis A.M., Brayer G.D., *J. Mol. Biol.* 1992, 223, 959.
- ❖ Bergstrom C.L., Beales P.A., Lv Y., Vanderlick T.K., Groves J.T., *Proc. Natl. Acad. Sci. U.S.A.* 2013, 110, 6269.
- ❖ Blouin C., Guillemette J.G., Wallace C.J., *Biophys. J.* 2001, 81, 2331.
- ❖ Blumberg W.E., Peisach J., Wittenberg B.A., Wittenberg J.B., *J. Biol. Chem.* 1968, 243, 1854.
- ❖ Bradley J. M., Silkstone G., Wilson M.T., Cheesman M.R., Butt J.N., *J. Am. Chem. Soc.* 2011, 133, 19676.
- ❖ Brautigan D.L., Feinberg B.A., Hoffman B.M., Margoliash E., Peisach, J., Blumberg W.E., *J. Biol. Chem.* 1977, 252, 574.
- ❖ Bushnell G.W., Louie G.V., Brayer G.D., *J. Mol. Biol.* 1990, 214, 585.
- ❖ Capdevila D.A., Oviedo Rouco S., Tomasina F., Tórtora V., Demicheli V., Radi R., Murgida D.H., *Biochemistry* 2015, 54, 7491.
- ❖ Caroppi P., Sinibaldi F., Santoni E., Howes B.D., Fiorucci L., Ferri T., Ascoli F., Smulevich G., Santucci R., *J. Biol. Inorg. Chem.* 2004, 9, 997.
- ❖ Ciaccio C., Tognaccini L., Battista T., Cervelli M., Howes B.D., Santucci R., Coletta M., Mariottini P., Smulevich G., Fiorucci L., *J. Inorg. Biochem.* 2017, 169, 86.
- ❖ Colón W., Roder H., *Nat. Struct. Biol.* 1996, 3, 1019.
- ❖ Colón, W.; Wakem, L. P.; Sherman, F.; Roder, H. *Biochemistry* 1997, 36, 12535.

- ❖ Döpner S., Hildebrandt P., Rosell F.I., Mauk A.G., *J. Am. Chem. Soc.* 1998, 120, 11246.
- ❖ Dyson H., Beattie J., *J. Biol. Chem.* 1982, 257, 2267.
- ❖ Fedurco M., Augustynski J., Indiani C., Smulevich G., Antalík M., Bano M., Sedlak E., Glascock M.C., Dawson J.H., *Biochim. Biophys. Acta* 2004, 1703, 31.
- ❖ Ferrer J.C., Guillemette J.G., Bogumil R., Inglis S.C., Smith M., Mauk A.G., *J. Am. Chem. Soc.* 1993, 115, 7507.
- ❖ Gadsby P.M., Peterson J., Foote N., Greenwood C., Thomson A.J., *Biochem. J.* 1987, 246, 43.
- ❖ Goto Y., Takahashi N., Fink A.L., *Biochemistry* 1990, 29, 3480.
- ❖ Hanske J., Toffey J.R., Morenz A.M., Bonilla A.J., Schiavoni K.H., Pletneva E.V., *Proc. Natl. Acad. Sci. U.S.A.* 2012, 109, 125.
- ❖ Hildebrandt P., *Biochim. Biophys. Acta* 1990, 1040, 175.
- ❖ Hildebrandt P., Scott R., Mauk A.G., University science books: Sausalito, CA:1996.
- ❖ Hobbs J.D., Shelnutt J.A., *J. Protein Chem.* 1995, 14, 19.
- ❖ Hong Y., Muenzner J., Grimm S.K., Pletneva E.V., *J. Am. Chem. Soc.* 2012, 134, 18713.
- ❖ Howes B.D., Feis A., Indiani C., Marzocchi M.P., Smulevich G., *J. Biol. Inorg. Chem.* 2000, 5, 227.
- ❖ Hu S., Morris I.K., Singh J.P., Smith K.M., Spiro T.G., *J. Am. Chem. Soc.* 1993, 115, 12446.
- ❖ Indiani C., De Sanctis G., Neri F., Santos H., Smulevich G., Coletta M., *Biochemistry* 2000, 39, 8234.
- ❖ Jentzen W., Song X.-Z., Shelnutt J.A., *The Journal of Physical Chemistry B* 1997, 101, 1684.
- ❖ Jentzen W., Ma J.G., Shelnutt J.A., *Biophys. J.* 1998, 74, 753.
- ❖ Jordan T., Eads J.C., Spiro T.G., *Protein Sci.* 1995, 4, 716.
- ❖ Kagan V.E., Tyurin V.A., Jiang J., Tyurina Y.Y., Ritov V.B., Amoscato A.A., Osipov A.N., Belikova N.A., Kapralov A.A., Kini V., Vlasova I.I., Zhao Q., Zou M., Di P., Svistunenko D.A., Kurnikov I.V., Borisenko G.G., *Nat. Chem. Biol.* 2005, 1, 223.
- ❖ Kagan V.E., Bayir H.A., Belikova N.A., Kapralov O., Tyurina Y.Y., Tyurin V.A., Jiang J., Stoyanovsky D.A., Wipf P., Kochanek P.M., Greenberger J.S., Pitt B., Shvedova A.A., Borisenko G., *Free Radical Biol. Med.* 2009, 46, 1439.
- ❖ Kalanxhi E., Wallace C.J., *Biochem. J.* 2007, 407, 179.
- ❖ Kapetanaki S.M., Silkstone G., Husu I., Liebl U., Wilson M.T., Vos M.H., *Biochemistry* 2009, 48, 1613.

- ❖ Kawai C., Prado F.M., Nunes G.L.C., Di Mascio P., Carmona-Ribeiro A.M., Nantes I.L., *J. Biol. Chem.* 2005, 280, 34709.
- ❖ Kerr E.A., Yu N.-T. (1988) Vibrational modes of coordinated CO, CN<sup>-</sup>, O<sub>2</sub> and NO. In *Biological applications of Raman spectroscopy: Resonance Raman spectra of hemes and metal-loproteins* (Spiro T.G., Ed.) Vol.3, pp. 39–95, John Wiley and Sons Inc., New York.
- ❖ Kitagawa T., Nagai K., *Nature* 1979, 281, 503.
- ❖ Kitagawa T. (1988) The heme protein structure and the iron histidine stretching mode. In *Biological applications of Raman spectroscopy: Resonance Raman spectra of hemes and metalloproteins* (Spiro T.G., Ed.) Vol.3, pp. 97–131, John Wiley and Sons Inc., New York.
- ❖ Kluck L.M., Ellerby H.M., Najem S., Yaffe M.P., Margoliash E., Bredesen D., Mauk A.G., Sherman F., Newmeyer D.D., *J Biol. Chem* 2000, 275, 16127.
- ❖ Kraus D.W., Wittenberg J.B., *J. Biol. Chem.* 1990, 265, 16043.
- ❖ Louie G.V., Brayer G.D., *J. Mol. Biol.* 1990, 214, 527.
- ❖ Ly H.K., Utesch T., Diaz-Moreno I., Garcia-Heredia J.M., De La Rosa M.A., Hildebrandt P., *J. Phys. Chem. B* 2012, 116, 5694.
- ❖ Margoliash E., Frohwirt N., *Biochem. J.* 1959, 71, 570.
- ❖ Milorey B., Serpas L., Pandiscia L., Schweitzer-Stenner R., *Biophys. J.* 2016, 110, 422a.
- ❖ Mitchell M.L., Li X.Y., Kincaid J.R., Spiro T.G., *J. Phys. Chem.* 1987, 91, 4690.
- ❖ Muenzner J., Toffey J.R., Hong Y., Pletneva E.V., *J. Phys. Chem. B* 2013, 117, 12878.
- ❖ Nielsen K.L., Indiani C., Henriksen A., Feis A., Becucci M., Gajhede M., Smulevich G., Welinder K.G., *Biochemistry* 2001, 40, 11013.
- ❖ O'Brien E.S., Nucci N.V., Fuglestad B., Tommos C., Wand A.J., *J. Biol. Chem.* 2015, 290, 30879.
- ❖ Oellerich S., Wackerbarth H., Hildebrandt P., *The Journal of Physical Chemistry B* 2002, 106, 6566.
- ❖ Orrenius S., Gogvadze V., Zhivotovsky B., *Annu. Rev. Pharmacol. Toxicol.* 2007, 47, 143.
- ❖ Othman S., Le Lirzin A., Desbois A., *Biochemistry* 1994, 33, 15437.
- ❖ Pandiscia L.A., Schweitzer-Stenner R., *J. Phys. Chem. B* 2015, 119, 12846.
- ❖ Patel C.N., Lind M.C., Pielak G.J., *Protein Expr. Purif.* 2001, 22:220.
- ❖ Pearce L.L., Gartner A.L., Smith M., Mauk A.G., *Biochemistry* 1989, 28, 3152.
- ❖ Phillips G.N., Teodoro M.L., Li T., Smith B., Olson J.S., *J. Phys. Chem. B* 1999, 103, 8817.

- ❖ Ranieri A., Millo D., Di Rocco G., Battistuzzi G., Bortolotti C.A., Borsari M., Sola M., *J. Biol. Inorg. Chem.* 2015, 20, 531.
- ❖ Rosell F.I., Ferrer J.C., Mauk A.G., *J. Am. Chem. Soc.* 1998, 120, 11234.
- ❖ Rytömaa M., Kinnunen P.K.J., *J. Biol. Chem.* 1994, 269, 1770.
- ❖ Rytömaa M., Kinnunen P.K.J., *J. Biol. Chem.* 1995, 270, 3197.
- ❖ Santoni E., Scatragli S., Sinibaldi F., Fiorucci L., Santucci R., Smulevich G., *J. Inorg. Biochem.* 2004, 98, 1067.
- ❖ Sinibaldi F., Piro M.C., Howes B.D., Smulevich G., Ascoli F., Santucci R., *Biochemistry* 2003, 42, 7604.
- ❖ Sinibaldi F., Mei G., Polticelli F., Piro M.C., Howes B.D., Smulevich G., Santucci R., Ascoli F., Fiorucci L., *Protein Sci.* 2005, 14, 1049.
- ❖ Sinibaldi F., Howes B.D., Piro M.C., Polticelli F., Bombelli C., Ferri T., Coletta M., Smulevich G., Santucci R., *J. Biol. Inorg. Chem.* 2010, 15, 689.
- ❖ Sinibaldi F., Droghetti E., Polticelli F., Piro M.C., Di Pierro D., Ferri T., Smulevich G., Santucci R., *J. Inorg. Biochem.* 2011, 105, 1365.
- ❖ Sinibaldi F., Howes B.D., Droghetti E., Polticelli F., Piro M.C., Di Pierro D., Fiorucci L., Coletta M., Smulevich G., Santucci R., *Biochemistry* 2013, 52, 4578.
- ❖ Scott R.A., Mauk A.G., *Cytochrome C: A Multidisciplinary Approach*, Univ Science Books 1996.
- ❖ Shelnutt J.A., Song X.-Z., Ma J.G., Jia S. L., Jentzen W., Medforth C.-J., *Chem. Soc. Rev.* 1998, 27, 31.
- ❖ Smulevich G., Mantini A.R., English A.M., Mauro J.M., *Biochemistry* 1989, 28, 5058.
- ❖ Smulevich G., Wang Y., Edwards S.L., Poulos T.L., English A.M., Spiro T.G., *Biochemistry* 1990, 29, 2586.
- ❖ Smulevich G., Miller M.A., Kraut J., Spiro T.G., *Biochemistry* 1991, 30, 9546-9558.
- ❖ Smulevich G., Bjerrum M.J., Gray H.B., Spiro T.G., *Inorg. Chem.* 1994, 33, 4629.
- ❖ Stein P., Mitchell M., Spiro, T.G., *J. Am. Chem. Soc.* 1980, 102, 7795.
- ❖ Stellwagen E., Cass R., *Biochem. Biophys. Res. Commun.* 1974, 60, 371.
- ❖ Streaks T.C., Spiro T.G., *Biochim. Biophys. Acta* 1974, 351, 237.
- ❖ Teraoka J., Kitagawa T., *Biochem. Biophys. Res. Commun.* 1980, 93, 694.
- ❖ Theorell H., Åkesson Å., *J. Am. Chem. Soc.* 1941, 63, 1818.

- ❖ Tognaccini L., Ciaccio C., D'oria V., Cervelli M., Howes B.D., Coletta M., Mariottini P., Smulevich G., Fiorucci L., *J. Inorg. Biochem.* 2016, 155, 56.
- ❖ Trusova V.M., Gorbenko G.P., Molotkovsky J.G., Kinnunen P.K.J., *Biophys. J.* 2010, 99, 1754.
- ❖ Tuominen E.K.J., Wallace C.J.A., Kinnunen P.K.J., *J. Biol. Chem.* 2002, 277, 8822.
- ❖ Verbaro D., Hagarman A., Soffer J., Schweitzer-Stenner R., *Biochemistry* 2009, 48, 2990.
- ❖ Zheng J., Ye S., Lu T., Cotton T.M., Chumanov G., *Biopolymers* 2000, 57, 77.
- ❖ Zhong S., Rousseau D.L., Yeh S.-R., *J. Am. Chem. Soc.* 2004, 126, 13934.



## Chapter 4

### **Resonance Raman structural markers of the coproheme-bound Coprohemedecarboxylase from *Listeria monocytogenes* to follow the catalytic conversion into heme *b***

Stefan Hofbauer, Georg Mlynek, **Lisa Milazzo**, Dominic Pühringer, Daniel Maresch, Irene Schaffner, Paul G. Furtmüller, Giulietta Smulevich, Kristina Djinović-Carugo, Christian Obinger, “Hydrogen peroxide-mediated conversion of coproheme to heme *b* by HemQ – Lessons from the first crystal structure and kinetic studies”, *FEBS J.* **2016**, 283, 4386.

**Lisa Milazzo**, Stefan Hofbauer, Barry D. Howes, Thomas Gabler, Paul G. Furtmüller, Christian. Obinger, Giulietta Smulevich, “Insights into the active site of coproheme decarboxylase from *Listeria monocytogenes*”, *Biochemistry* **2018**, 57, 2044.

**Lisa Milazzo**, Thomas Gabler, Vera Pfanzagl, Hanna Michlits, Paul G. Furtmüller, Christian Obinger, Stefan Hofbauer, Giulietta Smulevich, “The hydrogen bonding network of coproheme in *LmChdC*: impact on structure and catalysis”, *submitted to Journal of Inorganic Biochemistry*.

**Lisa Milazzo**, Thomas Gabler, Dominic Pühringer, Zuzana Jandova, Daniel Maresch, Hanna Michlits, Vera Pfanzagl, Kristina Djinović-Carugo, Chris Oostenbrink, Paul G. Furtmüller, Christian Obinger, Giulietta Smulevich, Stefan Hofbauer, “Redox cofactor twists during its stepwise decarboxylation – molecular mechanism of conversion of coproheme to heme *b*”, *in preparation*.

## 4.1 Introduction

In the last years, in addition to the well-known, textbook pathway for heme biosynthesis, an alternative and more ancient route has been described [Dailey 2015]. The last step of this biosynthetic pathway, performed mainly by monoderm, but also by some diderm, archaea, and intermediate bacteria [Dailey 2010, Dailey2015, Dailey 2107, Kosugi 2017, Pfanzagl 2018], is operated by the coproheme decarboxylase (ChdC, formerly known as HemQ from the name of the gene that encodes it [Dailey 2015]). This newly discovered enzyme catalyzes the decarboxylation of the two propionate groups in position 2 and 4 (p2, p4) of the iron coproporphyrin III (coproheme) to yield iron protoporphyrin IX (heme *b*), via a three-propionate mono-vinyl intermediate (harderoheme) [Dailey 2015, Celis 2015, Hobbs 2016] (**Figure 4.1**). The reaction is hydrogen peroxide driven (two H<sub>2</sub>O<sub>2</sub> molecules are needed to transform one coproheme to heme *b*) [Hofbauer 2016] and dependent on the porphyrin iron to perform the redox reaction; in fact, nickel and manganese substituted coprohemes do not react with hydrogen peroxide, making the substrate also the enzymatic co-factor [Dailey 2015, Celis 2017].

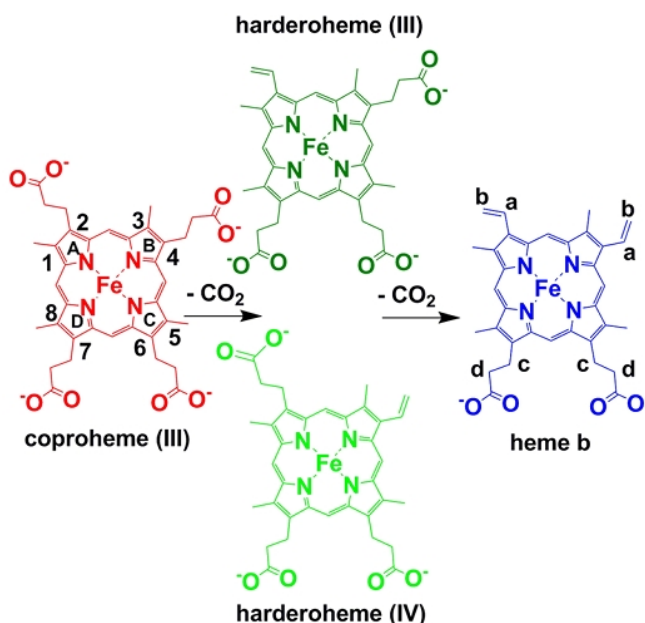


**Figure 4.1.** Initial substrate (coproheme), possible intermediates (harderoheme), and product (heme *b*) of the ChdC catalyzed reaction.

Heme rings are labelled A–D and substituted pyrrole carbons 1–8. Vinyl and propionate carbons are labelled a–d. Adapted from Celis 2015.

Many Firmicutes and Actinobacteria which perform the alternative heme biosynthetic pathway are pathogens and represent a major threat to public health, due to the development of multiple resistances to common antibiotics [Magiorakos 2012, Shen 2013]. Their steady-state iron uptake, heme biosynthesis, heme degradation, and iron release is crucial for the viability of these bacterial organisms and depend strongly on ChdC [Sheldon 2015]. Therefore ChdC might be a promising therapeutic target in the future. However, this requires a detailed knowledge of structure–function relationships. Many recent publications have elucidated the physiological role of ChdC [Mayfield 2013, Hobbs 2016, Dailey 2017], but its structure–function relationship as well as the catalytic mechanism is still not completely understood.

The interaction of apo-ChdC with coproheme has been recently investigated by means of spectroscopic techniques for both *Listeria monocytogenes* (*Lm*) [Hofbauer 2015, Hofbauer 2016 FEBS, Hofbauer 2016 Biochemistry] and *Staphylococcus aureus* (*Sa*) [Celis 2015, Celis 2017, Streit 2017], both belonging at the Firmicutes phylum. Moreover, crystal structures of the ferric form of coproheme bound ChdCs have been published. The structure, obtained by our coworkers (Professor Obinger’s group, BOKU University, Vienna) is that of the ferric iron-coproheme-ChdC complex from *Lm* at 1.69 Å resolution, [pdb code 5LOQ, Hofbauer 2016 FEBS]. In this structure only two out of four propionate groups of coproheme showed clear electron densities, whereas the other two positions were unresolved and therefore supposed to be highly flexible. Then, a second structure was published by DuBois and coworkers, which corresponds to the manganese-coproheme-ChdC complex from *Geobacillus stearothermophilus* (*Gs*) at 1.8 Å resolution, [pdb code 5T2K, Celis 2017]. In this structure the orientation of the manganese-coproheme is unambiguously defined by very clear electron densities.

Interestingly, the coprohemes of the two structures (5LOQ and 5T2K) were present in different orientations within the active site: 90° twisted with respect to each other. In particular, in the 5T2K from *Gs* unreactive propionates p6 and p7 are solvent exposed, whereas in the 5LOQ from *Lm* reactive p2 and unreactive p7 are facing the solvent. This mismatch has been explained on the basis of recent activity studies (followed by mass spectrometry) on different ChdCs that showed that coproheme can be converted partially to the three-propionate mono-vinyl intermediate and heme *b*, without the addition of hydrogen peroxide, most probably through oxygen activation [Pfanzagl 2018]. Therefore, it is likely that in the 5LOQ structure the electron densities of the cofactor were not well resolved for all propionates because the mono-vinyl and double-vinyl reaction products were already formed in the crystal. Conversely, the 5T2K structure has the advantage that the manganese-coproheme is completely unreactive towards hydrogen peroxide [Pfanzagl 2018] and, therefore, is not converted into the reaction products.

Hence, Obinger and coworkers have obtained a new crystal structure of the iron-coproheme-ChdC complex from *Lm*, pdb code 6FXJ [unpublished data], inhibiting the potential enzymatic activity during the crystallization process by the addition of 5 mM cyanide to the crystallization drop. Cyanide was diluted out of the crystals prior to freezing with mother liquor not containing any cyanide. This structure has a significantly better resolution of the coproheme itself in chains A and D, clearly showing three propionates (p2, p4, and p6). The coproheme orientation is the same as observed in the manganese-coproheme-ChdC complex from *Gs*.

Therefore, the discussion of the data and the figures of the active site structure presented in this thesis refer to the still unpublished 6FXJ structure which appears to be the correct one.

Both the coproheme-ChdC from *Lm* (**Figure 4.2**) and *Gs* are homopentameric. Moreover, the structures show that the coproheme iron of ChdC is weakly bound by a proximal histidine (H174 in *Lm*). On the distal side, no water molecules are coordinated to the iron atom, suggesting the presence of a 5-coordinated iron. The distal Gln residue (Q185 in *Sa*), conserved in Firmicutes (the phylum of *Lm*, *Sa*, and *Gs*)

ChdC, has been shown to be particularly important in the stabilization of the distal side since it interacts with incoming exogenous ligands, such as CO [Celis 2017]. Furthermore this residue controls together with a second Arg side chain (R179 in *Lm*) the substrate access channel of the active site [Hofbauer 2016 FEBS].

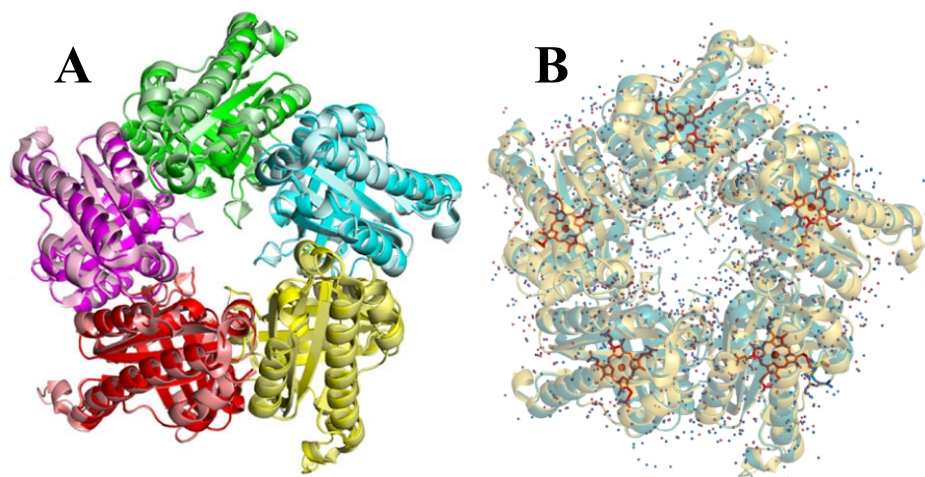


**Figure 4.2.** *LmChdC* homopentameric structure. A) The five subunits are differently colored. B) The five coproheme and the water molecule are shown. Adapted from Hofbauer 2016 FEBS.

Recently, hypothesis about the mechanism of the decarboxylation have been proposed. Time-resolved EPR spectroscopy revealed that the Tyr145 (*SaChdC* numbering; Tyr147 in *LmChdC* numbering) formed a radical species within 30 s of the reaction of the coproheme-*SaChdC* complex with  $H_2O_2$  [Streit 2018]. This radical disappears over the next 270 s, consistent with a catalytic intermediate. These results suggested the Tyr145 residue as the site of a catalytic radical involved in the decarboxylation. In particular, the authors proposed [Celis 2017, Streit 2018] that  $H_2O_2$  induces the formation of an oxo-ferryl porphyrin radical cation (known also as Compound I) which induces the formation of the Tyr145 radical. Then, the radical extracts a H radical atom from the  $\beta$ -carbon of the propionate in position 2, which is located at 2.5 Å from the Tyr145 radical oxygen. This is followed by migration of the

unpaired propionate electron to the coproheme iron to yield the ferric three-propionate intermediate and CO<sub>2</sub> (**Figure 4.3**). A further demonstration of the formation of the Tyr147 radical upon interaction of H<sub>2</sub>O<sub>2</sub> with the coproheme-*LmChdC* complex has been recently obtained through a spin trapping experiment [Obinger, unpublished]. Moreover formation of Compound I has also been demonstrated in the Y135A mutant of ChdC from *Corynebacterium diphtheriae*. This actinobacterial representative exhibits some differences in its reaction behavior from better studied Firmicutes ChdCs [Pfanzagl 2018] since the initial decarboxylation upon addition of hydrogen peroxide is significantly faster. Mutation of the catalytic tyrosine (Y135) yields completely inactive enzyme towards the decarboxylation reaction, but upon addition of hydrogen peroxide, Compound I formation is observed using UV-Vis spectroscopy.

While the proposed mechanism for the first decarboxylation of p2 is agreed upon, there are still open questions about the second decarboxylation step of p4 in which another hydrogen peroxide molecule turns the three-propionate mono-vinyl intermediate into heme *b*. It was proposed that a redox-active amino acid located near p4 (Tyr113, Trp157, or Trp198, *Sa* numbering) could act as Tyr145 towards p2 [Celis 2017], but recently it has been demonstrated that these residues are not involved. In fact, the coproheme complexes with W198F, W157F, or Y113S *SaChdC* mutants, always lead to the formation of the heme *b* final product instead of interrupting at the harderoheme intermediate step [Streit 2018]. Moreover, the reaction of the harderoheme-ChdC complex with H<sub>2</sub>O<sub>2</sub> leads to the formation of a radical species whose features are identical to those observed for the Tyr145 radical, thus suggesting that this aminoacid residue is also involved in the decarboxylation of p4. This suggests that after the decarboxylation of the p2, the three-propionate mono-vinyl intermediate must rotate of 90° in the protein cavity to allow the Tyr145 to decarboxylate p4 [Streit 2018].

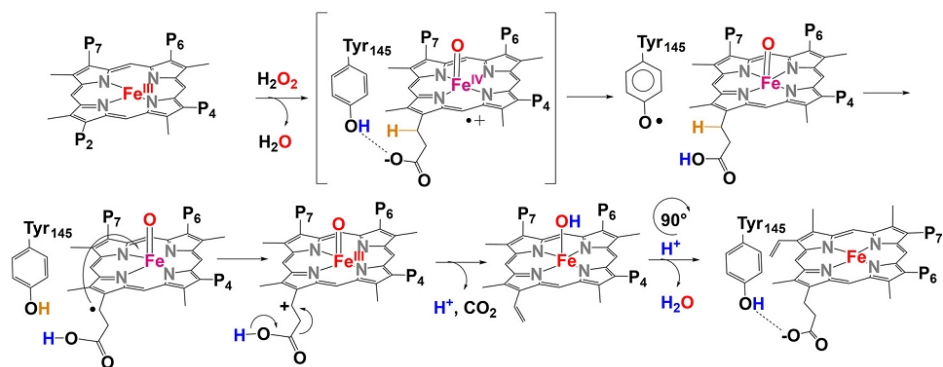


**Figure 4.3.** Proposed mechanism for coproheme decarboxylation. Coproheme Compound I is shown in brackets, the C $\beta$ -carbon from which a hydrogen atom is transferred is labelled in light brown, Fe(III) is reported in red and Fe(IV) in purple. After the decarboxylation of the p2, the three-propionate mono-vinyl intermediate rotates of 90° in the protein cavity and the Tyr145 decarboxylates the p4 too. Adapted from Streit 2018.

Based on all these published results, to obtain a better insight into the structure–function relationship, I started with the characterization of the coproheme-*LmChdC* WT complex. Then, I extended the study to coproheme-*LmChdC* complexes where residues considered to play an important role in maintaining the active site structure or in the catalytic mechanism were mutated. Finally, I studied the heme *b*-*LmChdC* WT and mutants complexes and I followed with UV-Vis and RR spectroscopy at 80 K the decarboxylation reaction which turns coproheme into heme *b*.

## 4.2 Materials

Ferric coproheme was purchased from Frontier Scientific, Inc. (Logan, Utah, USA) as lyophilized powder. A coproheme solution at pH 7.0 in 50 mM Hepes buffer was prepared by dissolving the coproheme powder in a 0.5 M NaOH solution and then diluting a small aliquot of this concentrated alkaline solution with an appropriate volume of 50 mM Hepes buffer, pH 7.0, ca. 400  $\mu$ M.

Apo-Mb (horse heart, HH, Sigma) was prepared using a modified extraction method by Teale, as described previously [Teale 1959, Le 2014, Hofbauer 2015].

All the protein-coproheme complexes were prepared by adding the coproheme solution at pH 7.0 to the apo-proteins dissolved in 50 mM Hepes buffer, pH 7.0. The imidazole complexes of coproheme- WT and coproheme-Mb were prepared by adding small aliquots of a 0.1 M imidazole solution in 50 mM Hepes buffer at pH 7.0 to coproheme-WT and coproheme-Mb solutions until no further UV-vis spectral changes were observed.

The ferric heme *b* complexes were prepared by adding small aliquots (3-10  $\mu$ L) of a concentrated solution of H<sub>2</sub>O<sub>2</sub> in 50 mM Hepes buffer, pH 7.0 to the corresponding coproheme-LmChdC complex.

Ferrous samples were prepared by addition of 2–3  $\mu$ L of a freshly prepared sodium dithionite solution (20 mg/mL) to the ferric forms (40 $\mu$ L) previously degassed with nitrogen.

The ferrous-CO adducts at pH 7.0 were prepared by flushing the ferric (40 $\mu$ L) coproheme/heme *b* complexes with <sup>12</sup>CO or <sup>13</sup>CO (Rivoira, Milan, Italy), and then reducing the coproheme/heme *b* by addition of 2–3  $\mu$ L of a freshly prepared sodium dithionite solution (20 mg mL).

Sample concentrations, in the range of 15-100  $\mu$ M for UV-vis and RR measurements, were determined using an extinction coefficient ( $\epsilon$ ) of 128800 M<sup>-1</sup> cm<sup>-1</sup> at 390 nm (coproheme) [Hofbauer 2016 FEBS]; 68000 M<sup>-1</sup> cm<sup>-1</sup> at 395 nm (coproheme-WT and mutants) [Hofbauer 2016 Biochemistry] 85800 M<sup>-1</sup> cm<sup>-1</sup> at 391 nm (coproheme-Mb); and 76600 M<sup>-1</sup> cm<sup>-1</sup> at 410 nm (heme *b*-LmChdC WT and mutants) [Hofbauer 2016 Biochemistry].

Titration of the coproheme-M149A complex with H<sub>2</sub>O<sub>2</sub>: the UV-Vis experiment was performed in a 1 mm cuvette. Small aliquots (1-10  $\mu$ L) of a diluted solution of H<sub>2</sub>O<sub>2</sub> in 50 mM Hepes buffer, pH 7.0 were added to 50  $\mu$ L of a 100  $\mu$ M coproheme-M149A complex buffered solution. When variations in the UV-Vis spectrum were observed, the sample was transferred in the THMS600 cryostat (see chapter 1.3), frozen at 80 K and RR spectra taken. After the RR spectra, the sample

was thawed, and the UV-Vis spectrum taken to be compared with the previous before freezing to ensure that no degradation occurred. Then titration with H<sub>2</sub>O<sub>2</sub> was carried on, until new variations in the UV-Vis spectrum appeared and the sample was frozen again. This experiment was repeated several times to ensure reproducibility.

The site direct mutagenesis, expression and purification of the LmChdC WT and variants Y147A/R220A/S225A, Y113A/K151A, M149A/Q187A, K151A, M149A, Y113A, R133A, R179A, and Q187A (Tyr147Ala/Arg220Ala/Ser225Ala triple mutant, Tyr113Ala/Lys151A and Met149Ala/Gln187Ala double mutants, Lys151Ala, Met149Ala, Tyr113Ala, Arg133Ala, Arg179Ala, and Gln187Ala single mutants) were performed by Professor Christian Obinger's group (BOKU University, Vienna).

They also:

- Measured the kinetics of coproheme binding to the apo-LmChdC proteins with a stopped-flow apparatus.
- Obtained the electronic circular dichroism (ECD) spectra in the far UV-region (190 - 260 nm) of the coproheme-WT and variants complexes for determination of the secondary structure.
- Determined the enzymatic activity of LmChdC WT and variants following spectroscopically and via mass spectrometry, the conversion of the coproheme complexes to the respective heme *b*.
- Crystallised the coproheme-ChdC WT complex in the ferric form and obtained the X-ray crystal structures (5LOQ and 6FXJ).

### 4.3 The coproheme-WT and -M149A complexes

I studied the coproheme-WT and -M149A complexes, being the M149 residue (**Figure 4.10**) thought to be important for its cross-linking capability towards the final product of the reaction, heme *b*. In fact, upon addition of excess hydrogen peroxide, the heme *b* prosthetic group is modified and becomes covalently bound to the protein as demonstrated by mass spectrometric analysis (**Figure 4.4**): for the ChdC-WT at excess of H<sub>2</sub>O<sub>2</sub> a total mass of 32950.5 Da was detected, which corresponds to the mass of the WT protein plus heme *b*

[Hofbauer 2016 FEBS]. By contrast, for ChdC-M149A the mass was 31917.0 Da even after incubation with excess of hydrogen peroxide. This clearly identifies Met149 as the site of covalent cross-linking. It is reasonable to assume that in the WT protein, excess H<sub>2</sub>O<sub>2</sub> mediates the linkage between the vinyl substituent at position 2 of heme *b* (which is close to the Met149 residue) and Met149 via a sulfonium ion bond, as demonstrated for human myeloperoxidase [Fiedler 2000, Zederbauer 2007, Brogioni 2008, Battistuzzi 2011].

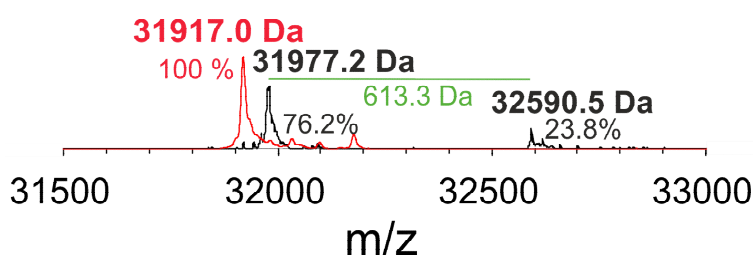


**Figure 4.4.** Crosslinking of heme *b* to LmChdC mediated by excess hydrogen peroxide. Mass spectrometric analysis of the entire protein of LmChdC WT (apo-form 31977.2 Da; crosslinked 32590.5 Da, black) and LmChdC M149A (31917.0 Da, red). The green line with its label shows the mass difference between apo-LmChd WT and holo-LmChdC WT. The Coproheme-LmChdC complexes were titrated with H<sub>2</sub>O<sub>2</sub> up to a two-fold excess, subsequently the mass spectroscopic measurements were performed on heme *b*- LmChdC WT and heme *b*- LmChdC M149A.

I compared the spectra of the coproheme-WT and -M149A complexes with those of i) coproheme to be sure that in the reconstituted complexes there is no trace of excess of unbounded coproheme; ii) coproheme-Mb used as reference compound, being both the UV-Vis and RR spectra of coproheme-proteins quite different from those of the heme *b*-proteins. In fact, unlike heme *b*, that has two propionates and two vinyl groups, coproheme has four propionates and no vinyl groups. Consequently, due to the lack of vinyl conjugation, an overall blue-shift of the UV-vis spectrum with respect to heme *b* proteins is predicted

[Marzocchi 2003] and the  $\nu_2$  core-size marker band in the RR spectrum is expected to be up-shifted by up to  $12\text{ cm}^{-1}$  [Choi 1982].

#### 4.3.1 Ferric form: UV-Vis and RR spectra at room temperature

Coproheme alone gives rise to a UV-Vis spectrum (**Figure 4.5**) that, considering the overall blue-shift due to the lack of the vinyl groups, is typical of a 5cHS species (Soret band at 390 nm, visible bands at 492 and 530 nm and a CT1 band at 614 nm).

The coproheme-Mb complex, conversely to Mb which is a pure 6cHS species, shows two Soret bands particularly evident in the second derivative spectrum: at 392 nm which similarly to the coproheme alone is likely due to a HS species, and another at 406 nm.

A species characterized by a Soret band at 406 nm and Q bands at 518 and 555 nm is present also in the UV-Vis spectrum of the coproheme-M149A complex, together with another species with Soret band at 393 nm, Q bands at 494 and 538 nm and a CT1 band at 630 nm which is the only species observed in the coproheme-WT complex. The wavelengths of this species resemble very closely those observed in the coproheme spectrum and therefore seem to be due to a 5cHS species.

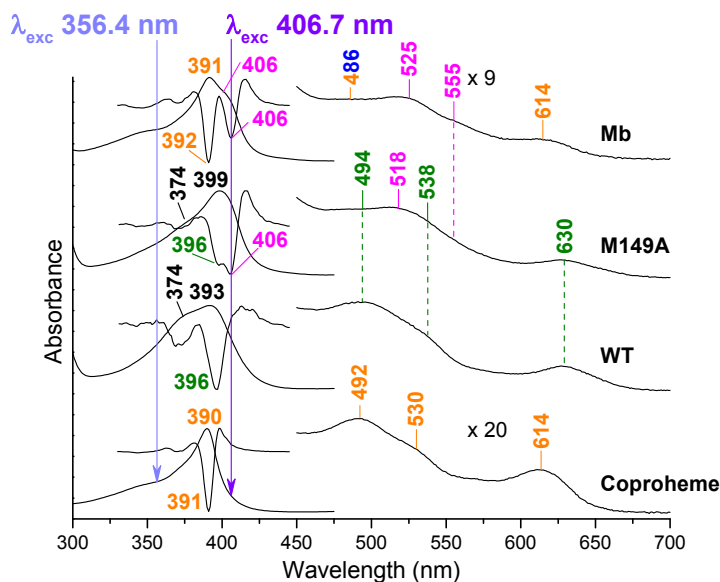


**Figure 4.5.** UV-vis absorption and second derivative ( $D^2$ ) spectra of coproheme and the coproheme complexes with LmChdC WT, its M149A mutant, and Mb. The band wavelengths assigned to 5cHS,

5cQS, 6cHS and 6cLS species are indicated in orange, olive green, blue, and magenta, respectively, (see text). The spectra have been shifted along the ordinate axis to allow better visualization. The 450–700 nm region of coproheme and the coproheme complexes spectra is expanded 20- and 9-fold, respectively. The excitation wavelengths used for the RR experiments are also shown in light violet (the 356.4 nm line) and in violet (the 406.7 nm line).

Since in the coproheme-M149A and -Mb complexes are present two species one with a maximum of absorption around 390 nm and the other around 406 nm, I performed the RR analysis using two excitation wavelengths at 356.4 nm (i.e. in resonance with the Soret at 390 nm) and 406.7 nm (i.e. in resonance with the Soret at 406 nm) to selectively intensified each species (**Figure 4.6**).

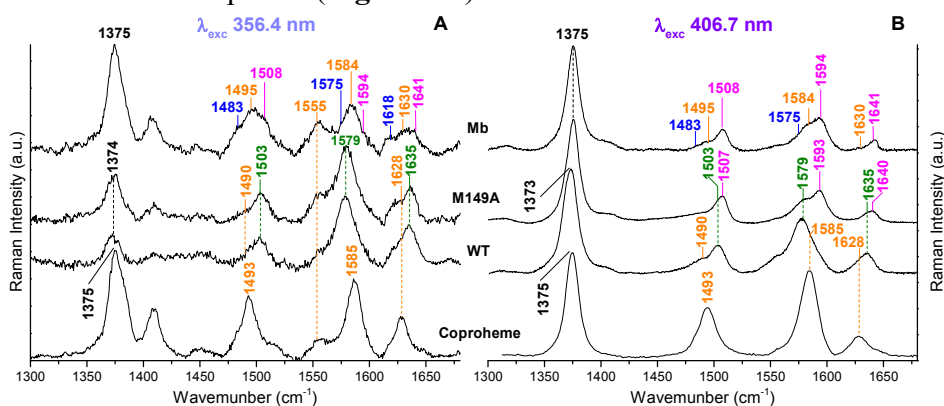


**Figure 4.6.** High frequency region RR spectra obtained at room temperature, with the 356.4 (Panel A) and 406.7 nm (Panel B) excitation wavelengths, of coproheme, and the coproheme complexes of LmChdC WT, its M149A mutant, and Mb. The band wavenumbers assigned to 5cHS, 5cQS, 6cHS and 6cLS species are indicated in orange, olive green, blue, and magenta, respectively, (see text). The spectra have been shifted along the ordinate axis to allow better visualization. Experimental conditions: (A) laser power at the sample 5 mW, average of 10 spectra with 120 min integration time (Coproheme); laser power at the sample 2 mW; average of 7 spectra with 70 min integration time (WT), 8 spectra with 80 min integration time (M149A), and 24 spectra with 240 min integration time (Mb). (B): laser power at the sample 5 mW; average of 2 spectra with 10 min integration time with 1800 grating (Coproheme), 9 spectra with 90 min integration time (WT), 4

spectra with 40 min integration time (M149A), and 6 spectra with 60 min integration time (Mb).

The RR spectra of the coproheme confirm that it is characterized by a pure 5cHS state (where the fifth ligand is a water molecule) with core-size RR bands, observed for both excitation wavelengths, at 1375 ( $\nu_4$ ), 1493 ( $\nu_3$ ), 1585 ( $\nu_2$ ) and 1628 ( $\nu_{10}$ )  $\text{cm}^{-1}$ . No bands of free coproheme are observed in the UV-Vis and the RR spectra of the coproheme-complexes. In coproheme-Mb the Soret band at 406 nm together with the Q bands at 525 and 555 nm, and the RR bands at 1508 ( $\nu_3$ ), 1594 ( $\nu_2$ ) and 1641 ( $\nu_{10}$ )  $\text{cm}^{-1}$ , selectively intensified in the spectrum obtained with the violet laser line at 406.7 nm, are assigned to a 6cLS species, being the RR frequencies typical of such species. The Q band maxima at 525 and 555 nm suggest that the sixth ligand is a nitrogen atom that, on the basis of the crystal structure of ferric HHMb (1YMB [Evans 1990]) very likely belongs to the distal His64 residue, located at 4.4 Å from the heme iron atom. In the RR spectrum obtained with the UV laser line at 356.4 nm, are selectively intensified the vibrational mode of the species with the Soret band at 392 nm that, together with the Q bands at 486 and 614 nm, are assigned to the overlapping contribution of a 5cHS and a 6cHS species: 5cHS: 1495 ( $\nu_3$ ), 1584 ( $\nu_2$ ) and 1630 ( $\nu_{10}$ )  $\text{cm}^{-1}$ ; 6cHS: 1483 ( $\nu_3$ ), 1575 ( $\nu_2$ ) and 1618 ( $\nu_{10}$ )  $\text{cm}^{-1}$ . To be noticed that with the 356.4 nm excitation, not only the 6cLS spectrum markedly decreases in intensity but, interestingly, the  $\nu_2$  band almost disappears. The loss of the  $\nu_2$  band with this excitation is taken as a useful marker for the assignment of a 6cLS species.

Similarly to the coproheme-Mb, in the spectrum of the coproheme-M149A complex obtained with the 406.7 nm laser line, in resonance with the Soret band at 406 nm, the most intense bands are at 1507 ( $\nu_3$ ), 1593 ( $\nu_2$ ) and 1640 ( $\nu_{10}$ )  $\text{cm}^{-1}$ ; and also in this case the  $\nu_2$  band almost disappears with the UV excitation, indicating the presence of a 6cLS species. The nature of the sixth ligand is intriguing since similar to the case of the coproheme-Mb complex, the Q band maxima at 518 and 555 nm suggest that the sixth ligand is a nitrogen atom, however, unlike Mb, in the distal cavity of ChdC no His residues are present [Hofbauer 2016

FEBS, Celis 2017]. In order to identify the endogenous ligand, i) the coproheme-M149A complex was studied with EPR and ii) the UV-Vis and RR study was extended to other coproheme-ChdC mutant complexes (see below, paragraphs 4.3.2 and 4.3.3, respectively). Interestingly, the RR spectra of the coproheme-M149A complex taken with the 356.4 nm laser line, in resonance with the Soret band at 396 nm, are almost identical to that observed for the WT, both in terms of the band frequencies and intensities.

The RR spectra of the coproheme-WT complex, taken with excitation wavelengths at 356.4 and 406.7 nm, i.e. on the blue and red sides of the Soret maximum (393 nm), respectively, are very similar and clearly indicate the presence of two species. A minor species with core size marker bands at 1490 ( $\nu_3$ ), 1585 ( $\nu_2$ ) and 1628 ( $\nu_{10}$ )  $\text{cm}^{-1}$ , frequencies typical of a 5cHS form, and a main species with core size marker bands at 1503 ( $\nu_3$ ), 1579 ( $\nu_2$ ) and 1635 ( $\nu_{10}$ )  $\text{cm}^{-1}$ . These frequencies might suggest the presence of a 6cLS species (being in fact similar to those observed in coproheme-Mb), but i) there is no evidence of a 6cLS heme in the UV-Vis spectrum, being the Soret band at 393 nm and the CT band at 630 nm consistent with a 5cHS species ii) in the RR spectrum taken with the 356.4 nm excitation the  $\nu_2$  band is the very intense. Therefore, the assignment of this species is not straightforward.

In order to rule out the presence of a 6cLS species in the coproheme-WT complex, I obtained 6cLS model compounds adding imidazole to both the coproheme-WT and -Mb complexes (**Figure 4.7**)

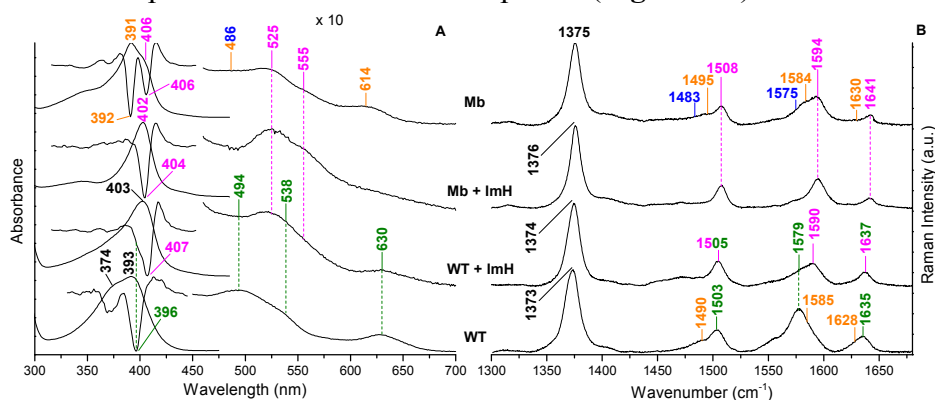


**Figure 4.7.** UV-vis absorption and second derivative spectra ( $D^2$ ) (Panel A) and RR spectra in the high frequency region (Panel B) of the

coproheme complexes of WT and Mb with and without the addition of imidazole (ImH). The band wavelengths and wavenumbers assigned to 5cHS, 5cQS, 6cHS and 6cLS species are indicated in orange, olive green, blue and magenta, respectively, (see text). The spectra have been shifted along the ordinate axis to allow better visualization. The 450–700 nm region of the spectra in Panel A is expanded 10-fold. Experimental conditions of the RR spectra: 406.7 nm excitation wavelength, laser power at the sample 5 mW; average of 9 spectra with 90 min integration time (WT), 10 spectra with 100 min integration time (WT + ImH), 5 spectra with 50 min integration time (Mb + ImH), and 6 spectra with 60 min integration time (Mb).

The exogenous imidazole binds completely the iron of the coproheme-Mb complex, giving rise to a pure 6cLS bis-His species (Soret band at 407 nm), with RR bands identical to those of the coproheme-Mb complex confirming that the His64 is its distal ligand.

On the contrary, the coproheme-WT complex does not fully bind the exogenous imidazole. However, the 6cLS heme obtained upon addition of imidazole shows a Soret maximum at 407 nm, and upshifted core size marker bands, compare to the coproheme-WT complex without imidazole, clearly demonstrating that the species present in the coproheme-WT spectrum is not a 6cLS species.

#### **4.3.2 Coproheme-WT complex: 5cQS species**

The fact that the UV-Vis spectrum is similar to that of a 5cHS species with a CT band at 630 nm, but the RR frequencies of the core size bands are typical of a 6cLS species, strongly suggests that the heme state of coproheme-WT, in analogy with the heme containing peroxidases belonging to Family 3 of the peroxidase-catalase superfamily, is a quantum mechanically mixed-spin (QS) state [Smulevich 2005, Zámocký 2015, Smulevich 2016]. In fact, as previously reported [Indiani 2000, Smulevich 2005], the 5cQS species gives rise to: (i) an electronic absorption spectrum similar to that of a 5cHS heme but with a shorter wavelength transitions; (ii) a CT band at 630-635 nm; (iii) RR

core size marker bands frequencies similar to that of a 6cLS species; (iv) EPR spectra with  $g_{12}$  values in the range  $4 < g_{12} < 6$ .

Therefore, to confirm this assignment, the X-band EPR spectrum (10 K) (**Figure 4.8**) together with the RR spectra at low temperature (80K,  $\lambda_{exc}$  at 356.4 and 406.7 nm) (**Figure 4.9**) of the coproheme-WT, -M149A and -Mb complexes were recorded.

In the EPR spectrum of the coproheme-WT complex three different species are present. The most abundant is characterized by  $g$  values at 5.90, 5.10, 2.00 ( $g_{12} = 5.50$ ), which confirms the presence of a 5cQS species. A 5cHS (6.30, 5.45, 2.00;  $g_{12} = 5.88$ ), and a small amount of a 6cLS species (2.90, 2.27, 1.60), are also observed.

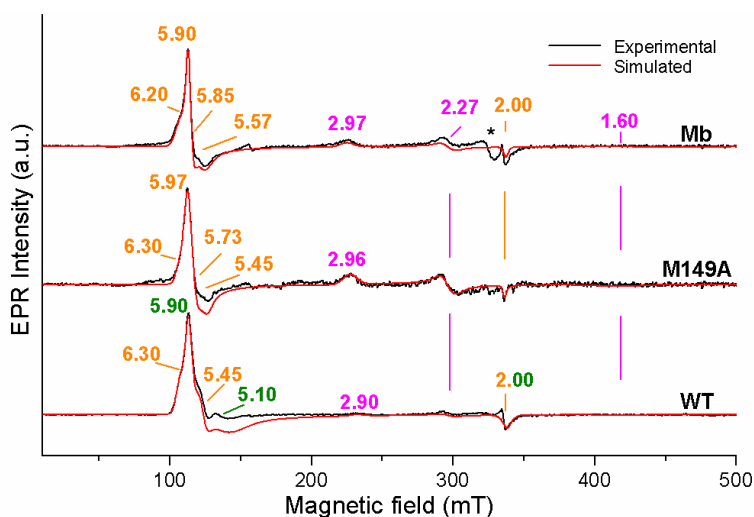


**Figure 4.8.** EPR spectra (experimental in black and simulated in red) of the coproheme-LmChdC WT (300  $\mu$ M, bottom), coproheme-LmChdC M149A (75  $\mu$ M, middle), and coproheme-Mb (200  $\mu$ M, top) complexes at pH 7.0 in 50 mM Hepes buffer. The  $g$  values of the bands due to the 5cHS, 5cQS, and 6cLS species are coloured in orange, olive green, and magenta, respectively. The spectra have been shifted along the ordinate axis to allow better visualization. Experimental conditions: temperature 10 K, microwave power 2.1 mW, modulation amplitude 10 G. The asterisk at ca. 330 mT indicates an artifact due to a cavity signal.

The comparison between the 80 K RR spectra obtained for excitation at 356.4 and 406.7 nm (**Figure 4.9**) confirms the presence of a 5cQS species ( $\nu_3$  1507,  $\nu_2$  1584 and  $\nu_{10}$  1637  $\text{cm}^{-1}$ ), a 5cHS species ( $\nu_3$  1490,

$\nu_2$  1570 and  $\nu_{10}$  1627  $\text{cm}^{-1}$ ), and a 6cLS form ( $\nu_3$  1507,  $\nu_2$  1594 and  $\nu_{10}$  1640  $\text{cm}^{-1}$ ). The 6cLS species is absent at room temperature, but this is not surprisingly since as previously found, lowering the temperature, heme proteins undergo to a temperature induced transition from high to low spin [Smulevich 1989, Smulevich 1990, Howes 2000, Nielsen 2001].

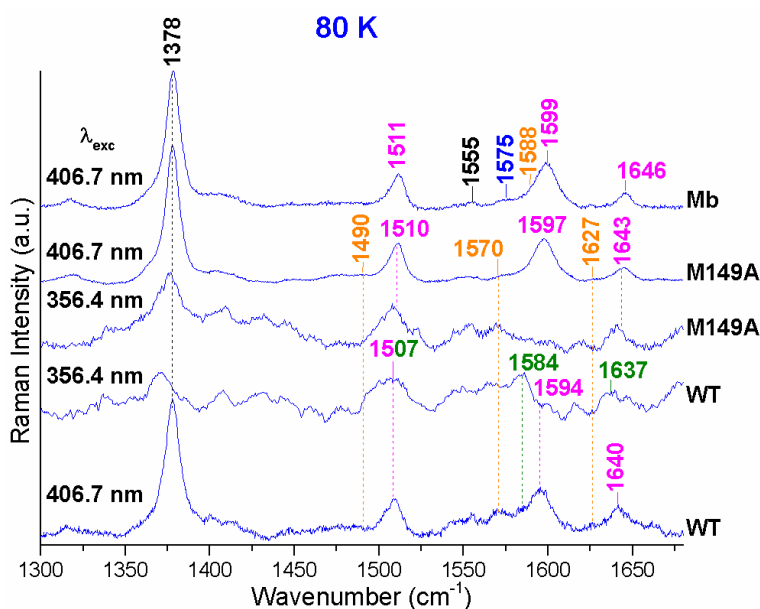


**Figure 4.9.** RR spectra in the high frequency region at 80 K of the coproheme complexes with WT, M149A, and Mb obtained with  $\lambda_{\text{exc}}$  at 356.4 and 406.7 nm. The frequencies of the bands due to the 5cHS, 5cQS, 6cHS and 6cLS species are coloured in orange, olive green, blue, and magenta, respectively. Experimental conditions: (356.4 nm), laser power at the sample 5 mW and average of 7 spectra with 140 min integration time (WT); laser power at the sample 10 mW, average of 12 spectra with 120 min integration time (M149A); (406.7 nm): laser power at the sample 6 mW (WT and M149A), average of 14 spectra with 280 min integration time (WT), 9 spectra with a 135 min integration time (M149A); laser power at the sample 7 mW, average of 7 spectra with 140 min integration time (Mb). The spectra have been shifted along the ordinate axis to allow better visualization.

In the EPR spectrum of the coproheme-M149A complex, in agreement with the RR spectra at room temperature, the most abundant species is a

6cLS form (2.96, 2.27, 1.60). Moreover, two different 5cHS species are present, one of which (6.30, 5.45, 2.00;  $g_{12}= 5.88$ ) is identical to that observed in the WT sample. Accordingly, the RR spectra at 80 K confirm the presence of a mainly a 6cLS ( $\nu_3$  1510,  $\nu_2$  1597 and  $\nu_{10}$  1643  $\text{cm}^{-1}$ ) with a small amount of 5cHS ( $\nu_3$  1490,  $\nu_2$  1570 and  $\nu_{10}$  1627  $\text{cm}^{-1}$ ). The absence of any 5cQS species in the EPR and 80 K RR spectra in the mutant, suggests that a structural rearrangement may occur following mutation at low temperature.

The EPR spectrum of the coproheme-Mb complex, in agreement with the RR spectra at room temperature, is characterized by a dominant 6cLS form (2.97, 2.27, 1.60), and two 5cHS species. One of the latter, the least abundant species, displays a very small rhombicity (5.90, 5.85, 1.99;  $g_{\perp}= 5.88$ ); hence, it can effectively be considered to be very close to a 6cHS form. Nevertheless, an alternative simulation using a pure 6cHS state produced a slightly poorer correspondence between experimental and simulated spectra. Accordingly, the 80 K RR spectrum is also characterized mainly by a 6cLS species ( $\nu_3$  1511,  $\nu_2$  1599 and  $\nu_{10}$  1646  $\text{cm}^{-1}$ ) and a small amount of 5cHS ( $\nu_2$  1588  $\text{cm}^{-1}$ ) and 6cHS ( $\nu_2$  1575  $\text{cm}^{-1}$ ) states.

The  $g$  values of the 6cLS species for all three coproheme complexes are similar to those of a bis-His heme coordination where the two imidazole planes are approximately parallel [Brautigan 1977, Walker 1999].

This i) definitely confirms the involvement of His64 as distal ligand in the coproheme-Mb complex; ii) is indicative of nitrogen distal ligation in the coproheme-M149A complex as suggested by the Q band maxima at 518 and 555 nm. Since no His residues are present in the distal cavity of ChdC [Hofbauer 2016 FEBS, Celis 2017], we have considered which other key residues in the distal cavity might be able to bind the Fe atom via a N atom. Since the distal Gln residue (Q187 in *Lm*), conserved in Firmicutes ChdC, has been shown to be particularly important in the stabilization of the distal side due to its interaction with incoming exogenous ligands, such as CO [Celis 2017], we focused on this residue by studying the single Q187A and double Q187/M149A variants (**Figure 4.10**).

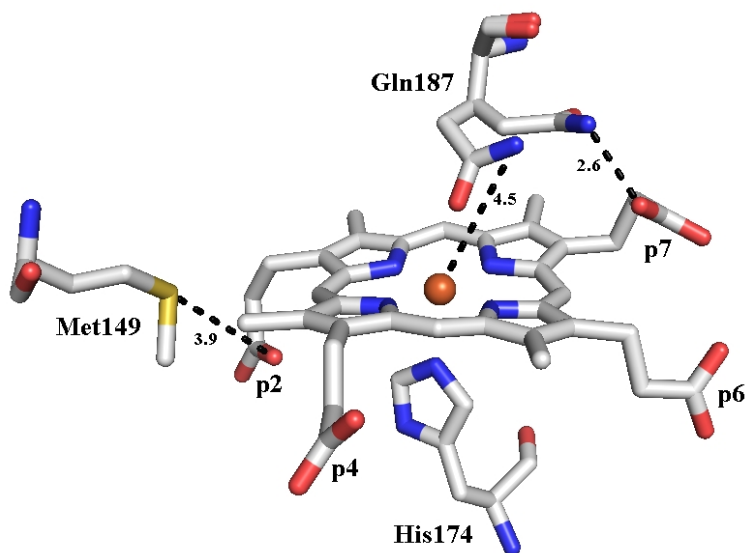


**Figure 4.10.** Coproheme active site in chain D (6FXJ). The proximal His174 together with the Met149 and Gln187 residues are represented as sticks. Moreover interatomic distances are reported. In the A and D subunits which are those with the best electron densities and are therefore the most reliable ones, the Gln187 residue, according to the electron densities, has been refined in a split conformation 50% in position 1 (Q187/1) and 50% in position 2 (Q187/2). Position 1 points away from the heme iron, towards the p7 with which is H-bonded; position 2 points towards the heme iron but is not H-bonded with the p7. See also Table 4.5. This indicates a certain flexibility of Gln187.

### 4.3.3 Coproheme-M149A: 6cLS His-Fe-Gln species

**Figure 4.11** compares the UV-Vis with their second derivative ( $D^2$ ) (A), and the RR spectra in the high frequency region (B) of the coproheme complexes of WT, the Q187A, M149A/Q187A and M149A mutants. In the absence of the Gln187 residue the spectra resemble very closely that of the coproheme-WT complex, completely disappearing the 6cLS species observed in the coproheme-M149A complex. This clearly demonstrates that the distal ligand of the 6cLS species of the coproheme-M149A complex is the Gln187 residue that binds the coproheme iron through its nitrogen atom. This result is quite peculiar since an axial Gln residue was never observed before in heme proteins.

Moreover, mutation of the Gln187 residue also gives rise to a small amount of a 6cHS species (blue bands,  $\nu_3$  and  $\nu_{10}$  at 1482 and 1614  $\text{cm}^{-1}$ , respectively) at the expense of the 5cQS form.

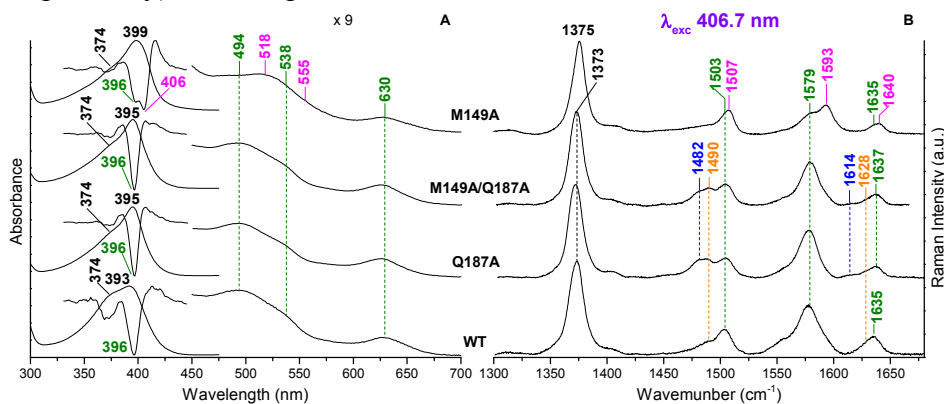


**Figure 4.11.** UV-vis absorption and second derivative ( $D^2$ ) spectra (A) and RR spectra in the high frequency region (B) of the coproheme complexes with WT and the Q187A, M149A/Q187A and M149A mutants. The band wavelengths and wavenumbers assigned to 5cHS, 5cQS, 6cHS and 6cLS species are indicated in orange, olive green, blue, and magenta, respectively. The spectra have been shifted along the ordinate axis to allow better visualization. The 450–700 nm region of the spectra in Panel A is expanded 9-fold. Experimental conditions of the RR spectra: 406.7 nm excitation wavelength, laser power at the sample of 5 mW, average of 9 spectra with a 90 min integration time (WT), 14 spectra with a 140 min integration time (Q187A), 10 spectra with a 100 min integration time (M149A/Q187A), and 4 spectra with a 40 min integration time (M149A).

**Figure 4.12** shows a scheme of the coproheme coordination of the coproheme-WT, -M149A and -Mb complexes determined by RR and EPR spectroscopy at room and low temperature.

**Tables 4.1, 4.2, and 4.3** report the assignment of the UV-Vis maxima, the main RR core-size marker bands, and the EPR parameters of the various species present in the coproheme complexes spectra.

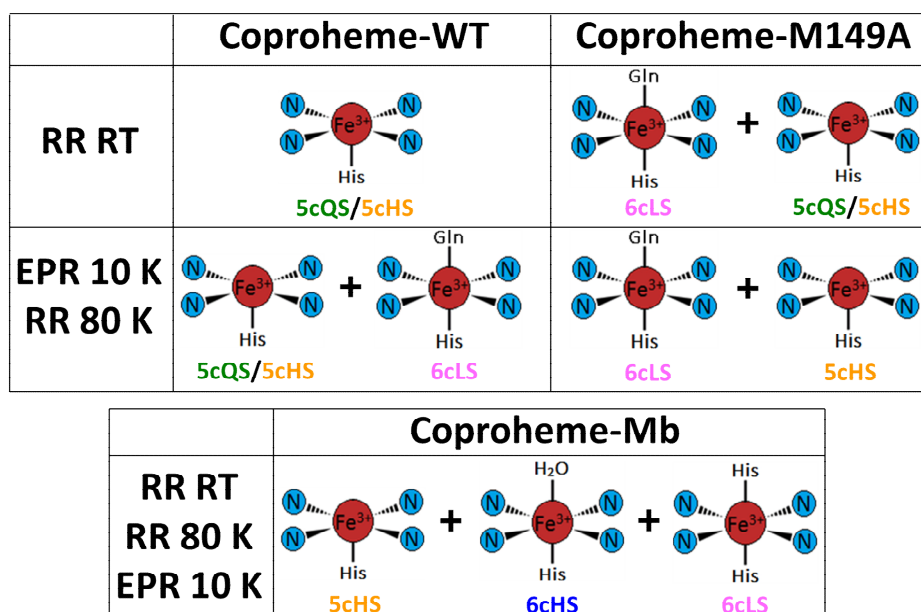


**Figure 4.12.** Scheme of the coproheme coordination for the coproheme-WT, -M149A and -Mb complexes determined by RR and EPR spectroscopy at room and low temperature.

**Table 4.1.** UV-Vis band assignments of coproheme and the coproheme-WT, -M149A, and -Mb complexes. The  $D^2$  values are reported in brackets.

	5cQS	5cHS	6cLS
Mb		391 (392), 486 <sup>a</sup> , 614	406 (406), 525, 555
M149A	399 (396), 494, 538, 630		406 (406), 518, 555
WT	393 (396), 494, 538, 630		
Coproheme		390 (391), 492, 530, 614	

<sup>a</sup>This band is due to the overlapping contributions of the  $\beta$  bands of 5c and 6c HS.

**Table 4.2.** RR core size band assignments of coproheme and the coproheme-WT, -M149A, and -Mb.

	v <sub>3</sub>				v <sub>2</sub>				v <sub>10</sub>			
	5cQS	5cHS	6cHS	6cLS	5cQS	5cHS	6cHS	6cLS	5cQS	5cHS	6cHS	6cLS
<b>Mb</b>		1495	1483	1508		1584	1575	1594		1630	1618	1641
<b>M.</b>	1503	1490		1507	1579	-		1593	1635	1628		1640
<b>WT</b>	1503	1490			1579	1585			1635	1628		
<b>C.</b>		1493				1585	-			1628		

M. = M149A; C. = Coproheme.

**Table 4.3.** EPR parameters of the coproheme-WT, -M149A, and -Mb complexes, compared to those of soybean peroxidase (SBP).

Protein	g <sub>1</sub>	g <sub>2</sub>	g <sub>3</sub>	g <sub>12</sub>	Species	R <sup>a</sup>	I <sup>b</sup>	g strain		
						%	%	g <sub>1</sub>	g <sub>2</sub>	g <sub>3</sub>
<b>WT</b>	6.30	5.45	2.00	5.88	5cHS	5.3	19	0.35	0.20	0.025
	5.90	5.10	2.00	5.50	5cQS	5.0	70	0.25	1.00	0.05
	2.90	2.27	1.60		6cLS		11	0.15	0.08	0.15
<b>M149A</b>	6.30	5.45	2.00	5.88	5cHS	5.3	12	0.35	0.20	0.025
	5.97	5.73	2.00	5.85	5cHS	1.5	23	0.30	0.40	0.015
	2.96	2.27	1.60		6cLS		65	0.15	0.08	0.15
<b>Mb</b>	6.20	5.57	2.00	5.89	5cHS	4.0	36	0.52	0.47	0.025
	5.90	5.85	2.00	5.88	5cHS	0.3	15	0.18	0.30	0.015
	2.97	2.27	1.60		6cLS		49	0.15	0.08	0.15
<b>SBP<sup>c</sup></b>	5.89	4.85	2.00	5.37	5cQS					
	3.25	2.07			6cLS					

<sup>a</sup>R, rhombicity of HS signals were calculated according to Peisach et al., 1971 ( $\Delta g/16$ ). <sup>b</sup>Approximate values. <sup>c</sup>Ref. Aasa 1975. The g<sub>3</sub> band of the 6cLS species is very broad/weak, hence, its value is approximate.

#### 4.3.4 Structural information and ferrous form

The experiments demonstrated that the main species present in the coproheme-WT from *Lm* is a 5cQS form. The electronic absorption spectrum is very similar to that obtained for the coproheme-WT from *Sa*, being characterized by Soret, visible  $\alpha/\beta$  and CT1 bands at 393, 494/538 and 630 nm, respectively the *Lm* and at 394, 497/533 and 630 nm, respectively the *Sa* [Celis 2015]. However, the RR spectra of the two proteins show differences, being the core size marker bands  $\nu_4$ ,  $\nu_3$ ,  $\nu_2$ ,  $\nu_{10}$ , at 1373, 1503, 1579 and 1635  $\text{cm}^{-1}$ , respectively for the *Lm* and at 1370, 1494 1575 and 1630  $\text{cm}^{-1}$ , respectively for the *Sa* [Celis 2015]. The authors commented that the Soret and visible bands of the coproheme-WT from *Sa* are typical of 5cHS Fe-porphyrins [Streit 2017] and that the EPR spectrum is largely high-spin ( $S = 5/2$ ) [Streit 2018]. Instead they did not comment further the RR spectrum.

The QS spin state reflects a quantum mechanical admixture of an intermediate ( $S = 3/2$ ) and high spin ( $S = 5/2$ ) states. It is very rare in heme proteins, being mainly found in the heme peroxidases belonging to Family 3 of the peroxidase-catalase superfamily [Smulevich 2005]. Moreover, not only its possible involvement in protein function is unclear, but the structural determinants of the 5cQS vs. the 5cHS spin states have also been a matter of extensive debate and remain elusive [Smulevich 2005, Hough 2015]. The formation of a 5cQS heme has been mainly associated with a weak axial ligand. However, this feature does not appear to be sufficient to cause a QS state. In fact, while the lack of a H-bonding partner for the proximal imidazole ligand may account for the presence of a 5cQS state in Cytochromes *c'* [Hough 2015], heme containing peroxidases are characterized by a conserved strong H-bond between the  $N_\delta$  hydrogen atom of the imidazole ligand and the carboxylate of an aspartic side chain, which acts as H-bond acceptor, imparting an imidazolate character to the histidine ligand [Smulevich 2005, Smulevich 2016]. Interestingly, in all the 5cHS ferrous coproheme-WT and -Met149 complexes from *Lm* (**Figure 4.13**) and coproheme-WT from *Sa* [Streit 2017], the  $\nu(\text{Fe-Im})$  stretching mode is observed at 214  $\text{cm}^{-1}$  (**Figure 4.14** for *Lm*) and [Celis 2015 for *Sa*], confirming that the  $N_\epsilon$  of the imidazole of the proximal His (H174)

is weakly bonded to the coproheme iron in agreement with the crystal structures.

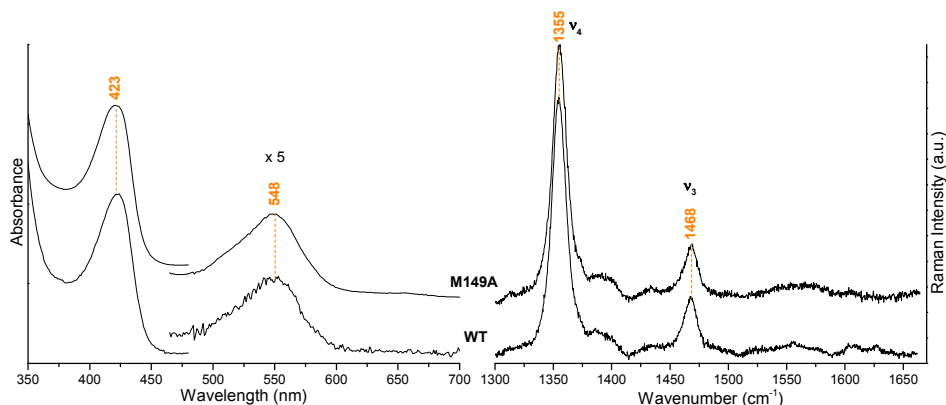


**Figure 4.13.** UV-vis absorption spectra (A) and RR spectra in the high frequency region (B) of the ferrous form of the coproheme-WT and -M149A complexes. The spectra have been shifted along the ordinate axis to allow better visualization. The 480–700 nm region of the UV-Vis spectrum is expanded 5-fold. RR experimental conditions: excitation wavelength 413.1 nm, laser power at the sample 5 mW; average of 6 spectra with 60 min integration time (WT), average of 4 spectra with 40 min integration time (M149A).

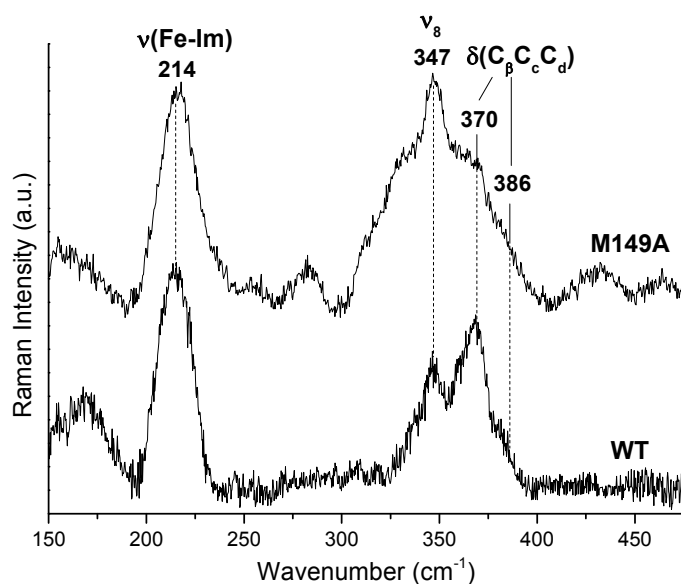


**Figure 4.14.** RR spectra in the low frequency region of the ferrous form of the coproheme-WT and -M149A complexes, showing the ν(Fe-Im) stretching mode together with the ν<sub>8</sub> and the propionate bending modes.

The spectra have been shifted along the ordinate axis to allow better visualization. Experimental conditions: excitation wavelength 441.6 nm, laser power at the sample 10 mW; average of 6 spectra (WT) with 30 min integration time and of 12 spectra (M149A) with 60 min integration time.

The data also highlight that mutation of the Met149 residue to Ala dramatically alters the heme coordination, which becomes 6cLS with the amide nitrogen atom of the Gln187 residue bound to the heme iron. The fact that the Gln187 is able to bind iron in absence of the Met149 residue means that the distal cavity is very flexible. This flexibility was confirmed by studying the ferrous-CO adducts (see paragraph 4.3.5). Surprisingly, however, the catalytic activity of the protein is not affected from the mutation since the M149A mutant is able to turn the coproheme in the heme *b* product as the WT protein. The only difference between the WT and its M149A variant is that the activity of the latter is slightly lower ( $k_{cat}/K_M = 1.5 \times 10^2 \text{ M}^{-1} \text{ s}^{-1}$ ) than that of the WT ( $k_{cat}/K_M = 1.8 \times 10^2 \text{ M}^{-1} \text{ s}^{-1}$ ) due to impaired H<sub>2</sub>O<sub>2</sub> accessibility caused by the sixth ligand of the 6cLS species.

#### 4.3.5 Ferrous-CO adducts

As for heme protein-CO complexes, the ferrous coproheme proteins bind CO giving rise to a 6cLS species. The UV-Vis spectra (**Figure 4.15, A**) are all blue shifted compared to heme *b* CO complexes due to the lack of conjugation of the vinyl groups.

Accordingly, the UV-Vis spectrum of the coproheme-CO complex is characterized by a Soret band at 399 nm, 12 nm blue-shifted compared to that of the free heme-CO complex [Ye 2005], with  $\nu(\text{FeC})$  and  $\nu(\text{CO})$  stretching modes at 530 and 1957  $\text{cm}^{-1}$  (**Figure 4.15, B**), very similar to those observed for the heme-CO complex (at 530 and 1955  $\text{cm}^{-1}$ ) [Ye 2005].

The correlation line of the  $\nu(\text{FeC})$  versus  $\nu(\text{CO})$  frequencies reported in **Figure 4.16** has been obtained according to eq. 1 of ref [Spiro 2005]. The  $\nu(\text{FeC})/\nu(\text{CO})$  position along the correlation line reflects the type and strength of distal polar interactions. Above the imidazole back-bonding correlation line another parallel line is typical of heme proteins

or model compounds with a trans ligand weaker than His [Vogel 2000], or no ligand at all [Spiro 2005, Ray 1994]. Similar to the free heme-CO complex, the free coproheme-CO complex lays on this line, in agreement with the formation of a 5cHS complex [Yeh 2005].

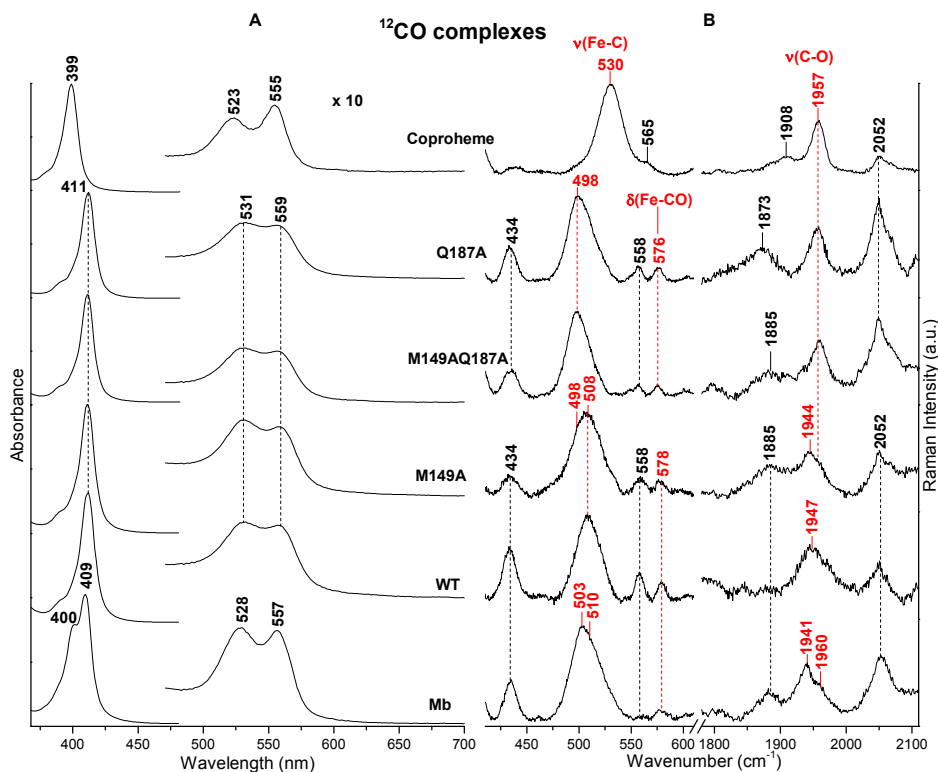


**Figure 4.15.** UV-vis (panel A) and RR (panel B) spectra in the low (left) and high (right) frequency regions of the  $^{12}\text{CO}$  adducts of the coproheme complexes of Mb, WT, M149A, M149AQ187A, Q187A, and coproheme. The frequencies of the  $\nu(\text{FeC})$ ,  $\delta(\text{FeCO})$  and  $\nu(\text{CO})$  modes are indicated in red. The spectra have been shifted along the ordinate axis to allow better visualization. Panel A: the 480–700 nm region is expanded 10-fold. Panel B: experimental conditions: Mb and coproheme:  $\lambda_{\text{exc}}$  406.7 nm, laser power at the sample 5 mW, average of 4 spectra with 40 min integration time and 10 spectra with 100 min integration time in the low and high frequency regions, respectively (Mb), average of 6 spectra with 60 min integration time and 12 spectra with 120 min integration time in the low and high frequency regions, respectively (coproheme); WT and its mutants,  $\lambda_{\text{exc}}$  413.1 nm, laser power at the sample 1-3 mW; average of 28 spectra with 280 min

integration time and 22 spectra with 220 min integration time in the low and high frequency regions, respectively (WT), average of 6 spectra with 60 min integration time and 18 spectra with 180 min integration time in the low and high frequency regions, respectively (M149A), average of 6 spectra with 60 min integration time and 15 spectra with 150 min integration time in the low and high frequency regions, respectively (M149A/Q187A), and average of 9 spectra with 90 min integration time and 15 spectra with 150 min integration time in the low and high frequency regions, respectively (Q187A).

Interestingly, the UV-Vis spectrum of coproheme-Mb-CO shows two bands in the Soret region at 400 and 409 nm. However, the RR spectra obtained with both the 406.7 and 413.1 nm excitation wavelengths are identical. For both excitation wavelengths, and on the basis of the isotope shift in  $^{13}\text{CO}$  versus  $^{12}\text{CO}$  (**Figure 4.17**), two CO conformers have been identified characterized by:

- $\nu(\text{FeC})$  at  $503\text{ cm}^{-1}$  and  $\nu(\text{CO})$  at  $1956\text{ cm}^{-1}$ ;
- $\nu(\text{FeC})$  at  $510\text{ cm}^{-1}$  and  $\nu(\text{CO})$  at  $1941\text{ cm}^{-1}$ .

Moreover, the weak band at  $578\text{ cm}^{-1}$  is assigned to the  $\delta(\text{FeCO})$  bending mode.

The two conformers found for the coproheme-Mb complex are reminiscent of those of (heme *b*) SWMbCO at neutral pH, namely the  $A_1$  ( $508/1946\text{ cm}^{-1}$ ) and  $A_3$  ( $518/1932\text{ cm}^{-1}$ ) conformers,  $A_1$  being the main species. In addition in SWMbCO, a very weak species,  $A_0$  ( $493/1965\text{ cm}^{-1}$ ) was observed, that increases at acid pH at the expense of the  $A_1$  conformer [Morikis 1989, Howes 2012]. The hydrogen bond between the oxygen of the CO and the distal His64 has been identified as responsible for the different conformers: a strong H-bond gives rise to the closed form,  $A_3$ , a weak-H-bond to the closed form  $A_1$ , and the absence of a H-bond to an open form  $A_0$  [Morikis 1989] (**Figure 4.16**). By analogy, the two conformers observed in the coproheme-Mb complex were named  $A_1$  ( $510/1941\text{ cm}^{-1}$ ) and  $A_0$  ( $503/1956\text{ cm}^{-1}$ ), however, this latter form is not completely open but shows only a decreased polar interaction with the distal residues.

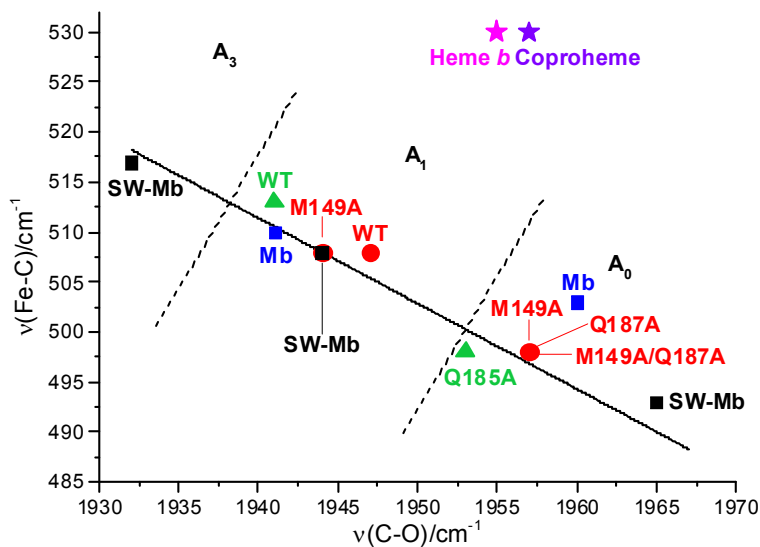


**Figure 4.16.** Back-bonding correlation line of the  $\nu(\text{Fe-C})$  and  $\nu(\text{C-O})$  stretching frequencies of the coproheme-CO complexes of Mb (blue solid squares), *Sa*ChdC WT, and selected mutant (green solid triangles), *Lm*ChdC WT and selected mutants (red solid circles), heme and coproheme (pink and violet star, respectively). The three conformers of SWMb (heme *b*) are also reported (black solid squares). The dotted lines indicate the approximate delineation between the frequency zones of the  $A_0$ ,  $A_1$ , and  $A_3$  states discussed in the text. The frequencies and references of the  $\nu(\text{Fe-C})$  and  $\nu(\text{C-O})$  stretching modes of the various CO adducts are reported in **Table 4.4**.

The electronic absorption spectra of the ferrous-CO adduct coproheme-WT complex (as those of its mutants) is characterized by Soret,  $\alpha$ , and  $\beta$  bands at 411 nm, 531 and 559 nm, respectively (**Figure 4.15, A**). The RR spectra show that CO binds WT giving rise to only one conformer  $A_1$  (with  $\nu(\text{FeC})$  at  $508\text{ cm}^{-1}$  and  $\nu(\text{CO})$  at  $1947\text{ cm}^{-1}$ ) where the CO is involved in a moderate H-bond or electrostatic interaction with one of the distal residues. This is in agreement with the form ( $513/1941\text{ cm}^{-1}$ ) previously reported for the ChdC-CO complex from *Sa*, where the CO interacts with the distal Gln185 residue [Celis 2017]. Upon replacement of the Q187 residue (Q187A mutants), the polar  $A_1$  conformer observed in the WT disappears, being replaced by an apolar open  $A_0$  form with

$\nu(\text{FeC})$  at  $498\text{ cm}^{-1}$  and  $\nu(\text{CO})$  at  $1957\text{ cm}^{-1}$ . This confirms that as for the *Sa*, in the *LmChdC* the CO interacts with the Gln187 residue.

Interestingly, the ferrous-CO adduct of the coproheme-M149A complex shows two conformers: a polar  $A_1$  form ( $508/1944\text{ cm}^{-1}$ ), very similar to that observed in the WT, and the open  $A_0$  form observed in the Q187A mutant ( $498/1957\text{ cm}^{-1}$ ). This suggests that in the coproheme-M149A complex the Gln187 residue has a similar role to that of the distal His64 in SWMb, confirming that the distal cavity of ChdC is quite flexible (see also **Figure 4.10** and the respective caption). In particular the Met149 residue which is located at  $\sim 4.0\text{ \AA}$  from the propionate group in position 2 has an important role in keeping the Gln187 residue correctly positioned to close the distal cavity.

**Table 4.4.**  $\nu(\text{Fe-C})$  and  $\nu(\text{C-O})$  stretching modes frequencies ( $\text{cm}^{-1}$ ) of the ferrous-CO adduct reported in **Figure 4.12**.

	Conformers	$\nu(\text{FeC})$	$\nu(\text{CO})$	
		<b>coproheme</b>		
<b>HH</b>				
<b>Mb</b>	$A_0$	503	1960	This work
<b>Mb</b>	$A_1$	510	1941	This work
<b>Lm ChdC</b>				
<b>WT</b>	$A_1$	508	1947	This work
<b>M149A</b>	$A_1$	508	1944	This work
<b>M149A</b>	$A_0$	498	1957	This work
<b>Q187A</b>	$A_0$	498	1957	This work
<b>Q187AM149A</b>	$A_0$	498	1957	This work
<b>SaChdC</b>				
<b>WT</b>	$A_1$	513	1941	Celis 2017
<b>Q185A</b>	$A_0/ A_1$	498	1953	Celis 2017
<b>Coproheme</b>		530	1957	This work
		<b>Heme <i>b</i></b>		
<b>SW</b>				
<b>Mb</b>	$A_3$	517	1932	Howes 2012
<b>Mb</b>	$A_1$	508	1944	Howes 2012
<b>Mb</b>	$A_0$	493	1965	Howes 2012
<b>Heme</b>		530	1955	Ye 2005

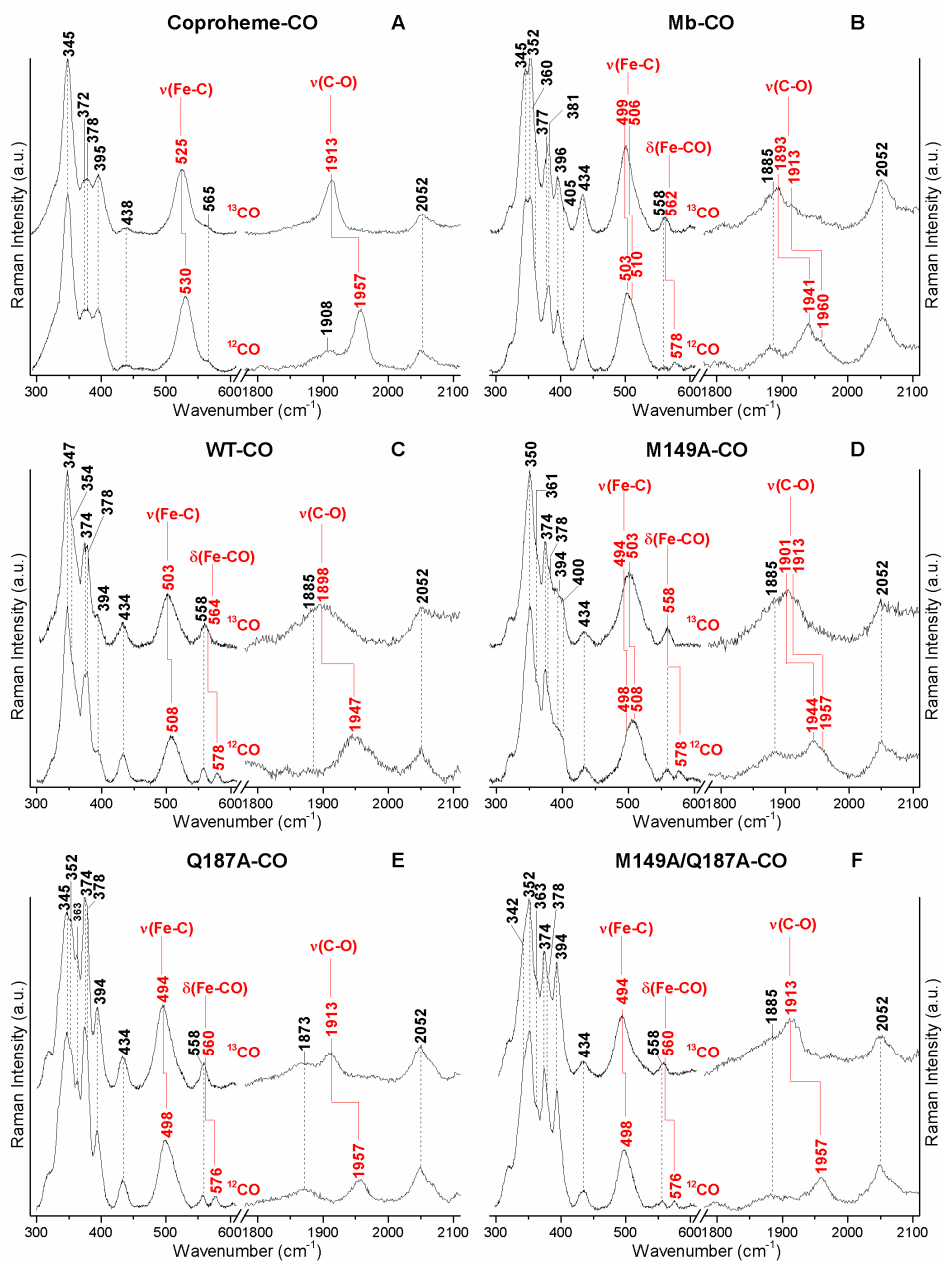


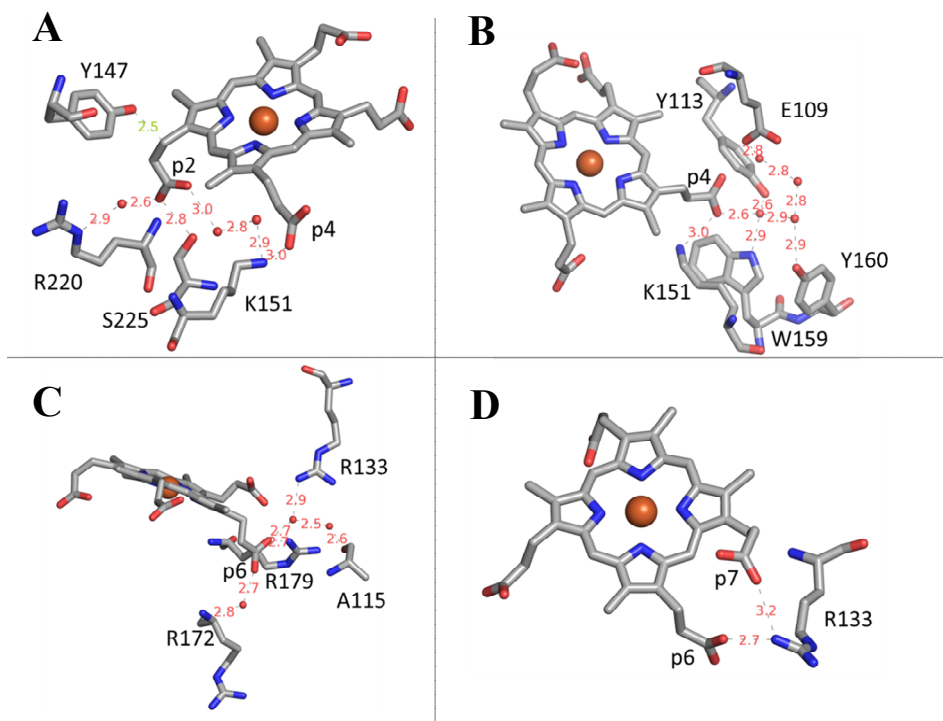
**Figure 4.17.** RR spectra in the low (left) and high (right) frequency regions of the <sup>12</sup>CO (bottom) and <sup>13</sup>CO (top) adducts of coproheme (panel A) and the coproheme complexes with Mb (panel B), WT (panel C), and the M149A (panel D), Q187A (panel E), M149A/Q187A (panel F) mutants. The frequencies of the  $\nu(\text{FeC})$ ,  $\delta(\text{FeCO})$  and  $\nu(\text{CO})$  modes, are indicated in red. The spectra have been shifted along the ordinate

axis to allow better visualization. Experimental conditions: coproheme and coproheme-Mb:  $\lambda_{\text{exc}}$  406.7 nm, laser power at the sample 5 mW, average of 6 spectra with 60 min integration time and 12 spectra with 120 min integration time in the low and high frequency regions, respectively ( $^{12}\text{CO}$ -coproheme), average of 9 spectra with 90 min integration time and 11 spectra with 110 min integration time, in the low and high frequency regions, respectively ( $^{13}\text{CO}$ -coproheme), average of 4 spectra with 40 min integration time and 10 spectra with 100 min integration time, in the low and high frequency regions, respectively ( $^{12}\text{CO}$ -Mb), average of 4 spectra with 40 min integration time and 7 spectra with 70 min integration time, in the low and high frequency regions, respectively ( $^{13}\text{CO}$ -Mb); coproheme-WT and its selected mutants,  $\lambda_{\text{exc}}$  413.1 nm, laser power at the sample 1-3 mW, average of 28 spectra with 280 min integration time and 22 spectra with 220 min integration time, in the low and high frequency regions, respectively ( $^{12}\text{CO}$ -WT), average of 8 spectra with 80 min integration time and 15 spectra with 150 min integration time, in the low and high frequency regions, respectively ( $^{13}\text{CO}$ -WT), average of 6 spectra with 60 min integration time and 18 spectra with 180 min integration time, in the low and high frequency regions, respectively ( $^{12}\text{CO}$ -M149A), average of 12 spectra with 120 min integration time and 18 spectra with 180 min integration time, in the low and high frequency regions, respectively ( $^{13}\text{CO}$ -M149A), average of 9 spectra with 90 min integration time and 15 spectra with 150 min integration time, in the low and high frequency regions, respectively ( $^{12}\text{CO}$ -Q187A), average of 7 spectra with 70 min integration time and 13 spectra with 130 min integration time, in the low and high frequency regions, respectively ( $^{13}\text{CO}$ -Q187A), average of 6 spectra with 60 min integration time and 15 spectra with 150 min integration time in the low and high frequency regions, respectively ( $^{12}\text{CO}$ -M149A/Q187A), average of 7 spectra with 70 min integration time and 12 spectra with 120 min integration time, in the low and high frequency regions, respectively ( $^{13}\text{CO}$ -M149A/Q187A).

#### **4.4 The coproheme complexes of other key residue mutants**

In order to understand if other residues, beyond Met149, are important for the architecture of the catalytic cavity, I studied the ferric form of several others coproheme-mutant complexes where residues involved in H-bonding interactions with the propionate groups have been mutated in the non H-bonding Ala.

In fact, the analysis of the H-bonds around the four propionate groups in chains A and D (which are those entirely modeled, since in these subunits the flexible loop forming the active site access channel is stabilized by crystal packing contacts) reveals an extensive network spanning from p2 to p4 (R220 - water - p2 - S225 - p2 - water - water - K151 - p4), the propionates that are decarboxylated to vinyl groups during catalysis (**Figure 4.18, Table 4.5**). The propionate at position 6 (p6) is also stabilized and by various H-bonds (R172, R179, R133 and A115) in contrast to p7 (potentially H-bonded to R179 in chain D or Q187 in chain A), whose position varies the most in all subunits, probably due to the lack of strong coordination.



**4.18.** Propionate environment of coproheme in chain D (6FXJ). Analysis of hydrogen bonding network in proximity to the four coproheme propionate groups: (A) p2 and p4, (B) p4, (C) p6, and (D) p7.

**Table 4.5.** Distances (Å) of the propionate groups in position 2, 4, 6 and 7 in the subunits A, B, C, D, E from the studied mutated residues. Hydrogen bonding networks are marked in bold and yellow.

	Propionate 2					Propionate 4				
	A	B	C	D	E	A	B	C	D	E
Q187/1	11.1	11.7	10.6	11.3	11.1	11.4	11.4	11.4	11.5	13.6
Q187/2	7.0	-	-	7.3	-	8.8	-	-	9.0	-
R133	14.6	14.7	13.3	14.6	14.6	11.4	10.7	10.7	13.0	11.8
R179	13.0	18.5	15.1	14.6	16.4	13.5	17.1	16.3	13.6	13.4
Y113	13.2	-	14.6	13.1	14.5	<b>2.6H2.8</b>	-	<b>2.6H3.0</b>	<b>2.5H2.7</b>	<b>2.6H2.7</b>
M149	4.0	4.7	3.8	4.0	4.6	8.7	8.4	7.7	8.8	7.9
K151	<b>2.9H2.5H3.0</b>	8.0	7.4	<b>2.7H2.8H2.9</b>	8.1	<b>2.9</b>	3.4	4.2	<b>3.0</b>	<b>2.9</b>
Y147	4.9	<b>2.6</b>	<b>2.9</b>	5.3	<b>2.5</b>	12.3	12.8	12.4	12.4	12.4
R220	<b>2.9H2.5</b>	<b>2.8H3.1</b>	<b>2.9H2.8H2.7</b>	<b>2.8H2.5</b>	<b>2.9H3.0</b>	14.8	15.7	15.0	15.1	15.3
S225	<b>2.6</b>	<b>2.8</b>	<b>2.7H2.7</b>	<b>2.7</b>	<b>2.8</b>	9.2	9.7	9.1	9.5	9.3
	Propionate 6					Propionate 7				
	A	B	C	D	E	A	B	C	D	E
Q187/1	7.3	5.5	8.2	7.2	7.1	<b>2.8</b>	4.7	4.2	<b>2.6</b>	5.4
Q187/2	8.0	-	-	8.0	-	5.1	-	-	3.8	-
R133	<b>3.2H2.5</b>	<b>3.0</b>	4.3	<b>3.2H2.9</b>	3.6	5.7	3.8	4.0	4.3	4.6
R179	<b>2.9</b>	8.9	8.3	<b>2.7</b>	3.6	5.4	4.7	5.9	<b>3.2</b>	3.5
Y113	13.8	-	11.4	12.7	14.5	17.8	-	18.0	14.8	16.2
M149	15.1	13.1	15.1	15.2	15.5	15.6	15.1	16.1	13.1	15.7
K151	11.7	11.6	13.6	11.7	13.3	15.5	14.3	16.6	12.8	14.5
Y147	15.1	13.9	16.4	15.2	15.9	12.6	14.2	14.1	13.5	14.7
R220	19.7	19.7	21.6	18.9	21.4	18.3	19.9	19.9	19.0	19.8
S225	13.0	15.2	15.7	13.2	15.8	15.0	15.1	15.8	14.3	14.9

Q187/1 and Q187/2: in the A and D subunits the Gln187 residue, according to the electron densities, has been refined in a split conformation 50% in position 1 (Q187/1) and 50% in position 2 (Q187/2). Position 1 points away from the heme iron, towards the p7 with which is H-bonded; position 2 points towards the heme iron but is not H-bonded with the p7. See also Table 4.5. This indicates a certain flexibility of Gln187.

Mutation to Ala of the residues interacting with the propionates in position 6 (R133 and R179, this latter also H-bonded to the p7) and 7 (Q187 and R179) do not alter the spin and coordination states of the coproheme iron, being both the UV-Vis and RR spectra identical to those of the coproheme-WT complex (**Figure 4.19, bottom spectra**). Conversely, mutation of the residues interacting with the propionates in position 2 (Y147, M149, R220 and S225) or 4 (Y113 and K151, this latter also part of a H-bond network involving p2), alter the heme cavity structure inducing the formation of a high amount of the 6cLS species,



with the propionate in position 2, 4, 6, and 7, are reported in beige, green, brown and light blue.

#### 4.5 The heme *b* complexes

Upon addition of hydrogen peroxide to the ChdC coproheme complex the propionate groups in position 2 and 4 are turned into vinyl groups leaving only the propionate in position 6 and 7, thus forming the heme *b* complex. Beside the heme *b*-WT and M149A complexes I also studied the heme *b* complex of all the mutants where residues involved in H-bonding interactions with the propionate groups in position 6 and 7 have been mutated in the non H-bonding Ala (i.e. Q187A, M149A/Q187A, R133A and R179A).

The formation of the vinyl groups upon conversion of the coproheme complex into heme *b* leads to an overall red-shift of the electronic absorption spectra compared to the coproheme complexes, (**Figure 4.20, A**) and to the appearance of two  $\nu(\text{C}=\text{C})$  vinyl stretching modes in the high frequency region of the RR spectrum at 1621 and 1632  $\text{cm}^{-1}$ , together with core size marker bands characteristic of a 6cLS species (1503 ( $\nu_3$ ), 1580 ( $\nu_2$ ), 1638 ( $\nu_{10}$ )  $\text{cm}^{-1}$ ) (**Figure 4.20, B**).

A vinyl stretching frequency of 1632  $\text{cm}^{-1}$  is quite high and indicates a fairly low degree of conjugation between the vinyl double bond and the porphyrin macrocycle [Marzocchi 2003] (see Chaptre 2). A lower degree of conjugation for one of the vinyl modes can explain the blue shift (by about 4-5 nm) of the Soret maximum of the heme *b*- LmChdC WT and mutant complexes (409-410 nm) compared to the Mb-imidazole complex, a 6cLS species characterized by a heme group with both vinyl groups conjugated, (Soret maximum at 414 nm and both vinyl bands coincident at 1621  $\text{cm}^{-1}$ ) [Feis 2007]. The visible bands of the heme *b*-LmChdC WT and mutant complexes are very similar (533/568 nm) to those of the Mb-imidazole complex (535/567nm) [Feis 2007], indicating that the sixth ligand is a nitrogen atom. In the RR spectra of the heme *b*-WT, -M149A, -R133A, and -R179A complexes the  $\nu_3$  and  $\nu_2$  bands are very broad and in particular the  $\nu_2$  region allows to clearly identify two different 6cLS species: one, absent in the heme *b*-Q187A and -M149A/Q187A complexes, containing as distal ligand the Gln187

residue (**violet**,  $\nu_3$  and  $\nu_2$  bands at 1507 and 1588  $\text{cm}^{-1}$ , respectively), and another, present in all the complexes, whose sixth ligand has not been yet identified (**magenta**,  $\nu_3$  and  $\nu_2$  bands at 1503 and 1580  $\text{cm}^{-1}$ , respectively).

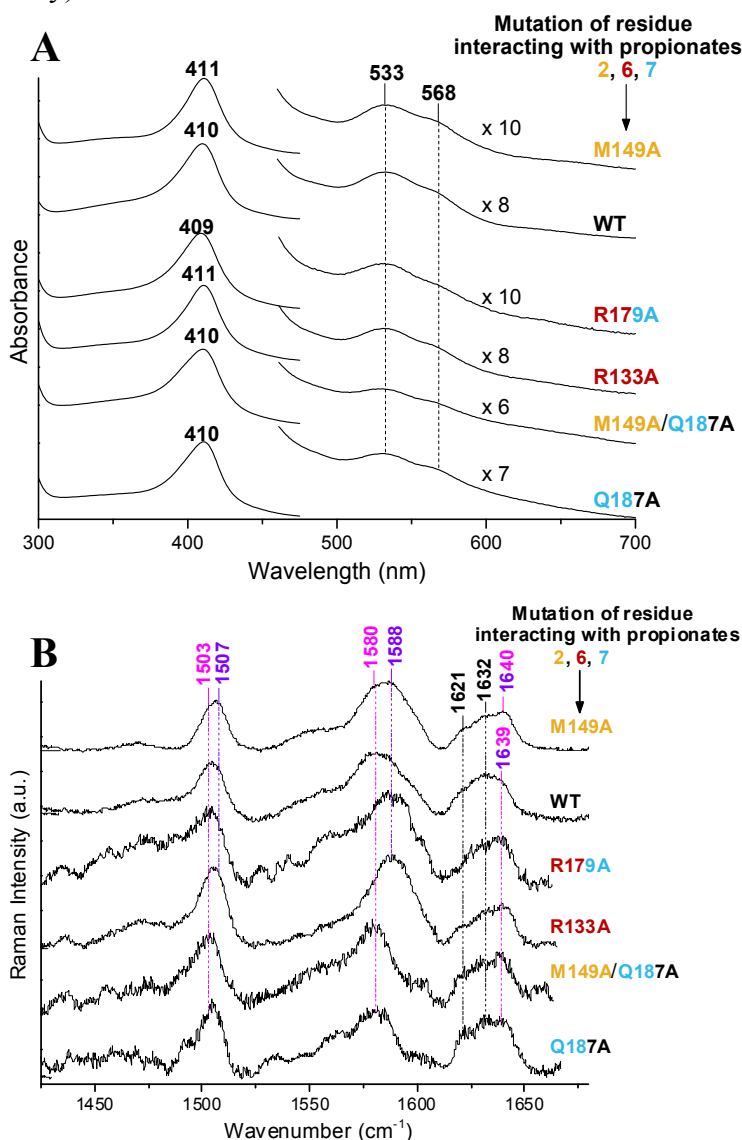


**Figure 4.20.** Comparison of the heme *b*-LmChdC complexes of the WT, Q187A, Q187A/M149A, R133A, R179A and M149A mutants. (A) UV-Vis and second derivative spectra of the Soret band ( $D^2$ ); (B) high frequency RR spectra ( $\lambda_{\text{exc}}$  406.7 nm). The frequencies of the **5cHS**, **5cQS** and the two **6cLS** species with the N atom of Gln187 and of a

sixth ligand not yet identified, are reported in **orange**, **green**, **violet** and **magenta**, respectively. Accordingly, the labels of the residues interacting with the propionate in position **2**, **6**, and **7** that have been mutated, are reported in **beige**, **brown** and **light blue**.

UV-Vis titration between pH 7 and 10 and the RR spectra of heme *b*-complexes rules out the possibility that the second LS species derives from a hydroxo ligated form. At alkaline pH the heme exits from the cavity. Moreover, the crystal structure of the coproheme complex does not evidence any other possible residue able to bind the iron atom apart the Gln187 residue. This means that upon formation of the heme *b* complex, structural rearrangement take place in the active site. Interestingly, the spectroscopic studies of the ferric heme *b* ChdC WT from *M. tuberculosis* [Dailey 2010] and *Sa* [Celis 2017] indicate that the proteins are 5cHS. Clearly, these results suggest that the heme *b* cavity architecture of LmChdC is different.

The fact that the ferric form of the heme *b* complexes are all 6cLS confirms again the crucial role of the H-bond interaction involving the propionate in position 2 and 4 in maintaining the active site architecture: when the 2 and 4 propionates are transformed into vinyl groups and the H-bond network does not exist anymore the heme *b* proteins become 6cLS. Accordingly, the ferrous-CO adduct of the heme *b*-WT complex (**Figure 4.21**), lacking the interaction between the Met149 residue and the propionate in position 2 that keeps the Gln187 residue correctly positioned to close the distal cavity, shows an open  $A_0$  conformer ( $\nu(\text{FeC})/\nu(\text{CO})$  at 500/1960  $\text{cm}^{-1}$ ). These data are in agreement with those found for the heme *b* ChdC-CO complex from *Sa* [Celis 2017]. Conversely, the proximal cavity, is not affected by the loss of the p2 and p4; the  $\nu(\text{Fe-Im})$  of both the coproheme (5cHS) and heme *b* (mainly 6cLS with a minor 5cHS species, **Figure 4.22**) complexes of the WT and M149A (**Figure 4.14** and **4.23**) remains at 214  $\text{cm}^{-1}$ , as for *Sa* ChdC [Streit 2017].

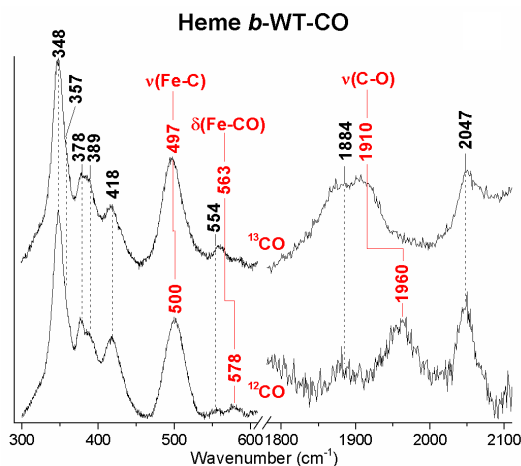


**Figure 4.23.** RR spectra in the low (left) and high (right) frequency regions of the  $^{12}\text{CO}$  (bottom) and  $^{13}\text{CO}$  (top) adducts of the heme *b* LmChdC WT complex. The frequencies of the  $\nu(\text{FeC})$ ,  $\delta(\text{FeCO})$  and  $\nu(\text{CO})$  modes, are indicated in red. The spectra have been shifted along the ordinate axis to allow better visualization. Experimental conditions:  $\lambda_{\text{exc}}$  413.1 nm, laser power at the sample 1 to 3 mW, average of 16 spectra with 160 min integration time and 12 spectra with 120 min integration time in the low and high frequency regions, respectively ( $^{12}\text{CO}$ -WT complex), average of 8 spectra with 80 min integration time and 12 spectra with 120 min integration time in the low and high frequency regions, respectively ( $^{13}\text{CO}$ -WT complex)..

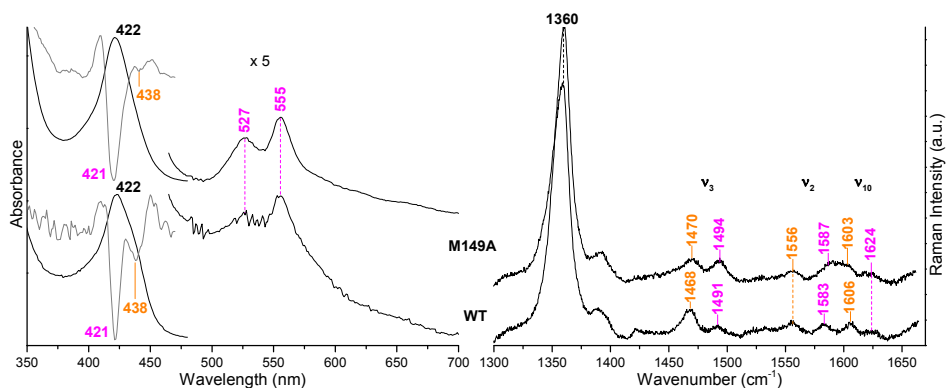


**Figure 4.24.** UV-vis absorption spectra (A) and RR spectra in the high frequency region (B) of the ferrous form of the heme *b*-WT and -M149A complexes. The spectra have been shifted along the ordinate axis to allow better visualization. The 480–700 nm region of the UV-Vis spectrum is expanded 5-fold. Experimental conditions: excitation

wavelength 413.1 nm, laser power at the sample 5 mW; average of 3 spectra with 60 min integration time (WT), average of 6 spectra with 60 min integration time (M149A).

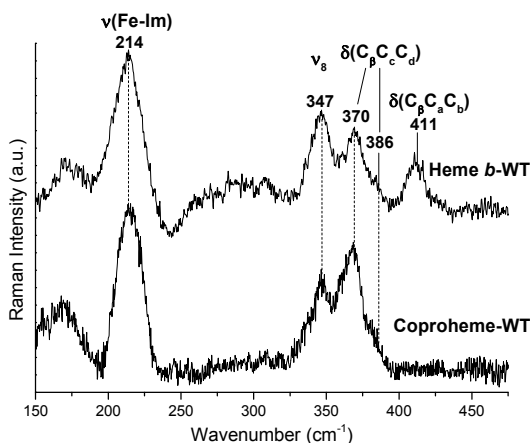


**Figure 4.25.** RR spectra in the low frequency region of the ferrous form of the coproheme- and heme *b*-WT complexes, showing the  $\nu(\text{Fe-Im})$  stretching mode together with the  $\nu_8$ , the propionate and vinyl bending modes. Experimental conditions: excitation wavelength 441.6 nm, laser power at the sample 10 mW; average of 6 spectra (coproheme-WT) and of 3 spectra (heme *b*-WT) with 30 min integration time.

#### 4.6 Assignment of the propionate bending modes

Via RR spectroscopy is possible to follow the conversion of the propionate in position 2 and 4 into vinyl groups, observing in the low frequency region the progressive intensity decrease of the  $[\delta(\text{C}_\beta\text{C}_\gamma\text{C}_\delta)]$  bending modes of the p2 and p4 and the concomitant intensity increase of the  $[\delta(\text{C}_\beta\text{C}_\alpha\text{C}_\gamma)]$  bending modes of the vinyl groups. Therefore it is fundamental to selectively assign the  $[\delta(\text{C}_\beta\text{C}_\gamma\text{C}_\delta)]$  bending modes to each propionate group p2, p4, p6 and p7.

The bending modes  $[\delta(\text{C}_\beta\text{C}_\gamma\text{C}_\delta)]$  of the propionate substituents are usually found between 366 and 376  $\text{cm}^{-1}$ . Since their frequencies are correlated to the H-bond strength between the propionate and the nearby amino acids (see Chapter 2), I studied the RR spectra of a series of mutants where the residues H-bonded with the p2 (Y147, R220 and S225), p4 (Y113 and K151, this latter also part of a H-bond network involving p2), p6 (R133 and R179, this latter also H-bonded to the p7),

and p7 (Q187 and R179) were replaced by the non H-bonding Ala residue (see **Figure 4.18** and **Table 4.5**). As compared to the WT, a decrease of the H-bond strength interaction with a propionate is expected to result in a frequency downshift of its corresponding RR bending mode. However, we should underline that due to the very extensive H-bond network spanning from p2 to p4 (see **Figure 4.18** and **Table 4.5**) and the presence of multiple coprohemes (five subunits), containing different H-bonds involving the propionate groups (**Table 4.5**), the spectra of the coproheme-mutant complexes might be more complicated than expected.

#### 4.6.1 Coproheme complexes

In the coproheme-WT RR spectrum at room temperature (**Figure 4.24**) out of the four, three propionate bending modes at 374, 392  $\text{cm}^{-1}$ , and at about 381  $\text{cm}^{-1}$  are observed.

p2: in the complex of coproheme with the Y147A/R220A/S225A triple mutant a new band at 386  $\text{cm}^{-1}$  can be identified (**Figure 4.24, beige**). This mutant lacks the H-bond interaction with the solely propionate group in position 2 (**Figure 4.18, Table 4.5**). Therefore, this new band is tentatively assigned to the bending mode of a non-H-bonded p2, which in the WT is expected to have a higher frequency. Accordingly, an intensity increase in this region is also observed in the spectra of all the coproheme-mutants where residues interacting with propionate in position 2 have been replaced with Ala, namely M149 and K151.

p4: in the coproheme-Y113A complex, which lacks the H-bond interaction with the propionate in position 4 (**Figure 4.18, Table 4.5**), the band at 381  $\text{cm}^{-1}$  (WT) downshifts to 379  $\text{cm}^{-1}$  and increases in intensity (**Figure 4.24, green**). This band is, therefore, assigned to the bending mode of the p4.

p6: this propionate is directly H-bonded to the R179 residue and, via a water molecule, to the R133 residue, (**Figure 4.18, Table 4.5**). In the coproheme-R179A complex the band at 374  $\text{cm}^{-1}$  (WT) unexpectedly upshifts to 377  $\text{cm}^{-1}$  (**Figure 4.24, brown**) suggesting that a strengthening of the H-bond interactions occurs after mutation, while the frequency is unchanged in coproheme-R133A complex spectrum.

*p7*: the Q187A mutant involves a residue which interacts with the *p7* only (**Figure 4.18, Table 3**). In its coproheme complex the band at 392  $\text{cm}^{-1}$  (WT) downshifts to 389  $\text{cm}^{-1}$  (**Figure 4.24, light blue**) and is, therefore, assigned to the *p7* bending mode. The spectrum of the coproheme-M149A/Q187A double mutant complex is roughly the average of the coproheme-M149A and -Q187A spectra.

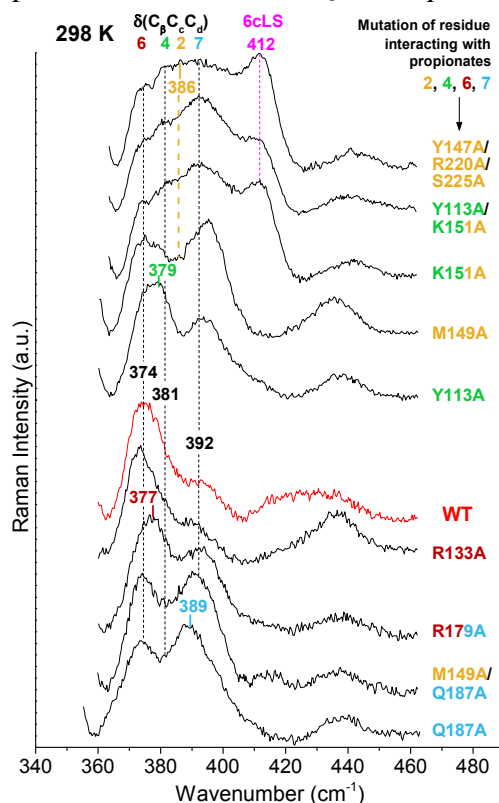


**Figure 4.24.** Comparison of the RR spectra in the low frequency region of the coproheme-LmChdC complexes of the WT and mutants obtained at 298 K ( $\lambda_{\text{exc}}$  406.7 nm). The bands tentatively assigned to the bending modes  $\delta(\text{C}_\beta\text{C}_\gamma\text{C}_\delta)$  of the propionate groups in position 2, 4, 6 and 7 are reported in beige, green, brown and light blue, respectively. Accordingly, the mutants label colours indicate the position of the propionate group/s with which the mutated residues interact. In magenta is reported the band due to the 6cLS species. The spectrum of the coproheme-WT complex is reported in red. The spectra have been shifted along the ordinate axis to allow better visualization. Experimental conditions: laser power at the sample 5 mW, average of 8 spectra with a 80 min integration time (Q187A); average of 12 spectra

with a 120 min integration time (M149A/Q187A); average of 10 spectra with a 100 min integration time (R179A and R133A); average of 15 spectra with 150 min integration time (WT); average of 9 spectra with a 90 min integration time (Y113A, M149A, and K151A); average of 12 spectra with a 120 min integration time (Y113A/K151A and Y147A/R220A/S225A).

To be noted that a new band at  $412\text{ cm}^{-1}$  (in the region of the vinyl bending modes) appears in the spectra of the coproheme-complexes which are mainly a 6cLS form, namely the coproheme-Y147A/R220A/S225A, -Y113A/K151A, and -K151A complexes (**Figure 4.19**). Since these mutants are catalytically inactive, they cannot form any heme *b* complex, and no band due to vinyl bending mode is expected. The origin of the band at  $412\text{ cm}^{-1}$  due to a mode of the 6cLS form, remains unclear.

With the aim to increase the resolution we extended the study of these mutants at 80K.

With the low temperature back-scattered setup, the plasma laser lines of the 406.7 nm excitation wavelength in the low frequency region are very intense. In particular, the lines at  $381$  and  $398\text{ cm}^{-1}$  overlap with the propionate bending modes, preventing their assignment. Therefore the low frequency region RR spectra were obtained with the 413.1 nm excitation wavelength. These spectra, however, are identical to those obtained with  $\lambda_{\text{exc}}$  406.7 nm as shown in **Figure 4.25** where are compared the spectra of the coproheme-WT and -Y113A complexes obtained with the two excitation wavelengths. The comparison of the spectra taken with  $\lambda_{\text{exc}}$  406.7 nm and  $\lambda_{\text{exc}}$  413.1 nm for all the other coproheme-mutant complexes gave the same result.

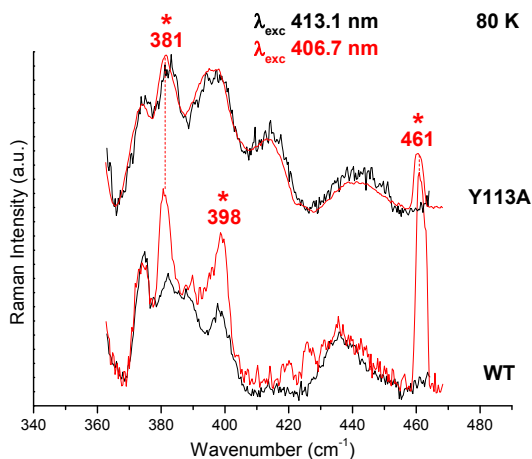


**Figure 4.25.** Comparison of the RR spectra in the low frequency region of the coproheme-WT and -Y113A complexes obtained at 80 K with  $\lambda_{\text{exc}}$  413.1 nm (black) and  $\lambda_{\text{exc}}$  406.7 nm (red). The plasma laser lines of the 406.7 nm  $\lambda_{\text{exc}}$  (red) are marked with an asterisk. Experimental conditions:  $\lambda_{\text{exc}}$  413.1 nm, laser power at the sample 10 mW, average of 5 spectra with 100 min integration time (WT); average of 9 spectra with a 180 min integration time (Y113A).  $\lambda_{\text{exc}}$  406.7 nm, laser power at the sample 5-10 mW, average of 4 spectra with 80 min integration time (WT); average of 6 spectra with a 120 min integration time (Y113A).

At 80 K the coproheme-WT spectrum shows four well-defined bands at 374, 383, 389 and 399  $\text{cm}^{-1}$  (**Figure 4.26**).

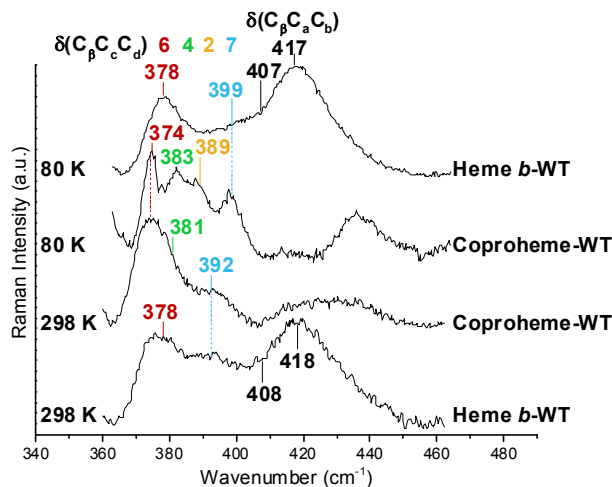


**Figure 4.26.** Comparison of the RR spectra in the low frequency region of the coproheme- and heme *b*-LmChdC WT complexes obtained at 298

K ( $\lambda_{\text{exc}}$  406.7 nm) and at 80 K ( $\lambda_{\text{exc}}$  413.1 nm). The bands tentatively assigned to the bending modes  $\delta(\text{C}_\beta\text{C}_c\text{C}_d)$  of the propionate groups in position **2**, **4**, **6** and **7** are reported in **beige**, **green**, **brown** and **light blue**, respectively. The bending mode  $\delta(\text{C}_\beta\text{C}_a\text{C}_b)$  of the vinyl groups are also shown. The spectra have been shifted along the ordinate axis to allow better visualization. Experimental conditions: laser power at the sample 5 mW, average of 15 spectra with 150 min integration time (298 K) and laser power at the sample 10 mW, average of 5 spectra with 100 min integration time (80 K).

Unlike the room temperature experiments, upon mutation no definitive assignment of the propionate bands can be obtained at 80 K, since the spectra show other effect induced by the temperature. As previously noted, at low temperature the amount of 6cLS increases [Smulevich 1989, Smulevich 1990, Howes 2000, Nielsen 2001], becoming the main species (**Figure 4.27**); as a consequence, the band at  $414\text{ cm}^{-1}$  becomes very strong and is also observed in the coproheme-M149A, -Y113A, -R179A and -R133A complexes (**Figure 4.28**). Moreover, an upshift of the p2 bending mode is observed in those mutants involved in the extensive H-bond network spanning from p4 to p2, suggesting a strengthening of the H-bond interaction induced by the low temperature. However, in agreement with the results at room temperature, in the coproheme-Y147A/R220A/S225A complex the band at  $389\text{ cm}^{-1}$  (WT) downshifts to  $387\text{ cm}^{-1}$ , supporting the assignment of this band to the bending mode of the p2. However, unlike the results obtained at room temperature, when the K151 residue is mutated to Ala, and therefore, the K151-p2-H-bond interaction mediated by two water molecules is removed, the  $389\text{ cm}^{-1}$  band upshifts to  $394\text{ cm}^{-1}$ , suggesting a strengthening of the H-bonds. A similar effect is also observed in the coproheme-M149A and -Y113A complex spectra. In this latter case, being the Y113 residue H-bonded only to p4, the upshift of the p2 is likely due to the strengthening of the p2 extensive H-bond network spanning from p4 to p2. Moreover, in the coproheme-Y113A complex the band at  $383\text{ cm}^{-1}$  (WT) does not downshift as at room temperature, but it is strongly intensified, supporting the assignment of this band to the bending mode of the p4. In the coproheme-Q187A complex the

band observed in the WT at  $399\text{ cm}^{-1}$  downshifts to  $393\text{ cm}^{-1}$ , supporting the assignment of this band to the p7 bending mode. However, a  $3\text{ cm}^{-1}$  upshift is also observed for the band at  $374\text{ cm}^{-1}$  and a new band at  $406\text{ cm}^{-1}$  appears whose origin is not clear. The spectrum of the coproheme-M149A/Q187A complex is a mixture of the coproheme-M149A and -Q187A spectra, accordingly with the room temperature data. Unlike the effect observed at room temperature, in the coproheme-R133A complex the p6 band at  $374\text{ cm}^{-1}$  (WT) remains at the same frequency.

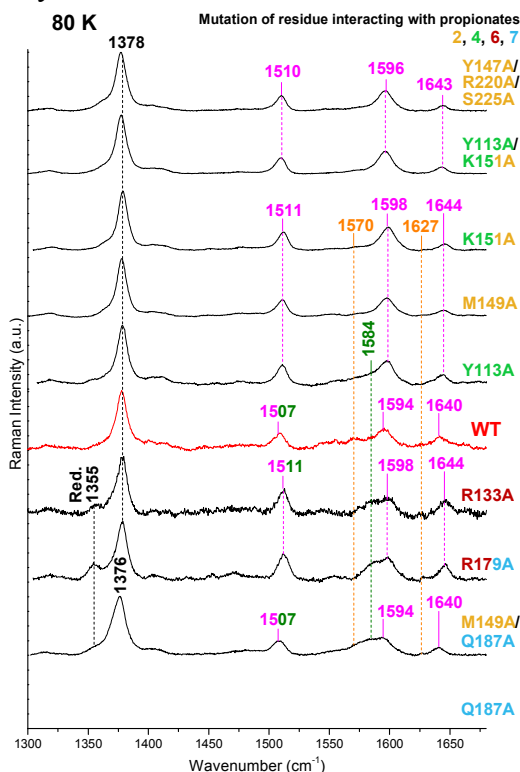


**Figure 4.27.** RR spectra in the high frequency region of the coproheme-LmChdC complexes of the WT and mutants obtained at 80 K ( $\lambda_{\text{exc}}$  406.7 nm). The band wavenumbers in **magenta** indicate the **6cLS** species, while those in **olive green** and **orange** are assigned to a minor **5cQS** and **5cHS** species, respectively. The mutants label colour, **beige**, **green**, **brown** and **light blue**, indicate the position **2**, **4**, **6**, and **7**, respectively, of the propionate group/s with which the mutated residues interact. In the coproheme-R133A, -R179A, and -M149A/Q187A complex spectra there is a small amount of the reduced form ( $\nu_4$  band at

1355 cm<sup>-1</sup>). Due to the very high fluorescent background, it was not possible to obtain the spectrum of the coproheme-Q187A complex. The spectra have been shifted along the ordinate axis to allow better visualization. Experimental conditions: laser power at the sample 5-10 mW, average of 6 spectra with a 60 min integration time (M149A/Q187A and R179A); average of 2 spectra with a 20 min integration time (R133A); average of 8 spectra with 160 min integration time (WT); average of 9 spectra with a 90 min integration time (Y113A); average of 12 spectra with a 120 min integration time (M149A); average of 6 spectra with a 60 min integration time (K151A); average of 8 spectra with a 40 min integration time (Y113A/K151A); average of 6 spectra with a 30 min integration time (Y147A/R220A/S225A).

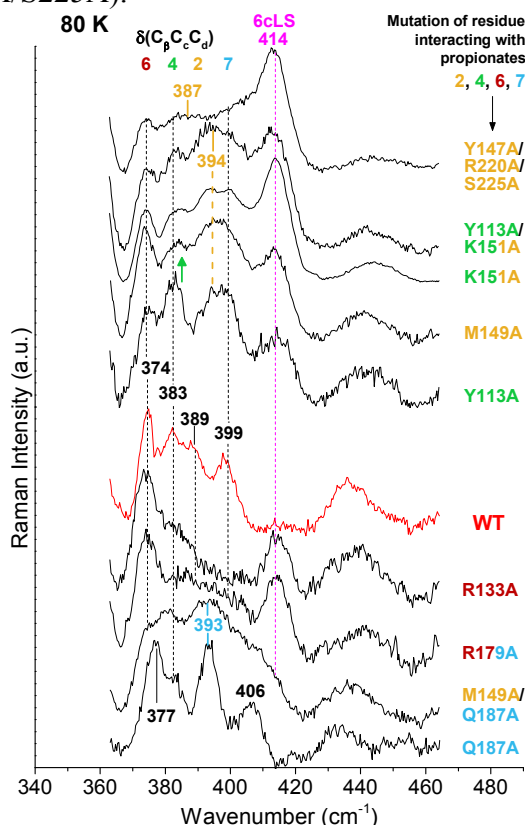


**Figure 4.28.** Comparison of the RR spectra in the low frequency region of the coproheme-LmChdC complexes of the WT and mutants obtained at 80 K ( $\lambda_{exc}$  413.1 nm). The bands tentatively assigned to the bending mode  $\delta(C_{\beta}C_cC_d)$  of the propionate groups in position 2, 4, 6 and 7 are reported in beige, green, brown and light blue, respectively.

Accordingly the mutants label colour indicate the position of the propionate group/s with which the mutated residues interact. In **magenta** is reported the band due to the **6cLS** species. The spectrum of the coproheme-WT complex is reported in **red**. The spectra have been shifted along the ordinate axis to allow better visualization. Experimental conditions: laser power at the sample 5-10 mW, average of 6 spectra with a 120 min integration time (Q187A); average of 10 spectra with a 200 min integration time (M149A/Q187A); average of 24 spectra with a 8 hours integration time (R179A); average of 15 spectra with a 5 hours integration time (R133A); average of 5 spectra with 100 min integration time (WT); average of 9 spectra with a 180 min integration time (Y113A); average of 6 spectra with a 120 min integration time (M149A); average of 7 spectra with a 140 min integration time (K151A); average of 4 spectra with a 80 min integration time (Y113A/K151A); average of 10 spectra with a 200 min integration time (Y147A/R220A/S225A).

#### 4.6.2 Heme *b* complexes

The assignment of the bending modes of the propionate in position 6 and 7 is confirmed by the spectra of the heme *b* complexes. In fact, in the conversion of the coproheme into heme *b*, the propionate groups in positions 2 and 4 are decarboxylated into vinyl groups, leaving only the propionate in position 6 and 7 (**Figure 4.26** and **Table 4.6**). At room temperature, in the WT protein spectrum the two bands at 377 and 394  $\text{cm}^{-1}$  are due to the  $[\delta(\text{C}_\beta\text{C}_c\text{C}_d)]$  propionate bending modes and the broad band centred at 418  $\text{cm}^{-1}$  to the two overlapped  $[\delta(\text{C}_\beta\text{C}_a\text{C}_b)]$  vinyl bending modes. The presence of two vinyl bending modes, collapsed in one large band, is confirmed by the presence in the high frequency region of the RR spectra at 298 K of two vinyl stretching modes at 1621 and 1632  $\text{cm}^{-1}$  (**Figure 4.20**).

As compared to the coproheme-WT complex, the p6 frequency is 4  $\text{cm}^{-1}$  upshifted, maybe reflecting an increase of the H-bond network strength, while the p7 frequency is unchanged. Accordingly, as previously observed for the coproheme-WT complex, the temperature lowering does not affect the frequency of p6, that remains at 378  $\text{cm}^{-1}$ , while causes about 7  $\text{cm}^{-1}$  upshift of the p7 band (from 392 to 399  $\text{cm}^{-1}$ ).

**Figure 4.29** compares the heme *b* RR spectra of WT (see also **Table 4.6**) and selected mutants obtained at 298 (**left**) and 80 K (**right**).

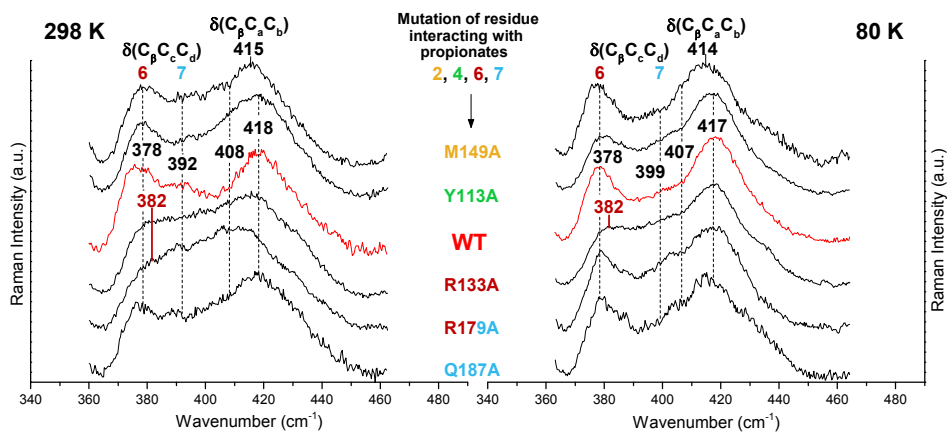


**Figure 4.29.** Comparison of the RR spectra in the low frequency region of the heme *b*-LmChdC complexes of the WT and mutants obtained at 298 K (Left) and 80 K (Right) (both  $\lambda_{\text{exc}}$  413.1 nm). The bands tentatively assigned to the bending mode  $\delta(\text{C}_\beta\text{C}_\alpha\text{C}_d)$  of the propionate groups in position **6** and **7** are reported in **brown** and **light blue**, respectively. Accordingly, the mutants label colour, **beige**, **green**, **brown** and **light blue**, indicate the position **2**, **4**, **6**, and **7**, respectively, of the propionate group/s with which the mutated residues interact. The bending mode  $\delta(\text{C}_\beta\text{C}_\alpha\text{C}_b)$  of the vinyl groups are also shown. The spectra of the heme *b*-WT complex are reported in **red**. The spectra have been shifted along the ordinate axis to allow better visualization. Experimental conditions: (298 K) laser power at the sample 5-10 mW, average of 13 spectra with a 130 min integration time (Q187A); average of 10 spectra with a 200 min integration time (R179A); average of 9 spectra with a 180 min integration time (R133A); average of 4 spectra with 40 min integration time (WT); average of 4 spectra with a 80 min integration time (Y113A); average of 12 spectra with a 120 min integration time (M149A). (80 K) laser power at the sample 10 mW, average of 9 spectra with a 180 min integration time (Q187A, R179A and Y113A); average of 10 spectra with a 200 min integration time (R133A); average of 16 spectra with 320 min integration time (WT); average of 6 spectra with a 120 min integration time (M149A).

As expected, the spectrum of the heme *b*-M149A complex is almost identical to that of the WT as concerned the propionate bands, while the

vinyl bending modes are centred at 415 cm<sup>-1</sup>, 3 cm<sup>-1</sup> downshifted as compared to the WT. In the heme *b*-R179A and -R133A spectra an upshift of 4 cm<sup>-1</sup> of the p6 band from 378 (WT) to 382 cm<sup>-1</sup> is observed, similarly to the coproheme-R179A complex (where the band upshifts of 3 cm<sup>-1</sup>, from 374 (WT) to 377 cm<sup>-1</sup>). A clear shift of 4 cm<sup>-1</sup> of the p6 band from 378 (WT) to 382 cm<sup>-1</sup>, is observed in the heme *b*-R133A mutant, while no change in the frequency of p7 could be monitored since this weak band is partially covered by the intense vinyl bending modes. At low temperature the vinyl bending modes are clearly observed at 407 and 414 cm<sup>-1</sup>. Unfortunately, due to the very high fluorescence background we were unable to collect the RR spectra in the high frequency region at 80 K, but the stretching modes at 1621 and 1632 cm<sup>-1</sup> observed in RR spectra at 298 K (**Figure 4.20**) are consistent with the bending modes at 407 and 417 cm<sup>-1</sup>, respectively [Smulevich 1996, Marzocchi 2003].

**Table 4.6.** Frequency (cm<sup>-1</sup>) of the propionate [ $\delta(C_{\beta}C_cC_d)$ ] and vinyl [ $\delta(C_{\beta}C_aC_b)$ ] bending modes of the coproheme- and heme *b*-WT complexes both at 298 and 80 K.

	Coproheme		Heme <i>b</i>	
	298 K	80 K	298 K	80 K
<b>p6</b>	374	374	378	378
<b>p4</b>	381	383		
<b>p2</b>	389	389		
<b>p7</b>	392	399	392	399
<b>vinyls</b>	-	-	408, 418	407, 417

#### 4.7 Titration of the coproheme-M149A complex with H<sub>2</sub>O<sub>2</sub>

With the aim of separating the decrease/increase of the propionate/vinyl bending modes upon decarboxylation to get deeper inside the catalytic mechanism, I followed the conversion of coproheme into heme *b* titrating the coproheme-M149A complex with hydrogen peroxide. I performed the titration on this mutant because the coproheme-M149A complex is much less fluorescent than that of the WT, allowing a better resolution of the propionate bands. Moreover, the heme *b*-M149A and -

WT complexes are identical in the propionate region, differing only for the center of the large vinyl band, as described.

**Figure 4.30** and **4.31** show the titration of the coproheme-M149A complex with hydrogen peroxide followed by UV-Vis (298 K) and RR (80 K) spectroscopies, respectively. In the beginning the addition of hydrogen peroxide causes the decrease of the 6cLS species of the coproheme complex, as indicated by the decrease of the Soret band at 406 nm in the second derivative spectrum and the blue shift of the maximum in the UV-Vis spectrum (**Figure 4.30, spectra a, b**).

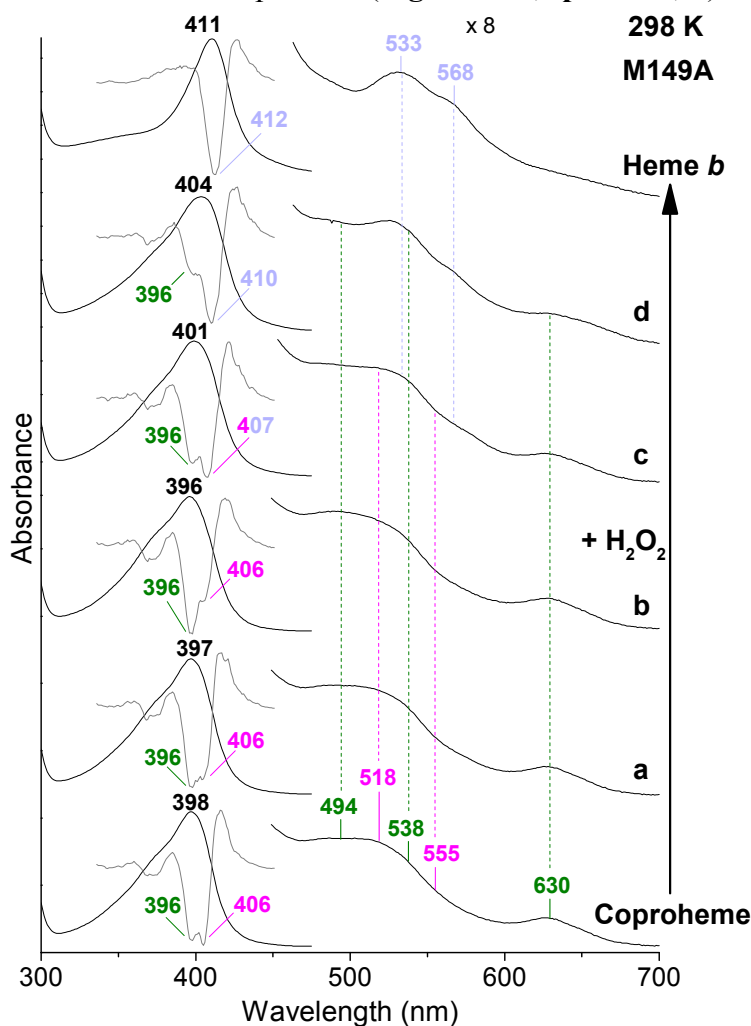


**Figure 4.30.** UV-vis absorption and second derivative ( $D^2$ ) spectra of the coproheme-M149A complex titrated at 298 K with hydrogen

peroxide until the complete conversion into the heme *b*-M149A complex. The band wavelengths assigned to the **5cQS**, **6cLS of the coproheme complex** and **6cLS of the heme *b* complex** are indicated in **olive green**, **magenta**, and **light violet** respectively. The spectra have been shifted along the ordinate axis to allow better visualization. The 450–700 nm region is expanded 8-fold.

In the **c spectrum** the 6cLS species of heme *b* complex appears as highlighted from the red shift of the maximum of the spectrum from 396 (**b spectrum**) to 401 nm. This species grows in to its final form (obtained for a 2:1 H<sub>2</sub>O<sub>2</sub>:protein molar ratio) characterized by a Soret band at 411 nm.

As previously discussed, a distinctive difference between the coproheme and heme *b* complexes is the p<sub>6</sub> band frequency which upshift from 374 cm<sup>-1</sup> (**Figure 4.31, coproheme complex**) to 378 (**Figure 4.31, heme *b* complex**) cm<sup>-1</sup>. The formation of the heme *b* band is clearly observed during the titration, since addition of hydrogen peroxide to the coproheme-M149A complex causes an increasing broadening at 378 cm<sup>-1</sup> (**Figure 4.31, spectra b-d**), with the concomitant decrease of the p<sub>2</sub> band at 393 cm<sup>-1</sup>. Conversely, the p<sub>7</sub> band at 399 cm<sup>-1</sup> does not change. Due to the upshift of the p<sub>6</sub>, it is impossible to follow the disappearance of p<sub>4</sub> band at 383 cm<sup>-1</sup>.

The formation of two vinyl bands at 407 and 414 cm<sup>-1</sup> is clearly observed. Despite the presence of the spurious band at 414 cm<sup>-1</sup> (due to the 6cLS species), it is likely that the first vinyl to be formed (**Figure 4.31, spectra a, b**) is that at 407 cm<sup>-1</sup>. Then (**Figure 4.31, spectrum c**), the second vinyl bending mode appears and becomes very intense in the spectrum of the final heme *b* complex.

Regarding the catalytic mechanism, the RR data cannot support the hypothesis that after the decarboxylation of the p<sub>2</sub>, the three-propionate mono-vinyl intermediate rotates of 90° in the protein cavity allowing the Tyr145 to decarboxylate p<sub>4</sub> [Streit 2018]. In fact, upon rotation variations in the intensity and position of the propionate bands should be observed. However, we must take into consideration that upon titration, both the hardoreheme intermediate and the heme *b* final product are formed, and, therefore, the broadening of the propionate

bands observed in the RR spectra upon titration, prevents any detailed frequency assignment.

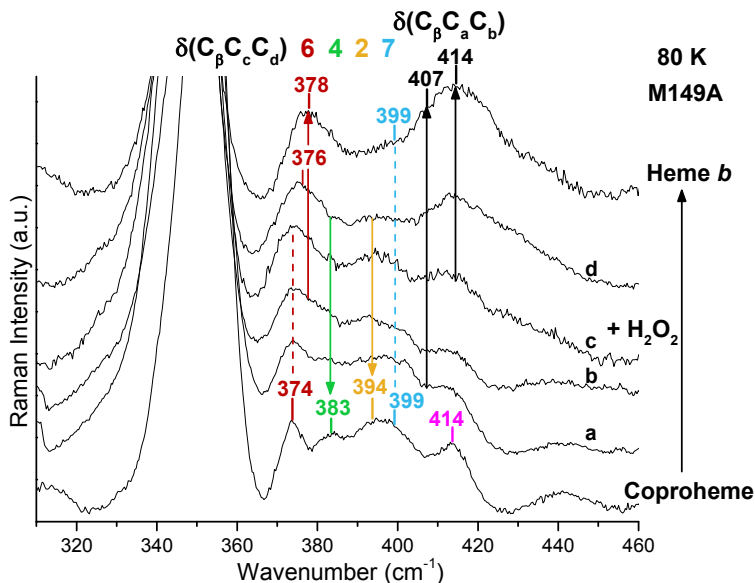


**Figure 4.31.** RR spectra in the low frequency region, obtained at 80 K ( $\lambda_{\text{exc}}$  413.1 nm), of the coproheme-M149A complex titrated with hydrogen peroxide until the complete conversion into the heme *b*-M149A complex. The bands tentatively assigned to the bending mode  $\delta(\text{C}_\beta\text{C}_c\text{C}_d)$  of the propionate groups in position 2, 4, 6 and 7 are reported in beige, green, brown and light blue, respectively. The bending modes  $\delta(\text{C}_\beta\text{C}_a\text{C}_b)$  of the vinyl groups are reported in black. In magenta is reported the band due to the 6cLS species. The spectra have been shifted along the ordinate axis to allow better visualization. Experimental conditions: laser power at the sample 10 mW, average of 6 spectra with a 120 min integration time (each spectrum).

#### 4.8 Conclusion

I have investigated the active site architecture of coproheme- and heme *b*-ChdC WT and selected variants from *Lm* using various spectroscopic techniques.

1. I have discovered that the native ferric form of coproheme-ChdC from *Lm* is a 5cQS species which is very unusual in biological systems.
2. The residues H-bonded with the propionate in position 2 and 4 are crucial to maintain the architecture and stability of the

protein: when mutated in the non H-bonding Ala, a 6cLS species with the Gln187 residue as distal ligand is formed. Moreover the data on the CO adducts show that the Met149 residue located near the p2 has an important role in keeping the Gln187 residue correctly positioned for the closure of the distal cavity.

3. The work on the mutants allowed me to obtain the assignment of the p2, p4, p6, and p7 propionate bending modes.
4. The UV-Vis (298 K) and RR (80 K) titration of coproheme-ChdC to heme *b*-ChdC allowed to follow the progressive disappearance/appearance of the p2/p4 and v2/v4 bands. The data suggest that the first vinyl to be formed is that at 407 cm<sup>-1</sup>. The second vinyl bending mode appears and becomes very intense only in the spectrum of the final heme *b* complex.

However, our data, due to the broadening of the propionate bands deriving from the overlapping contribution of the harderoheme and heme *b*, do not allow to confirm the hypothesis that after the decarboxylation of the p2, the three-propionate mono-vinyl intermediate rotates of 90° in the protein cavity.

## References

- ❖ Aasa R., Vännngard T., J. Magn. Reson. 1975, 19, 308.
- ❖ Battistuzzi G., Stampler J., Bellei M., Vlasits J., Soudi M., Furtmüller P.G., Obinger C., Biochemistry 2011, 50, 7987.
- ❖ Brautigan D.L., Feinberg B.A., Hoffman B.M., Margoliash E., Peisach, J., Blumberg W.E., J. Biol. Chem. 1977, 252, 574.
- ❖ Brogioni S., Stampler J., Furtmüller P.G., Feis A., Obinger C., Smulevich G., Biochim. Biophys. Acta, Proteins Proteomics 2008, 1784, 843.
- ❖ Celis A.I., Streit B.R., Moraski G.C., Kant R., Lash T.D., Lukat-Rodgers G.S., Rodgers K.R., DuBois J.L., Biochemistry 2015, 54, 4022.
- ❖ Celis A.I., Gauss G.H., Streit B.R., Shisler K., Moraski G.C., Rodgers K.R., Lukat-Rodgers G.S., Peters J.W., DuBois J.L., J. Am. Chem. Soc. 2017, 139, 1900.
- ❖ Cerda-Colón J.F., Silfa E., López-Garriga J., J. Am. Chem. Soc. 1998, 120, 9312.
- ❖ Choi S., Spiro T.G., Langry K.C., Smith K.M., Budd D.L., La Mar G.N., J. Am. Chem. Soc. 1982, 104, 4345.

- ❖ Dailey T.A., Boynton T.O., Albetel A.N., Gerdes S., Johnson M.K., Dailey H.A., *J. Biol. Chem.* 2010, 285, 25978.
- ❖ Dailey H.A., Gerdes S., Dailey T.A., Burch J.S., Phillips J.D., *Proc. Natl. Acad. Sci. U.S.A.* 2015, 112, 2210.
- ❖ Dailey H.A., Dailey T.A., Gerdes S., Jahn D., Jahn, M., O'Brian M R., Warren M.J., *Microbiol. Mol. Biol. Rev.*, 2017, 81, e00048.
- ❖ Evans S.V., Brayer G.D., *J. Mol. Biol.* 1990, 213, 885.
- ❖ Feis A., Tofani L., De Sanctis G., Coletta M., Smulevich G., *Biophys. J.* 2007, 92, 4078.
- ❖ Fiedler T.J., Davey C.A., Fenna R.E., *J. Biol. Chem.* 2000, 275, 11964.
- ❖ Hobbs C., Dailey H.A., Shepherd M., *Biochem. J.* 2016, 473, 3997.
- ❖ Hofbauer S., Hagmüller A., Schaffner I., Mlynek G., Krutzler M., Stadlmayr G., Pirker K.F., Obinger C., Daims H., Djinić-Carugo K., Furtmüller P.G. *Arch. Biochem. Biophys.* 2015, 574, 36.
- ❖ Hofbauer S., Dalla Sega M., Scheiblbrandner S., Jandova Z., Schaffner I., Mlynek G., Djinić-Carugo K., Battistuzzi G., Furtmüller P.G., Oostenbrink C., Obinger C., *Biochemistry* 2016, 55, 5398.
- ❖ Hofbauer S., Mlynek G., Milazzo L., Puhlinger D., Maresch D., Schaffner I., Furtmüller P.G., Smulevich G., Djinić-Carugo K., Obinger C., *FEBS J.* 2016, 283, 4386.
- ❖ Hough M.A., Andrew C.R., *Adv. Microb. Physiol.* 2015, 67, 1.
- ❖ Howes B.D., Feis A., Indiani C., Marzocchi M.P., Smulevich G., *J. Biol Inorg. Chem.* 2000, 5, 227.
- ❖ Howes B.D., Helbo S., Fago A., Smulevich G., *J. Inorg. Biochem.* 2012, 109, 1.
- ❖ Indiani C., Feis A., Howes B.D., Marzocchi M.P., Smulevich G., *J. Inorg. Biochem.* 2000, 79, 269.
- ❖ Kosugi N., Araki T., Fujita J., Tanaka S., Fujiwara, T., *PLoS One* 2017, 12, e0189913.
- ❖ Le P., Zhao J., Franzen S., *Biochemistry* 2014, 53, 6863.
- ❖ Magiorakos A.P., Srinivasan A., Carey R.B., Carmeli Y., Falagas M.E., Giske C.G., Harbarth S., Hindler J.F., Kahlmeter G., Olsson-Liljequist B., Paterson D.L., Rice L.B., Stelling J., Struelens M.J., Vatopoulos A., Weber J.T., Monnet D.L., *Clin. Microbiol. Infect.* 2012, 18, 268.
- ❖ Marzocchi M., Smulevich G., *J. Raman Spectrosc.* 2003, 34, 725.
- ❖ Mayfield J.A., Hammer N.D., Kurker R.C., Chen T.K., Ojha S., Skaar E.P., DuBois J.L., *J. Biol. Chem.* 2013, 288, 23488.

- ❖ Morikis D., Champion P., Springer B., Sligar S., *Biochemistry* 1989, 28, 4791.
- ❖ Nagao S., Ishikawa H., Yamada T., Mizutani Y., Hirota S., *J. Biol. Inorg. Chem.* 2015, 20, 523.
- ❖ Nielsen K.L., Indiani C., Henriksen A., Feis A., Becucci M., Gajhede M., Smulevich G., Welinder K.G., *Biochemistry* 2001, 40, 11013.
- ❖ Pfanzagl V., Holcik L., Maresch D., Gorgone G., Michlits H., Furtmüller P.G., Hofbauer S., *Arch. Biochem. Biophys.* 2018, 640, 27.
- ❖ Ray G., Li X., Ibers J., Sessler J., Spiro T.G., *J. Am. Chem. Soc.* 1994, 116, 162.
- ❖ Sheldon J.R., Heinrichs D.E., *FEMS Microbiol. Rev.* 2015, 39, 592.
- ❖ Shen J., Wang Y., Schwarz S., *J. Antimicrob. Chemother.* 2013, 68, 1697.
- ❖ Smulevich G., Mantini A.R., English A.M., Mauro J.M., *Biochemistry* 1989, 28, 5058.
- ❖ Smulevich G., Wang Y., Edwards S.L., Poulos T.L., English A.M., Spiro T.G., *Biochemistry* 1990, 29, 2586.
- ❖ Smulevich G., Mantini A.R., Paoli M., Coletta M., Geraci G., *Biochemistry* 1995, 34, 7507.
- ❖ Smulevich G., Hu S., Rodgers K.R., Goodin D.B., Smith K.M., Spiro T.G., *Biospectroscopy* 1996, 2, 365.
- ❖ Smulevich G., Feis A., Howes B.D., *Acc. Chem. Res.* 2005, 38, 433.
- ❖ Smulevich G., Howes B.D., Droghetti E., (2016) Structural and Functional Properties of Heme-containing Peroxidases: a Resonance Raman Perspective for the Superfamily of Plant, Fungal and Bacterial Peroxidases, In *Heme Peroxidases* (Raven, E., and Dunford, B., Eds.), pp 61–98, The Royal Society of Chemistry.
- ❖ Spiro T.G., Wasbotten I.H., *J. Inorg. Biochem.*, 2005, 99, 34.
- ❖ Streit B.R., Celis A.I., Shisler K., Rodgers K.R., Lukat-Rodgers G.S., DuBois J.L., *Biochemistry* 2017, 56, 189.
- ❖ Streit B.R., Celis A.I., Moraski G.C., Shisler K., Shepard E.M., Rodgers K.R., Lukat-Rodgers G.S., DuBois J.L., *J. Biol. Chem.* 2018, 293, 3989.
- ❖ Teale F.W., *Biochim. Biophys. Acta* 1959, 35, 543.
- ❖ Vogel K., Kozłowski P., Zgierski M., Spiro T., *Inorg. Chim. Acta* 2000, 297, 11.
- ❖ Walker F., *Coord. Chem. Rev.* 1999, 185, 471.
- ❖ Ye X., Yu A., Georgiev G.Y., Gruia F., Ionascu D., Cao W., Sage J.T., Champion P.M., *J. Am. Chem. Soc.* 2005, 127, 5854.

- ❖ Zámocký M., Hofbauer S., Schaffner I., Gasselhber B., Nicolussi A., Soudi M., Pirker K.F., Furtmüller P.G., Obinger C., Arch. Biochem. Biophys. 2015, 574, 108.
- ❖ Zederbauer M., Furtmüller P.G., Ganster B., Moguilevsky N., Obinger C., Biochem. Biophys. Res. Commun. 2007, 356, 450.

## Chapter 5

### **Resonance Raman to prove the lack of orientation selectivity of the heme insertion in murine Neuroglobin**

Cécile Exertier, **Lisa Milazzo**, Ida Freda, Linda Celeste Montemiglio, Antonella Scaglione, Gabriele Cerutti, Giacomo Parisi, Massimiliano Anselmi, Giulietta Smulevich, Carmelinda Savino, Beatrice Vallone, “Proximal and distal control for ligand binding in neuroglobin: role of the CD loop and evidence for His64 gating”, *Scientific Reports*, **2018**, under revision.

**Lisa Milazzo**, Cécile Exertier, Ida Freda, Maurizio Becucci, Beatrice Vallone, Giulietta Smulevich, “Lack of orientation selectivity of the heme insertion in murine Neuroglobin evidenced by resonance Raman spectroscopy”, *in preparation*.

#### **5.1 Introduction**

Neuroglobin (Ngb) is one of the lately discovered globins and has been characterized as a phylogenetically ancient representative of this superfamily of proteins, present in both vertebrates and invertebrates [Burmester 2000].

It consists of a single polypeptide chain of 151 amino acids disposed in 8 helices named from A to H (the so-called 3-on-3  $\alpha$ -helical sandwich [Holm 1993]), having only a small sequence similarity with the vertebrate globins Myoglobin (Mb) (21%) and Hemoglobin (Hb) (25%). Nevertheless, all key determinants of globins [Bashford 1987] are conserved: a proximal histidine residue His96(F8) links the polypeptide chain to the heme iron, a distal histidine residue His64(E7) resides close

to the binding site of the diatomic ligand, and a phenylalanine residue Phe42(CD1) is involved in  $\pi$ - $\pi$  stacking interactions with the heme [Pesce 2003, Vallone 2004].

Unlike Mb and Hb which are phylogenetically less ancient than Ngb and display a His residue and a water molecule as axial ligand (6cHS aquo), the crystal structures and RR spectra of the Ngbs from different organisms (murine [Vallone 2004, Coture 2001], human [Pesce 2003], Antarctic fishes [Giordano 2012]), show that in the ferric and ferrous forms, in the absence of an exogenous ligand, both the proximal and the distal ligands are His residues (6cLS, bis-His conformation). The current hypothesis is that hexacoordination could be the oldest coordination scheme, furthermore the bis-His ligation has been proposed to play a role in gas sensing [Dewilde 2001].

Moreover, in agreement with solution NMR data [Du 2003] that reported a heme orientational disorder with a 2:1 predominance of the inverted geometry, the crystal structure of the ferric form of murine Ngb WT highlights the presence of two conformer with different heme insertion [Vallone 2004] (**Figure 5.1**):

- the main conformer (70% occupancy), shows a heme orientation 180° rotated with respect to the  $\alpha$ - $\gamma$  meso axis as compared with the heme insertion in sperm whale (SW) Mb, and was therefore defined reversed or A;
- the minor conformer (30% occupancy), shows the same heme orientation as in SW Mb, and was therefore defined canonical or B.

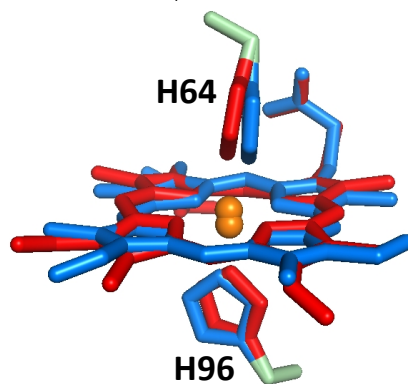


**Figure 5.1.** Double heme intersection of the ferric WT Ngb (1Q1F [Vallone 2004]): the A (reversed) and B (canonical) conformers are

shown in red and blue, respectively, together with the proximal (96) and distal (64) His residues. The figure was made with: The PyMOL Molecular Graphics System, Version 1.7.5.0 Schrödinger, LLC.

Ngb is predominantly expressed in neurons of the central and peripheral nervous systems [Fabrizius 2016] and it clearly seems to be involved in neuroprotection [Raida 2013, Raida 2012]. It has been shown that Ngb is overexpressed in hypoxic conditions and it may be involved in gas/redox sensing, radical scavenging, and/or signal transducing [Watanabe 2008, Taylor 2014, Tiwari 2015, Baez 2016, Wang 2017]. However, its exact mechanism of action still remains to be clarified. Like a majority of heme proteins, Ngb function is likely related to its ability to reversibly bind diatomic gases, such as O<sub>2</sub>, NO and CO. Notably, hexacoordination in Ngb is responsible for a peculiar structural rearrangement and complex kinetics upon ligand binding [Dewilde 2001, Kiger 2004, Kriegl 2002, Abbruzzetti 2009, Smagghe 2006, Trent 2001, Fago 2004, Hamdane 2003, Nienhaus 2005, Trent 2002], which is achieved when the distal histidine (His(E7)64), engaged in internal hexacoordination of the iron, dissociates from the heme. The dissociation of the distal histidine is the rate-limiting step for ligand binding and structurally it gives rise to the sliding of the heme more deeply (iron displacement of 2 Å) into a large internal cavity, associated with the concomitant motion of helices and loops [Vallone 2004 PNAS, Moschetti 2009], probably conferring a more stable conformation. Artificial mutants of Ngb have been utilized to highlight major structure determinants regulating ligand binding. In particular:

- heme pocket mutants M144W, and F106W show slow CO binding due to mutated residues hampering the heme sliding, affecting both binding velocity and affinity [Avella 2014];
- by swapping the CD corners of human Ngb and SWMb from one protein to the other, it has been demonstrated that SWMb gains the bis-His axial coordination typical of Ngb, meaning that the CD corner sequence and structure are involved in the fine tuning of iron coordination [Boron 2015].

Moreover, engineer Ngb to observe structural and dynamic alterations associated with perturbation in ligand binding could shed light on key features potentially related to its mechanism of action.

To probe the role of heme sliding in the internal cavity, facilitated by reducing the hindrance in position 106 and the role of the CD-loop in governing ligand affinity and hexacoordination, we studied the ferrous-CO adducts of both the WT [Vallone 2004 PNAS] and the following mutants: F106A, a CD loop mutant with enhanced flexibility (Gly-loop, see paragraph 5.2 and **Figure 5.2** for more details) and the double Gly-loop/F106A. The RR data support the crystallographic results obtained by Professor Beatrice Vallone's group (La Sapienza University, Rome).

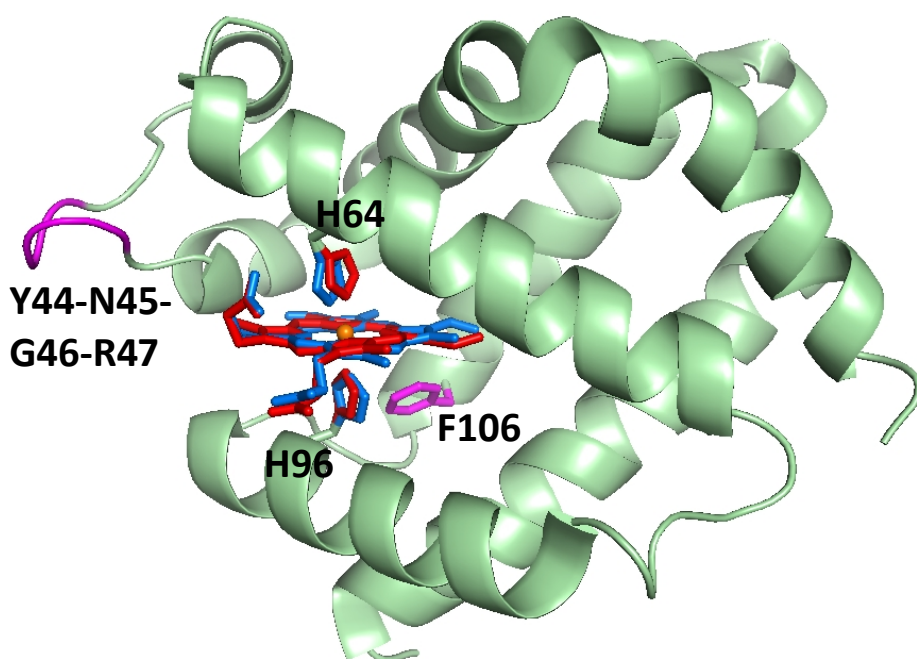


**Figure 5.2.** Ribbon diagram of WT Ngb (1Q1F [Vallone 2004]). This figure highlights the double heme insertion (the reversed and canonical conformers are reported in red and blue, respectively), the proximal (96) and distal (64) His ligands and in magenta the mutated residue (Phe106 and the in the CD-loop the Tyr44-Asn45-Gly46-Arg47 fragment). The figure was made with: The PyMOL Molecular Graphics System, Version 1.7.5.0 Schrödinger, LLC.

However, I obtained the most interesting RR result, studying the ferric (and ferrous) form of the WT and mutant proteins. In fact, in agreement with the crystal structure [Vallone 2004], the high frequency RR spectra show a double set of core size marker bands, suggesting the presence of two 6cLS species, one for each conformer, canonical and reversed. This is the first time that a reversed heme insertion is identified with RR in a native protein, since the only previous works described a reversed heme insertion in a Mb model compound (pure 6cHS) [Rwere 2007, Rwere 2008, Rwere 2014]. A careful analysis of the ferric (and ferrous) form of the RR spectra were performed to find the marker bands of the reversed conformer, useful to identify this less common insertion.

## 5.2 Materials

Cloning, expression and purification of the recombinant murine Ngbs WT and mutant proteins (**Figure 5.2**)

- F106A (Phe106Ala),
  - Gly-loop (Tyr44Gly/Asn45Gly/Gly46/Arg47Gly that forms a GGGG fragment, called Gly-loop),
  - Gly-loop/F106A (Tyr44Gly/Asn45Gly/Gly46/Arg47Gly/Phe106Ala)
- were performed by Professor Beatrice Vallone's group (La Sapienza University, Rome).

All the samples were in 100 mM Hepes pH 7.4. The ferrous samples were prepared by addition of 2–3  $\mu\text{L}$  of a freshly prepared sodium dithionite solution (20 mg/mL) to the ferric forms (40 $\mu\text{L}$ ) previously flushed with nitrogen. The ferrous-CO adducts were prepared by flushing the ferric forms (40 $\mu\text{L}$ ) with  $^{12}\text{CO}$  or  $^{13}\text{CO}$  (Rivoira, Milan, Italy), and then reducing the heme by addition of 2–3  $\mu\text{L}$  of a freshly prepared sodium dithionite solution (20 mg/mL). Protein concentration in the range 40–150  $\mu\text{M}$  was used for electronic absorption and RR spectroscopies at room temperature. The protein concentration was estimated on the basis of the extinction coefficient of the ferric form at 532 nm, = 10700  $\text{M}^{-1} \text{cm}^{-1}$ (1) [Fago 2004].

## 5.3 Ferric form

### 5.3.1 The WT and the double Gly-loop/F106A mutant

The Soret band at 413/411 and the Q bands at 533 and 562 nm in the UV-Vis absorption spectra of the WT and Gly-loop/F106A mutant (**Figure 5.3**), typical of a 6cLS His-Fe-His species [Smulevich 1991], are similar to those of other Ngbs [Dewilde 2001, Giordano 2012].

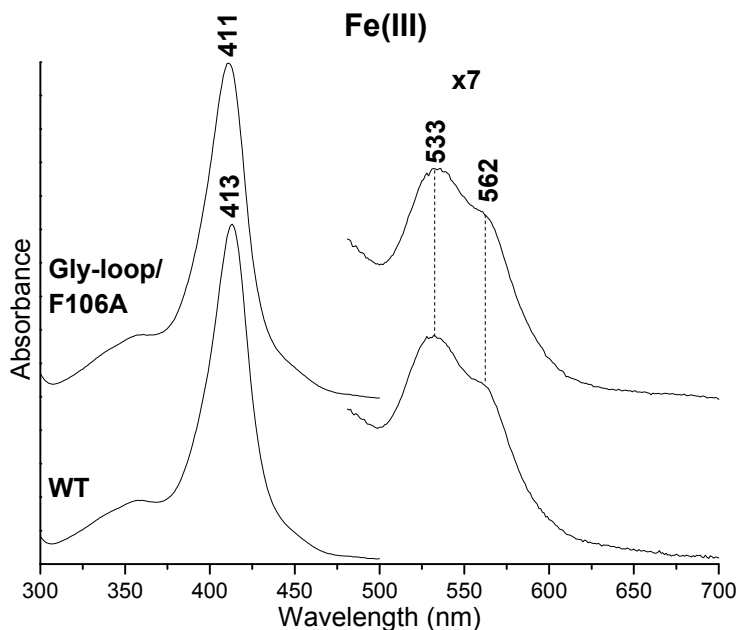


**Figure 5.3.** UV-Vis absorption spectra of WT (bottom) and Gly-loop/F106A mutant (top) Ngbs. The spectra have been shifted along the ordinate axis to allow better visualization. The 480–700 nm region is expanded 7-fold.

In agreement with the UV-Vis spectra the frequencies of the RR core size marker bands ( $\nu_4$ ,  $\nu_3$ ,  $\nu_2$ ,  $\nu_{10}$  at ca. 1374, 1506, 1580 and 1638  $\text{cm}^{-1}$ , respectively) (**Figure 5.4**) confirm the presence of a 6cLS species. However, in the WT spectrum the  $\nu_3$  mode shows the coexistence of two bands, at 1506  $\text{cm}^{-1}$  and 1500  $\text{cm}^{-1}$ , this latter being a shoulder gaining intensity in the double mutant spectrum.

Accordingly, also the  $\nu_2$  and  $\nu_{10}$  bands of the Gly-loop/F106A mutant are shifted towards lower frequencies (at 1576 and 1637  $\text{cm}^{-1}$ , respectively) with respect to those of the WT (at 1578 and 1639  $\text{cm}^{-1}$ , respectively).

On the basis of the inverse correlation between the RR band frequencies and the porphyrin core size [Hoard 1973, Spaulding 1975, Choi 1982, Sparks 1994], the data suggest the presence of two 6cLS species with different core size.

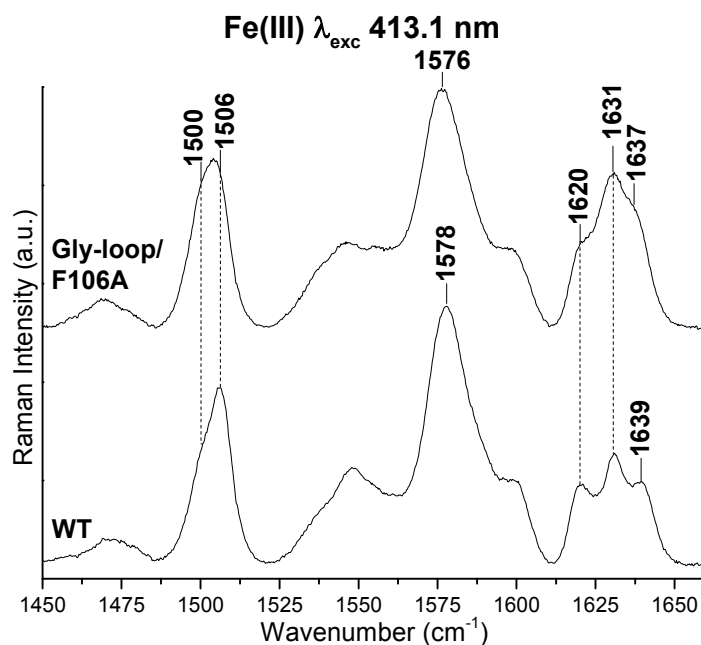


**Figure 5.4. High frequency region RR spectra of WT (bottom) and Gly-loop/F106A mutant (top) Ngbs.** The spectra have been shifted along the ordinate axis to allow better visualization. Experimental conditions: 413.1 nm excitation wavelength, laser power at the sample 10 mW; average of 21 spectra with 210 min integration time (WT), average of 22 spectra with 220 min integration time (Gly-loop/F106A). The intensities of the RR spectra are normalized to that of the  $\nu_4$  band (not shown).

For a better understanding of the vinyl/ $\nu_{10}$  region ( $1600\text{-}1650\text{ cm}^{-1}$ ) of both the WT and Gly-loop/F106A mutant, RR spectra using two different excitation wavelengths, at 413.1 and at 514.5 nm, in resonance with the Soret and Q bands, respectively, have been obtained. This allowed a correct assignment of the overlapped  $\nu(\text{C}=\text{C})$  stretching modes and the  $\nu_{10}$  core size, selectively intensified with the violet and green laser line, respectively. In fact, upon Soret excitation ( $\lambda_{\text{exc}}$  at 413.1 nm), the RR spectrum is characterized by strong bands due to  $A_{1g}$

modes ( $\nu_4$ ,  $\nu_3$ , and  $\nu_2$ ), weak bands due to Jahn-Teller active  $B_{1g}$  ( $\nu_{10}$  and  $\nu_{11}$ ) and  $B_{2g}$  ( $\nu_{28}$  and  $\nu_{29}$ ) modes, and  $\nu(\text{C}=\text{C})$  stretching modes of the vinyl substituents.  $E_u$  modes ( $\nu_{37}$  and  $\nu_{38}$ , IR active) are also weakly activated in the RR spectra of protoporphyrin IX due to the conjugation of the asymmetrically disposed vinyl substituents with the porphyrin system. Conversely, in the spectra obtained upon Q excitation ( $\lambda_{\text{exc}}$  at 514.5 nm), the  $B_{1g}$ ,  $B_{2g}$  and  $A_{2g}$  modes become predominantly enhanced, while the  $\nu(\text{C}=\text{C})$  stretching modes of the two vinyl substituents are absent or very weak.

Moreover, for both the excitation wavelengths, I also obtained spectra in polarized light (parallel // and perpendicular  $\perp$ ) with the aim to distinguish the contribution of the polarized ( $A_{1g}$  modes and  $\nu(\text{C}=\text{C})$  stretching modes, with theoretical depolarization ratio,  $\rho_{\perp//} = 1/8$ ), depolarized ( $B_{1g}$  and  $B_{2g}$ , with theoretical depolarization ratio  $\rho_{\perp//} = 3/4$ ) and anomalously polarized ( $A_{2g}$  with theoretical depolarization ratio  $\rho_{\perp//} > 3/4$ ) bands.

The spectra obtained with the two excitation wavelengths and in polarized light (**Figure 5.5**) allow to:

- clearly observe two  $\nu_{10}$  bands at 1635, and 1639  $\text{cm}^{-1}$ , the band at 1635  $\text{cm}^{-1}$  gaining intensity in the double mutant spectra,
- assign the bands at 1620 and 1631  $\text{cm}^{-1}$  to the  $\nu(\text{C}=\text{C})$  vinyl stretching modes. In fact, these bands lose intensity with  $\lambda_{\text{exc}}$  514.5 nm (as expected) and are polarized in the spectra taken with the  $\lambda_{\text{exc}}$  413.1 nm (experimental  $\rho_{\perp//} = 1/4$  vs theoretical  $\rho_{\perp//} = 1/8$ ).

The complete assignment of the high frequency region RR spectra of the ferric WT and Gly-loop/F106A mutant is reported in **Figure 5.6**.

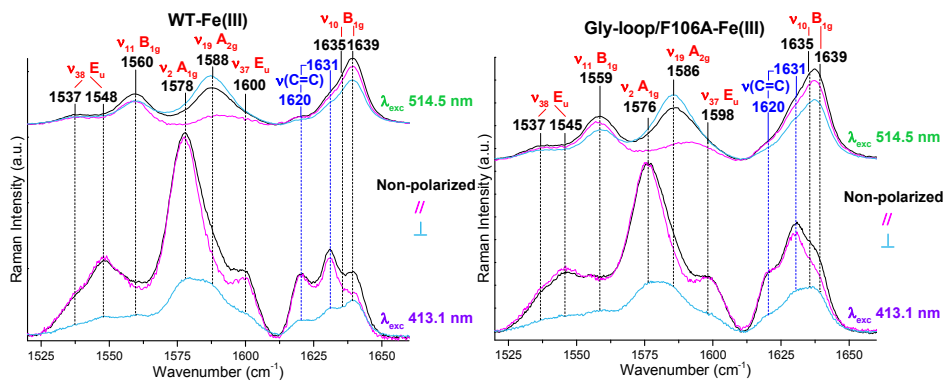


**Figure 5.5.** High frequency RR spectra ( in the  $\nu_2 - \nu_{10}$  region) of WT (Panel A) and Gly-loop/F106A mutant (Panel B) Ngbs, obtained with the 413.1 (bottom) and 514.5 nm (top) excitation wavelengths. Non-polarized (black traces), parallel polarized (magenta traces) and perpendicularly polarized (light blue traces) are reported. The spectra have been shifted along the ordinate axis to allow better visualization. The assignment of the bands is reported in red. WT experimental conditions: 413.1 nm excitation wavelength, laser power at the sample 10 mW; average of 21 spectra with 210 min integration time (non-polarized), average of 4 spectra with 40 min integration time (parallel polarized) and average of 13 spectra with 130 min integration time (perpendicularly polarized); 514.5 nm excitation wavelength, laser power at the sample 70 mW; average of 6 spectra with 30 min integration time (non-polarized), average of 3 spectra with 30 min integration time (parallel polarized) and average of 6 spectra with 60 min integration time (perpendicularly polarized). Gly-loop/F106A mutant experimental conditions: 413.1 nm excitation wavelength, laser power at the sample 10 mW; average of 22 spectra with 220 min integration time (non-polarized), average of 6 spectra with 60 min integration time (parallel polarized) and average of 12 spectra with 120 min integration time (perpendicularly polarized); 514.5 nm excitation wavelength, laser power at the sample 70 mW; average of 3 spectra with 30 min integration time (non-polarized), average of 4 spectra with 40 min integration time (parallel polarized) and average of 8 spectra with 80 min integration time (perpendicularly polarized).

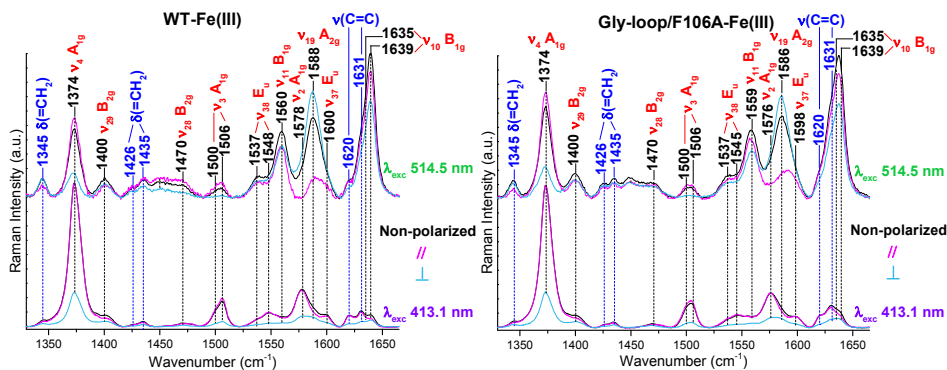


**Figure 5.6.** Non-polarized (black traces), parallel polarized (pink traces) and perpendicularly polarized (light blue traces) high frequency region RR spectra of WT (Panel A) and Gly-loop/F106A mutant (Panel B) Ngbs, obtained with the 413.1 (bottom) and 514.5 nm (top) excitation wavelengths. The spectra have been shifted along the ordinate axis to allow better visualization. The assignment of the bands is reported in red. The experimental conditions are reported in Figure 5.5.

The RR spectra in the LF region are typical of a 6cLS heme [Smulevich 1996] and confirmed the presence of two species with a different heme orientation (**Figure 5.7**), showing three vinyl bending modes  $\delta(C_{\beta}C_{\alpha}C_{\beta})$  at 404, 416, and 428  $\text{cm}^{-1}$ , instead of the usual two bands (one for each vinyl group). Their relative intensity vary in the WT and double mutant, the  $\delta(C_{\beta}C_{\alpha}C_{\beta})$  modes at 404 and 416  $\text{cm}^{-1}$  gaining intensity in the Gly-loop/F106A mutant spectrum.

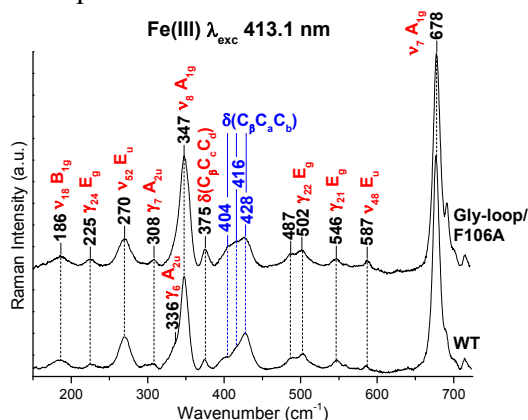


**Figure 5.7.** Low frequency region RR spectra of WT (bottom) and B/F106A mutant (top) Ngbs. The spectra have been shifted along the ordinate axis to allow better visualization. The assignment of the bands

is reported in red. Experimental conditions: 413.1 nm excitation wavelength, laser power at the sample 5 mW; average of 6 spectra with 60 min integration time (WT), average of 6 spectra with 60 min integration time (Gly-loop/F106A). The intensities of the RR spectra are normalized to that of the  $\nu_7$  band.

Summarizing, the two 6cLS species are characterized by different core size which result in different RR band frequencies:

- one species has a smaller core size with the  $\nu_3$ ,  $\nu_2$ ,  $\nu_{10}$ , bands at 1506, 1578 and 1639  $\text{cm}^{-1}$ , respectively,
- the other species has a bigger core size with the  $\nu_3$ ,  $\nu_2$ ,  $\nu_{10}$ , bands at 1500, 1576 and 1635  $\text{cm}^{-1}$ , respectively.

These results agrees perfectly with the crystal structure of the WT [Vallone 2004], where two different His96(proximal)-Fe-His64(distal) conformers rotated relative to each other of  $180^\circ$  with respect to the heme  $\alpha$ - $\gamma$  meso axis, called A (reversed, 70%) and B (canonical, 30%) have been identified. In the two conformers the His96-Fe-His64 angle is different, being planar ( $177.3^\circ$ , with a 0.20 Å out-of-plane displacement of the heme iron in the distal direction) for the reversed form and distorted ( $156.0^\circ$ , with a 0.27 Å out-of-plane displacement of the heme iron in the proximal direction) for the canonical form.

Therefore, since a planar heme configuration is expected to have a smaller core size with respect to a distorted heme configuration, the species with a smaller core ( $\nu_3$ ,  $\nu_2$ ,  $\nu_{10}$ , bands at 1506, 1578 and 1639  $\text{cm}^{-1}$ , respectively) was assigned to the planar, reversed A conformer and that with a bigger core ( $\nu_3$ ,  $\nu_2$ ,  $\nu_{10}$ , bands at 1500, 1576 and 1635  $\text{cm}^{-1}$ , respectively) was assigned to the distorted canonical B conformer, this latter increasing in the double mutant at the expense of the A form.

Another marker of the heme orientation could be the bands of the vinyl substituents since substantial changes in the disposition of the peripheral vinyl groups are expected to give rise to marked spectral changes in the RR spectra. In principle, in the Ngb WT, the reversed (A, 70%) and the canonical (B, 30%) conformers, should give rise each to two vinyl stretching and two vinyl bending modes. The presence of three bending

and only two stretching modes clearly suggests that the vinyl vibrations may overlap.

To get deeper inside, I measured (1Q1F [Vallone 2004]) the vinyl torsion angles ( $\tau$ ), formed between the  $C_a=C_b$  vinyl double bonds and the  $C_\alpha=C_\beta$  of the pyrrole (**Figure 2.7**, see Chapter 2), which express the vinyl orientation with respect to the porphyrin plane and are correlated with the vinyl stretching frequencies [Marzocchi 2003]. In fact the  $\nu(C=C)$  stretching mode frequency down-shifts with the increase of conjugation between the vinyl double bonds and the porphyrin aromatic macrocycle, this latter depending on the vinyl orientation in the following order: *trans* (high conjugation; lower frequency) > *twist* > *cis* (low conjugation; higher frequency).

On the contrary, no clear correlation has been found between the vinyl bending mode  $\delta(C_\beta C_a C_b)$  frequencies and the vinyl orientation. A certain association between the bending frequency with the vinyl groups in position 2 or 4 can be made only by selective isotopic labeling of specific vinyl atoms. However, it is generally accepted that:

- a lower frequency of the vinyl bending mode is associated with a higher degree of conjugation between the vinyl and the pyrrole (and so to a lower frequency of the respective stretching mode),
- a higher frequency of the vinyl bending mode is associated with a less conjugated configuration (and so to a higher frequency of the respective stretching mode).

Based on the previous considerations and on the torsional angles, the vinyl bands of the canonical B conformer of murine Ngb WT are assigned as follows (**Table 5.1**):

- vinyl in position 2 ( $\tau = 23.3^\circ$ , *cis*): bands at  $1631\text{ cm}^{-1}$  (stretching) and  $416\text{ cm}^{-1}$  (bending);
- vinyl in position 4 ( $\tau = -173.6^\circ$ , *trans*): bands at  $1620\text{ cm}^{-1}$  (stretching) and  $404\text{ cm}^{-1}$  (bending).

This assignment is in agreement with Cytochrome *c* peroxidase (CCP) D235N mutant at pH 8.5 (a pure 6cLS His-Fe-His), which contains only a canonical heme insertion and shows two  $\nu(C=C)$  vinyl stretching modes at  $1619$  and  $1628\text{ cm}^{-1}$  and two vinyl bending modes  $\delta(C_\beta C_a C_b)$  at  $406$  and  $418\text{ cm}^{-1}$  [Smulevich 1988, Smulevich 1996].

Both the vinyl groups of the reversed A conformer of the Ngb WT, instead, are in the *cis* conformation [ $\tau(2\text{-vinyl}) = 32.1^\circ$  and  $\tau(4\text{-vinyl}) = 27.4^\circ$ ], therefore, their  $\nu(\text{C}=\text{C})$  stretching modes overlap at  $1631\text{ cm}^{-1}$ , being the corresponding bending vibration assigned to the band at  $428\text{ cm}^{-1}$ .

In conclusion, only the 4-vinyl group appears to be markedly affected by the heme flipping, changing from the *trans* (canonical conformer) to the *cis* (reversed conformer) conformation. This is in agreement with the results obtained for the reversed form of Mb [Rwere 2014] where the conformation of the 2-vinyl remains unchanged with respect to the canonical conformer, while the 4-vinyl group changes from the *trans* (native) to the *cis* (reversed) conformation (**Table 5.1**).

**Table 5.1.** Vinyl orientations (*cis* and *trans*), torsion angle ( $\tau$ ) and the corresponding RR stretching and bending frequencies of the A and B conformer of murine Ngb WT, together with the native [Marzocchi 2003] and reversed [Rwere 2014] conformer of Mb (for comparison).

Ferric WT	Ngb-Conf. A Reversed		Ngb-Conf. B Canonical		Mb Reversed		Mb Native	
	2	4	2	4	2	4	2	4
<b>Conformation</b>	<i>cis</i>	<b><i>cis</i></b>	<i>cis</i>	<b><i>trans</i></b>	<i>trans</i>	<b><i>cis</i></b>	<i>trans</i>	<b><i>trans</i></b>
$\tau$ ( $^\circ$ )	32.05	27.39	23.34	-173.6		40-75	-97.8	-134.0
$\nu(\text{C}=\text{C})$ ( $\text{cm}^{-1}$ )	1631	<b>1631</b>	1631	<b>1620</b>	1620	<b>1630</b>	1620	<b>1620</b>
$\delta(\text{C}_\beta\text{C}_a\text{C}_b)$ ( $\text{cm}^{-1}$ )	428	<b>428</b>	416	<b>404</b>	422	<b>439</b>	439	<b>408</b>

This conclusion, however, is only partially confirmed by the comparison between the Ngb WT and double mutant. In fact, according to RR core size bands, in the double mutant the canonical conformer B slightly increases at the expense of the reversed conformer A. Accordingly, in the low frequency region the  $\delta(\text{C}_\beta\text{C}_a\text{C}_b)$  bending mode at  $416\text{ cm}^{-1}$  (B conformer) increases at the expense of the band at  $428\text{ cm}^{-1}$  (A conformer). However, in the high frequency region the RR spectrum of the mutant is characterized by an intensity increase of the band at  $1631\text{ cm}^{-1}$ . In any case, it is difficult to predict how the relative intensities of the bands of the vinyl groups should vary in the A and B conformers.

### 5.2.2 Comparison with the single Gly-loop and F106A mutants

Also the single F106A and Gly-loop mutants are a mixture of the A and B conformers, being their UV-Vis (**Figure 5.8**) and RR spectra (**Figure 5.9**) very similar to those of the WT and double Gly-loop/F106A mutant. The RR spectra of the single mutants upon Soret excitation shows a small intensity increase of the B conformer ( $\nu_3$  and  $\nu_{10}$  bands at  $1500\text{ cm}^{-1}$  and  $1635\text{ cm}^{-1}$ , respectively). However, with the 514.5 nm excitation wavelength, the frequency of the  $\nu_{10}$  band clearly downshifts in the order: WT, F106A, Gly-loop, and Gly-loop/F106A double mutant which still remains the one with the higher amount of B conformer.

The  $\nu(\text{C}=\text{C})$  stretching at  $1620\text{ cm}^{-1}$  maintain a similar intensity in all the proteins and the intensity of the band at  $1631\text{ cm}^{-1}$  slightly increases in the F106A and Gly-loop mutants as compared to the WT; the  $\delta(\text{C}_\beta\text{C}_\alpha\text{C}_\beta)$  bending modes at  $404\text{ cm}^{-1}$  and  $416\text{ cm}^{-1}$  slightly increases only in the Gly-loop/F106A, while the  $\delta(\text{C}_\beta\text{C}_\alpha\text{C}_\beta)$  bending mode at  $428\text{ cm}^{-1}$  decreases in the Gly-loop mutant, being the less intense in the double Gly-loop/F106A and, unexpectedly, in the F106A mutant.

Altogether these data indicate that the B form increases in the order: WT, F106A, Gly-loop, and Gly-loop/F106A double mutant which is the one with the higher amount of B conformer.

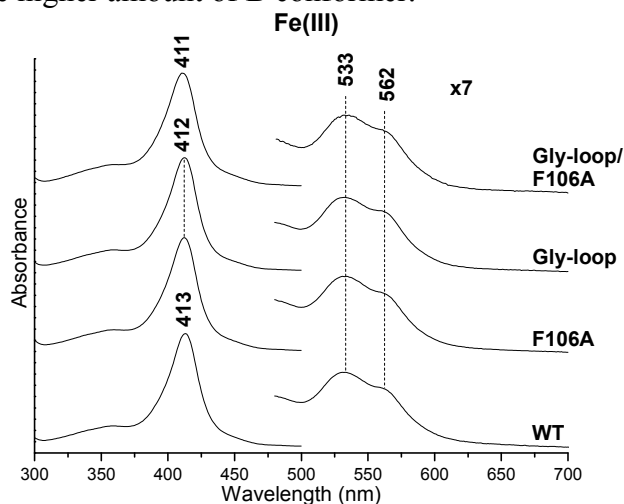


**Figure 5.8.** UV-Vis absorption spectra, from the bottom to the top, of WT, F106A, Gly-loop, and Gly-loop/F106A mutants Ngbs. The spectra have been shifted along the ordinate axis to allow better visualization. The 480–700 nm region is expanded 7-fold.

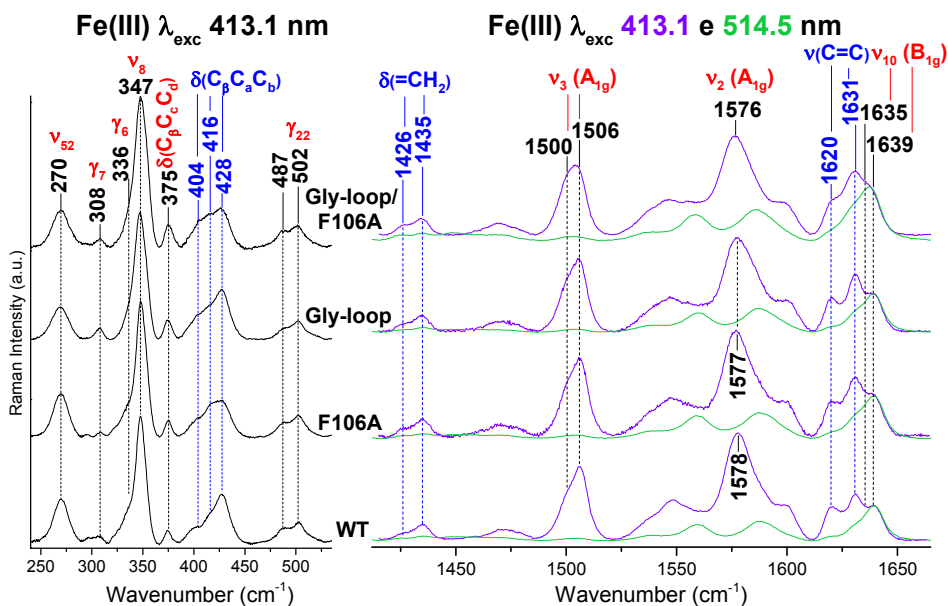


**Figure 5.9.** Right: high frequency region RR spectra obtained with the 413.1 (violet traces) and 514.5 nm (green traces) excitation wavelengths; from the bottom to the top, WT, F106A, Gly-loop, and Gly-loop/F106A mutants NGBs. The spectra have been shifted along the ordinate axis to allow better visualization. Experimental conditions: 413.1 nm excitation wavelength, laser power at the sample 10 mW; average of 21 spectra with 210 min integration time (WT), average of 4 spectra with 40 min integration time (F106A), average of 4 spectra with 40 min integration time (Gly-loop), and average of 22 spectra with 220 min integration time (Gly-loop/F106A); 514.5 nm excitation wavelength, laser power at the sample 70 mW; average of 6 spectra with 30 min integration time (WT), average of 17 spectra with 68 min integration time (F106A), average of 12 spectra with 60 min integration time (Gly-loop), and average of 3 spectra with 30 min integration time (Gly-loop/F106A).

Left: low frequency region of the RR spectra, from the bottom to the top, of WT, F106A, Gly-loop, and Gly-loop/F106A mutants NGBs. Experimental conditions: 413.1 nm excitation wavelength, laser power at the sample 5 to 10 mW; average of 6 spectra with 60 min integration time (WT), average of 9 spectra with 90 min integration time (F106A), average of 9 spectra with 90 min integration time (Gly-loop), average of 6 spectra with 60 min integration time (Gly-loop/F106A). The intensities of the RR spectra are normalized to that of the  $\nu_7$  band (not shown).

## 5.4 Ferrous form

In agreement with the ferric form, the Soret bands at 425 and the Q bands at 529 and 559 nm of the UV-Vis absorption spectra (**Figure 5.10**), are typical of a pure 6cLS His-Fe-His species [Li et al. 2003] and similar to those of other Ngbs [Dewilde 2001, Giordano 2012]. No 5cHS species is observed.

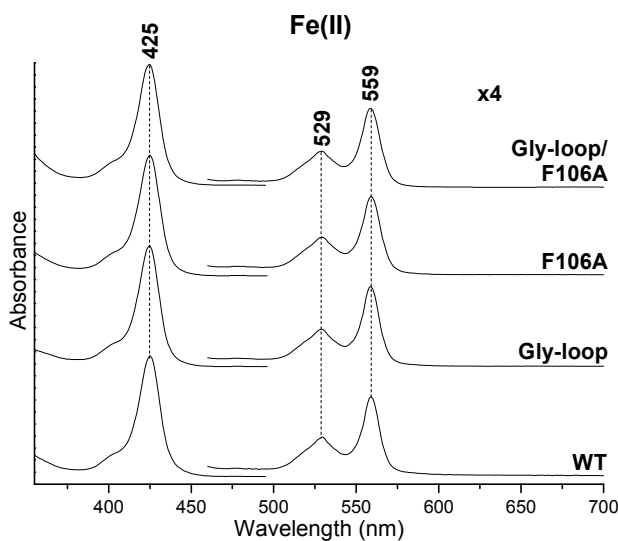


**Figure 5.10.** UV-Vis absorption spectra, from the bottom to the top, of WT, Gly-loop, F106A and Gly-loop/F106A mutants Ngbs. The spectra have been shifted along the ordinate axis to allow better visualization. The 460–700 nm region is expanded 4-fold.

In the high frequency of the RR spectra (**Figure 5.11**), as expected for a 6cLS species, the core size marker bands  $\nu_4$ ,  $\nu_3$ ,  $\nu_2$  and  $\nu_{10}$  are observed at 1361, 1493/1492, 1581/1580 and 1619  $\text{cm}^{-1}$ , respectively. The  $\nu(\text{C}=\text{C})$  stretching modes are at 1617  $\text{cm}^{-1}$  (overlapped with the  $\nu_{10}$ ) and 1628-1630  $\text{cm}^{-1}$ .

Similarly to the ferric form, on the basis of the WT and the Gly-loop/F106A double mutant spectra in polarized light, which show the biggest differences from each other, the overlapped  $\nu_{10}$  and  $\nu(\text{C}=\text{C})$  stretching mode have been identified (**Figure 5.12**).

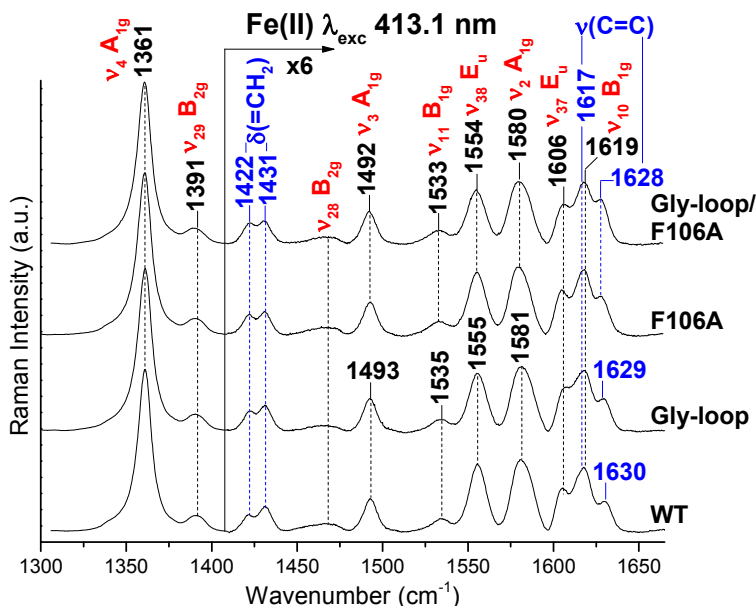


**Figure 5.11. High frequency region RR spectra, from the bottom to the top, of WT, Gly-loop, F106A and Gly-loop/F106A mutants Ngbs.** The spectra have been shifted along the ordinate axis to allow better visualization. The assignment of the bands is reported in red. Experimental conditions: 413.1 nm excitation wavelength, laser power at the sample 10 mW; average of 4 spectra with 40 min integration time (Gly-loop, F106A); average of 13 spectra with 130 min integration time (WT); average of 7 spectra with 70 min integration time (Gly-loop/F106A).

In agreement with the ferric form, the ferrous form of the double mutant, as compared to the WT, shows:

- lower frequencies of the core size marker bands ( $\nu_3$  1492  $\text{cm}^{-1}$  and  $\nu_2$  at 1580  $\text{cm}^{-1}$ );
- intensity increases of the vinyl stretching mode at 1628  $\text{cm}^{-1}$  which also downshift of 2  $\text{cm}^{-1}$ , being that of the WT at 1630  $\text{cm}^{-1}$ ;
- intensity loss of the vinyl the bending mode at 426  $\text{cm}^{-1}$  (**Figure 5.13**).

Except for the  $\delta(\text{C}_\beta\text{C}_\alpha\text{C}_\beta)$  vinyl bending region (which show difference in the relative intensities of the band at 426  $\text{cm}^{-1}$ ), the low frequency RR

spectra of the WT and mutants (**Figure 5.13**), are similar and are characteristic of a 6cLS heme, in agreement with the high frequency.

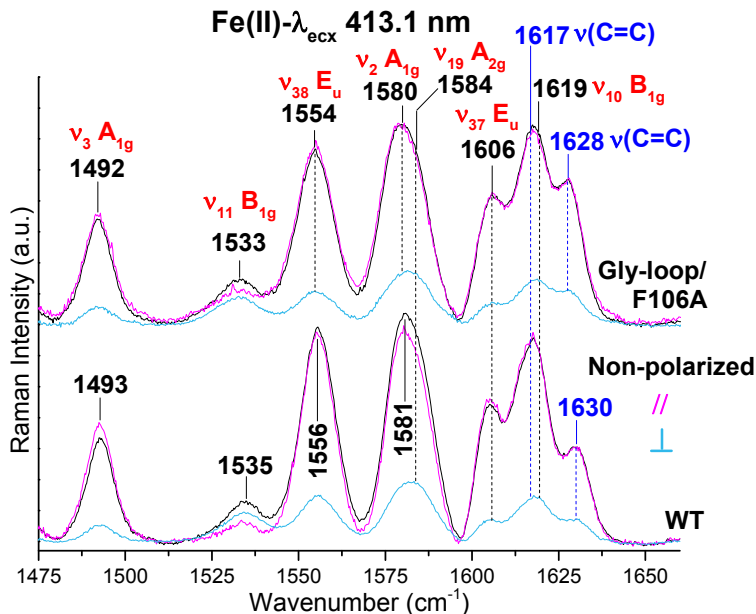


**Figure 5.12.** High frequency RR ( $\nu_3 - \nu_{10}$  region) spectra of WT (bottom) and Gly-loop/F106A mutant (top) Ngbs, obtained with the 413.1 nm excitation wavelength. Non-polarized (black traces), parallel polarized (magenta traces) and perpendicularly polarized (light blue traces). The spectra have been shifted along the ordinate axis to allow better visualization. The assignment of the bands is reported in red. Experimental conditions: 413.1 nm excitation wavelength, laser power at the sample 10 mW; average of 13 spectra with 130 min integration time (WT non polarized), average of 3 spectra with 30 min integration time (WT parallel polarized) and average of 8 spectra with 80 min integration time (WT perpendicularly polarized); average of 7 spectra with 70 min integration time (Gly-loop/F106A non polarized), average of 2 spectra with 20 min integration time (Gly-loop/F106A parallel polarized) and average of 3 spectra with 30 min integration time (Gly-loop/F106A perpendicularly polarized).

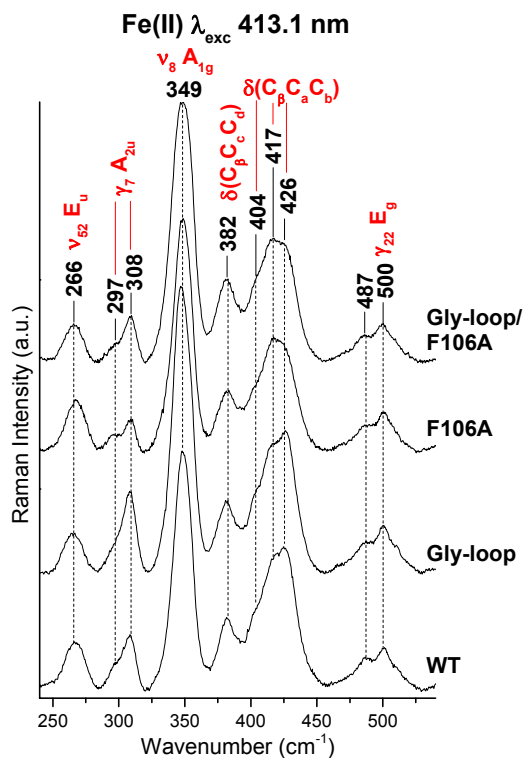


**Figure 5.13. Low frequency region RR spectra, from the bottom to the top, of WT, Gly-loop, F106A and Gly-loop/F106A mutants Ngbs.** The spectra have been shifted along the ordinate axis to allow better visualization. The assignment of the bands is reported in red. Experimental conditions: 413.1 nm excitation wavelength, laser power at the sample 10 mW; average of 5 spectra with 50 min integration time (Gly-loop, F106A); average of 6 spectra with 60 min integration time (WT); average of 6 spectra with 60 min integration time (Gly-loop/F106A).

In general, the spectra of the ferrous forms are in perfect agreement with the spectra of the ferric forms.

### 5.5 Ferrous-CO adducts

Experiments of CO-binding highlight that the double mutant Gly-loop/F106A has an increased velocity in CO binding (Exertier, manuscript in revision). This might be a consequence of the presence of some pentacoordinated species due to the modification of the CD loop [Daura 1999]. However, RR spectroscopy did not reveal any 5cHS

species (characterized by core size marker bands at 1357 ( $\nu_4$ ), 1471 ( $\nu_3$ ), 1562 ( $\nu_2$ ) and 1604 ( $\nu_{10}$ )  $\text{cm}^{-1}$ , and an intense band due to the iron-imidazole stretching mode,  $\nu(\text{Fe-Im})$  between 200 and 250  $\text{cm}^{-1}$ , all selectively intensified with the 441.6 nm excitation line in resonance with ferrous 5cHS Soret band generally around 430-435 nm) nor in the ferrous form nor in the photolyzed CO sample (**Figure 5.14**).

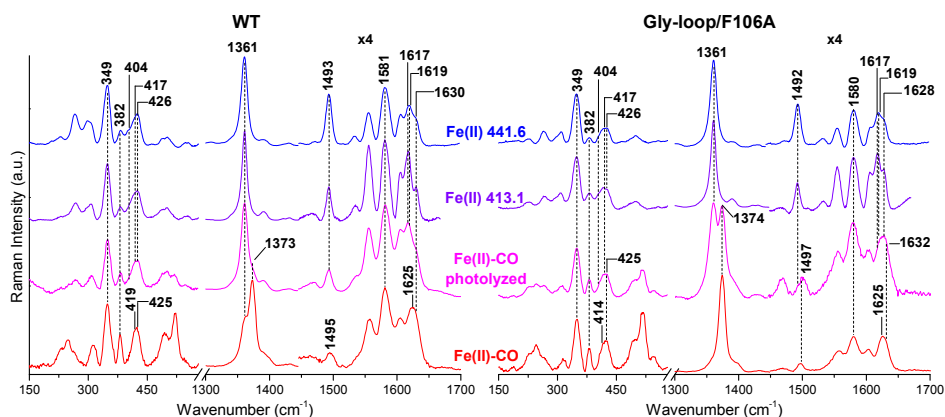


**Figure 5.14.** RR spectra of WT (left) and Gly-loop/F106A mutant (right) Ngbs. Low and high frequency regions obtained with the 413.1 nm excitation wavelength of the Fe(II)-CO adduct (red), photolyzed Fe(II)-CO adduct (magenta) and Fe(II) form, (violet). The RR spectrum of the Fe(II) (blue) form obtained with the 441.6 nm excitation wavelength is also reported for comparison, to ensure that no 5cHS is present. The spectra have been shifted along the ordinate axis to allow better visualization. Experimental conditions: Fe(II)-CO: laser power at the sample 1 mW, average of 2 spectra with 20 min integration time (WT and Gly-loop/F106A); Fe(II)-CO photolyzed: laser power at the sample 10 mW, average of 6 spectra with 6 min integration time (WT) and laser power at the sample 20 mW, 1 spectrum with 1 min integration time (Gly-loop/F106A); Fe(II): 413.1 nm excitation wavelength, laser power at the sample 10 mW; average of 6 spectra with 6 min integration time (grating with 1800 grooves per mm) and average of 4 spectra with 20 min integration time (grating with 3600 grooves per mm) in the low and high frequency regions, respectively (WT); average of 6 spectra with 6 min integration time (grating with 1800 grooves per mm) and average of 2 spectra with 20 min integration time (grating with 3600 grooves per mm) in the low and high frequency regions, respectively (Gly-loop/F106A); 441.6 nm excitation

wavelength, laser power at the sample 20 mW; average of 5 spectra with 15 min integration time (grating with 1800 grooves per mm) and average of 5 spectra with 10 min integration time (grating with 1800 grooves per mm) in the low and high frequency regions, respectively (WT and Gly-loop/F106A).

The RR spectra of the ferrous-CO adducts of the WT and mutants murine Ngbs, in common with other Ngbs [Giordano 2012; Couture 2001; Ishikawa 2007; Sawai 2005], show two isotope-sensitive bands either in the low and the high frequency regions (**Figure 5.15**). Thus two CO conformers have been identified (**Figure 5.16** and **Table 5.2**):

- a minor open form  $A_0$  ( $\nu(\text{FeC})$  at  $496 \text{ cm}^{-1}$  and  $\nu(\text{CO})$  at  $1970 \text{ cm}^{-1}$ ) where the distal His64 is not H-bonded with the CO;
- and a more abundant closed form  $A_3$  ( $\nu(\text{FeC})$  at 521 (WT) and 518 (mutants)  $\text{cm}^{-1}$ , and  $\nu(\text{CO})$  at  $1933 \text{ cm}^{-1}$ ), where the distal His64 is strongly H-bonded with the CO.

In one conformer the His64 residue strongly interacts with the CO, closing the distal cavity, while in the other conformer the His64 has swung out far from the CO, leaving the distal cavity open. The bands of the open form  $A_0$  strongly increases in the Gly-loop mutant.

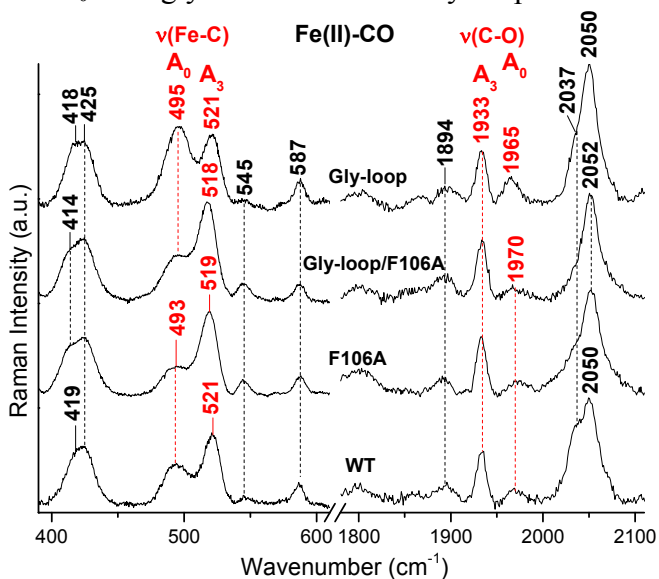


**Figure 5.15.** RR spectra in the low (left) and high (right) frequency regions of the  $^{12}\text{C}$ O adducts of the WT, F106A, Gly-loop/F106A and

Gly-loop mutant Ngbs. The frequencies of the  $\nu(\text{FeC})$  and  $\nu(\text{CO})$  modes are indicated in red. The spectra have been shifted along the ordinate axis to allow better visualization. Experimental conditions: 413.1 nm excitation wavelength; laser power at the sample 1 mW, average of 19 spectra with 190 min integration time and 14 spectra with 140 min integration time in the low and high frequency regions, respectively (WT); laser power at the sample 2 mW, average of 9 spectra with 90 min integration time and 16 spectra with 160 min integration time in the low and high frequency regions, respectively (F106A) and average of 7 spectra with 70 min integration time and 16 spectra with 160 min integration time in the low and high frequency regions, respectively (Gly-loop); laser power at the sample 5 mW, average of 8 spectra with 80 min integration time and 9 spectra with 90 min integration time in the low and high frequency regions, respectively (Gly-loop/F106A).

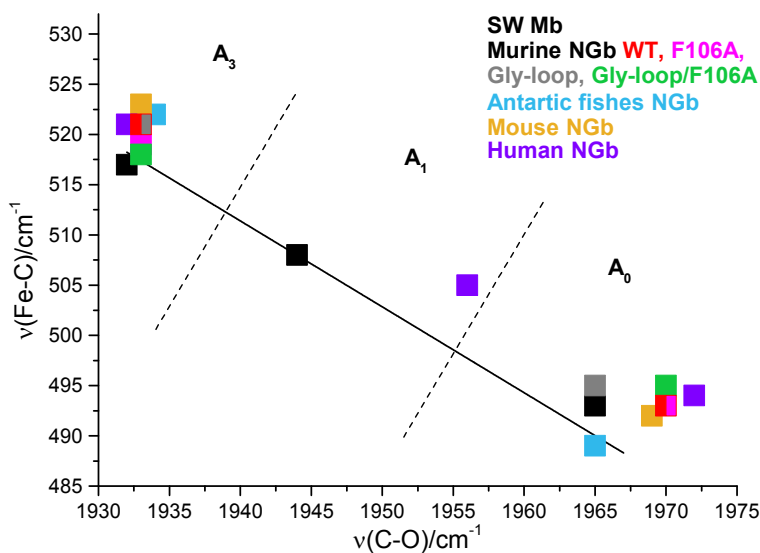


**Figure 5.16.** Back-bonding correlation line of the  $\nu(\text{FeC})$  and  $\nu(\text{CO})$  stretching frequencies of various Ngbs: *C. aceratus* and *D. mawsoni* Antarctic fishes (light blue), mouse (light brown), human (violet), murine WT (red), F106A (magenta), Gly-loop (grey) and Gly-loop/F106A (green) mutants. The corresponding data of sperm whale Mb are also reported (black). The human Ngb and SWMb show also a third weak H-bonded conformer ( $A_1$ ) at 505/ 1956 and 508/ 1946  $\text{cm}^{-1}$ , respectively, not reported in the Table 5.3. The dotted lines indicate the approximate delineation between the frequency zones of the  $A_0$ ,  $A_1$ , and  $A_3$  forms.

**Table 5.2.**  $\nu(\text{Fe-C})$  and  $\nu(\text{C-O})$  stretching frequencies of various Ngbs: *C. aceratus* and *D. mawsoni* Antarctic fishes [Giordano 2012] (light blue), mouse [Couture 2001] (light brown), human [Ishikawa 2007, Sawai 2005] (violet), murine WT (red), F106A (magenta), Gly-loop (grey) and Gly-loop/F106A (green) mutants. The corresponding data of sperm whale Mb are also reported (Morikis 1989, Howes 2012) (black). The human Ngb and sperm whale Mb show also a third weak H-bonded conformer ( $A_1$ ) at 505/1956 and 508/1946  $\text{cm}^{-1}$ , respectively, not reported in the table.

	<b>(A<sub>0</sub>) Open form No H-bond</b>		<b>(A<sub>3</sub>) Closed form Strong H-bond</b>	
	$\nu(\text{Fe-C})$	$\nu(\text{CO})$	$\nu(\text{Fe-C})$	$\nu(\text{CO})$
<b>Ngb</b>				
<i>C. aceratus</i> <sup>a</sup>	489	1965	522	1934
<i>D. mawsoni</i> <sup>a</sup>	489	1965	522	1934
Mouse <sup>b</sup>	492	1969	523	1933
Human <sup>c,d</sup>	494	1972	521	1932
Murine Wt <sup>this work</sup>	493	1970	521	1933
Murine F106A <sup>this work</sup>	493	1970	519	1933
Murine Gly-loop <sup>this work</sup>	495	1965	518	1933
Murine Gly-loop/F106A <sup>this work</sup>	495	1970	518	1933
Mb (Sperm Whale) <sup>e</sup>	493	1965	517	1932

<sup>a</sup> Giordano 2012; <sup>b</sup> Couture 2001; <sup>c</sup> Ishikawa 2007; <sup>d</sup> Sawai 2005; <sup>e</sup> Morikis 1989, Howes 2012.

These data agree well with the kinetics and structural data, which highlight that the control of external ligand binding is mainly dependent on (Exertier, manuscript in revision):

- the barriers to the heme sliding within its crevice consisting of residues on the proximal side, mostly Phe106,
- the spontaneous dissociation of the distal His64. The crystal structure of the CO bound Gly-loop mutant (where the 44-47 residues are mutated in Gly) shows that in the absence of the constraint imposed by the H-bond interaction between the Tyr44 residue and the heme propionate group (**Figure 5.17**), a state with a swung out His64, but with the heme still in the unslid

position is spontaneously formed. Accordingly, the RR data on the CO adduct of the Gly-loop mutant show that the fraction of the  $A_0$  open conformation is increased as compared to the WT CO adduct, while in the Gly-loop/F106A, where the main barrier to sliding is removed, the  $A_0/A_3$  ratio (open/closed) is restored to a value similar to the one observed for the CO adduct of WT Ngb. Consequently, as expected, in the Gly-loop mutant the velocity of CO binding is increased by one order of magnitude, reaching a much faster rate limiting step with respect to WT Ngb. Hence a possible sequence of events for ligand binding in Ngb is proposed:

- 1) spontaneous rupture of the 6<sup>th</sup> coordination bond of His64 to the heme iron,
- 2) coordination of the exogenous diatomic ligand upon swinging out of His64,
- 3) heme sliding within the heme crevice with partial return of His64 in the distal cavity as indicated by the RR data.

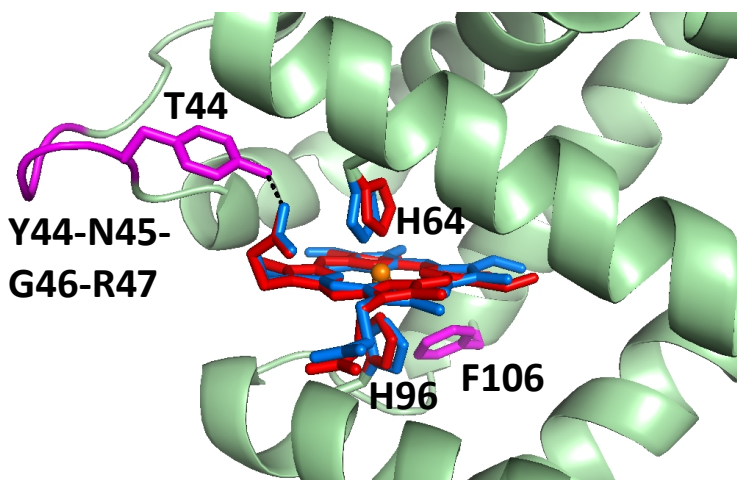


**Figure 5.17.** Ribbon diagram of the WT Ngb active site (1Q1F [Vallone 2004]). This figure highlights the double heme insertion (the reversed and canonical conformers are reported in red and blue, respectively), the proximal (96) and distal (64) His ligands and in magenta the mutated residue (Phe106 and in the CD-loop the Tyr44-Asn45-Gly46-Arg47 fragment). Moreover the H-bond interaction between the Tyr44 residue and one of the heme propionate groups is reported. The figure was made

with: The PyMOL Molecular Graphics System, Version 1.7.5.0  
Schrödinger, LLC.

## 5.6 Conclusions

The crystal structure of ferric WT Ngb [Vallone 2004] reveals the presence of two 6cLS bis-His species, which differ for the heme insertion, being 180° rotated one to each other with respect to the  $\square$ - $\square$  meso axis, namely reversed (A, 70% occupancy) and canonical (B, 30% occupancy) conformers. Accordingly, the RR data of WT and selected mutants with enhanced CO binding capabilities (F106A, Gly-loop and Gly-loop/F106A) show a double set of core size marker bands, confirming the presence of two 6cLS species, a canonical, with a distorted heme and bigger core size, and the reversed, with planar heme and smaller core. The canonical conformer slightly increases in the mutants at the expense of the reversed one. Moreover, only the 4-vinyl group appears to be markedly affected by the heme flipping, changing from the *trans* (canonical) to the *cis* conformation (reversed) as observed from the up-shift of the  $\nu(\text{C}=\text{C})$  stretching frequency. This is the first time that a reversed heme insertion is identified by RR in a native protein.

The CO-adducts give similar results to those previously obtained for other Ngbs, suggesting the existence of two Ngb conformations after CO binding: one where the distal His64 strongly interacts with the CO, closing the distal cavity, and one with His64 swung out far from the CO, leaving the distal cavity open. In agreement with the crystal structure of the CO-bound Gly-loop mutant, the relative RR spectrum contains an increased fraction of the open conformation as compared to the WT, while in the double Gly-loop/F106A, the open/closed conformation ratio is restored to a value similar to the WT.

## References

- ❖ Abbruzzetti S., Faggiano S., Bruno S., Spyrakis F., Mozzarelli A., Dewilde S., Moens L., Viappiani C., Proc. Natl. Acad. Sci. U.S.A. 2009, 106, 18984.
- ❖ Avella G., Ardiccioni C., Scaglione A., Moschetti T., Rondinelli C., Montemiglio L.C., Savino C., Giuffrè A., Brunori M., Vallone B.,

Acta Crystallographica Section D: Biological Crystallography, 2014, 70, 1640.

- ❖ Baez E., Echeverria V., Cabezas R., Ávila-Rodríguez M., Garcia-Segura L.M., Barreto G.E., *Frontiers in neurology* 2016, 7, 146.
- ❖ Bashford D., Chothia C., Lesk A.M., *J. Mol. Biol.* 1987, 196, 199.
- ❖ Boron I., Capece L., Pennacchietti F., Wetzler D.E., Bruno S., Abbruzzetti S., Chisari L., Luque F.J., Viappiani C., Marti M.A., Estrin D.A., Nadra A.D., *Biochim. Biophys. Acta - Gen Subj.* 2015, 1850, 169.
- ❖ Burmester T., Weich B., Reinhardt S., Hankeln T., *Nature* 2000, 407, 520.
- ❖ Choi S., Spiro T.G., Langry K.C., Smith K.M., Budd D.L., La Mar G.N., *J. Am. Chem. Soc.* 1982, 104, 4345.
- ❖ Couture M., Burmester T., Hankeln T., Rousseau D.L., *J. Biol. Chem.* 2001, 276, 36377.
- ❖ Daura X., Gademann K., Jaun B., Seebach D., Van Gunsteren W.F., Mark A.E., *Angewandte Chemie International Edition* 1999, 38, 236.
- ❖ Dewilde S., Kiger L., Burmester T., Hankeln T., Baudin-Creuzat V., Aerts T., Marden M.C., Caubergs R., Moens L., *J. Biol. Chem.* 2001, 276, 38949.
- ❖ Du W., Syvitski R., Dewilde S., Moens L., La Mar G.N., *J. Am. Chem. Soc.* 2003, 125, 8080.
- ❖ Fabrizius A., Andre D., Laufs T., Bicker A., Reuss S., Porto E., Burmester T., Hankeln T., *Neuroscience* 2016, 337, 339.
- ❖ Fago A., Hundahl C., Dewilde S., Gilany K., Moens L., Weber R.E., *J. Biol. Chem.* 2004, 279, 44417.
- ❖ Giordano D., Boron I., Abbruzzetti S., Van Leuven W., Nicoletti F.P., Forti F., Bruno S., Cheng C.-H.C., Moens L., Di Prisco G., Nadra A., Estrin D., Smulevich G., Dewilde S., Viappiani C., Verde C., *PLoS ONE* 2012, 7, e44508.
- ❖ Hamdane D., Kiger L., Dewilde S., Green B.N., Pesce A., Uzan J., Burmester T., Hankeln T., Bolognesi M., Moens L., Marden M.C., *J. Biol. Chem.* 2003, 278, 51713.
- ❖ Hoard J.L., *Ann. NY Acad. Sci.* 1973, 206, 18.
- ❖ Holm L., Sander C., *FEBS Letters* 1993, 315, 301.
- ❖ Howes B.D., Helbo S., Fago A., Smulevich G., *J. Inorg. Biochem.* 2012, 109, 1.
- ❖ Ishikawa H., Finkelstein I.J., Kim S., Kwak K., Chung J.K., Wakasugi K., Massari A.M., Fayer M.D., *Proc. Natl. Acad. Sci. U.S.A* 2007, 104, 16116.

- ❖ Kiger L., Uzan J., Dewilde S., Burmester T., Hankeln T., Moens L., Hamdane D., Baudin-Creuzat V., Marden M.C., *IUBMB Life* 2004, 56, 709.
- ❖ Kriegl J.M., Bhattacharyya A.J., Nienhaus K., Deng P., Minkow O., Nienhaus G.U., *Proc. Natl. Acad. Sci. U.S.A.* 2002, 99, 7992.
- ❖ Li Q.C., Mabrouk P.A., *J. Biol. Inorg. Chem.* 2003, 8, 83.
- ❖ Marzocchi M.P., Smulevich G., *J. Raman Spectrosc.* 2003, 34, 725.
- ❖ Morikis D., Champion P., Springer B., Sligar S., *Biochemistry* 1989, 28, 4791.
- ❖ Moschetti T., Mueller U., Schulze J., Brunori M., Vallone B., *Biophys J.* 2009, 97, 1700.
- ❖ Nienhaus K., Nienhaus G.U., *J. Biol. Phys.* 2005, 31, 417.
- ❖ Pesce A., Dewilde S., Nardini M., Moens L., Ascenzi P., Hankeln T., Burmester T., Bolognesi M., *Structure* 2003, 11, 1087.
- ❖ Raida Z., Hundahl C.A., Kelsen J., Nyengaard J.R., Hay-Schmidt A., *Experimental & translational stroke medicine* 2012, 4, 15.
- ❖ Raida Z., Hundahl C.A., Nyengaard J.R., Hay-Schmidt A., *PLoS ONE* 2013, 8, e76565.
- ❖ Rwere F., Mak P.J., Kincaid J.R., *Biopolymers* 2007, 89, 179.
- ❖ Rwere F., Mak P.J., Kincaid J.R., *Biochemistry* 2008, 47, 12869.
- ❖ Rwere F., Mak P.J., Kincaid J.R., *J. Raman Spectrosc.* 2014, 45, 97.
- ❖ Sawai H., Makino M., Mizutani Y., Ohta T., Sugimoto H., Uno T., Kawada N., Yoshizato K., Kitagawa T., Shiro Y., *Biochemistry* 2005, 44, 13257.
- ❖ Smaghe B.J., Sarath G., Ross E., Hilbert J.L., Hargrove M.S., *Biochemistry* 2006, 45, 561.
- ❖ Smulevich G., Mauro J.M., Fishel L.A., English A.M., Kraut J., Spiro T.G., *Biochemistry* 1988, 27, 5477.
- ❖ Smulevich G., Miller M.A., Kraut J., Spiro T.G., *Biochemistry* 1991, 30, 9546.
- ❖ Smulevich G., Hu S., Rodgers K.R., Goodin D.B., Smith K.M., Spiro T.G., *Biospectroscopy* 1996, 2, 365.
- ❖ Sparks L.D., Anderson K.K., Medforth C.J., Smith K., Shelnut J.A., *Inorg. Chem.* 1994, 33, 2297.
- ❖ Spaulding L.D., Chang C.C., Yu N.T., Felton R.H., *J. Am. Chem. Soc.* 1975, 97, 2517.
- ❖ Taylor J.M., Kelley B., Gregory E.J., Berman N.E.J., *Neurosci. Lett.* 2014, 577, 125.
- ❖ Tiwari, P. B., Astudillo, L., Pham, K., Wang, X., He, J., Bernad, S., Derrien V., Sebban P., Miksovska J., Darici, Y., *Inorganic Chemistry Communications* 2015, 62, 37.

- ❖ Trent J.T., Watts R.A., Hargrove M.S., *J Biol Chem.* 2001, 276, 30106.
- ❖ Trent J.T., Hargrove M.S., *J. Biol. Chem.* 2002, 277, 19538.
- ❖ Vallone B., Nienhaus K., Brunori M., Nienhaus G.U., *Proteins: Structure, Function, and Bioinformatics* 2004, 56, 85.
- ❖ Vallone B., Nienhaus K., Matthes A., Brunori M., Nienhaus G.U., *PNAS* 2004, 101, 17353.
- ❖ Wang Y., *Neurochem. Res.* 2017, 42, 2208.
- ❖ Watanabe S., Wakasugi K., *Biochem. Biophys. Res. Commun.* 2008, 369, 695.

## Chapter 6

### **Ligand binding in the truncated hemoglobin of the Antarctic marine bacterium *Pseudoalteromonas haloplanktis* TAC125, Ph-trHbO-2217**

Daniela Coppola, Daniela Giordano, **Lisa Milazzo**, Barry D. Howes, Paolo Ascenzi, Guido di Prisco, Giuletta Smulevich, Robert K. Poole, Cinzia Verde,

“Coexistence of multiple globin genes conferring protection against nitrosative stress to the Antarctic bacterium *Pseudoalteromonas haloplanktis* TAC125”,

*Nitric Oxide* **2018**, 73, 39.

Alessandro Feis, Barry D. Howes, **Lisa Milazzo**, Daniela Coppola, Giuletta Smulevich,

“Structural determinants of ligand binding in truncated hemoglobins: Resonance Raman spectroscopy of the native states and their carbon monoxide and hydroxide complexes”,

*Biopolymers* **2018**, e23114.

#### **6.1 Introduction**

Phylogenetic analysis of protein sequences has indicated that globins are present in all kingdoms of life and can be collected within a single superfamily that contains three main lineages: (i) truncated haemoglobins (trHbs), (ii) protoglobins (Pgbs) and related globin-coupled sensors (GCSs), and (iii) flavohaemoglobins and related single-domain globins (the family of the classical vertebrate Hbs) [Frey 2003, Vinogradov 2013a, Vinogradov 2008; Wajcman 2009, Wittenberg 2002].

Structurally the trHbs differ from the Pgbs and single-domain globins, the latter showing the classical 3-on-3  $\alpha$ -helical motif vs the 2-on-2  $\alpha$ -helical sandwich of the trHbs.

The the 2-on-2 globin display less than 20% overall identity with respect to the 3-on-3 globins, the most striking differences in the globin folds being: (i) the drastically shortened helix A; (ii) a brief C-E interhelical region; (iii) the presence of a long polypeptide segment (pre-F) in extended conformation, and (iv) a variable-length helix F that effectively supports the proximal HisF8 residue coordinated to the heme Fe atom [Pesce 2013] (Figure 6.1).

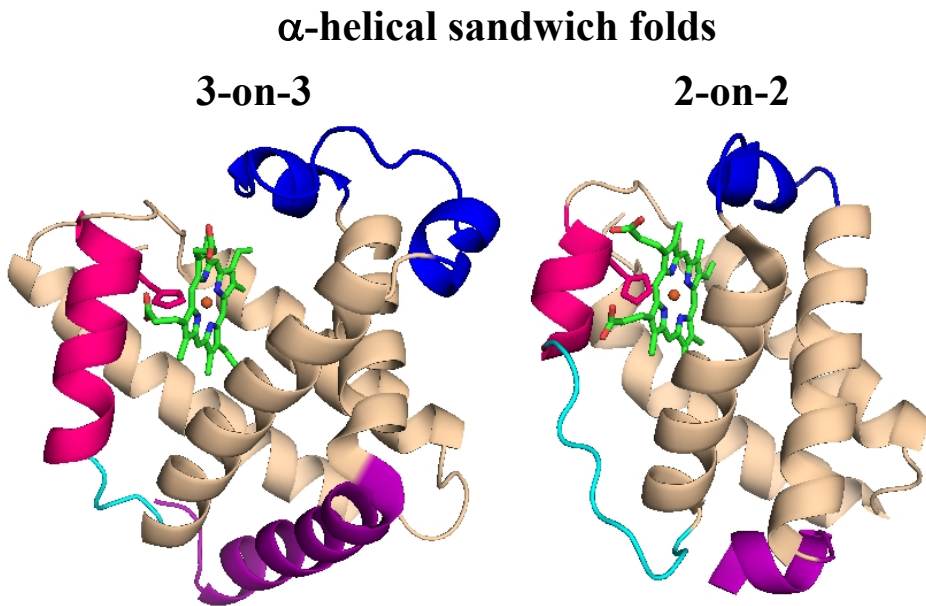


**Figure 6.1.** The 3-on-3  $\alpha$ -helical helical sandwich fold in sperm whale (SW) Mb (1EBC [Bolognesi 1999]) and the 2-on-2  $\alpha$ -helical sandwich fold in the trHb of *Paramecium caudatum*, the first hemoglobins found a unicellular organism [Sato 1937] (1DLW [Pesce 2000]).

On the basis of specific structural features related to sequence motifs, helices in their folds and protein matrix tunnel(s), heme cavity, distal pocket structure and polarity, as well as ligand stabilization and ligand entry/exit mechanisms distinguish each group [Vuletich 2006, Pesca 2013], TrHbs can be conveniently classified into three groups: I (trHbN),

II (trHbO), and III (trHbP). Recently a novel, small group named trHbIV (or Q) containing only bacterial sequences has been added [Bustamante 2016]. TrHbs share seven key residues in the heme pocket at topologically relevant positions, namely B9, B10, CD1, E7, E11, E14, and F8 of which only the HisF8, PheB9 and TyrB10 are highly conserved and are thus thought to be of critical importance for ligand binding which is very likely related with the protein function.

A distinct aspect of groups I and II is the presence of cavities inside the structure linking the protein surface to the distal heme, responsible for storage and diffusion of ligands to/from the heme. TrHbs bind diatomic ligands, namely O<sub>2</sub>, CO, NO, OH, and cyanide, with varying thermodynamic and kinetic parameters [Milani 2005]. In general, the H-bond stabilization is provided by TyrB10, TrpG8, His, or Tyr at CD1 and GlnE11 [Bustamante 2016, Pesce 2013]. Such a marked diversity between TrHbs might be associated with diverse functional properties concerned with ligand recognition and/or ligand affinity.

TrHbs are widely distributed in eubacteria, cyanobacteria, protozoa, and plants, but not in animals [Vinogradov 2013b, Wittenberg 2002, Milani 2005]. Some of the organisms hosting the trHbs are pathogenic bacteria, others perform photosynthesis, fix nitrogen or may display distinctive metabolic capabilities [Pesce 2013 and refs therein]. Accordingly, a variety of functions have been proposed, including protection from reactive O<sub>2</sub>(ROS) and nitrogen (RNS) species, O<sub>2</sub> and NO detoxification, sulfide, nitrite, and peroxyxynitrite chemistry [Pesce 2013, Pesce 2016, Gardner 2005, De Marinis 2009, Boubeta 2016, Ascenzi 2009, Ascenzi 2014].

Moreover in some cases, trHbs from more than one group can coexist in the same organism, indicating diversification of their functions [Vinogradov 2013b]. However despite the large number of trHbs recently discovered, our knowledge of their physiological functions is presently not fully clarified yet.

The genome of the cold-adapted bacterium *Pseudoalteromonas haloplanktis* TAC125 (PhTAC125) contains multiple genes encoding distinct TrHbs [Giordano 2007], supporting the hypothesis of their

involvement in several functions, including protection against oxidative and nitrosative stress in the cold and O<sub>2</sub>-rich environment of Antarctica. In particular, PhTAC125 hosts two distinct trHbs of group II: Ph-2/2HbO-0030 and Ph-2/2HbO-2217, encoded by the PSHAA0030 and PSHAA2217 genes, respectively.

The Ph-2/2HbO-0030 protein has been extensively characterized by spectroscopic analysis, kinetic measurements, computer simulation and X-ray crystallography [Giordano 2011, Giordano 2013, Giordano 2015, Howes 2011, Johnson 2013]. The results indicate unique adaptive structural properties that enhance the overall flexibility of the protein [Giordano 2015].

The aim of my work is to obtain structural information about Ph-trHbO-2217 and compare the results with those previously obtained for Ph-2/2HbO-0030 [Giordano 2015] and for another well characterized trHb of group II, *Thermobifida fusca* (Tf-trHbO) from the thermophilic actinobacterium [Nicoletti 2013] to highlight the differences in ligand binding and stabilization.

## 6.2 Materials

Cloning, expression and purification of the Ph-trHbO-2217 protein were performed by Dr. Cinzia Verde's group (Naples CNR).

Ferric Ph-trHbO-2217 at pH 6.0, 7.6 and 9.9 was prepared in 50 mM MES [2-(*N*-morpholino) ethanesulfonic acid], 20 mM Tris-HCl and 50 mM glycine, respectively. The hydroxyl complex in isotopically enriched water was prepared by washing *Ph-2/2HbO-2217* in 20 mM Tris-HCl pH 7.6 with 0.1 mM glycine pD 10.2 prepared with D<sub>2</sub>O (99.8%) (Merck AG, Darmstadt, Germany). Ferrous samples at pH 7.6 were prepared by addition of 2-3 μL of a freshly prepared sodium dithionite solution (10 mg/mL) to the ferric forms (40 μL) previously flushed with nitrogen. The Fe(II)-CO complex at pH 7.6 was prepared by flushing ferric *Ph-2/2HbO-2217* (40 μL) firstly with nitrogen, then with <sup>12</sup>CO or <sup>13</sup>CO (Rivoira, Milan, Italy), and reducing the heme by addition of 2-3 μL of a freshly prepared sodium dithionite solution (10 mg/mL).

Protein concentration in the range 10–30  $\mu\text{M}$  was used for electronic absorption and RR spectroscopies at both room and low temperature. The concentration used for EPR spectroscopy was 100  $\mu\text{M}$ . The protein concentration was estimated on the basis of the molar absorptivity of the ferric form at 408 nm,  $\epsilon = 131 \text{ mM}^{-1} \text{ cm}^{-1}$ .

### 6.3 Structural comparison

**Figure 6.2** shows the sequence alignments of Ph-trHbO-2217, Ph-trHbO-0030, and Tf-trHbO. The sequence identity between the two Antarctic globins is only 24%, whereas it is 33 and 27% between Tf-trHbO and Ph-trHbO-0030, and Ph-trHbO-2217, respectively. In the heme pocket, the three proteins have His and Trp residues at positions F8 and G8, respectively, and the Phe-Tyr motif at positions B9-B10. However, position CD1 is occupied by a His residue in the Antarctic globins and a Tyr in Tf-trHbO (**Figure 6.4**).

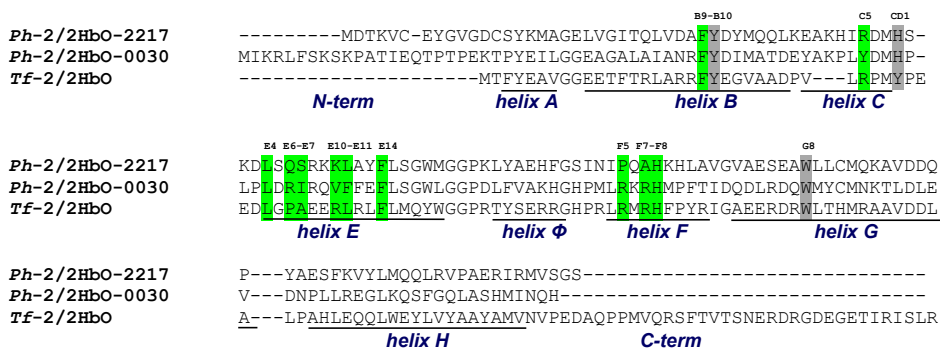


**Figure 6.2.** Sequence alignment, carried out by Clustal Omega, of Ph-trHbO-2217, Ph-trHbO-0030 and Tf-trHbO. Manual adjustments have been based on known crystal structures adapted from [Giordano 2015]. Key functionally important residues are shown in green; residues (B10, CD1, and G8) specific for trHbs of group-II are in grey; helical regions (A–H, are indicated by black bars and helix  $\Phi$ , specific for trHbs of group-II, is also shown. The numbering of residues is based on the position of residues in the helices of sperm whale Mb.

The structure of Ph-trHbO-2217 has not been yet solved; however, the Ph-trHbO-0030 structure has been used as template to obtain the Ph-trHbO-2217 homology model. In this regard, it is important to note that

although the use of structural templates can be a valuable resource in the absence of the crystallographic structure of a protein, its limitations should be borne in mind. The overlay of the two heme pockets reported in **Figure 6.3** shows that stabilization of the heme occurs through interactions of the propionate groups with different cavity residues in the two proteins. In particular, while in Ph-trHbO-0030, propionates D and A are stabilized by an H-bond with Arg(95)F7 and Arg(64)E6, respectively, in Ph-trHbO-2217, positions F7 and E6 are occupied by Ala and Gln, respectively. However, the key distal (TyrB10, TrpG8, HisCD1) and proximal (HisF8) residues appear to be almost completely overlapped.

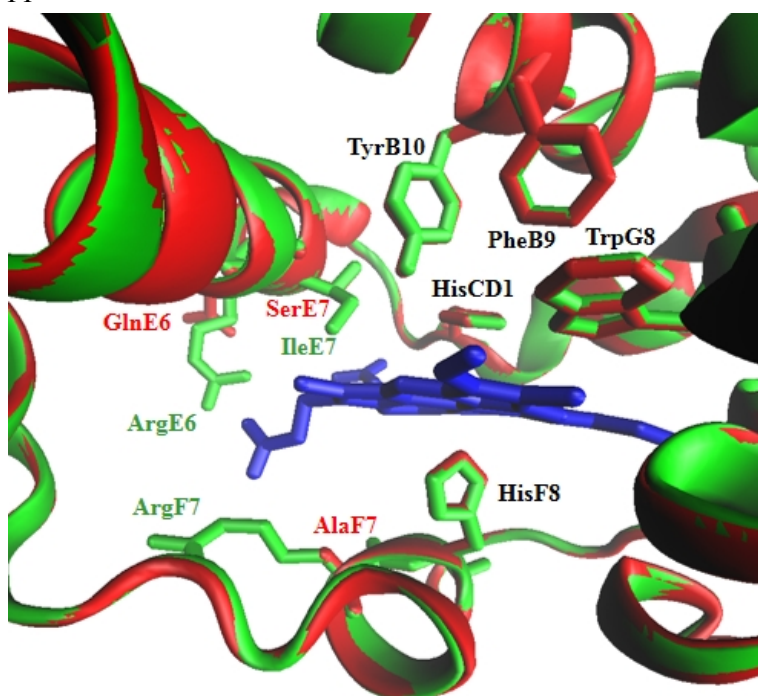


**Figure 6.3.** Superimposition of the heme pockets of the Ph-trHbO-2217 homology model (red) and the Ph-2/2HbO-0030 template structure (green). The heme group is shown in blue.

From the comparison of the heme cavities of Tf-trHbO acetate-bound (2BMM [Bonamore 2005]) and Ph-trHbO-0030 (4UUR [Giordano 2015]) (**Figure 6.4**) it can be seen that they share some characteristics:

- on the proximal side, the F8 imidazole ligand ring is in a staggered azimuthal orientation relative to the heme pyrrole N atoms (in common with other trHbs),
- the distal cavities are very polar and characterized by extended H-bond networks involving TyrB10, TrpG8, and Tyr/HisCD1 residues and water molecules. The residues in positions G8 (Trp) and B10 (Tyr) are conserved, while the CD1 residue is a Tyr in Tf-trHbO and a His in Ph-trHbO-0030. Moreover, in Tf-trHbO structure an acetate ion is bound almost perpendicularly to the ferric heme iron (Fe–O 1.67 Å). The anion is stabilized by H-bonds with Tyr(67)CD1 and Trp(119)G8. In addition, the OH group of Tyr54B10 is H-bonded to a water molecule, which in turn is H-bonded to another water molecule. In Ph-trHbO-0030 structure one of the water molecules involved in the distal H-bond network is coordinated to the ferric heme iron (Fe–O 2.2 Å).

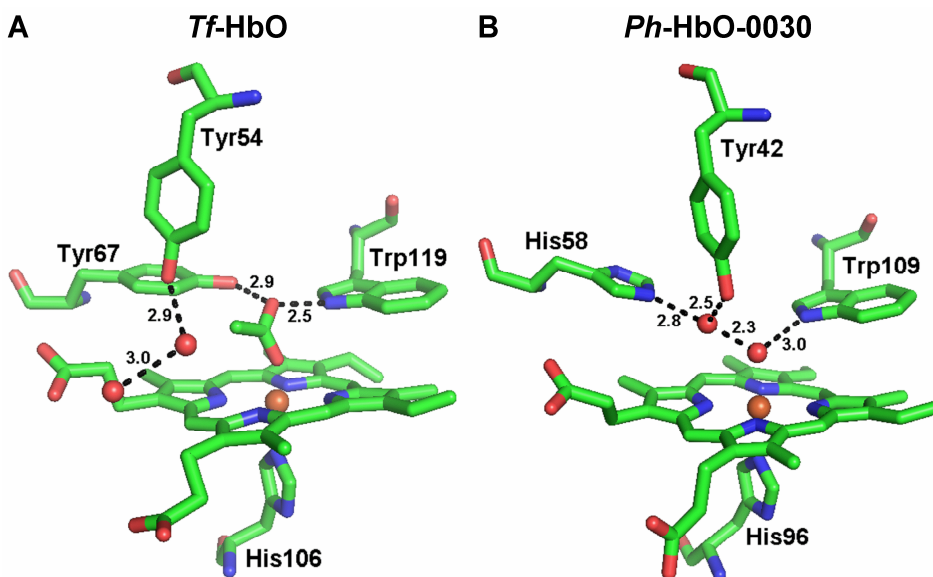


**Figure 6.4.** Comparison of the heme cavities of A) Tf-trHbO (2BMM [Bonamore 2005]) and B) Ph-trHbO-0030 (A chain) (4UUR [Giordano 2015]). The figures were made with The PyMOL Molecular Graphics System, Version 1.7.5.0 Schrödinger, LLC.

## 6.4 Ferric forms

**Figure 6.5** compares the UV-Vis and the RR high-frequency region (at 298 and 80K) spectra of ferric Ph-2/2HbO-2217 at different pH.

At pH 6.0, room-temperature spectra (**A**, **B**) are characteristic of a predominantly 6cHS aquo form [ $\alpha$  band at 501 nm, charge-transfer (CT1) band at 632 nm and RR bands at 1483 ( $\nu_3$ ), 1558 ( $\nu_2$ )  $\text{cm}^{-1}$ ]. However, a weak 6cLS form [ $\alpha$  band at 577 nm, RR bands at 1509 ( $\nu_3$ ), 1641 ( $\nu_{10}$ )  $\text{cm}^{-1}$ ], is also present. Ph-trHbO-2217 undergoes an acid-alkaline transition, hence, upon increasing the pH, the 6cHS aquo species decreases, and new  $\text{OH}^-$  ligated forms, both 6cHS [1477 ( $\nu_3$ ), 1559 ( $\nu_2$ )  $\text{cm}^{-1}$ ] and 6cLS [1501 ( $\nu_3$ ), 1575 ( $\nu_2$ ), 1638 ( $\nu_{10}$ )  $\text{cm}^{-1}$ ], grow in until pH 9.9, where the UV-Vis and RR spectra are typical of  $\text{OH}^-$  ligated forms.

Notably, the frequency of RR core size bands of the 6cLS species observed at pH 6.0 [1509 ( $\nu_3$ ), 1641 ( $\nu_{10}$ )  $\text{cm}^{-1}$ ] progressively downshift until pH 9.0 [1501 ( $\nu_3$ ), 1575 ( $\nu_2$ ), 1638 ( $\nu_{10}$ )  $\text{cm}^{-1}$ ]. This suggests that the sixth ligand of the 6cLS species at pH 6.0 is different from the  $\text{OH}^-$  ion present at alkaline pH. This was confirmed by the RR spectra at 80 K (**Figure 6.5, C**) where the sharpening of the bands and the presence of only a 6cLS  $\text{OH}^-$  ligated form at alkaline pH allowed the identification of different 6cLS forms at pH 6.0 and 9.9 characterised by different RR frequencies, which are, on the other hand, both present at intermediate pH 7.6. Accordingly, in addition to a 6cHS form ( $g_{\perp} \sim 6$  and  $g_{\parallel} 2.00$ ), the EPR spectrum at pH 7.6 (**Figure 6.6**) displays two 6cLS forms: one with  $g_1 = 2.95$ , and the other with  $g_1 = 2.71$ , this latter typical of His-Fe- $\text{OH}^-$  coordination.

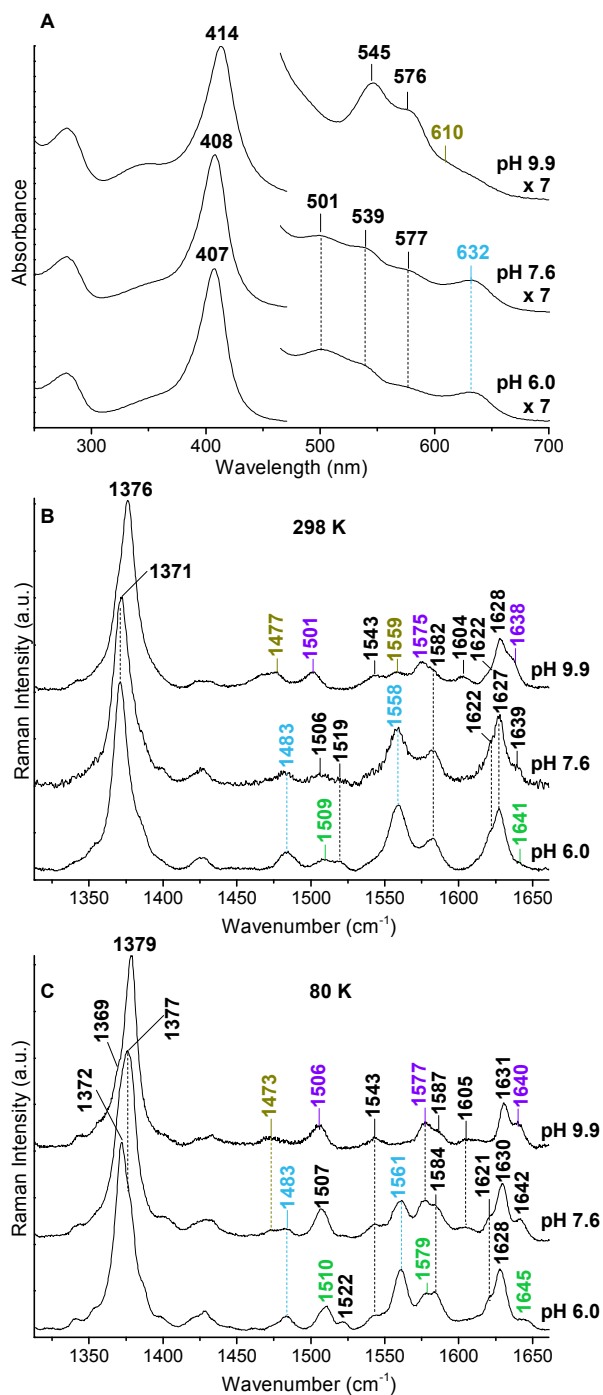


**Figure 6.5.** Comparison of the UV-Vis (panel A) and RR spectra in the high frequency region at 298 K (panel B) and 80 K (panel C) of ferric

Ph-trHbO-2217 at pH 6.0 (bottom), 7.6 (middle) and 9.9 (top). The spectra in all the panels have been shifted along the ordinate axis to allow better visualisation. The 470–700-nm region of the UV-Vis spectra has been expanded 7-fold. RR experimental conditions: 298 K: excitation wavelength 406.7 nm; (pH 6.0), laser power at the sample 5 mW, average of 4 spectra with 20-min integration time; (pH 7.6), laser power at the sample 4 mW, using a cylindrical lens and cooling the sample with a gentle flow of N<sub>2</sub> passed through liquid N<sub>2</sub>, average of 13 spectra with 13-min integration time; (pH 9.9), excitation wavelength 413.1 nm, laser power at the sample 10 mW, average of 3 spectra with 15-min integration time; 80 K: (pH 6.0 and 7.6), excitation wavelength 406.7 nm, laser power at the sample 10 mW, average of 3 spectra with 30-min integration time; (pH 9.9), excitation wavelength 413.1 nm, laser power at the sample 5 mW; average of 12 spectra with 60-min integration time. The intensities of the RR spectra are normalised to that of the  $\nu_4$  band. The band positions (wavelengths and frequencies), assigned to the 6cHS aquo, 6cHS hydroxo, 6cLS hydroxo, and 6cLS bound to Tyr, species (see text), are reported in light blue, dark yellow, violet, and green, respectively.

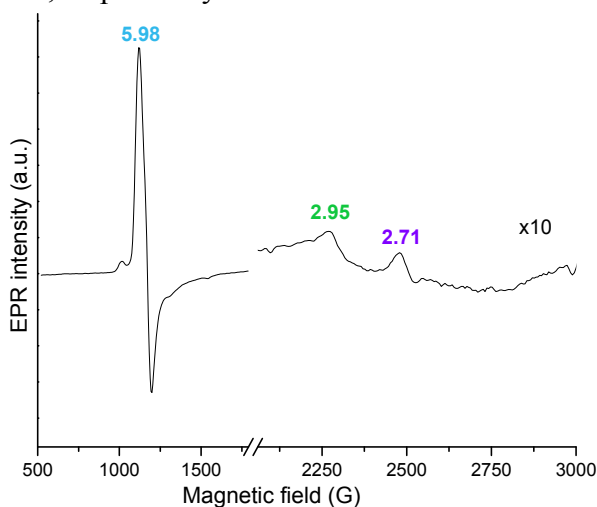


**Figure 6.6.** X-band EPR spectrum of Ph-trHbO-2217 at pH 7.6. The spectrum was recorded at 5 K, 9.39 GHz microwave frequency, 1 mW microwave power and 10 G modulation amplitude. The spectrum for magnetic fields greater than 2000 G is multiplied 10-fold. At magnetic fields > 3000 G, the spectrum is obscured by a broad intense cavity signal, which after subtraction leaves a badly distorted line shape.

These results are very similar to those obtained for the Ph-trHbO-0030 protein (**Figure 6.7** and **6.8**). The absorption maxima of the LS form of the Ph-trHbO-0030 at pH 7.6 [Giordano 2015], is reminiscent of those containing a tyrosinate coordinated to the heme iron atom, such as ferric *Chlamydomonas* chloroplast Hb [Das 1999a] and the hemophore HasA proteins from *Serratia marcescens* and *Pseudomonas aeruginosa* [Caillet-Saguy 2008, Alontaga 2009] EPR [ $g_1 = 2.95$ ] and RR spectra have confirmed the presence of a tyrosinate coordinated to the heme iron [Giordano 2015]. In particular the RR spectra obtained with the 514.5 nm excitation wavelength, in resonance with the Fe(III)-Tyrosinate charge transfer band (near 500 nm) [Que 1988], allowed the identification of the characteristic vibrational frequencies of bound phenolate  $\nu(\text{Fe}-\text{O}_{\text{Tyr}})$ ,  $\nu_{\text{Tyr}}(\text{C}-\text{O})$ , and  $\nu_{\text{Tyr}}(\text{C}=\text{C})$  at 590, 1312, and 1509  $\text{cm}^{-1}$ , respectively, not present in the spectrum upon excitation at 413.1 nm. The assignment to a 6cLS Fe(III)-Tyrosinate species was moreover strengthened from the comparison with the UV and visible RR spectra of various ferric-heme proteins which show a Tyrosinate (deprotonated Tyr) as distal ligand for which the band at 590  $\text{cm}^{-1}$  is very indicative [Das 1999a, Nagai 1989, Eakanunkul 2005, Aki 2010]. Based on the sequence alignments and the location of distal heme residues determined from the crystal structure (**Figure 6.4**), the distal TyrB10 is proposed to be the sixth ligand [Giordano 2015]. Remarkably, the crystal structure of Ph-trHbO-0030 does not give any indication of TyrB10 coordination to the heme iron atom. Therefore, the heme coordination is affected by the physical and/or environmental conditions experienced by the protein and this result highlights that the heme pocket of the cold-adapted truncated Ph-trHbO-0030 is highly flexible. Differences in heme coordination between solution and crystalline states have been described previously. In particular, analogous results have been reported in the *B. subtilis* dye-decolorizing peroxidase. A 6cHS state is mainly detected in the crystal, whereas in solution the protein is a 6cLS state [Sezer 2013].

Therefore, the 6cLS species present at pH 6.0 in the spectra of the Ph-trHbO-2217 protein and characterized by RR bands (298 K) at 1509 ( $\nu_3$ ),

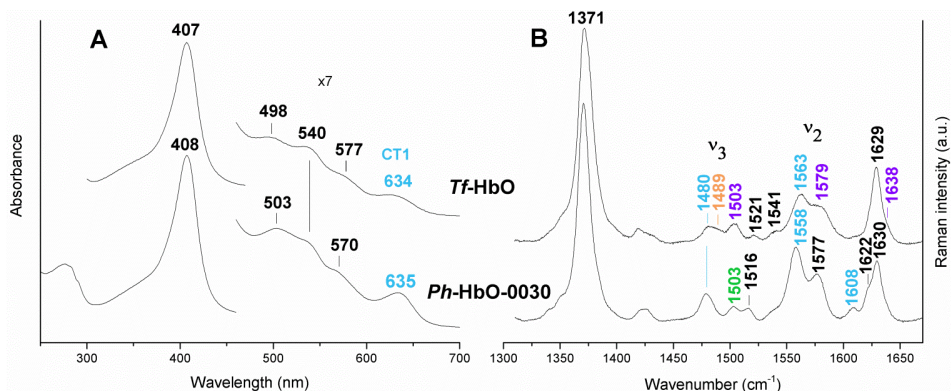


**Figure 6.7.** Electronic absorption (A), and high frequency RR (B), spectra obtained with the 413.1 nm excitation wavelength of ferric Tf-trHbO (top) [Nicoletti 2013] and Ph-trHbO-0030 (bottom) [Giordano 2015] at pH 6.0 and 7.6, respectively. The band positions (wavelengths and frequencies), assigned to the 6cHS aquo, 6cLS hydroxo, 6cLS bound to Tyr, and 5cHS species (see text), are reported in light blue, violet, green and orange, respectively.

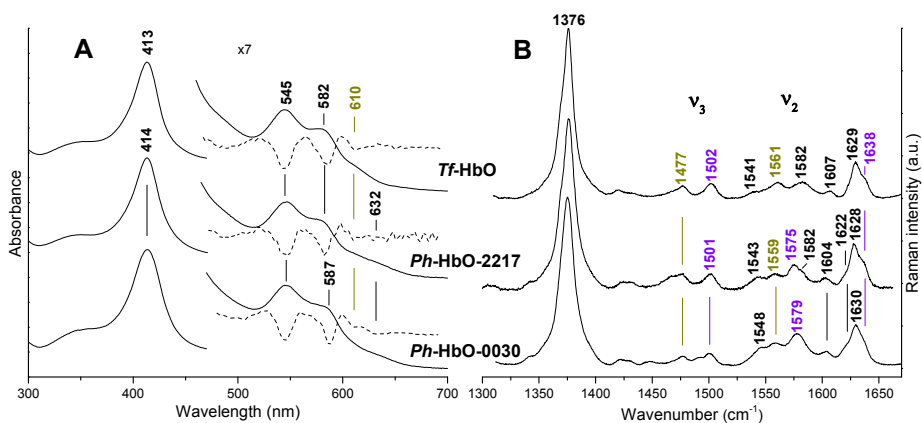


**Figure 6.8.** Electronic absorption (A), and high frequency RR (B), spectra obtained with the 413.1 nm excitation wavelength of ferric Tf-trHbO (top) [Nicoletti 2013], Ph-trHbO-2217 (middle), and Ph-trHbO-0030 (bottom) [Giordano 2015] at alkaline pH. The band positions (wavelengths and frequencies), assigned to the 6cLS and 6cHS, hydroxo ligated species (see text), are reported in violet and dark yellow, respectively.

1641 ( $\nu_{10}$ )  $\text{cm}^{-1}$  and the EPR  $g_1 = 2.95$ , in analogy with the Ph-trHbO-0030 at pH 7.4, was assigned to a Fe(III)-Tyrosinate species.

Similarly to Ph-trHbO-2217, in the Ph-trHbO-0030 protein at neutral pH the 6cLS Fe(III)-Tyrosinate species coexists with the main 6cHS aquo species (**Figure 6.7**). Lowering the pH (**Figure 6.8**) these two species progressively disappears, being the spectrum at alkaline pH dominated by the presence of  $\text{OH}^-$  ligated forms with a predominant LS [ $1501(\nu_3)$ ,  $1579(\nu_2)$ ,  $1638(\nu_{10}) \text{cm}^{-1}$ ] and a minor HS [ $1477(\nu_3)$ ,  $1559(\nu_2) \text{cm}^{-1}$ ] contribution.

Also the Tf-trHbO at neutral pH (**Figure 6.7**) is a mixture of a 6cHS aquo species [CT1 at 635 nm and RR core-size marker bands at 1480 ( $\nu_3$ ),  $1560(\nu_2) \text{cm}^{-1}$ ] and a 6cLS species [ $1503(\nu_3)$ ,  $1579(\nu_2)$ ,  $1638(\nu_{10}) \text{cm}^{-1}$ ]. The frequencies of this latter species remain almost unvaried also in the spectrum at alkaline pH, being therefore assigned to a hydroxo complex (**Figure 6.8**).

The  $\nu(\text{Fe-OH})$  stretching frequency is very sensitive to the distal environment. In the absence of any H-bond interaction, typical  $\nu(\text{Fe-OH})$  stretches are around 490 and  $550 \text{cm}^{-1}$  for 6cHS and 6cLS species, respectively. An increase of the H-bond strength between the hydroxo group and nearby proton donor/acceptor residues determines a decrease of the Fe-O electron density, and, as a consequence, a decrease in the frequency of the  $\nu(\text{Fe-OH})$  stretching mode.

Therefore, in order to obtain detailed information on the interaction between the distal residues of the Ph-trHbO-2217 protein and the hydroxo ligand, RR spectra in the low frequency region have been obtained at both room and low temperature (12-15 K). At low temperature the mixture of HS and LS OH ligated forms, becomes an almost pure 6cLS species. However, spectra of the LS form are almost identical between the two temperatures, with the advantage that at low temperature the resolution is higher, enabling the weak  $\nu(\text{Fe-OH})$  bands to be more easily identified thanks to its sensitivity to D and  $^{18}\text{O}$  isotopic substitution. Unfortunately, the Ph-trHbO-2217 protein was not stable in the  $\text{H}_2^{18}\text{O}$  buffer, therefore the  $\nu(\text{Fe-OH})$  band was assigned only on the on the basis of to the effect upon D substitution. **Figure 6.9** compares the low-frequency RR spectra of Ph-trHbO-2217 at alkaline

pH in H<sub>2</sub>O and D<sub>2</sub>O buffered solutions, at 298 K (**A, left**) and 80 K (**B, left**) together with the difference spectra H<sub>2</sub>O - D<sub>2</sub>O (**right**).

The 450-530 cm<sup>-1</sup> region of the spectra is quite complex, due to the porphyrin modes. However, on the basis of the isotopic substitution, the bands at 507 and 510 cm<sup>-1</sup> at 298 and 80 K, respectively, which shift to 496 and 499 cm<sup>-1</sup> in D<sub>2</sub>O at 298 and 80 K, respectively, have been assigned to the  $\nu(\text{Fe-OH})$  mode of a His-Fe-OH<sup>-</sup> 6cLS form. Accordingly, the difference spectrum at 80 K shows narrow and well-defined bands at 499 and 512 cm<sup>-1</sup>. The difference spectrum at 298 K shows two broad bands at 497 and 512 cm<sup>-1</sup>, possibly due to the concomitant presence of a His-Fe-OH<sup>-</sup> 6cHS form observed at room temperature in the RR high-frequency region (**Figure 6.5, B**).

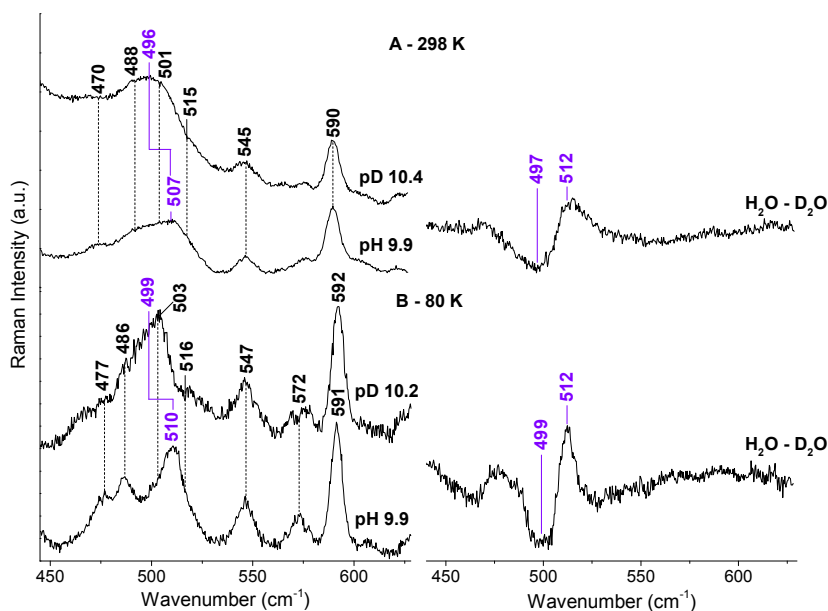


**Figure 6.9.** Comparison of the low-frequency region RR spectra at alkaline pH of ferric Ph-2/2HbO-2217 at room (panel A, left) and low temperature (panel B, left) in H<sub>2</sub>O (bottom) and D<sub>2</sub>O (top). The corresponding difference spectra H<sub>2</sub>O and D<sub>2</sub>O are also shown (panels A and B, right). The  $\nu(\text{Fe-OH})$  and  $\nu(\text{Fe-OD})$  mode frequencies are reported in violet. The spectra have been shifted along the ordinate axis to allow better visualisation. The intensity of the spectra is normalised to that of the  $\nu_4$  band. Experimental conditions: excitation wavelength 413.1 nm; pH 9.9; laser power at the sample 10 mW, average of 9 spectra with 45-min integration time (298 K) and of 3 spectra with 60-

min integration time (80K); pD 10.2: laser power at the sample 10 mW, average of 7 spectra with 70-min integration time (298 K) and laser power at the sample 5 mW, average of 4 spectra with 40-min integration time (80 K).

The frequency of the Ph-trHbO-2217  $\nu(\text{Fe-OH})$  mode at 80 K at  $512 \text{ cm}^{-1}$  is (**Figure 6.10**):

- $16 \text{ cm}^{-1}$  lower than that observed for Ph-trHbO-0030 ( $528 \text{ cm}^{-1}$  at 12 K [Giordano 2015]) indicating that in Ph-trHbO-2217 the H-bond interactions involving the hydroxo ion and the distal residues are stronger;
- $27 \text{ cm}^{-1}$  higher than that observed for Tf-trHbO ( $485 \text{ cm}^{-1}$  at 15 K [Nicoletti 2013]) indicating that in Ph-trHbO-2217 the H-bond interactions involving the hydroxo ion and the distal residues are weaker.

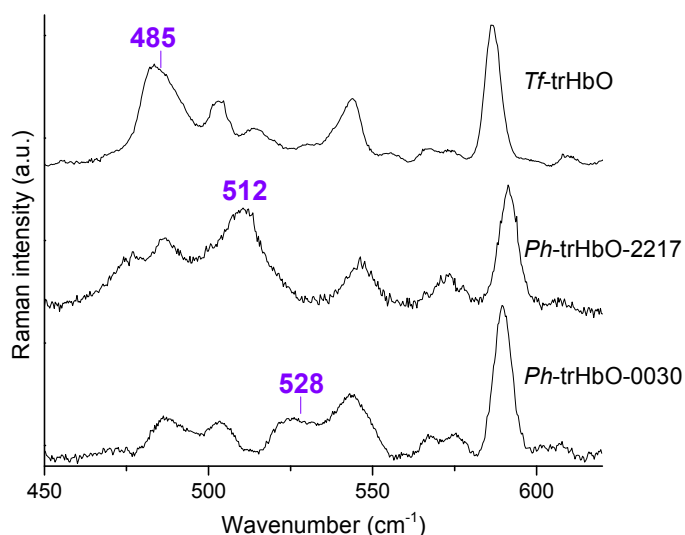


**Figure 6.10.** Comparison of the low-frequency region RR spectra of the ferric forms of Tf-trHbO (top) [Nicoletti 2013], Ph-trHbO-2217 (middle), and Ph-trHbO-0030 [Giordano 2015] (bottom) at alkaline pH, showing in violet the  $\nu(\text{Fe-OH})$  stretching modes of the 6cLS hydroxo species. The spectra have been obtained with the 413.1 nm excitation wavelength.

Interesting considerations could be done on the basis of the results of molecular dynamics (MD) simulations performed on the Tf-trHbO [Nicoletti 2014].

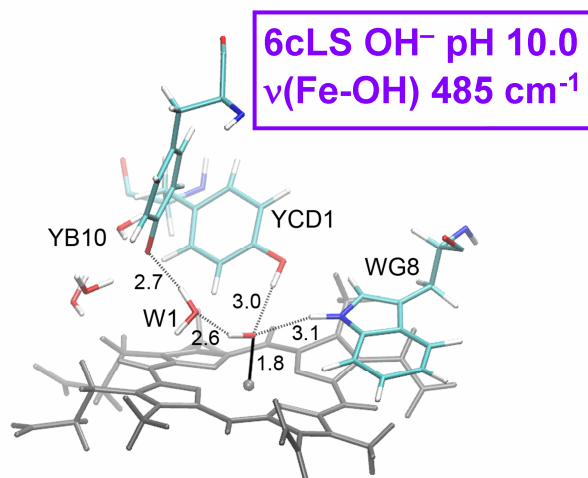


**Figure 6.11.** Schematic representations obtained on the basis of MD simulations of the distal side of Tf-trHbO at alkaline (right) [Nicoletti 2014] pH showing the hydrogen-bond network stabilizing the iron-bound H<sub>2</sub>O and OH<sup>-</sup>, respectively.

At alkaline pH, the MD simulation obtained with a deprotonated TyrB10 residue shows a conformation where the hydroxo ligand [Nicoletti 2014] (**Figure 6.11**):

- accepts direct H-bonds from the TrpG8 and TyrCD1 residues,
- donates a H-bond to a water molecule concomitantly H-bonded with the TyrB10 residue.

Therefore, as predicted by the extremely low  $\nu(\text{Fe-OH})$  RR frequency, the OH<sup>-</sup> ligand is stabilized by multiple (three) H-bonds, revealing a situation never observed so far in any other heme protein.

On the basis of these results, it can be hypothesized the presence of two H-bonds in Ph-trHbO-2217 and only one in Ph-trHbO-0030. The presence of only one H-bond interaction in Ph-trHbO-0030 is also confirmed by its similarity with the alkaline form of another representative of group II trHbs, Mt-trHbO from *Mycobacterium tuberculosis* in which the hydroxo ion is H-bonded with either the CD1 or B10 Tyr residue [Mukai 2002].

The different capability in ligand binding of the distal cavities of the three trHbs was further confirmed by the results obtained on the ferrous-carbon monoxide complexes (see below).

### 6.5 Ferrous forms

Upon reduction, the UV-Vis and RR high-frequency-region spectra of Ph-trHbO-2217 clearly reveal the presence of a 6cLS form (Soret band at 420 nm and RR bands at 1493 ( $\nu_3$ ), 1577 ( $\nu_2$ )  $\text{cm}^{-1}$ ) and a 5cHS form (Soret band at 435 nm and RR bands at 1470 ( $\nu_3$ ), 1558 ( $\nu_2$ ) and 1603 ( $\nu_{10}$ )  $\text{cm}^{-1}$ ), (**Figure 6.12**). Also the ferrous form of the Ph-trHbO-0030 is characterized by the presence of a 6cLS and a 5cHS species, being this latter less abundant than in the Ph-trHbO-2217. On the contrary, the Tf-trHb displays electronic absorption and RR spectra typical of a 5cHS species [Droghetti 2010].

The RR low-frequency-region spectra of the three trHbs is characterized by very strong band at: 227  $\text{cm}^{-1}$  for the Ph-trHbO-2217 (**Figure 6.12**), 222  $\text{cm}^{-1}$  for the Ph-trHbO-0030 [Giordano 2011], and 223  $\text{cm}^{-1}$  for the Tf-trHbO [Droghetti 2010], assigned to the  $\nu(\text{Fe-Im})$  stretching mode. These frequencies are similar to those of other trHbOs [Egawa 2005] and consistent with a staggered orientation (**Figure 6.13**), of the imidazole ring of the proximal His with respect to the four pyrrole nitrogen atoms of the porphyrin ring. Hence, the higher frequency of the  $\nu(\text{Fe-Im})$  stretching modes could, in part, be a consequence of the weakening of the repulsive interactions between the heme and the proximal His, which would allow a stronger Fe coordination. These observations are in agreement with the crystallographic data of Ph-trHbO-0030 [Giordano 2015] and Tf-trHbO [Bonamore 2005].

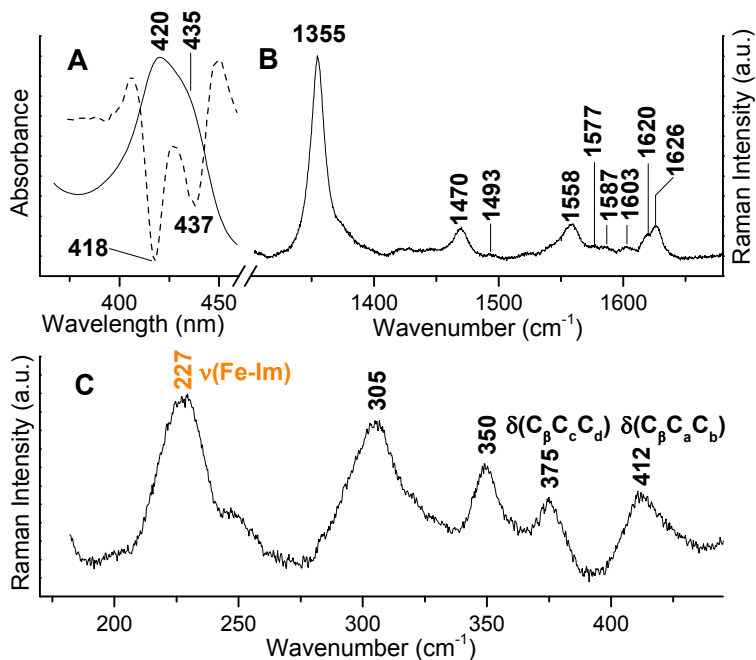


**Figure 6.12.** UV-Vis and its second derivative spectrum ( $D^2$ ) (dashed line) (A), RR spectra in the high- (B) and low-frequency region (C) of ferrous Ph-trHbO-2217 at pH 7.6. The spectra have been shifted along the ordinate axis to allow better visualisation. The  $\nu(\text{Fe-Im})$ , mode frequency is reported in orange. RR experimental conditions: excitation wavelength 441.6 nm; laser power at the sample 10 mW, average of 4 spectra with 20-min integration time.

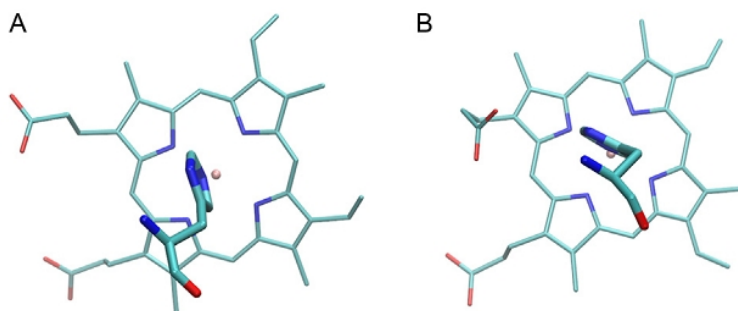


**Figure 6.13.** View of the proximal side of Tf-trHb (A) and Mb (B). The proximal histidine plane of Tf-trHb is shown to be staggered with respect to the heme nitrogen atoms, whereas that of Mb is eclipsed. Data from PDB entries 2BMM [Bonamore 2005] and 1VXG [Yang 1996], respectively. This figure has been taken from [Howes 2015b].

## 6.6 Ferrous-CO adducts

As already stated, the  $\nu(\text{FeC})$  and  $\nu(\text{CO})$  stretching frequencies can give information on the architecture of the distal heme pocket being the Fe-CO back-bonding very sensitive to the formation of H-bonds between the bound CO and the distal protein residues. The  $\nu(\text{Fe-C})$  and  $\nu(\text{CO})$  of the ferrous CO adduct of the Ph-trHbO-2217 are at  $506\text{ cm}^{-1}$  and  $1940\text{ cm}^{-1}$ , respectively (**Figure 6.14** and **6.15**), indicating a moderately polar form.

An analogous CO conformer is observed also in the ferrous CO adduct of the Tf-trHbO [form 1 with  $\nu(\text{FeC})$  and  $\nu(\text{CO})$  at  $509$  and  $1940\text{ cm}^{-1}$ , respectively], together with another more polar [form 2 with  $\nu(\text{FeC})$  and  $\nu(\text{CO})$  at  $518$  and  $1920\text{ cm}^{-1}$ , respectively] [Droghetti 2010] (**Figure 6.14** and **6.15**).

Accordingly, MD simulations on Tf-trHbO indicated that the CO molecule interacts with TrpG8 in form 1, and with both TrpG8 and TyrCD1 in form 2.

Similarly to Tf-trHbO form 1, it can be hypothesize that also in the Ph-trHbO-2217 cavity the CO is involved in one H-bond interaction.

Conversely the  $\nu(\text{Fe-C})$  and  $\nu(\text{CO})$  of the ferrous CO adduct of the Ph-trHbO-0030, are at  $494\text{ cm}^{-1}$  and  $1960\text{ cm}^{-1}$ , respectively [Giordano 2011] (**Figure 6.15**). The frequencies of this form are at the extreme right of the correlation plot (**Figure 6.16**) together with those of the triple YB10F-YCD1F-WG8F mutant of Tf-trHbO, where all the polar distal residue (TyrB10(54), TyrCD1(67), and TrpG8(119)) were mutated in non H-bonding Phe [ $\nu(\text{FeC})$  at  $494\text{ cm}^{-1}$  and  $\nu(\text{CO})$  at  $1957\text{ cm}^{-1}$ ] [Droghetti 2010]. This clearly indicates that in these latter proteins no distal interactions with the bound CO can be envisaged.

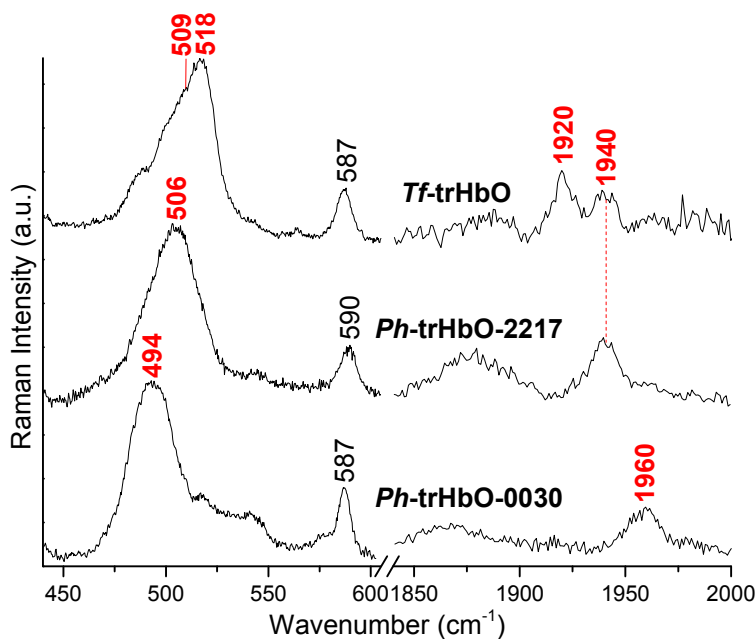


**Figure 6.14.** Comparison of the  $^{12}\text{CO}$  complexes of Tf-trHbO (top) [Droghetti 2010], Ph-trHbO-2217 (middle), and Ph-trHbO-0030 [17] (bottom) in the low-frequency (left) and high-frequency (right) RR regions showing in red the  $\nu(\text{Fe-C})$  and  $\nu(\text{CO})$  stretching modes, respectively. The spectra have been obtained with the 413.1 nm excitation wavelength.

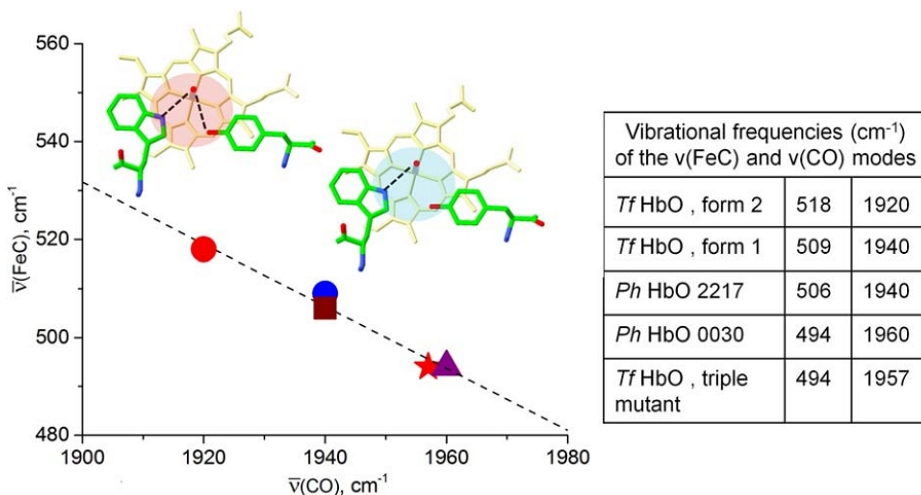


**Figure 6.15.** Correlation line between the  $\nu(\text{FeC})$  and  $\nu(\text{CO})$  frequencies of the two conformers of Tf-trHbO (form 1, blue circle, and form 2, red circle) and its YB10FYCD1FWG8F triple mutant (red star),

Ph-HbO-0030 (purple triangle), and Ph-HbO-2217 (brown square). The schematic representation of the distal side of Tf-trHb, showing the H-bonds involving the iron-bound CO determined on the basis of MD simulations are also reported.

The overall data strongly indicate the different ligand binding capabilities of the trHbOs from the thermophilic actinobacterium *Thermobifida fusca* and the Antarctic bacterium *Pseudoalteromonas haloplanktis*. In particular the ligand binding is strongly stabilized in Tf-trHbO (by two and three H-bonds for the CO and OH<sup>-</sup> ion, respectively), while in the two Ph-trHbO the stabilization is weaker, probably due to the replacement of the CD1 residue from Tyr (Tf-trHbO) to His (Ph-trHbOs).

However, the two Ph-trHbOs do not behave in the same way. Ph-HbO-2217 binds ligands more strongly than Ph-trHbO-0030, indicating that the ligand binding mechanism is not determined exclusively by interactions with distal polar residues, but that other changes in the sequence are also involved, being accordingly the sequence identity between the two Antarctic trHbs of only the 24%.

## 6.7 Conclusions

Ligand binding in heme-containing proteins is determined by a number of factors, including the nature and conformation of the distal residues and their capability to stabilize the heme-bound ligand via hydrogen-bonding and electrostatic interactions.

The spectroscopic study on the Ph-trHbO-2217 and the comparison with the data obtained for other two trHbO proteins, Ph-trHbO-0030 and Tf-trHbO, reveal that despite the high similarity of the distal cavity the ligand binding capability of these three proteins is quite different, being stronger in Tf-trHbO. Moreover the finding that Ph-trHbO-2217 binds ligands more strongly than Ph-trHbO-0030 indicates that the ligand binding mechanism is not determined exclusively by interactions with distal polar residues, but that other changes in the sequence are also involved, being accordingly the sequence identity between the two Antarctic trHbs of only the 24%. This different behavior might be correlated to possible different functional roles in bacterial physiology

of the two proteins, taking into account that the axial ligand strength is a fundamental property of a heme protein, capable of influencing the kinetics of ligand binding as well as providing alternative functional roles.

Another interesting result concerns the internal ligand-coordination, which gives rise to a 6cHS aquo species in equilibrium with a 6cLS form where the distal residue is an hydroxo ion in Tf-trHbO and a tyrosinate ion (likely due to TyrB10) in Ph-trHbOs. This latter form, however, is present only in solution, as the 6cHS aquo state is the stable form observed in crystals [Giordano 2011, Giordano 2015, Howes 2011, Russo 2013].

## References

- ❖ Aki Y., Nagai M., Nagai Y., Imai K., Aki M., Sato A., Kubo M., Nagatomo S., Kitagawa T., *J. Biol. Inorg. Chem.* 2010, 15, 147.
- ❖ Alontaga A.Y., Rodriguez J.C., Schonbrunn E., Becker A., Funke T., Yukl E.T., Hayashi T., Stobaugh J., Monne-Loccoz P., Rivera M., *Biochemistry* 2009, 48, 96.
- ❖ Ascenzi P., De Marinis E., Visca P., Ciaccio C., Coletta M., *Biochem. Biophys. Res. Commun.* 2009, 380, 392.
- ❖ Ascenzi P., Di Masi A., Tundo G.R., Pesce A., Visca P., Coletta M., *PLoS One* 2014, 9, e102811.
- ❖ Bolognesi M., Rosano C., Losso R., Borassi A., Rizzi M., Wittenberg J.B., Boffi A., Ascenzi P., *Biophys. J.* 1999, 77, 1093.
- ❖ Bonamore A., Ilari A., Giangiacomo L., Bellelli A., Morea V., Boffi A., *FEBS J.* 2005, 272, 4189.
- ❖ Boubeta F.M., Bari S.E., Estrin D.A., Boechi L., *J. Phys. Chem. B* 2016, 120, 9642.
- ❖ Bustamante J.P., Radusky L., Boechi L., Estrin D.A., Ten Have A., Marti M.A., *PLoS Comp. Biol.* 2016, 12, e1004701.
- ❖ Caillet-Saguy C., Turano P., Piccioli M., Lukat-Rodgers G.S., Czjzek M., Guigliarelli B., Izadi-Pruneyre N., Rodgers K.R., Delepierre M., Lecroisey A., *J. Biol. Chem.* 2008, 283, 5960.
- ❖ Das (a) T.K., Couture M., Lee H.C., Peisach J., Rousseau D.L., Wittenberg B.A., Wittenberg J.B., Guertin M., *Biochemistry* 1999, 38, 15360.
- ❖ Das (b) T.K., Franzen S., Pond A., Dawson J.H., Rousseau D.L., *Inorg. Chem.* 1999, 38, 1952.

- ❖ De Marinis E., Casella L., Ciaccio C., Coletta M., Visca P., Ascenzi P., IUBMB Life 2009, 61, 62.
- ❖ Droghetti E., Nicoletti F.P., Bonamore A., Boechi L., Arroyo-Manez, P., Estrin D.A., Boffi A., Smulevich G., Feis A., Biochemistry 2010, 49, 10394.
- ❖ Eakanunkul S., Lukat-Rodgers G.S., Sumithran S., Ghosh A., Rodgers K.R., Dawson J.H., Wilks A., Biochemistry 2005, 44, 13179.
- ❖ Egawa T., Yeh S.R., J. Inorg. Biochem. 2005, 99, 72.
- ❖ Frey A.D., Kallio P T., FEMS Microbiol. Rev. 2003, 27, 525–545.
- ❖ Gardner P.R., J. Inorg. Biochem. 2005, 99, 247.
- ❖ Giordano D., Parrilli E., Dettaï A., Russo R., Barbiero G., Marino G., Lecointre G., di Prisco G., Tutino M.L., Verde C., Gene 2007, 398, 69.
- ❖ Giordano D., Russo R., Ciaccio C., Howes B.D., di Prisco G., Marden M.C., Hui G., Hoa B., Smulevich G., Coletta M., Verde C., IUBMB Life 2011, 63, 566.
- ❖ Giordano D., Coppola D., Russo R., Tinajero-Trejo M., di Prisco G., Lauro F., Ascenzi P., Verde C., Adv. Microb. Physiol. 2013, 63 329.
- ❖ Giordano D., Pesce A., Boechi L., Bustamante J.P., Caldelli E., Howes B.D., Riccio A., di Prisco G., Nardini M., Estrin D., Smulevich G., Bolognesi M., Verde C., FEBS J. 2015, 282, 2948.
- ❖ Howes B.D., Rodriguez-Lopez J.N., Smith A.T., Smulevich G., Biochemistry 1997, 36, 1532.
- ❖ Howes B.D., Giordano D., Boechi L., Russo R., Mucciacciaro S., Ciaccio C., Sinibaldi F., Fittipaldi M., Martí M.A., Estrin D.A., di Prisco G., Coletta M., Verde C., Smulevich G., J. Biol. Inorg. Chem. 2011, 16, 299.
- ❖ Howes (a) B.D., Boechi L., Boffi A., Estrin D.E., Smulevich G., Recent Adv. Microb. 2015, 67, 85.
- ❖ Howes (b) B.D., Boechi L., Boffi A., Estrin D.E., Smulevich G. (2015). Bridging Theory and Experiment to Address Structural Properties of Truncated Haemoglobins: Insights from *Thermobifida fusca* HbO. In *Advances in microbial physiology* (Poole R.K. Ed.) vol. 67, pp. 85-126, Academic Press, Oxford, UK.
- ❖ Johnson E.A., Lecomte J.T., Adv. Microb. Physiol. 2013, 63, 195.
- ❖ Li X.Y., Spiro T.G., J. Am. Chem. Soc. 1988, 110, 6024.
- ❖ Lukat-Rodgers G.S., Rodgers K.R., J. Biol. Inorg. Chem. 1998, 3, 274.
- ❖ Milani M., Pesce A., Nardini M., Ouellet H., Ouellet Y., Dewilde S., Bocedi A., Ascenzi P., Guertin M., Moens L., Friedman J.M., Wittenberg J.B., Bolognesi M., J. Inorg. Biochem. 2005, 99, 97.

- ❖ Mukai M., Savard P.Y., Ouellet H., Guertin M., Yeh S.R., *Biochemistry* 2002, 41, 3897.
- ❖ Nagai M., Yoneyama Y., Kitagawa T., *Biochemistry* 1989, 28, 2418.
- ❖ Nicoletti F.P., Droghetti E., Howes B.D., Bustamante J.P., Bonamore A., Sciamanna N., Estrin D.A., Feis A., Boffi A., Smulevich G., *Biochim. Biophys. Acta Proteins Proteom.* 2013, 1834, 1901.
- ❖ Nicoletti F.P., Bustamante J.P., Droghetti E., Howes B.D., Fittipaldi M., Bonamore A., Baiocco P., Feis A., Boffi A., Estrin D.A., Smulevich G., *Biochemistry* 2014, 53, 8021.
- ❖ Pesce A., Couture M., Dewilde S., Guertin M., Yamauchi K., Ascenzi P., Moens L., Bolognesi M., *EMBO J.* 2000, 19, 2424.
- ❖ Pesce A., Bolognesi M., Nardini M., *Adv. Microb. Physiol.* 2013, 63, 49.
- ❖ Pesce A., Bustamante J.P., Bidon-Chanal A., Boechi L., Estrin D.A., Luque F.J., Sebilo A., Guertin M., Bolognesi M., Ascenzi P., Nardini M., *FEBS J.* 2016, 283, 305.
- ❖ Phillips G.N., Teodoro M.L., Li T.S., Smith B., Olson J.S., *J. Phys. Chem. B* 1999, 103, 8817.
- ❖ Que L., *Biol. Appl. Raman Spectrosc.* 1988, 3, 491.
- ❖ Sato T., Tamiya H. (1937) *Cytologia*, pp. 1133-1138, Fujii Jubilee Volume.
- ❖ Ray G.B., Li X.Y., Ibers J.A., Sessler J.L., Spiro T.G., *J. Am. Chem. Soc.* 1994, 116, 162.
- ❖ Russo R., Giordano D., Di Prisco G., Hui Bon Hoa G., Marden M.C., Verde C., Kiger L., *Biochim. Biophys. Acta* 2013, 1834, 1932.
- ❖ Sezer M., Santos A., Kielb P., Pinto T., Martins L.O., Todorovic S., *Biochemistry* 2013, 52, 3074.
- ❖ Smulevich G., Miller M.A., Kraut J., Spiro T.G., *Biochemistry* 1991, 30, 9546.
- ❖ Spiro T.G., Wasbotten I. H., *J. Inorg. Biochem.* 2005, 99, 34.
- ❖ Vinogradov S.N., Moens L., *J. Biol. Chem.* 2008, 283, 8773.
- ❖ Vinogradov (a) S.N., Bailly X., Smith D.R., Tinajero-Trejo M., Poole R.K., Hoogewijs D., *Adv. Microb. Physiol.* 2013, 63, 391.
- ❖ Vinogradov (b) S.N., Tinajero-Trejo M., Poole R.K., Hoogewijs D., *Biochim. Biophys. Acta Proteins Proteom.* 2013, 1834, 1789.
- ❖ Vuletich D.A., Lecomte J.T., *J. Mol. Evol.* 2006, 62, 196.
- ❖ Wajcman H., Kiger L., Marden M.C., *C.R. Biol.* 2009, 332, 273.
- ❖ Wittenberg J.B., Bolognesi M., Wittenberg B.A., Guertin M., *J. Biol. Chem.* 2002, 277, 871.
- ❖ Yang, F., Phillips G.N Jr., *J. mol. biol.*, 1996, 256, 762.

## Chapter 7

### **The structural similarity of the heme crevice of the hemoglobins of the Greenland shark *Somniosus microcephalus* with that of human hemoglobin**

Roberta Russo, Daniela Giordano, Gianluca Paredi, Francesco Marchesani, **Lisa Milazzo**, Giovanna Altomonte, Pietro Del Canale, Stefania Abbruzzetti, Paolo Ascenzi, Guido di Prisco, Cristiano Viappiani, Angela Fago, Stefano Bruno, Giulietta Smulevich, Cinzia Verde,

“The Greenland shark *Somniosus microcephalus* - Hemoglobins and ligand-binding properties”,

*PloS one* **2017**, 12 (10), e0186181.

#### **7.1 Introduction**

Organisms living in polar environments are exposed to extremely challenging conditions. Arctic regions are inhabited by cold-adapted species like cartilaginous fishes, such as sharks and skates, that are notably present, with about 8% of the species [Mecklenburg 2011]. Greenland sharks typically inhabit deep and extremely cold waters, although distribution is quite wide [MacNeal 2012]. *Somniosus microcephalus* is the largest fish species in the Arctic Ocean and likely plays an important ecological role in the marine ecosystem. In fact, widespread changes in the Arctic ecosystem, as a consequence of climate, have led to an increased attention on trophic dynamics and on the role of potential apex predators such as *S. microcephalus* in the structure of Arctic marine food webs [MacNeal 2012]. Recent results demonstrated that *S. microcephalus* is one of the longest-living vertebrate species, with the largest captured animal (502 cm) estimated

to be almost 400 years old [Nielsen 2016]. The remarkable evolutionary success of such species has raised considerable interest in their respiratory control mechanisms [Butler 1988]. Nevertheless, the hemoglobins (Hbs) of polar cartilaginous fishes have not still been studied extensively, probably due to the presence of multiple isoforms [Pennelly 1975, Dickinson 1981, Brittain 1982, Weber 1983, Wells 1985, Verde 2005], complicating the investigation of the structure-function relationships. The present study was aimed to study the structural properties of the Hbs (Hb1, Hb2, Hb3) of *S. microcephalus* to gain information on the heme cavity, heme oxidation and coordination states.

## 7.2 Materials

Cloning, expression and purification of the *S. microcephalus* Hb1, Hb2 and Hb3 protein were performed by the Dr. Cinzia Verde's group (Naples CNR).

Ferric *S. microcephalus* Hbs at pH 5.0, 7.6, and 10.6 were prepared in 50 mM MES [2-(N-morpholino) ethanesulfonic acid], 20 mM Tris-HCl and 50 mM glycine, respectively. The hydroxyl complex in isotopically enriched water was prepared by washing Hbs in 20 mM Tris-HCl pH 7.6 with 0.1 mM glycine pH 11.0 prepared with D<sub>2</sub>O (99.8%; purchased from Merck AG, Darmstadt, Germany). Ferrous samples at pH 7.6 were prepared by addition of 2-3  $\mu$ L of a freshly prepared sodium dithionite solution (10 mg/mL) to the ferric forms (40  $\mu$ L) previously degassed with nitrogen. The Fe(II)-CO complexes at pH 7.6 were prepared by flushing ferric Hbs (40  $\mu$ L) firstly with nitrogen, then with CO and reducing the heme by addition of 2-3  $\mu$ L a freshly prepared sodium dithionite solution (10 mg/mL). Isotopically enriched gaseous CO was purchased from Rivoira (Milan, Italy). The Fe(II)-O<sub>2</sub> complexes at pH 7.6 were prepared by reduction of the ferric form (50  $\mu$ L) with 2-3  $\mu$ L of a freshly prepared sodium dithionite solution (10 mg/mL), followed by gel filtration on a Sephadex G-25 Medium column equilibrated with the Tris-HCl buffer. Protein concentrations in the range 5-30  $\mu$ M were used. The protein concentration was estimated on the basis of the molar absorptivity,  $\epsilon = 150 \text{ mM}^{-1} \text{ cm}^{-1}$  at 405 nm.

### 7.3 UV-Vis and Resonance Raman characterization

The three isoforms of *S. microcephalus* Hbs display identical electronic absorption and RR spectra, therefore, only the results obtained for Hb3 are reported. In **Figure 7.1** are reported the spectra of the ferric form which are very similar to those of human HbA [Perutz 1974, Feis 1994]. At pH 5.0, a pure six-coordinated (6c) aquo high-spin (HS) species is observed and remains predominant at pH 7.6, where weak bands assigned to the alkaline species grows in. At pH 10.6 the spectra are typical of a His-Fe-OH<sup>-</sup> ligation. As in HbA, the CT band at 603 nm together with the RR core size marker bands clearly indicate the presence of a hydroxo ligand bound to the heme iron, which exists in a spin-state equilibrium at room temperature, giving rise to a mixture of low- and high-spin species.

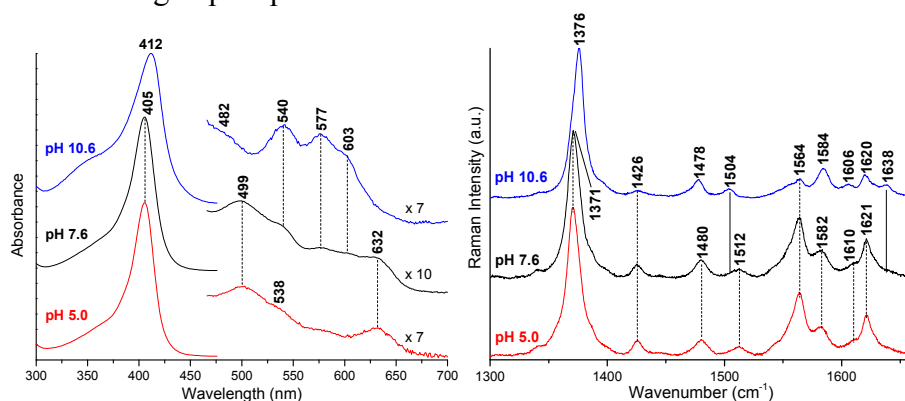


**Figure 7.1.** Spectra of the ferric form of Hb3 at pH 5.0 (red), 7.6 (black) and 10.6 (blue). Left: UV-Vis spectra, the 470–700 nm region of the spectra is expanded 7 or 10-fold. Right: RR spectra in the high frequency region. The intensity of the spectra is normalized to that of the  $\nu_4$  band. Experimental conditions: excitation wavelength 406.7 nm, laser power at the sample 5 mW, average of 4 spectra with 20 min integration time (pH 5.0) and average of 2 spectra with 10 min integration time (pH 7.6); excitation wavelength 413.1 nm, laser power at the sample 5 mW, average of 6 spectra with 30 min integration time (pH 10.6). The spectra have been shifted along the ordinate axis to allow better visualization.

Upon reduction, the protein gives rise to a 5cHS form, which fully binds either O<sub>2</sub> or CO, as shown by the corresponding typical electronic absorption spectra (**Figure 7.2**).

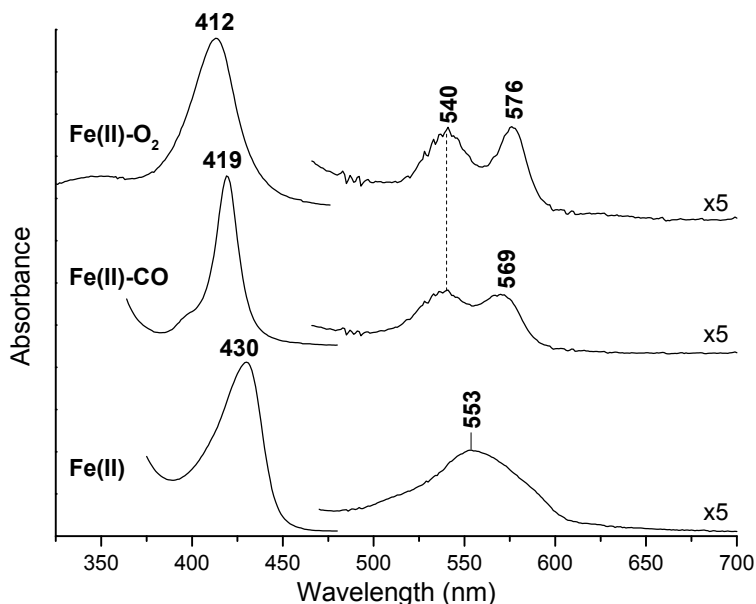


**Figure 7.2.** UV-Vis spectra of Hb3. From the bottom: ferrous form, Fe(II)-CO and Fe(II)-O<sub>2</sub> complexes. The 470–700 nm region of the spectra is expanded 5-fold. The spectra have been shifted along the ordinate axis to allow better visualization.

In order to obtain information on the ligand strength and interaction with the proximal and distal cavity residues, RR spectra in the low-frequency region have been obtained. **Figure 7.3** shows the low-frequency RR spectra of the ferric form at neutral and alkaline pH, and of the ferrous species before and after addition of O<sub>2</sub> and CO. The comparison between the RR spectra of the ferric forms at pH 7.6 and 10.6, together with the D<sub>2</sub>O experiments at alkaline pH (**Figure 7.4**), allowed identification of the isotope sensitive  $\nu(\text{Fe-OH})$  stretching modes at 493 and 556 cm<sup>-1</sup>, for the HS and LS species, respectively. Their frequencies are very similar to those observed in HbA (**Table 7.1**) [Feis 1994]. Moreover, the  $\delta(\text{C}_\beta\text{C}_\gamma\text{C}_\delta)$  propionate bending mode downshifts by about 3-4 cm<sup>-1</sup> in D<sub>2</sub>O as respect to H<sub>2</sub>O. This was already observed for HbA [Feis 1994] where propionate groups are H-

bonded to adjacent side chains [Ladner 1977] and the H/D shift is due to the different strengths of H- and D-bonds. Similarly, for *S. microcephalus* Hb3 the frequency shift upon H/D exchange could be due to an alteration of the H-bond network involving the propionate groups.

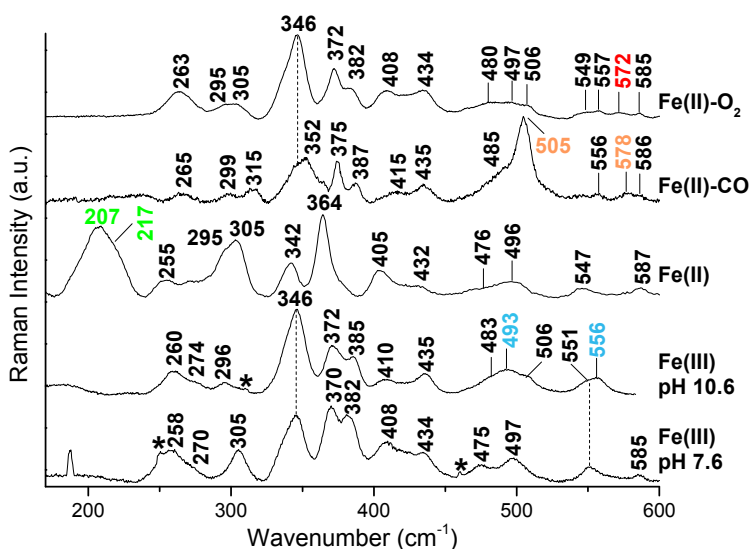


**Figure 7.3.** RR spectra in the low-frequency region of the ferric form at pH 7.6 and 10.6, ferrous form at pH 7.6, Fe(II)-CO and Fe(II)-O<sub>2</sub> complexes of Hb3. Experimental conditions: [Fe(III), pH 7.6]: excitation wavelength 406.7 nm, laser power at the sample 5 mW, average of 5 spectra with 25-min integration time; [Fe(III), pH 10.6]: excitation wavelength 413.1 nm, laser power at the sample 5 mW, average of 21 spectra with 105-min integration time; [Fe(II)]: excitation wavelength 441.6 nm, laser power at the sample 10 mW, average of 10 spectra with 50-min integration time; [Fe(II)-CO]: excitation wavelength 413.1 nm, laser power at the sample 0.8mW with cylindrical lens, average of 28 spectra with 140-min integration time; [Fe(II)-O<sub>2</sub>]: excitation wavelength 413.1 nm, laser power at the sample 5mW with cylindrical lens, average of 56 spectra with 280-min integration time. The  $\nu(\text{Fe-OH})$ ,  $\nu(\text{Fe-Im})$ ,  $\nu(\text{Fe-C})$  and the  $\delta(\text{C-O})$ , and the  $\nu(\text{Fe-O}_2)$  bands are shown in light blue, green, orange, and red respectively. The spectra have been shifted along the ordinate axis to allow better visualisation.

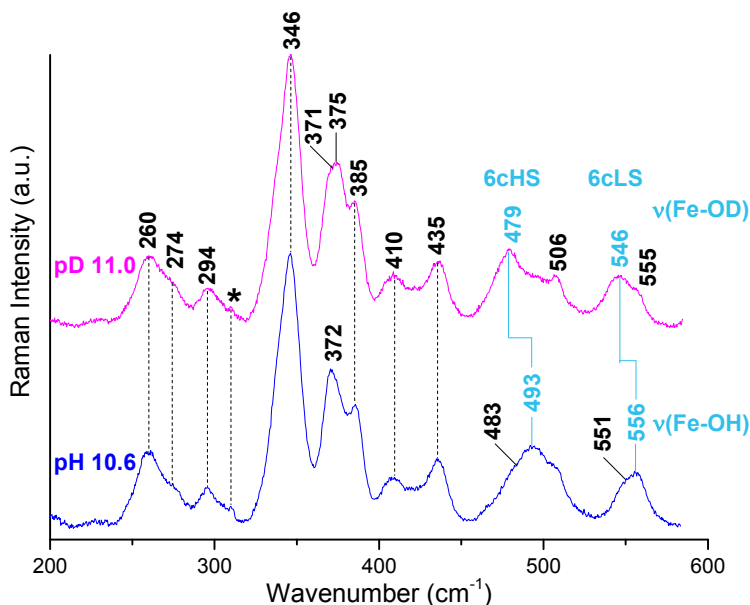


**Figure 7.4.** RR spectra in the low frequency region of the ferric form of Hb3 at alkaline pH in H<sub>2</sub>O (blue) and D<sub>2</sub>O (magenta). The spectra have been shifted along the ordinate axis to allow better visualization. The intensity of the spectra is normalized to that of the  $\nu_4$  band. Experimental conditions: excitation wavelength 413.1 nm, laser power at the sample 5 mW, average of 21 spectra with 105 min integration time (pH 10.6) and average of 12 spectra with 60 min integration time (pD 11.0). The  $\nu(\text{Fe-OH})$  (bottom) and  $\nu(\text{Fe-OD})$  (top) stretching modes are shown in light blue.

In the low-frequency RR spectra of the CO adduct, three isotope sensitive bands are identified (**Figure 7.5**) at 505, 578 and 1951  $\text{cm}^{-1}$ , and are assigned to the  $\nu(\text{Fe-CO})$ ,  $\delta(\text{Fe-CO})$  and  $\nu(\text{CO})$  modes, respectively. These frequencies are almost identical to those of HbA [Tsubaki 1982].

The  $\nu(\text{Fe-O}_2)$  stretching mode of the oxy complex of Hb3 was assigned to the band at 572  $\text{cm}^{-1}$  (568  $\text{cm}^{-1}$  in HbA [Brunner 1974, Nagai 1980a]) on the basis of its pronounced intensity decrease at high laser power (data not shown). However, the intensity decrease is not solely due to photolysis of the O<sub>2</sub> ligand, since upon increasing the laser power formation of the ferric form is observed, probably due to faster auto-

oxidation of Hb3 with respect to HbA (as demonstrated by autoxidation kinetics, performed by others).

**Table 7.1.** Comparison of the Fe-ligand mode frequencies of *S. microcephalus* Hbs (Hb1, Hb2, Hb3) with those of human HbA.

	$\nu(\text{Fe-O}_2)$	Fe-CO [ $\text{Fe-}^{13}\text{CO}$ ]			$\nu(\text{Fe-OH})$ [ $\text{Fe-OD}$ ] <sup>a</sup>		$\nu(\text{Fe-Im})$	
		$\nu(\text{Fe-CO})$	$\delta(\text{Fe-CO})$	$\nu(\text{CO})$	HS	LS	215 (T) <sup>b</sup>	
HbA	568 <sup>c</sup>	506 <sup>d</sup>	578 <sup>d</sup>	1951 <sup>e</sup>	492 [479]	553 [544]	203- 207 ( $\alpha$ )	217- 220 ( $\beta$ ) <sup>b,f</sup>
Hb1 Hb2 Hb3	572	505 [500]	578 [560]	1951 [1985]	493 [479]	556 [546]	207 ( $\alpha$ )	217 ( $\beta$ )

<sup>a</sup> Feis 1994, <sup>b</sup> Nagatomo 2015, <sup>c</sup> Hirota 1994, <sup>d</sup> Rajani 1998, <sup>e</sup> Tsubaki 1982, <sup>f</sup> Nagai 1980b.

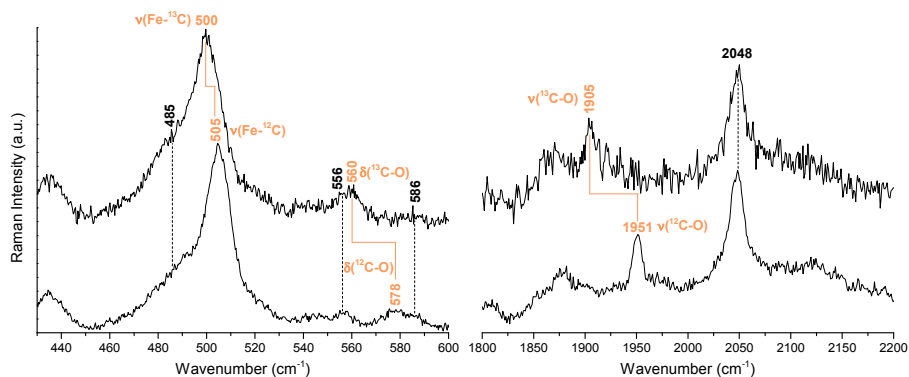


**Figure 7.5.** RR spectra in the low (left) and high (right) frequency region the of the Fe(II)-<sup>12</sup>CO (bottom) and Fe(II)-<sup>13</sup>CO (up) complexes. The spectra have been shifted along the ordinate axis to allow better visualization. Experimental conditions: excitation wavelength 413.1 nm, laser power at the sample 0.8 mW with cylindrical lens, average of 28 spectra with 140 min integration time (left, Fe(II)-<sup>12</sup>CO complex) and of 21 spectra with 105 min integration time (right, Fe(II)-<sup>12</sup>CO complex); excitation wavelength 413.1 nm, laser power at the sample 0.2 mW with cylindrical lens, average of 12 spectra with 60 min integration time (left, Fe(II)-<sup>13</sup>CO complex) and of 20 spectra with 100 min integration time

(right, Fe(II)-<sup>13</sup>CO complex). The  $\nu(\text{Fe-C})$ ,  $\delta(\text{C-O})$  and  $\nu(\text{C-O})$  bands are shown in orange.

The ferrous form is a pure 5cHS species (**Figure 7.2**) and in the low-frequency RR spectra for excitation in resonance with the Soret band ( $\lambda_{\text{exc}}$  441.6 nm) shows a strong band at  $207\text{ cm}^{-1}$  with a shoulder at  $217\text{ cm}^{-1}$  (**Figure 7.3**) which is assigned to the  $\nu(\text{Fe-Im})$  stretching mode. In fact, the  $\nu(\text{Fe-Im})$  stretching mode is only observed in the 5cHS ferrous heme proteins for Soret excitation and decreases in the RR spectrum obtained with  $\lambda_{\text{exc}}$  413.1 nm (**Figure 7.6**) [Kitagawa 1988, Hori 1980, Stein 1980]. The  $\nu(\text{Fe-Im})$  stretching mode is observed at  $215\text{ cm}^{-1}$  for deoxyHbA under physiological conditions [Nagai 1980a, Nagai 1980b, Kitagawa 1979, Kitagawa 1988, Matsukawa 1985]. Although this wavenumber is regarded as a marker of the T state, the observed  $\nu(\text{Fe-Im})$  RR band contains contributions from both the  $\alpha$  and  $\beta$  subunits. Studies of valency-hybrid Hbs, including HbM Boston ( $\alpha\text{MFe}^{3+}$ - $\beta\text{Fe}^{2+}$ ), HbM Milwaukee ( $\alpha\text{Fe}^{2+}$ - $\beta\text{MFe}^{3+}$ ),  $\alpha(\text{Fe}^{3+}\text{-CN})\beta(\text{Fe}^{2+}\text{-deoxy})$  and  $\alpha(\text{Fe}^{2+}\text{-deoxy})\beta(\text{Fe}^{3+}\text{-CN})$ , demonstrated a clear difference in the  $\nu(\text{Fe-Im})$  frequencies between the  $\alpha$  and  $\beta$  subunits. It is now established that the  $\nu(\text{Fe-Im})$  modes of deoxyHb in the T state are located at  $203\text{-}207$  and  $217\text{-}220\text{ cm}^{-1}$  in the  $\alpha$  and  $\beta$  subunits, respectively [Nagai 1980b], consistent with the longer Fe-Im bond-length in the  $\alpha$  compared to  $\beta$  subunits observed in the crystal structure [Park 2006]. Therefore, the two bands of Hb3 have been assigned to the  $\nu(\text{Fe-Im})$  of the  $\alpha$  ( $207\text{ cm}^{-1}$ ) and  $\beta$  ( $217\text{ cm}^{-1}$ ) subunits.

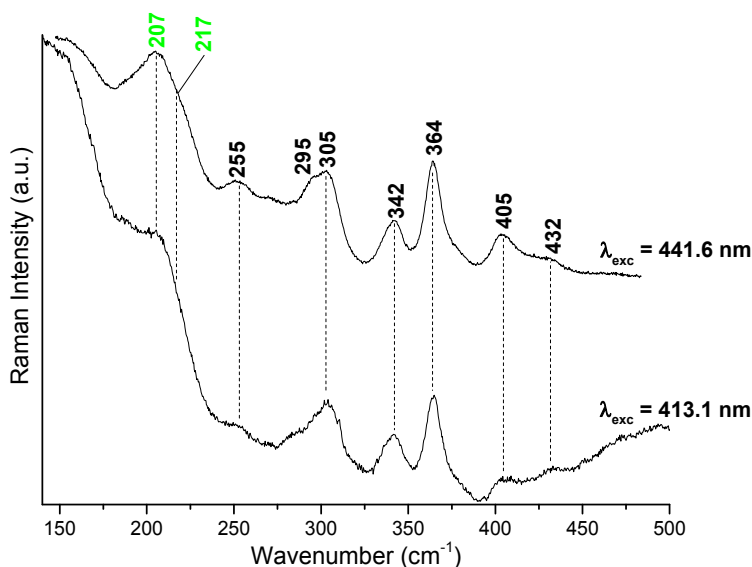


**Figure 7.6.** RR spectra in the low frequency region of the ferrous form of Hb3 obtained with the 413.1 nm (bottom) and 441.6 nm (up) laser lines. The spectra have been shifted along the ordinate axis to allow better visualization. Experimental conditions: excitation wavelength 413.1 nm, laser power at the sample 10 mW, average of 14 spectra with 70 min integration time (bottom); excitation wavelength 441.6 nm, laser power at the sample 10 mW, average of 10 spectra with 50 min integration time (up). The  $\nu(\text{Fe-Im})$  bands are shown in green.

#### 7.4 Conclusions

The spectroscopic characterisation of the three major Hbs expressed in the red blood cells of the Greenland shark *S. microcephalus* revealed that:

- the heme cavities of the three isoforms are identical both in the ferric and ferrous forms;
- in the ferric state the proteins undergo an alkaline transition from a pure 6cHS aquo species at pH 5.0 to His-Fe-OH<sup>-</sup> ligated forms, both 6cHS and 6cLS at pH 10.6;
- in the ferrous form the proteins are all 5cHS, being the  $\nu(\text{Fe-Im})$  of the  $\alpha$  and  $\beta$  subunits at 207 cm<sup>-1</sup> and 217 cm<sup>-1</sup>, respectively,
- the three Hb isoforms equally bind OH<sup>-</sup>, O<sub>2</sub> and CO ligands.

The results suggest that the *S. microcephalus* Hbs are structurally very similar to human HbA rather than to other Hbs from cold-adapted organisms where a hemichrome species (His-Fe-His) is the main form around pH 7.0 [Vitagliano 2004, Merlino 2011]. Accordingly, functional studies revealed no evidence for differentiation among the three isoforms, similar to other cartilaginous fishes, and also no cold-adaptation patterns to Arctic environment were found in the structure/function relationship of *S. microcephalus* Hbs.

## References

- ❖ Bigelow H.B., Schroeder W.C. (1948) Sharks. In Fishes of the Western Brittain T., Barber D., Greenwood C., Wells R.M., Comp. Biochem. Physiol. 1982, 72, 689.
- ❖ Brunner H., Naturwissenschaften 1974, 61, 129.
- ❖ Butler P.J., Metcalfe J.D. (1988) Cardiovascular and respiratory systems. In Physiology of elasmobranch fishes (Shuttleworth T.J. Ed.) pp. 1-47, Springer-Verlag, Berlin.
- ❖ Colbert E.H. (1955) Evolution of vertebrates (Wiley J. Ed.) New York.
- ❖ North Atlantic, Part 1 (Tee-Van J. Ed.) pp. 59-546, Yale University, New Haven, Connecticut.
- ❖ Dickinson F.M., Gibson Q.H., Biochem. J. 1981, 197, 436.
- ❖ Feis A., Marzocchi M.P., Paoli M., Smulevich G., Biochemistry 1994, 33, 4577.
- ❖ Fisk A.T., J. Fish Biol. 2012, 80, 991
- ❖ Hirota S., Ogura T., Appelman E.H., Shinzawa-Itoh K., Yoshikawa S., Hori H., Kitagawa T., J. Am. Chem. Soc. 1980, 102, 3608.
- ❖ Kitagawa T., Nagai K., Tsubaki M., FEBS Lett. 1979, 104, 376.
- ❖ Kitagawa T. (1988) The heme protein structure and the iron histidine stretching mode. In Biological Applications of Raman Spectroscopy: Resonance Raman spectra of hemes and metalloproteins (Spiro T.G. Ed.) Vol. 3, pp. 97-131, Wiley J. & Sons Inc., New York.
- ❖ Kitagawa T., J. Am. Chem. Soc. 1994, 116, 10564.
- ❖ Kovacs K.M., Lydersen C., Treble M.A., Skomal G.B., Ramsey M., Ladner R.C., Heidner E.J., Perutz M.F., J. Mol. Biol. 1977, 114, 385.
- ❖ MacNeil M.A., McMeans B.C., Hussey N.E., Vecsei P., Svavarsson J., Matsukawa S., Mawatari K., Yoneyama Y., Kitagawa T., J. Am. Chem. Soc. 1985, 107, 1108.

- ❖ Mecklenburg C.W., Møller P.R., Steinke D., *Mar. Biodiv.* 2011, 41, 109.
- ❖ Merlino A., Howes B.D., di Prisco G., Verde C., Smulevich G., Mazzarella L., Vergara A. *IUBMB Life* 2011, 63, 295-303.
- ❖ Nagai (a) K., Kitagawa T., Morimoto H., *J. Mol. Biol.* 1980, 136, 271.
- ❖ Nagai (b) K., Kitagawa T., *Proc. Natl. Acad. Sci. USA* 1980, 77, 2033.
- ❖ Nagatomo S., Nagai Y., Aki Y., Sakurai H., Imai K., Mizusawa N., Ogura T., Kitagawa T., Nagai M., *PLoS One* 2015, 10, e0135080.
- ❖ Nielsen J., Hedeholm R.B., Heinemeier J., Bushnell P.G., Christiansen J.S., Olsen J., Bronk Ramsey C., Brill R.W., Simon M., Steffensen K.F., Park S.Y., Yokoyama T., Shibayama N., Shiro Y., Tame J.R.H., *J. Mol. Biol.* 2006, 360, 690.
- ❖ Pennelly R.R., Noble R.W., Riggs A., *Comp. Biochem. Physiol.* 1975, 52, 83.
- ❖ Perutz M.F., Ladner J.D., Simon S.R., Ho C., *Biochemistry* 1974, 13, 2163.
- ❖ Rajani C., Kincaid R.J., *J. Am. Chem. Soc.* 1998, 120, 7278.
- ❖ Steffensen J., *Science* 2016, 353, 702.
- ❖ Skomal G.B., Benz G.W., *Mar. Biol.* 2004, 145, 489.
- ❖ Stein P., Mitchell M., Spiro T.G., *J. Am. Chem. Soc.* 1980, 102, 7795.
- ❖ Tsubaki M., Srivastava R.S., Yu N.T., *Biochemistry* 1982, 21, 1132.
- ❖ Verde C., De Rosa M.C., Giordano D., Mosca D., de Pascale D., Raiola L., Cocca E., Carratore V., Giardina B., di Prisco G., *Biochem. J.* 2005, 389, 297.
- ❖ Vitagliano L., Bonomi G., Riccio A., di Prisco G., Smulevich G., Mazzarella L. *European Journal of Biochemistry* 2004, 271, 9, 1651-1659.
- ❖ Weber R.E., Wells R.M., Rossetti J.E., *J. Exp. Biol.* 1983, 103, 109.
- ❖ Wells R.M., Davie P.S., *Comp. Biochem. Physiol.* 1985, 81, 643.